January 2016

STRUCTURE, GEOLOGY, AND ENGINEERING PROPERTIES OF TWO CARBONATIC FINE-GRAINED SOILS

Alain El Howayek
Purdue University

Graduate School Form
30 Updated 12/26/2015

PURDUE UNIVERSITY
GRADUATE SCHOOL
Thesis/Dissertation Acceptance

This is to certify that the thesis/dissertation prepared

By ALAIN EL HOWAYEK

Entitled
STRUCTURE, GEOLOGY, AND ENGINEERING PROPERTIES OF TWO CARBONATIC FINE-GRAINED SOILS

For the degree of Doctor of Philosophy

Is approved by the final examining committee:

ANTONIO BOBET Co-chair	DARREL G. SCHULZE
MARIA CATERINA SANTAGATA Co-chair	
DARRYL GRANGER	
JOSEPH V. SINFIELD	

To the best of my knowledge and as understood by the student in the Thesis/Dissertation Agreement, Publication Delay, and Certification Disclaimer (Graduate School Form 32), this thesis/dissertation adheres to the provisions of Purdue University's "Policy of Integrity in Research" and the use of copyright material.

Approved by Major Professor(s): Antonio Bobet and Maria Caterina Santagata

Approved by: DULCY ABRAHAM 7/14/2016

Head of the Departmental Graduate Program Date

STRUCTURE, GEOLOGY, AND ENGINEERING PROPERTIES OF TWO CARBONATIC FINE-GRAINED SOILS

A Dissertation

Submitted to the Faculty

of

Purdue University

by

Alain El Howayek

In Partial Fulfillment of the

Requirements for the Degree

of

Doctor of Philosophy

August 2016

Purdue University

West Lafayette, Indiana

FOR MY FAMILY

ACKNOWLEDGEMENTS

I would like to express my deep gratitude and appreciation to my major professors, Prof. Marika Santagata and Prof. Antonio Bobet for their continuous support and guidance throughout time at Purdue. They made my journey at Purdue very pleasant and unforgettable. Alongside my major professors, I would also like to thank the rest of my research committee members, Prof. Darryl Granger, Prof. Darrel Schulze, and Prof. Joseph Sinfield for their great assistance and support.

My work also received substantial help from the following people whom I am greatly indebted to: Mr. Sulaiman Dawood, Mr. Sriram Valavala, Ms. Francesca Palmieri, Ms. Mariah Schroeder, and Mr. Mohammad Sassar, for all their support and help with the experimental work; Dr. Gnanasiri Premachandran “Prema” in the Soil Chemistry laboratory of Purdue University’s Agronomy Department for his help on TGA and XRD tests; Ms. Debby Sherman who performed the SEM imaging; and Prof. Paul Muzikar and Mr. Ken Mueller who performed the radiocarbon dating. Special thanks to Prof. Vincent Drnevich, Prof. Philippe Bourdeau, Prof. Cliff Johnston, Prof. Jan Olek, Dr. Tommy Nantung, and Dr. Jusang Lee for their continuous encouragement and valuable advice.

Funding throughout my research was provided by the Joint Transportation Research Program administered by the Indiana Department of Transportation and Purdue University. Without their aid, this research work would have not been possible.

Many thanks to the wonderful friends I met at Purdue, whose company and support highlighted some of my most colorful and cheerful moments over the past few years: Amy Getchell, Fei Tao, Yu-Chung Lin, Sung Soo Park, Jeehee Lim, Linna Duan, Pao-Tsung Huang, Qiang Li, Yu Tian, Ursula Merchak, Gabriella Alvarado, and Ruben Tovar. I express my sincere gratitude to my parents for their prayer, support and unconditional love.

TABLE OF CONTENTS

Page

Page

Page

Page

Page

LIST OF TABLES

Table Page

Table Page

LIST OF FIGURES

Figure Page

Figure Page

Figure Page

Appendix Figure

Figure Page

Figure Page

Figure Page

Figure Page

Figure Page

Figure Page

Figure Page

Figure Page

ABSTRACT

El Howayek, Alain. Ph.D., Purdue University, August 2016. Structure, Geology, and Engineering Properties of Two Carbonatic Fine-Grained Soils. Major Professors: Marika Santagata and Antonio Bobet.

Soft, carbonate-rich, fine-grained soils are commonly found in the glaciated regions of the northern United States and throughout Canada. In addition to the high compressibility potential and low shear strength, these sediments are typically characterized by alternating layers of silts and clays as well as high calcium carbonate content. The unique properties of these deposits make them challenging soils for geotechnical engineers. Despite the prevalence of soft carbonatic soils in Indiana and the concerns associated with their behavior, very limited work has been done to study their engineering properties. This was the motivation for the research, which is founded on an in-depth characterization of a glaciolacustrine carbonatic fine-grained soil deposit formed about 22,000 calendar years ago in the southwestern part of the State of Indiana, USA. The aim of the investigation was the developing of improved knowledge of the behavior of carbonatic fine-grained soils.

The project involved field tests (seismic cone penetration tests, standard penetration tests, field vane shear tests), and laboratory experiments (index tests, incremental and constant rate of strain consolidation tests, and K_0-consolidated undrained triaxial tests) conducted on high quality Shelby tube samples. Additionally, the mineralogy and microstructure of the soil was studied in detail.

The laboratory tests revealed that the deposit was not homogeneous, as was initially anticipated, but was, instead, formed by two types of soils that repeated

in horizontal thin layers. These two soils, referred to as ‘soil M’ and ‘soil C’, both had very high calcium carbonate content, but show distinct index and engineering properties that were ascribed to differences in mineralogy and composition. This stratification was not detected by the field tests. A detailed study of the local geology combined with the observations of the differences between the morphology of pyrite and the clay mineral composition between the two soils, as well as the presence of biological intrusions in only one of the two soils, suggest that different source materials and sedimentary environments alternated during the formation process of the deposit.

The microstructural investigation showed that the soil consisted of clay platelets that were covered by a thin layer of a carbonatic coating and interconnected by carbonatic bridges to form aggregates. The laboratory results showed that these interparticle bonds altered the macroscopic behavior of the soil (i.e. index and engineering properties).

The consolidation tests showed that the deposit had an overconsolidation ratio (OCR) less than 2 and compressibility parameters markedly dependent on stress. K_0-consolidated undrained compression triaxial tests showed that both soils exhibited normalized behavior and that the relationship between strength and stress history was well described by the SHANSEP equation (although the SHANSEP parameters differed for the two soils).

Comparison of the field data and laboratory results provided the means to validate published correlations for interpretation of the geotechnical properties of carbonatic soils from field results. For the site examined, correlations to estimate shear wave velocity, stress history, and undrained strength from cone penetration tests (CPT) results were identified.

Keywords: Carbonatic soil, marl, lacustrine deposit, cementation, mineralogy, structure, geologic origin, radiocarbon dating, depositional environment, consolidation properties, undrained shear strength, SHANSEP

CHAPTER 1. INTRODUCTION

1.1. Problem Statement

Fine-grained carbonatic soils are commonly found in glaciated regions of the northern United States and throughout Canada (Boone & Lutenegger, 1997; IDOT, 1999; INDOT, 2010; MDOT, 2009; ODOT, 2010), and Europe (Bozzano et al., 1999; Jamiolkowski et al., 1995; Hawkins et al., 1988; Tsiambaos, 1991; Anagnostopoulos et al., 1991; Paaza et al., 1998; and Lamas et al., 2002). The properties of these soils vary depending on their origin, geological history, mineral composition, and the percentage of calcium carbonate, which typically precipitates at the inter-particle contacts resulting in a form of cementation (bonding). Depending on the degree of cementation, these materials can vary from very soft weakly-cemented sediments (e.g. Boone & Lutenegger, 1997) to abnormally stiff deposits (e.g. Anagnostopoulos et al., 1991).

There has been a wide discussion in the literature about the impact of cementation on the mechanical properties of soils, including compressibility, shear strength, stiffness and sensitivity. For instance, many researchers have investigated the effect of cementation on the compressibility characteristics of natural deposits (e.g. Bjerrum & Wu, 1960; Kenney et al., 1967; Loiselle et al., 1971; Sangrey, 1972; Fischer et al., 1978; McGown & Ladd, 1982; Jamiolkowski et al., 1985; Allman & Poulos, 1988; Burghignoli et al. 1991; Boone & Lutenegger, 1997; Burghignoli et al., 2010). They all reported that cementation typically creates an apparent preconsolidation stress that is larger than the geological preconsolidation stress, which is attributed to the interparticle cementation bonds.

Soft carbonatic soils deposits are found in the State of Indiana with layers as thick as 6 m, at relatively shallow depths (3 to 5 m) below the ground surface. These sediments are commonly fine-grained glacio-lacustrine deposits. The characteristic of these deposits, as in most glacial lake deposits, are the high calcium carbonate content (e.g. Boone & Lutenegger, 1997) and the alternating layers of silts and clays (e.g. Thornbury, 1950; DeGroot & Lutenegger, 2003; and Long, 2003). They are also characterized by high natural water content and Atterberg limits; high compressibility and creep potential; and low shear strength.

The unique properties of soft carbonatic deposits make them challenging soils for geotechnical engineers in many aspects: (1) the increased sensitivity caused by carbonate cementation results in a material that is more susceptible to disturbance during construction or excavation; (2) carbonate cemented soils can be subject to decalcification induced by groundwater flow and/or intense rainfall events, which can lead into the degradation of the mechanical properties and enhance slope instability (e.g. Monastero Bormida landslide, Italy [Musso et al., 2008]); (3) the heterogeneity caused by the alternating layers of carbonatic silts and carbonatic clays creates difficulties when relating laboratory test results to anticipated field behavior; (4) the high compressibility and low shear strength poses concerns related to excessive settlement, slope instability, and increased downdrag on deep foundations. When constructing on these soils, wick drains are commonly used to accelerate consolidation and/or preloading to improve the shear strength of the deposit and, in some cases, more costly solutions such as deep foundations are employed (Andromalos et al., 2001).

Despite the prevalence of carbonatic soils around the world and the challenges associated with their macroscopic engineering behavior, there is still a lack of fundamental understanding of the microstructure of these soils and the different forms of carbonates that may be present in the soil altering particle-level interactions at the microscopic scale. This was the motivation for the research

presented in this thesis which is founded on an in-depth characterization of two soft carbonatic fine-grained soils. The soils are found as alternating layers in a glaciolacustrine carbonatic deposit formed about 22,000 calendar years ago in the southwestern part of the State of Indiana, USA. The characterization pertains not only to the mechanical properties of the soil through intensive geotechnical field tests and laboratory consolidation and shear tests on intact samples, but also to the relationship of these properties with their mineralogy at the nano- and micro-scale; electro-chemical bonding between particles at micro-scale; the biological intrusions (fossils and algae) at the meso-scale; and the depositional environments at the macro- and geological scale.

1.2. Research Objectives and Approach

Within the broad scope of developing an improved knowledge of the behavior of carbonatic fine-grained soils, the specific objectives of the research presented in this thesis are:

a) Characterize the engineering properties (i.e. consolidation, creep and undrained shear strength behavior) of a glaciolacustrine carbonatic deposit using state of the art methods for conducting and interpreting tests to provide a framework that could aid in better understanding the engineering behavior of soft carbonatic fine-grained soils;
b) Gain a fundamental understanding of the relationship between the geological depositional environment and the differences in mineralogy, microstructure, and mechanical properties observed between the two alternating carbonatic soils in the deposit.
c) Assess the influence of carbonate cementation at the inter-particle contacts on the macro-behavior of the soil and gain a fundamental understanding of the different forms of bonding that can be caused by carbonates precipitated between particles;
d) Integrate the laboratory and field data to develop recommendations for the interpretation of geotechnical properties from field results.

The research objectives outlined above were pursued through an extensive experimental program that included:

a) Field program: a site characterized by a layer of soft carbonatic soil of significant thickness was selected in the southwestern part of the State of Indiana, USA. Seismic cone penetration tests with pore pressure measurements (SCPTu); standard penetration tests (SPT) for soil profiling and collection of disturbed samples; and field vane shear tests to determine the undrained shear strength and soil sensitivity were conducted as part of the in-situ testing program. Additionally, an open pipe piezometer was installed to locate the groundwater table. High quality Shelby tube samples were obtained for laboratory tests.

b) Analysis of the mineralogy and the microstructure: X-ray diffraction (XRD), thermogravimetric analysis (TGA), and scanning electron microscopy (SEM) equipped with energy dispersive X-ray (EDX) spectroscopy, optical light microscopy (LM), and carbonate dissolution using chemical treatment were performed on samples of the two main soil types identified in the carbonatic soil layer.

c) Assessment of the index properties: this portion of the experimental program consisted of performing index tests (Atterberg limits, natural water content, LOI, $CaCO_3$ content, pH, salinity, specific gravity, and particle size distribution analysis) on samples over the entire thickness of the deposit.

d) Assessment of the engineering properties: this included (i) incremental and constant rate of strain consolidation tests to derive the stress history, consolidation and creep properties; (ii) shear strength tests for derivation of the undrained shear strength profiles and the soil's SHANSEP parameters.

e) Integration of field and lab results: this portion of the work focused on the analysis of the field vane (FV) shear tests and the cone penetration test

(CPT) data in conjunction with the laboratory results to develop site-specific correlations.

1.3. Organization of the Thesis

This thesis is organized in five chapters that present the outcome of an intensive experimental characterization of two carbonatic fine-grained soils obtained from the lacustrine deposit in Southwestern Indiana. Chapters 2, 3, and 4 are extracted from draft manuscripts to be submitted for publication. The content of each of the five chapters that form this thesis is briefly described in the following paragraphs.

Chapter 1 presents a concise description of the problem under investigation and a general overview of the topic. It explains the motivation for the research presented in this thesis, framing it in the context of other carbonatic soils reported in the literature; and outlines the objectives and approach of the work.

Chapter 2 provides a thorough investigation of the site geology and the age of the deposit, which aims at understanding the geological depositional environment and relating geology to the differences observed between the properties of the two carbonatic soils that were found in alternating layers. This chapter also presents the study of the mineralogy of the soils, which plays an important role on their macro-behavior.

Chapter 3 deals with the characterization of the microstructure of the two carbonatic soils through a combination of direct microscopic observations by SEM and indirect examinations by EDX, carbonate dissolution using chemical treatment, XRD, Atterberg limits, and particle size analyses. The unusual index and consolidation properties exhibited by the soils are related to the effect of carbonates cementation at the interparticle contacts. This chapter also proposes a novel laboratory technique to produce artificially cemented clays that better

resembles the natural formation process of carbonatic soils in lacustrine sediments.

Chapter 4 deals with the engineering properties of the carbonatic deposit based mainly on laboratory consolidation and shear tests on intact samples of the soil. The chapter highlights the differences observed between the properties of the two carbonatic soils and relates these engineering properties to the fundamental differences in the geological depositional environment, mineralogy, and microstructure.

The main conclusions drawn from this work are summarized in Chapter 5, which also provides recommendations for future research work.

This thesis also includes twelve appendices that are extracted from the report “Engineering properties of marls” by El Howayek et al. (2015). These appendices present a brief literature review on the origin of carbonates in lacustrine deposits and structured soils (APPENDIX A), as well as in-depth characterization of two soft fine-grained carbonatic soils located in the State of Indiana. This includes a thorough investigation of the geological properties of the site and geotechnical field testing program (APPENDIX B); an intensive experimental characterization of the mineralogy, microstructure and index properties (APPENDIX C); and engineering properties (APPENDIX D); an integration of laboratory and field data to develop recommendations for the interpretation of geotechnical properties from field results (APPENDIX E). Additional supporting information is provided in the remaining appendices: summary of boring logs (APPENDIX F), piezocone penetration profiles (APPENDIX G), field vane shear tests results (APPENDIX H), summary log showing the depth and location of the laboratory engineering tests (APPENDIX I), carbon dating calibration curves (APPENDIX J), properties of an artificially cemented clay (APPENDIX K), and derivation of calcite solubility as a function of CO_2 partial pressure (APPENDIX L).

1.4. References

Allman, M.A. & Poulos, H.G. (1988). Stress-strain behaviour of an artificially cemented calcareous soil. Proceedings of International Conference on Calcareous Soil (Perth), Balkema, 1, pp. 51-60.

Anagnostopoulos, A.G., Kalteziotis, N., Tsiambaos, G.K., & Kavvadas M. (1991). Geotechnical properties of the Corinth Canal marls. Geotechnical and Geological Engineering, 9, pp. 1-26.

Andromalos, K., Hegazy, Y., & Jasperse, B. (2001). Stabilization of soft soils by soil mixing. In J.L. Hanson & R.J. Termaat (Eds.), Soft ground technology (pp. 194-205). ASCE, Noordwijkerhout, the Netherlands.

Bjerrum, L. & Wu, T.H. (1960). Fundamental shear strength properties of the Lilla Edet clay. Geotechnique, 10, pp. 101-109.

Boone, S.J. & Lutenegger, A.J. (1997). Carbonates and cementation of glacially derived cohesive soils in New York State and southern Ontario. Canadian Geotechnical Journal, 34, pp. 534-550.

Bozzano, F., Marcoccia, S., & Barbieri, M. (1999). The role of calcium carbonate in the compressibility of Pliocene lacustrine deposits. Quarterly Journal of Engineering Geology, 32, pp. 271-289.

Burghignoli, A., Cavalera, L., Chieppa, V., Jamiolkowski, M., Mancuso, C., Marchetti, S., Pane, V., Paoliani, P., Silvestri, F., Vinale, F., & Vittori, E. (1991). Geotechnical characterization of Fucino clay. 10th European Conference on Soil Mechanics and Foundation Engineering (Florence), 1, pp. 27-40.

Burghignoli, A., Miliziano, S., & Soccodato, F.M. (2010). Cementation effects in two lacustrine clayey soils. Geotech Geol Eng, 28, pp. 815-833.

DeGroot, D.J. & Lutenegger, A.J. (2003). Geology and engineering properties of Connecticut Valley Varved Clay, Proceedings of the International Workshop on Characterization and Engineering Properties of Natural Soils, 1, pp. 695-724.

El Howayek, A., Santagata, M., Bobet, A., & Siddiki, N.Z. (2015). Engineering properties of marls. Publication FHWA/IN/JTRP-2015/11. Joint Transportation Research Program, Indiana Department of Transportation and Purdue University, West Lafayette, Indiana.

Fischer, K.P., Andersen, K.H., & Moum, J. (1978). Properties of an artificially cemented clay. Canadian Geotechnical Journal, 15, pp. 322-331.

Hawkins, A.B., Lawrence, M.S., & Privett, K.D. (1988). Implication of weathering on the engineering properties of the Fuller's Earth formation. Geotechnique, 38, pp. 517-532.

IDOT (1999). Geotechnical Manual. Illinois Department of Transportation. Springfield.

INDOT (2010). Geotechnical Manual. Indiana Department of Transportation. Indianapolis.

Jamiolkowski, M., Lancellotta, R., & Lo Presti, D.C.F. (1995). Remarks on the stiffness at small strains of six Italian clays. Pre-failure Deformations of Geomaterials, 2, pp. 817-836.

Kenney, T.C., Moum, J., & Berre, T. (1967). An experimental study of bonds in a natural clay. Proceedings of the Geotechnical Conference (Oslo), 1, pp. 65-69.

Lamas, F., Irigaray, C., & Chacon, J. (2002). Geotechnical characterization of carbonate marls for the construction of impermeable dam cores. Engineering Geology, Elsevier, 66, pp. 283-294.

Loiselle, A., Massiera, M., & Sainani, U.R. (1971). A study of the cementation bonds of the sensitive clays of the Outardes River region. Canadian Geotechnical Journal, 8, pp. 479-498.

Long, M. & Lunne, T. (2003). Stiffness of Onsoy clay. In Deformation Characteristics of Geomaterials, Di Benedetto et al. (Eds.), Swete & Zeitlinger, Lisse, pp. 151-158.

McGown, A.F. & Ladd, C.C. (1982). Effects of cementation on the compressibility of Pierre shale. In: K.R. Demars & R.C. Chaney (Eds.). Geotechnical properties, behaviour and performance of calcareous soils. ASTM Special Technical Publication, pp. 320-339.

MDOT (2009). Uniform Field Soil Classification System (Modified Unified Description). Michigan Department of Transportation. Lansing.

Musso, G., Chighini, S., & Romero, E. (2008). Mechanical sensitivity to hydrochemical proceses of Monastero Bormida clay. Water Resources Research, 44.

ODOT (2010). Specifications for Geotechnical Explorations. Ohio Department of Transportation. Columbus.

Paaza, E.A., Lamas, F., Irigaray, C., & Chacon, J. (1998). Engineering geological characterization of Neogene marls in the southeastern Granada basin, Spain. Engineering Geology, 50, pp. 165-175.

Sangrey, D.A. (1972). On the causes of natural cementation in sensitive soils. Canadian Geotechnical Journal, 9, pp. 117-119.

Thornbury, W.D. (1950). Glacial sluiceways and lacustrine plains of southern Indiana. Indiana Geological Survey Bulletin, 4, 21 p.

Tsiambaos, G. (1991). Correlation of mineralogy and index properties with residual strength of Iraklion marls. Engineering Geology, 30, pp. 357-369.

CHAPTER 2. GEOLOGIC ORIGIN EFFECTS ON MINERALOGY, INDEX PROPERTIES AND FABRIC OF A FINE-GRAINED CARBONATIC DEPOSIT[1]

2.1. Introduction

The mechanical properties of soils depend directly upon the chemical and mineralogical compositions and the state of structure – defined by Lambe & Whitman (1969) as the combination of "fabric" (i.e., the arrangement of particles) and interparticle "bonding" (i.e., the electro-chemical forces at the inter-particle contacts). Geologic origin and depositional (and post-depositional) environments play a critical role in determining both composition and structure, and are ultimately responsible for the extraordinary range in behavior observed in natural soils, as well as for the "unusual" response exhibited by some geomaterials.

A number of examples can be cited to illustrate the effects of the depositional environment on the characteristics of lacustrine deposits, which represent the focus of this paper: the unique properties (high porosity, plasticity, compressibility, friction angle and linear threshold) of Mexico City clay, the upper section of the Pleistocenic fill underlying Mexico City, derive from the deposition on the water of the lake of volcanic ash and other pyroclastic materials, as well as from the lake conditions that promoted proliferation of diatoms and other microorganisms (e.g. Covarrubias, 1994); varved clays (e.g. DeGroot & Lutenegger, 2003), formed by the alternation of silt-fine sand and clay layers, and encountered in the glaciated regions of North America and Europe, illustrate how changes in the seasonal

[1] This chapter is extracted from the draft manuscript "geologic origin effects on mineralogy, index properties and fabric of a fine-grained carbonatic deposit", to be

depositional environment can lead to a soil structure characterized by repeating layers and marked cross-anisotropy; the variation in clay mineral composition and distribution in the Atchafalaya basin in Louisiana demonstrates the effects of differences in energy and geochemistry of the depositional environments (e.g. backswamp versus lacustrine) responsible for the formation of these soils (Stewart & Patrick, 1990).

This paper intends to further the understanding of the relationship between the characteristics of natural soils and their geologic history of sedimentation, by contributing findings for a soft lacustrine carbonatic deposit formed during the Wisconsin glaciation (~ 22,000 calendar years ago) in the southwestern part of the State of Indiana, USA. The work is founded on an in-depth characterization of an approximately 4m thick soft soil layer formed by the repetition of small layers of two different soils with distinct composition and engineering properties. The paper discusses in detail the differences in index properties between these two soils and their relationship to the mineralogical composition derived from XRD analyses. Scanning electron microscopy observations are used to provide a detailed description of the microstructure of the two soils, including the biological intrusions present and the morphology of select minerals.

Collectively, these observations, complemented by a study of the local geology, are used to formulate hypotheses on the geologic processes and depositional environments responsible for the formation of the deposit.

2.2. Geographical Location and Soil Profile

The site investigated in this work is located at the intersection of County Road 900 E and County Road 1650 N, Madison, Daviess County, Indiana, about 85 miles southwest of Indianapolis (see Figure 2-1).

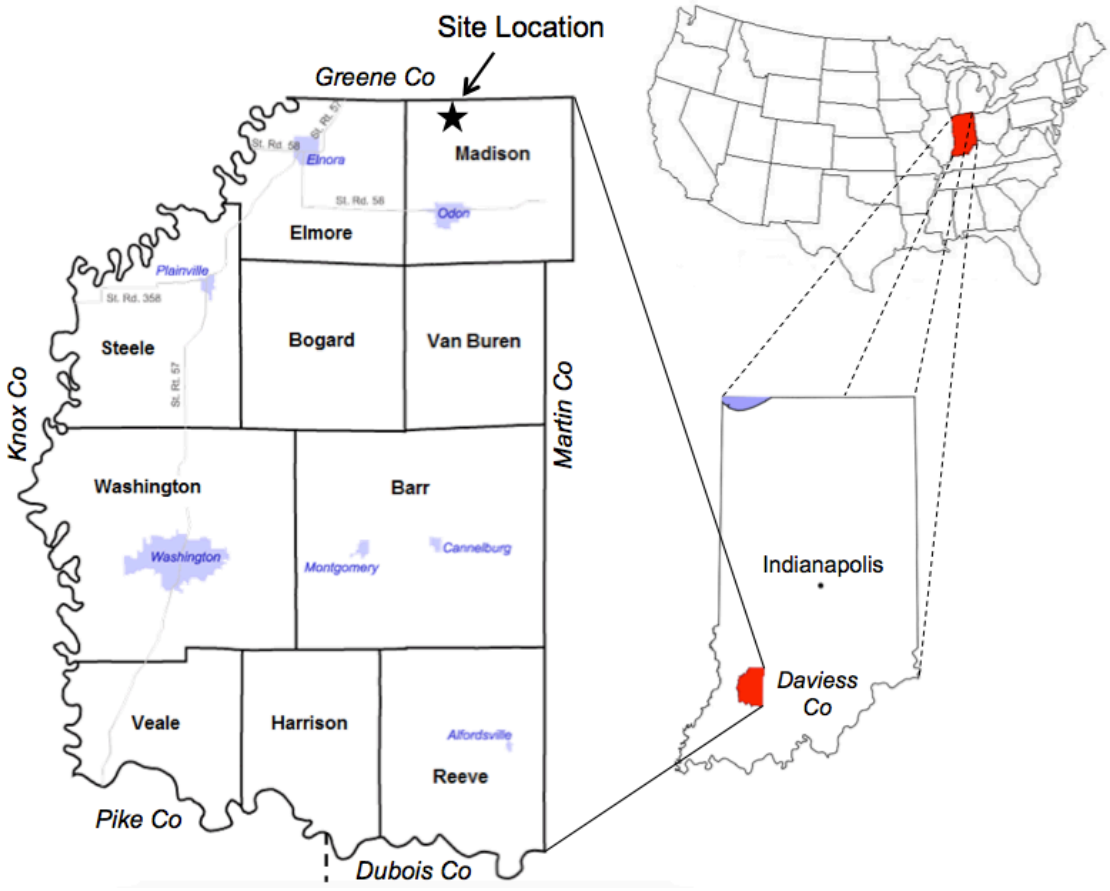

Figure 2-1: Map showing the location of the site in Daviess County (Indiana, USA)

The average ground elevation of the site was determined using a leveler as 150.8 m. The site is adjacent to a creek (First Creek), which controls the water table, and produces frequent flooding (Isee, 2016). Monitoring of the water table level in a 50.8 mm diameter open pipe piezometer over a period of 16 days in November-December 2011 showed an average depth of the water table of 1.9 m below the ground surface. Groundwater conditions are hydrostatic.

Seven seismic cone penetration tests with pore pressure measurements (SCPTu) were conducted at the site in an area approximately 7 m x 9 m. Figure 2-2 shows the variation with depth of tip resistance, skin friction and pore water pressure measured immediately behind the cone tip (u_2), obtained from the seven CPTs (dashed gray lines), as well as the average curve (continuous black line). The

CPT results clearly identify the presence of a very soft (q_t ~ 500 kPa and f_s ~ 7 kPa), low permeability (high u_2) layer at a depth ranging between approximately 4.5 m and 10.4 m.

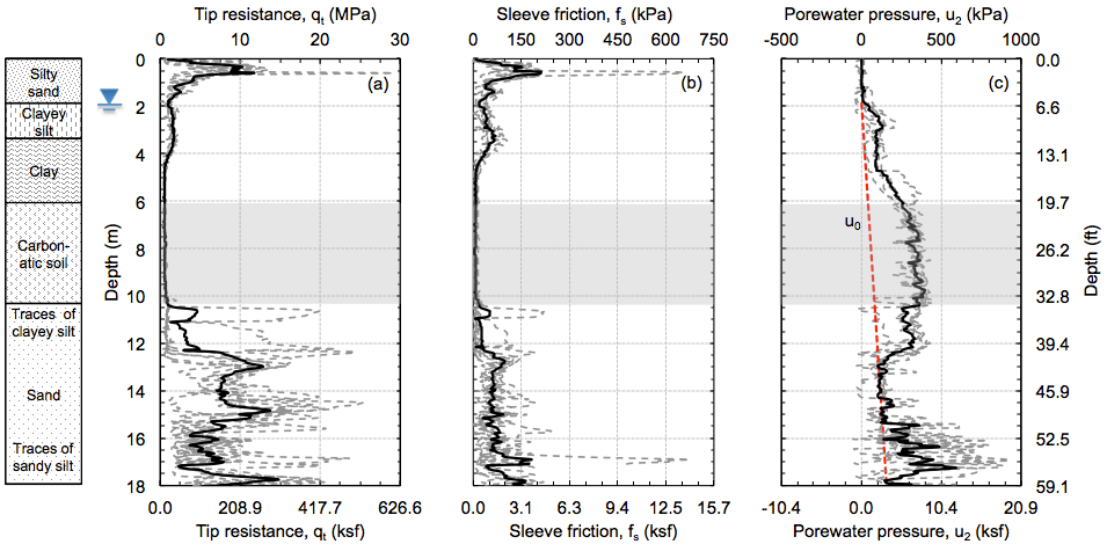

Figure 2-2: CPT results: (a) tip resistance, (b) skin friction, and (c) porewater pressure versus depth

Within this portion of the deposit, starting at a depth of 6.1 m, with a thickness of ~4.3 m, lies the soft carbonatic soil layer examined in this work (highlighted in gray in Figure 2-2). This is shown in Figure 2-3 which presents the average soil profile determined based on observations made in the field, examination of the samples used for the laboratory tests and the results of the SCPT tests. Above the carbonatic layer are about 1.9 m of silty sand, 1.5 m of clayey silt and 2.7 m of clay. Below it is a sand layer with occasional traces of clayey silt and sandy silt. The bedrock, mostly sandstone with highly weathered surface, is located at a depth of about 37 m.

A total of 69 boreholes, drilled as part of the construction of the interstate I-69 (Alt & Witzig, 2010; Earth Exploration, 2010), were used to develop the geotechnical crossection at the site shown in Figure 2-4. The bedrock, mostly sandstone with a highly weathered surface, has a basin shape with depth as great as ~37 m in

the middle of the site and as shallow as ~3 m at the edges, which favored the formation of the glacial lake in which the soil was deposited. The carbonatic deposit is found in the middle of the basin with a width of approximately 1,150 m and a maximum thickness of approximately 10 m.

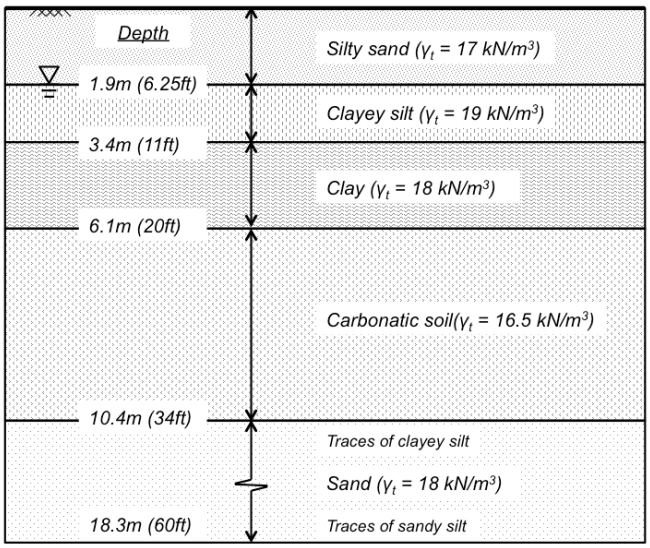

Figure 2-3: Stratigraphy of the site

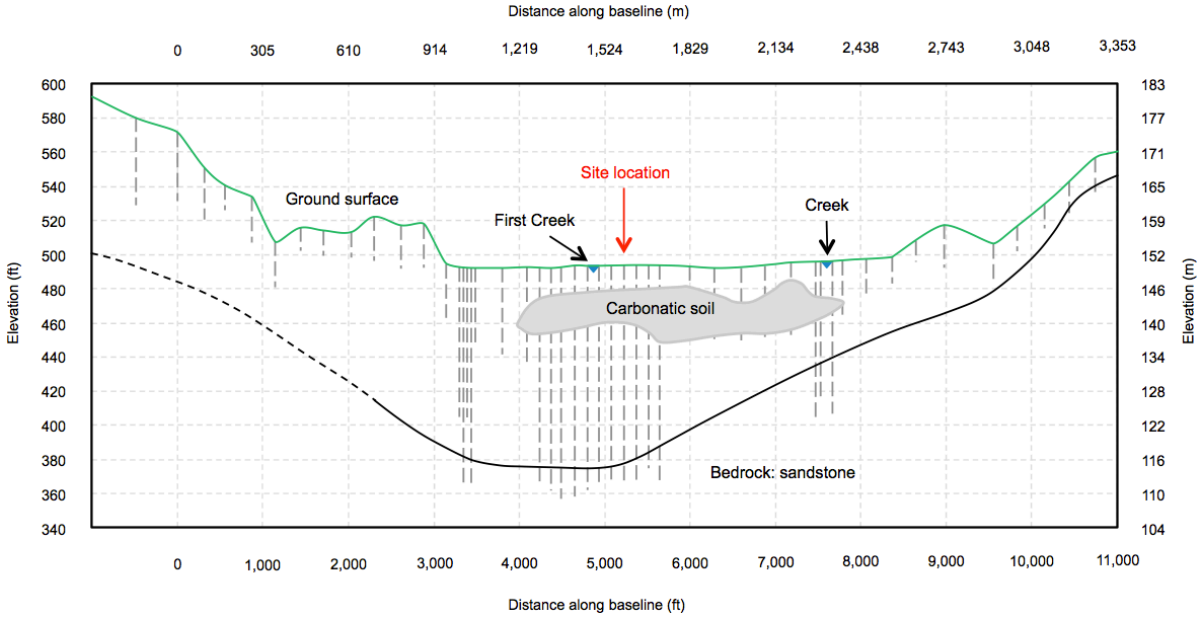

Figure 2-4: Geotechnical cross-section of the deposit

2.3. Soil Characteristics

2.3.1. A Dual Layer Repeating Deposit

Extensive characterization of the soft soil layer comprised between 6.1 m and 10.4 m was performed in the laboratory relying on Shelby tube samples collected in the field in the same area investigated by the SCPTs. Examination of these samples revealed that the layer was not homogenous as was initially anticipated, but was formed by two types of soils, both rich in carbonates, that repeated in horizontal thin sublayers. These two soils are herein referred to as “soil M” and “soil C”. This denomination was selected based on the fact that, as will be shown below, the soils can be classified as a silt and clay, respectively, according to the Unified Soil Classification System (ASTM D2487-11, 2011). Figure 2-5 shows soil samples composed of both soil M and soil C. The figure highlights the clear difference between the two sublayers in terms of color and texture, with shells identified in soil M. Soil C was found in thin layers of thickness ranging between 0.5 cm and 10 cm, whereas soil M was found in thicker layers and represented the majority of the carbonatic layer. The field exploration failed to detect the presence of these sublayers.

As discussed in more detail below, both soils are characterized by high calcium carbonate content (over 55% and close to 40%, for soil M and soil C, respectively), but show distinct index and engineering properties, requiring that they be characterized separately.

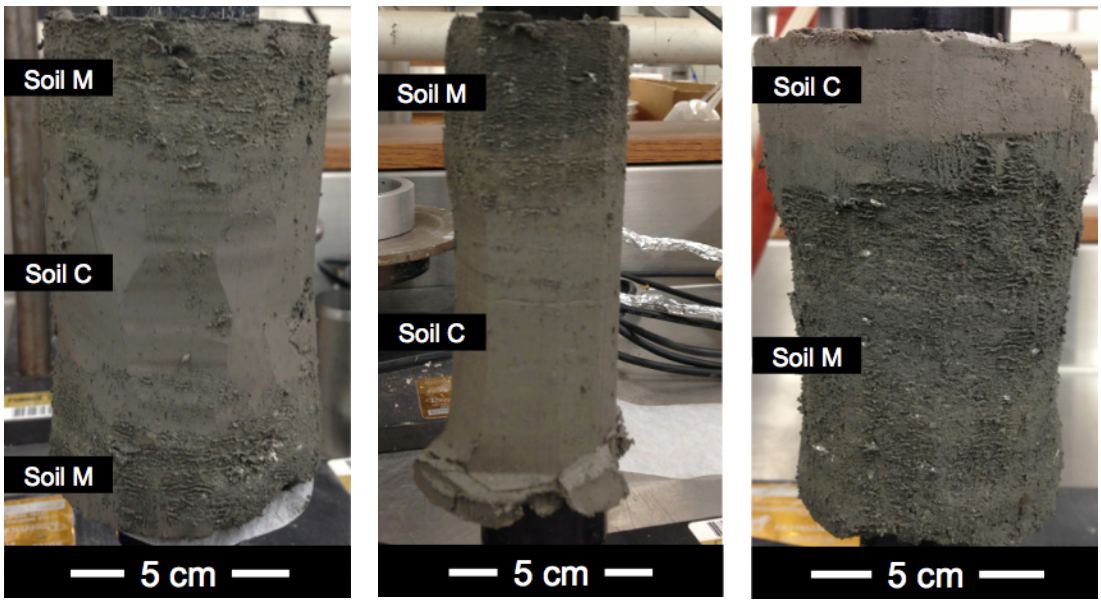

Figure 2-5: Soil samples showing layers of soil M and soil C

2.3.2. Index Properties

Index tests were conducted on a total of 28 soil samples obtained from different depths of the soil deposit. Index properties measured included: loss on ignition (as a means to quantify the organic content), calcium carbonate content, Atterberg limits, natural water content, particle size distribution, specific gravity, void ratio, total unit weight, degree of saturation, salt concentration, and pH. See APPENDIX C for a description of the methods used and a detailed presentation and discussion of the results. Key index properties for soils M and C are summarized in Figure 2-6 and Table 2-1. In general, soil M is characterized by lower specific gravity, unit weight and clay content, and higher void ratio, water content, Atterberg limits, and $CaCO_3$ content. In particular, the average $CaCO_3$ content of soil M is about 55%, compared to 38% for soil C. A characteristic specific to soil M is the presence of shells, which is, in part, responsible for the higher void ratio. In general, for each soil type the index properties show no particular trend with depth. An exception is the void ratio of soil M, which decreases with depth.

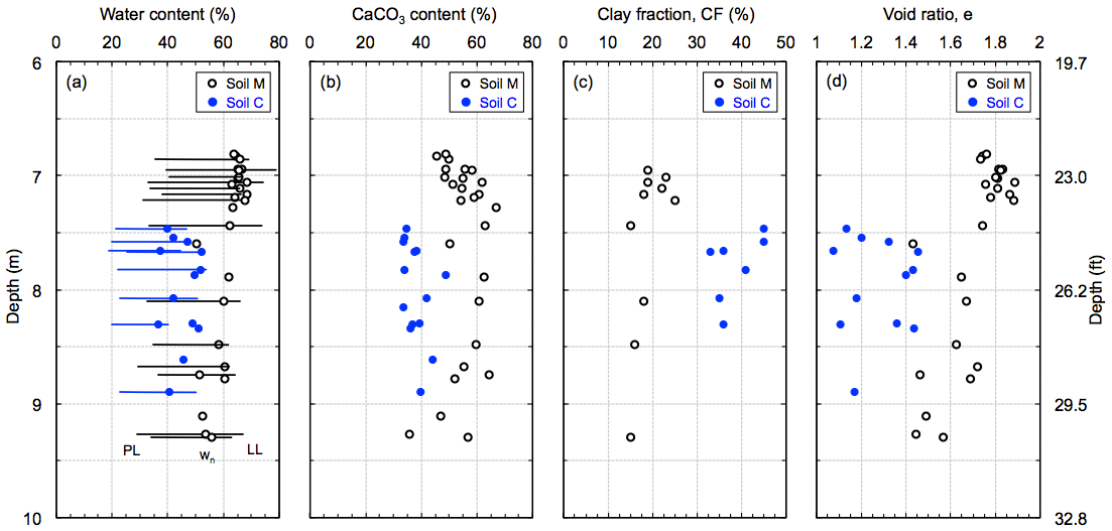

Figure 2-6: (a) Water content and Atterberg limits, (b) calcium carbonate content, (c) clay fraction, and (d) void ratio profiles of the carbonatic soil

The liquid limit (LL) and the plasticity index (PI) of all the specimens from the carbonatic soil layer are plotted on the plasticity chart in Figure 2-7. For the most part, the data points for soil M plot below the A-line, leading to classify this soil as an elastic silt (MH) according to the unified soil classification system (USCS). The results for soil C plot above the A-line and the soil is classified as a lean clay (CL) according to the USCS.

Figure 2-8 shows the particle size distribution curves obtained from fourteen hydrometer tests, with the curves for soil M and soil C falling on two distinct bands. Both soils have a fine fraction (<75 μm) greater than 96%. The small percentage of sand-size particles found in soil M (< 4%) consists mainly of shells. As summarized in Table 2-1, the average percentage of clay size particles in soil C is approximately twice that observed in samples of soil M.

The higher plasticity of soil M is not consistent with typical trends reported in the literature of increasing LL and PI with higher clay content. It is also inconsistent with the data reported by other researchers (e.g. Lamas et al., 2002; Cotecchia & Chandler, 1995) for other carbonatic fine-grained soils, which show that LL and

PI tend to both decrease with increasing calcium carbonate. As discussed in the following section, this difference can be ascribed to variations in the mineralogy of the clay fraction of the two soils, as both the type and amount of clay in a soil influence the Atterberg limits.

Table 2-1: Summary of index properties

	Soil M		Soil C	
	Range	Mean ± SD[a]	Range	Mean ± SD[a]
Loss on ignition (%)[b]	2.0 – 4.3	3.0 ± 0.6	1.7 – 3.2	2.5 ± 0.4
$CaCO_3$ content (%)[c]	35.9 – 66.8	55.2 ± 7.6	33.7 – 48.8	38.1 ± 4.5
Water content, w_n (%)	50.5 – 68.5	61.6 ± 5.8	36.6 – 52.2	44.3 ± 5.7
Plastic limit, PL (%)	29.0 – 40.6	34.4 ± 3.4	18.8 – 25.5	21.6 ± 2.1
Liquid limit, LL (%)	61.7 – 78.8	67.4 ± 5.0	40.1 – 53.7	48.3 ± 4.4
Liquidity index, LI	0.5 – 1.1	0.8 ± 0.2	0.6 – 1.0	0.8 ± 0.1
Silt content (%)	69.0 – 82.0	76.7 ± 3.9	54.0 – 66.0	60.6 ± 5.2
Clay fraction, CF (%)	15.0 – 25.0	19.0 ± 3.4	33.0 – 45.0	38.7 ± 4.9
Specific gravity, G_s	2.68 – 2.76	2.71 ± 0.02	2.76 – 2.82	2.78 ± 0.02
Void ratio, e	1.4 – 1.9	1.7 ± 0.2	1.1 – 1.5	1.3 ± 0.1
Total unit weight, γ_t (kN/m^3)	15.4 – 16.8	15.9 ± 0.4	16.8 – 18.3	17.5 ± 0.5
Degree of saturation, S_i (%)	95.3 – 100	97.9 ± 1.4	93.2 – 100	97.9 ± 1.8
Salt concentration (g/l)	2.1 – 3.8	3.0 ± 0.5	2.2 – 5.1	3.6 ± 1.2
Salt concentration (g/kg)	1.4 – 2.2	1.9 ± 0.2	0.9 – 1.9	1.5 ± 0.4
1:1 water pH	7.5 – 7.9	7.8 ± 0.1	7.6 – 7.9	7.8 ± 0.1

[a] SD: Standard Deviation

[b] LOI measured following 6 hours at 455ºC based on AASHTO T267-86 (AASHTO, 2008)

[c] Based on sequential loss on ignition method (455ºC for 6 hours and 800ºC for additional 6 hours) (Jung et al., 2011)

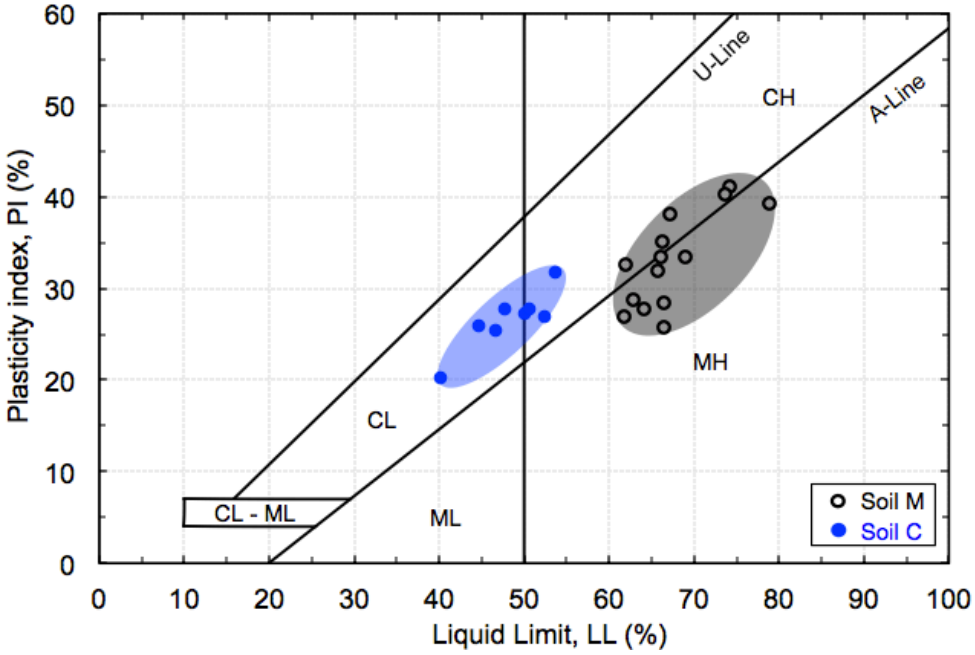

Figure 2-7: Plasticity chart with data for soils M and C

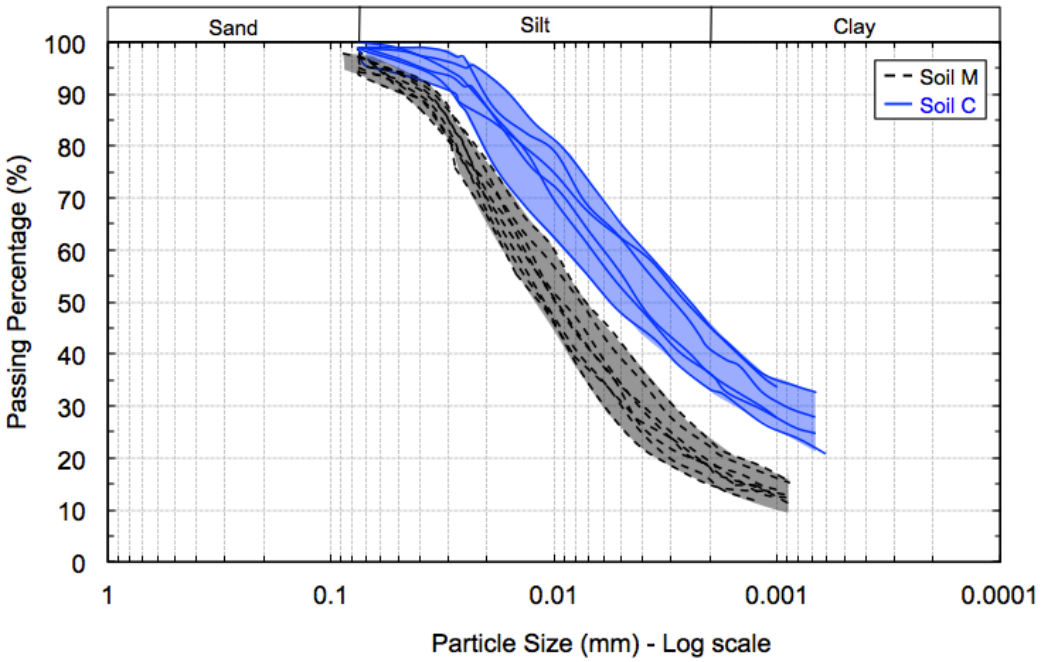

Figure 2-8: Results of particle size analyses on soils M and C

2.3.3. Mineral Composition

The mineral composition of the two soils identified in the soft carbonatic layer (soils M and C) was determined using X-ray diffraction (XRD) analysis on both randomly-oriented powder and oriented aggregates. The former requires a random orientation of the particles and is typically used to identify the non-clay minerals found in the soil (e.g. quartz, feldspars, and carbonates), while the latter requires all platy particles to have preferred orientation in the XRD samples and is generally used to identify clay minerals. Details on the procedures, analyses, and results are provided in APPENDIX C. X-ray diffraction patterns were obtained using a PANalytical B.V. (Model X'Pert PRO diffractometer; Almelo, Netherlands) diffractometer using Co radiation of 1.79 Å. A total of 5 specimens were obtained from different boreholes at various depths (3 specimens of soil M and 2 specimens of soil C) and analyzed using XRD. While no variations in mineral composition were observed with depth, as discussed below, the mineralogy varied significantly between soil M and soil C.

Figure 2-9(a) and Figure 2-9(b) show representative XRD patterns for randomly-oriented powder samples obtained from soil M and soil C, respectively. Each peak in the figures is labeled with the mineral name, the Miller index (hkl), and the d-spacing. Figure 2-10(a) and Figure 2-10(b) summarize the XRD patterns of oriented clay aggregate subjected to different treatments, for soil M and soil C, respectively. Each figure shows six patterns: Mg^{2+}-saturated (Mg), ethylene glycol-solvated sample (MgEG), K^{+}-saturated sample x-rayed after air-drying at room temperature (K-23ºC), K^{+}-saturated sample x-rayed after heating at 100ºC for 2 hours (K-100ºC), 300ºC for 2 hours (K-300ºC), and 550ºC for 2 hours (K-550ºC). These patterns allow accurate identification of the clay minerals. As an example, smectite is identified by a strong peak at ~14.2 Å in the sample saturated with Mg^{2+}, which shifts to 16.9 Å when solvated with ethylene glycol (EG), and collapses to ~11 Å and ~10 Å with K^{+} saturation and heating at 100ºC and 550ºC, respectively. Illite, instead, is identified by peaks at 9.96 Å, 4.98 Å,

and 3.33 Å that do not change position with K^+ or Mg^{2+} saturation, or with ethylene glycol solvation and persist in K^+-saturated samples heated up to 550ºC. All XRD patterns are corrected for position shifts using corundum as a standard (corundum disks were used as sample holders).

The different minerals identified in the samples based on the XRD analyses are summarized in Table 2-2 in decreasing order of predominance.

Table 2-2: Mineralogy of carbonatic soils (in decreasing order of predominance) as observed in XRD analyses

Soil	Mineral type	Minerals Identified
Soil M	Non-clay minerals	Calcite, quartz, dolomite, aragonite, plagioclase feldspar, K-feldspar
	Clay minerals (19%)[a]	Smectite (50%), illite (27%), chlorite (12%), kaolinite (11%)[b]
Soil C	Non-clay minerals	Quartz, dolomite, calcite, plagioclase feldspar, K-feldspar
	Clay minerals (39%)[a]	Illite (62%), chlorite (30%), smectite (5%), kaolinite (3%)[b]

[a] Based on particle size analysis – see Table 2-1

[b] Based on XRD semi-quantitative analysis

In all soil samples the dominant non-clay mineral components are calcite, dolomite, and quartz, with small quantities of feldspars also identified. Smectite, illite, chlorite, and kaolinite are the minerals making up the clay size fraction of both soils.

Despite similarities in the overall mineralogy, the XRD patterns shown in Figure 2-9 and Figure 2-10 and the summary of the results presented in Table 2-2, reveal some significant differences between the matrix of soil M and that of soil C. In particular:

a) Consistent with the results of the sequential LOI tests (Table 2-1) and of

thermogravimetric analyses presented in APPENDIX C, soil M is observed to be richer in carbonates compared to soil C.

b) Soil M has more calcite than soil C, which might be partially attributed to the presence of calcite mesocrystals precipitated during soil deposition. This is confirmed by scanning electron microscopy (SEM) observations (presented in the following subsection). These crystals are identified in soil M but are not found in soil C.

c) Soil C is richer in dolomite compared to soil M.

d) Aragonite is identified in soil M but is absent in soil C. This is expected due to the presence of shells in soil M and their absence in soil C.

e) Soil M has a smaller clay content than soil C, which is consistent with the results of the particle size analyses.

f) The clay fraction of soil M is mainly composed of smectite (50%) and illite (27%), whereas that of soil C is mainly composed of Illite (62%) and chlorite (30%). The different nature of the clay minerals present in the two soils, and, in particular, the significantly greater smectite content of soil M (10% of the bulk soil compared to 2% of the bulk soil for soil C) can explain the larger values of LL and PI reported above for soil M compared to soil C, despite the lower clay size fraction. This is due to the high specific surface and high water sorption capacity of smectite (De Kimpe et al., 1979).

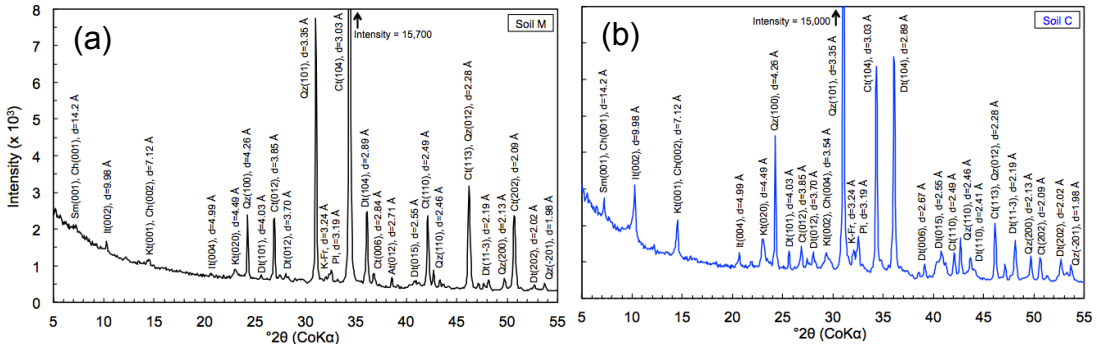

Figure 2-9: XRD patterns (randomly-oriented powder) of (a) soil M and (b) soil C. Mineral codes: Sm = smectite, Ch = chlorite, It = Illite, Kt = kaolinite, Qz = quartz, Dt = dolomite, Ct = calcite, K-Fr = K-feldspar, Pl = plagioclase feldspar, At = aragonite

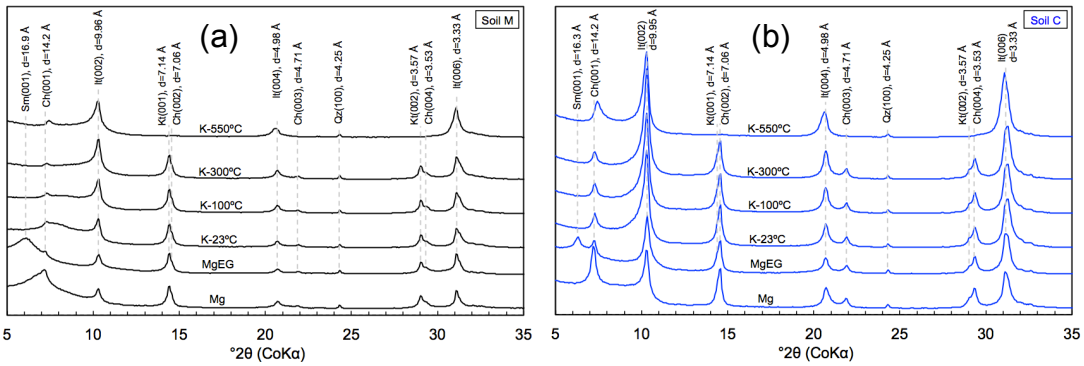

Figure 2-10: XRD patterns (oriented samples) of the clay fraction (<2 μm) of (a) soil M and (b) soil C. Mineral codes: Sm = smectite, Ch = chlorite, It = Illite, Kt = kaolinite, Qz = quartz

2.3.4. Microstructure

Scanning electron microscopy was employed to gain insight into the microstructure of soils M and C. Samples to be imaged through SEM were allowed to dry at room temperature for ~1 week and then broken to create a free fractured face that was mounted on a sampler holder using graphite paste. All samples were imaged without coating to avoid the interference of the coating material with the interpretation of the chemical elements in the EDXS analysis. Images were obtained at Purdue University's Life Science Microscopy facility with the FEI Quanta 3D FEG SEM using the low vacuum LVSED detector as well as the backscattered BSE detector (with 20kV, Spot 6.0, and 10mm WD). Magnifications ranged between 130x and 40,000x. X-ray analysis (EDXS) was done to analyze the chemical composition of objects of interest identified in the SEM micrographs, using an Oxford INCA Xstream-2 with Xmax80 detector (Oxford Instruments, Peabody, MA) with 20kV, 6.5 spot, 10mm WD, 50μm objective aperture.

Select scanning electron micrographs for soil M and soil C are shown in Figure 2-11 and Figure 2-12. Figure 2-11 compares the matrix of soils M and C at two different magnifications, and highlights the more open microstructure of soil M compared to soil C. This observation is consistent with the void ratio values reported earlier (e ~ 1.7 for soil M versus e ~ 1.2 for soil C).

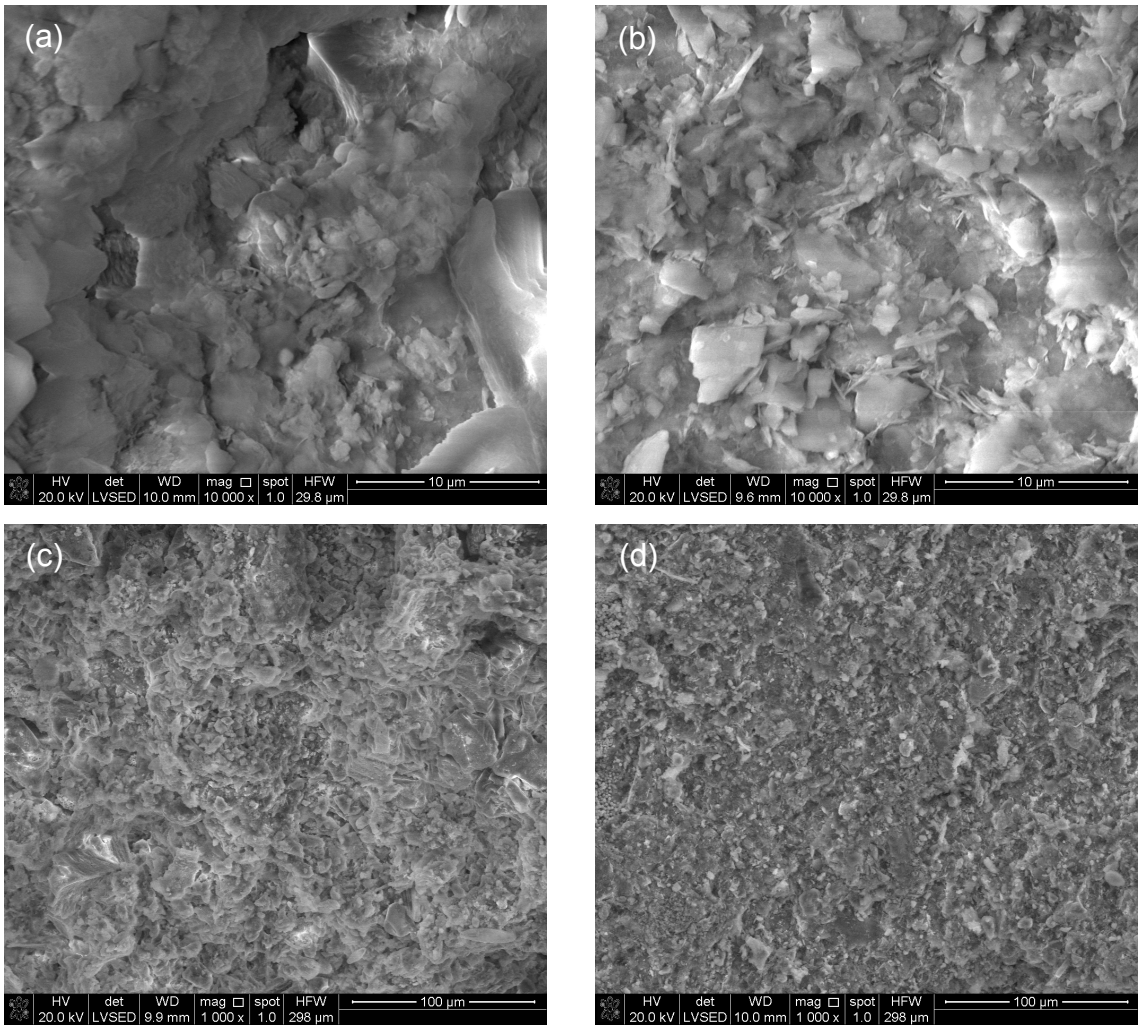

Figure 2-11: SEM micrographs showing (a) soil M (mag. 10,000x), (b) soil C (mag. 10,000x), (c) soil M (mag. 1,000x), and (d) soil C (mag. 1,000x)

Figure 2-12 highlights some features characteristic of soil M, all of which were, where necessary, identified using EDXS. Specifically, the images show the presence of microfossils and shells of snails (Figure 2-12(a)), bivalves (Figure 2-12(b)) as well as calcite mesocrystals (Figure 2-12(c)). The latter are an integral part of the soil matrix and result in a higher calcite content of soil M relative to soil C, as reported in the XRD results. The micrographs also show the presence of diatoms and 5 – 30 micron framboidal pyrite (iron sulfide), consisting of crystallites ranging from 0.5 to 3 microns (Figure 2-12(d)).

For soil C the SEM observations confirm the absence of shells, and no calcite crystals are observed. Iron sulfide is detected, although not in the framboidal form observed in soil M. This aspect is discussed further below.

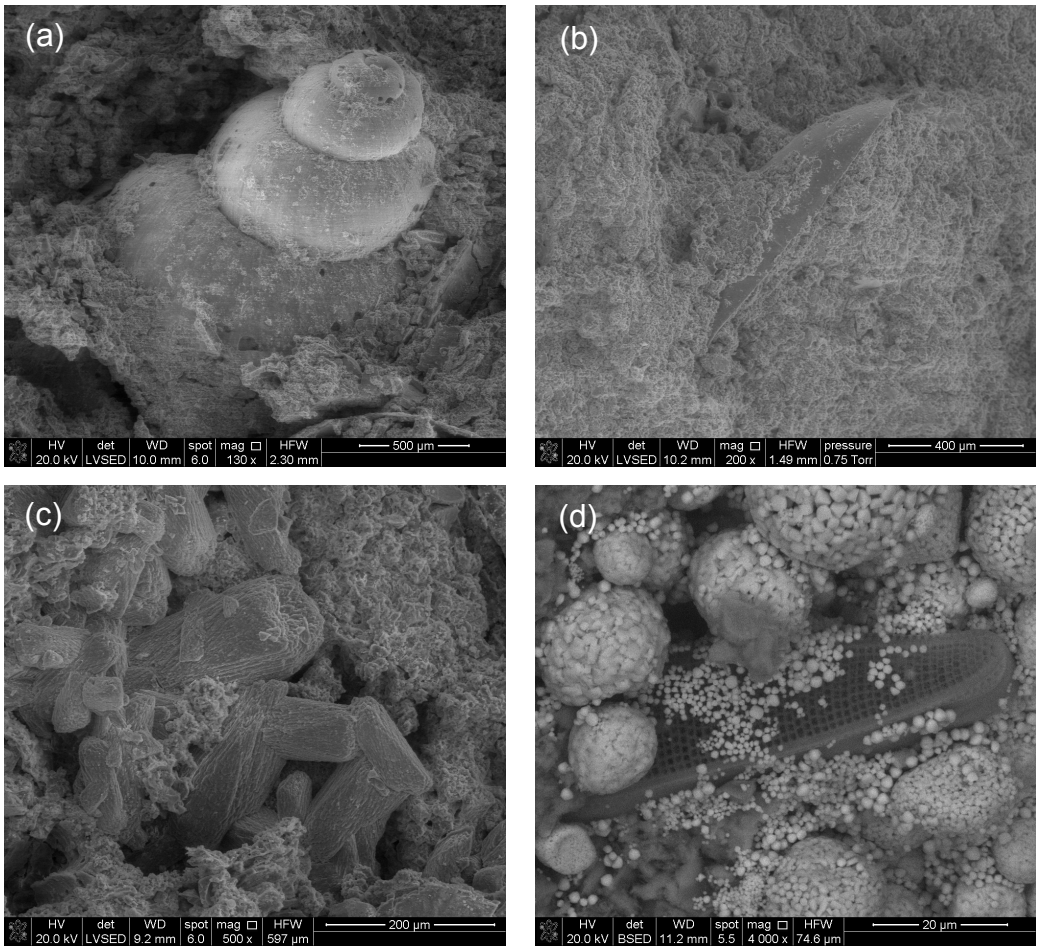

Figure 2-12: Scanning electron micrographs of soil M showing: (a) snail shell, (b) bivalve shell, (c) calcite mesocrystals, and (d) diatom and framboidal pyrite.

2.3.5. Select Geotechnical Properties

An extensive testing program comprising incremental and constant rate of consolidation tests, SHANSEP and recompression K_0-consolidated undrained triaxial compression tests, and resonant column tests was performed on both soil M and soil C using high quality Shelby tube samples collected at the site at various depths. The results of these tests, which are analyzed in detail in APPENDIX D (compressibility and strength data) and Dawood (2014) (shear

stiffness data), indicate that the differences in mineralogy, index properties and microstructure highlighted in the previous sections translate in clear trends in the strength (e.g. soil M presents a higher normally consolidated undrained strength ratio and friction angle), stiffness (e.g. soil M presents higher G_{max} at the same void ratio and confining stress), and one-dimensional compression behavior. An illustration of the differences in the observed one-dimensional compression behavior is presented in Figure 2-13 and Figure 2-14. Figure 2-13(a,b) show compression curves obtained from both incremental loading tests and the constant rate of strain consolidation stage of both CRS and K_0-consolidated triaxial tests, performed on soil M and soil C, respectively. In addition to the above highlighted difference in the initial (in situ) void ratio, soil M is seen to be characterized by a higher maximum virgin compression index (C_c=0.71±0.08) compared to soil C (C_c=0.52±0.13). Moreover, Figure 2-14(a) shows that the values of the preconsolidation stress (σ'_p) derived using the strain energy method (Becker et al. 1987) from the individual tests conducted on the two soils fall on two distinct bands, with soil M consistently exhibiting a higher σ'_p, and thus higher OCR (Figure 2-14(b)) at any given depth.

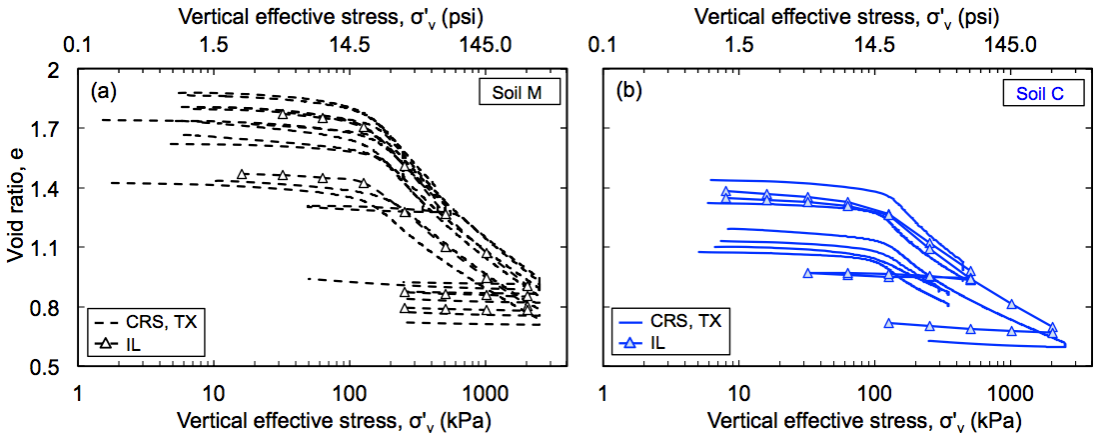

Figure 2-13: Compression curves from IL, CRS consolidation and SHANSEP $CK_0UTC(L)$ tests on (a) soil M, and (b) soil C.

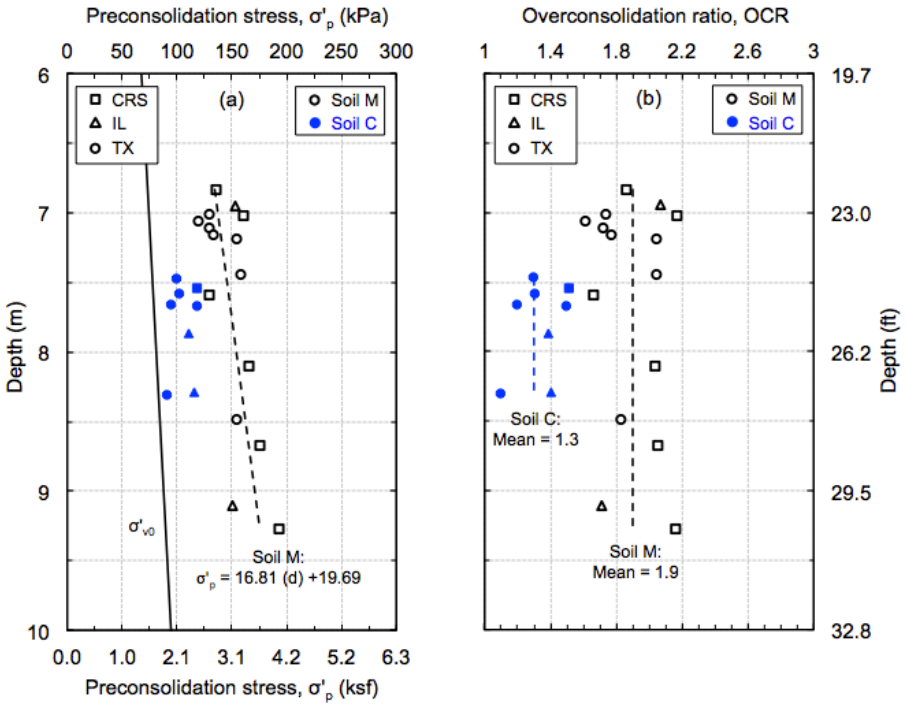

Figure 2-14: Stress history profile: variation of (a) preconsolidation stress and (b) OCR with depth

2.4. Discussion: Linking Soil Characteristics to Origin of Deposit and Sedimentary Environment

2.4.1. Origin and Age of Deposit

The shape of the bedrock shown in the cross-section presented in Figure 2-4, as well as the analysis of the topography in the area surrounding the site suggest that the deposit investigated in this study is of lacustrine origin, as commonly encountered in the states of Indiana, Illinois, and Ohio. Plains in these regions were caused by the advance and retreat of the ice sheets that extended into the northern part of the Midwest during glaciation.

This hypothesis on the origin of the deposit is further supported by the analysis through optical light microscopy of the fossil shells of small gastropods extracted from samples of soil M obtained at depths varying between 7.3 m and 10.1 m. All shells collected are < 5 mm in maximum dimension and are classified as minute (2-5 mm) and micro (< 2 mm) gastropods (Pigati et al., 2010). A total of six

different species shown in Figure 2-15 were identified from the images based on the extensive study conducted by Burch and Tottenham (1980) on North American species. These gastropods are all identified as freshwater snails, confirming the hypothesis of lacustrine origin of the deposit.

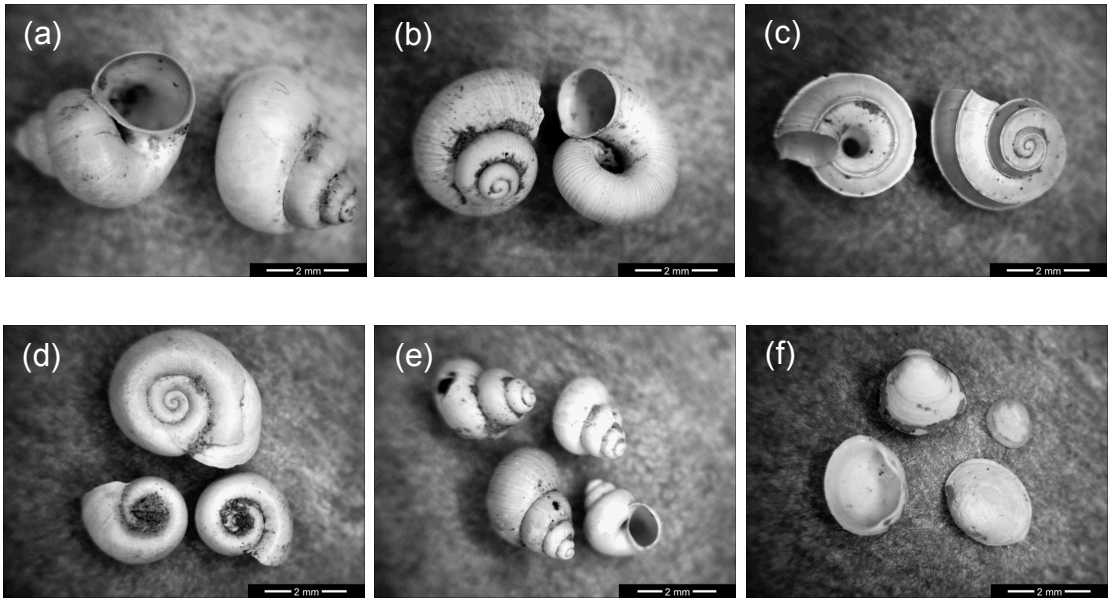

Figure 2-15: Images of the different types of gastropods collected from samples of soil M: (a) Amnicola (family: Hydrobiidae, subfamily: Amnicolinae), (b) Valvata sincera (family: Valvatidae), (c) Valvata tricarinata (family: Valvatidae), (d) Gyraulus (family: Planorbidae, subfamily: Planorbinae), (e) Cincinnatia (family: Hydrobiidae, subfamily: Nymphophilinae), and (f) Pisidium (family: Sphaeriidae, subfamily: Pisidiinae)

Figure 2-16 identifies the location of the site investigated in this research on a map highlighting the position of the Wisconsin and Illinoian glacial boundaries. The Illinoian glaciation and Wisconsin glaciation are the two most recent glacial periods experienced by North America during the Pleistocene. (Wayne and Thornbury, 1951). The first occurred from approximately 300,000 to 130,000 years ago, whereas the latter occurred during the last years of the Pleistocene, from approximately 85,000 to 11,000 years ago (Fidlar, 1948, and Gibbard & van Kolfschoten, 2004). The Illinoian ice sheet advanced into Indiana as two large lobes covering most of the state, with the southeastern lobe advancing to the Ohio River, and the southwestern lobe covering nearly all Indiana (Figure 2-16).

The Wisconsin ice sheet covered most of central Indiana reaching as far as south of Indianapolis.

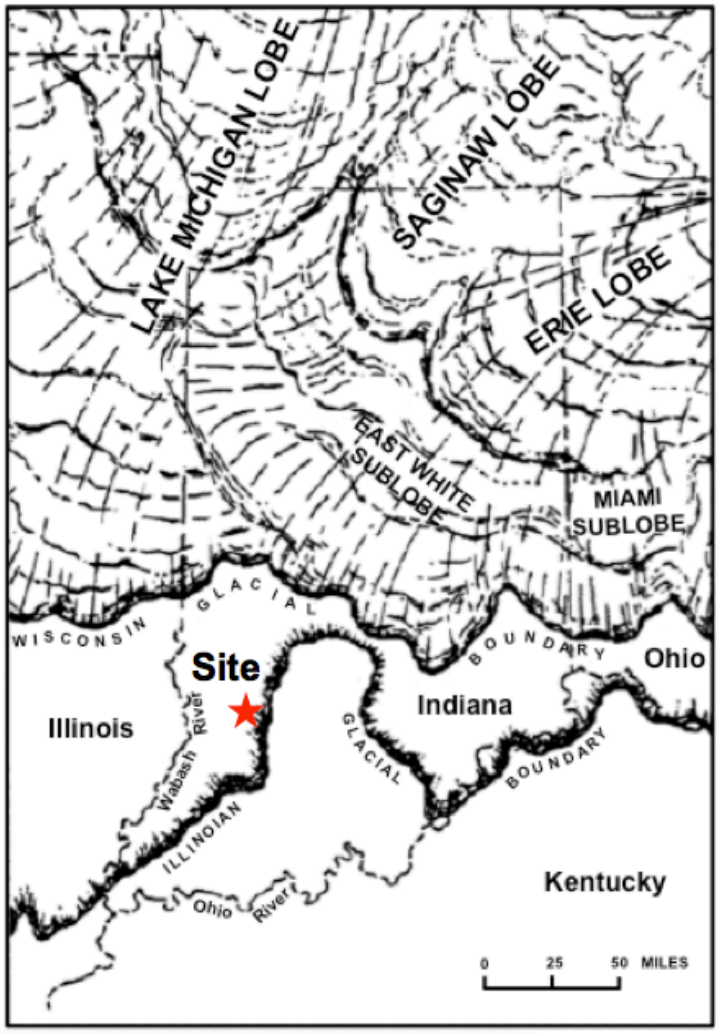

Figure 2-16: Map showing site location relative to the Wisconsin and Illinoian glacial boundaries (modified from Thornbury & Deane, 1955 and Wayne 1965)

Thornbury (1937, 1940, and 1950) conducted extensive research on the lacustrine plains in southern Indiana and reported that these plains are generally formed under two different conditions of distinct ages and origins. The first system of lakes came into existence during the Illinoian glaciation period as a result of ponding of the southwest drainage along the ice front of the southwestern glacial lobe. The second and more extensive system of lakes

occurred during the Wisconsin glaciation period south of the Wisconsin glacial boundary. In this case deposition was an indirect rather than direct effect of glaciation, as the major streams acted as glacial sluiceways for Wisconsin melt-waters carrying detritus that caused the formation of extensive valley trains. The streams in the tributary valleys were ponded, which resulted in the formation of an extensive system of lakes. Lacustrine plains of this origin are widely developed along the tributaries of the Wabash, Ohio, and White Rivers.

This appears to be the origin of the deposit investigated in this study. This is suggested by the analysis of the elevation contour map (elevations varying between ~152 m (500 ft) and ~198 m (650 ft)) of the site presented in Figure 2-17, based on which hypotheses can be drawn on the ponding phenomenon responsible for the formation of the glacial lake during the Wisconsin age (85,000 to 11,000 years ago), and the extent of the lake itself. Figure 2-17 shows First Creek flowing northwest at an elevation of ~152 m (500 ft), passing through the site (see Figure 2-4), and eventually joining the west fork of the White River. It is hypothesized that the White River acted as glacial sluiceways for melt-waters, carrying detritus that caused the formation of extensive valley trains, creating a natural dam for First Creek, one of its tributaries, which was ponded leading to the formation of a lake. Figure 2-17 shows the hypothesized location and extent of this lake that would have covered an area of about 2.5 km^2. Due to natural drainage, evaporation and/or other geophysical processes that occurred over time, the water was drained from the lake, leaving the deposited sediments behind.

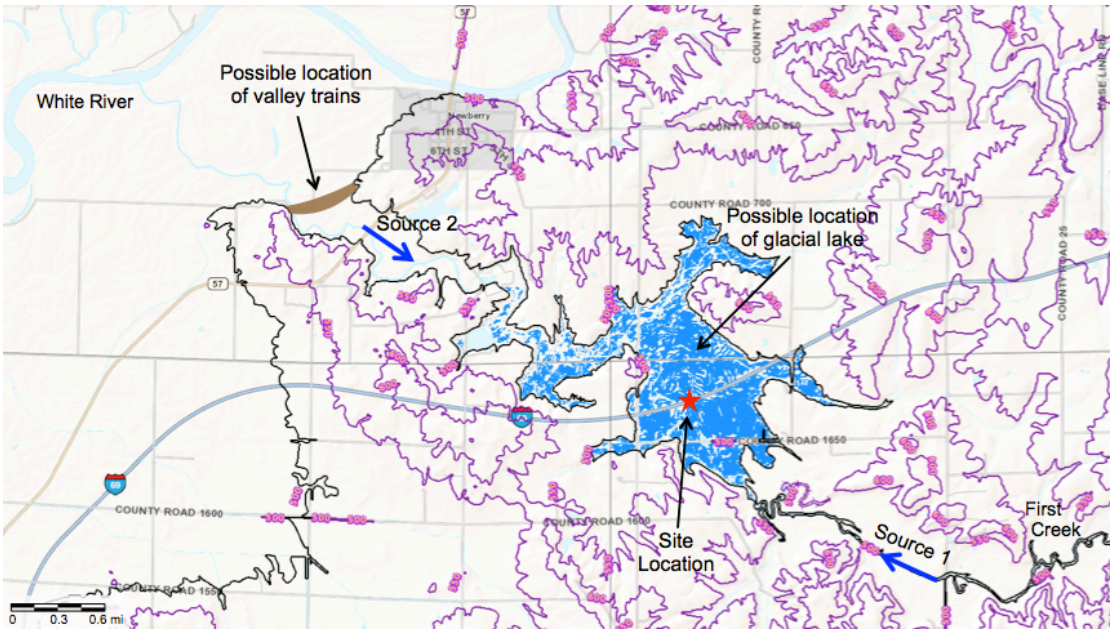

Figure 2-17: Topographic map of the site showing the hypothesized extent of the glacial lake and the valley trains along the White River

To support the above outlined hypotheses on the geology and the age of the deposit, radiocarbon dating using accelerator mass spectrometry (AMS) was conducted on fossil shells obtained from the deposit as well as plants (pieces of wood) (i.e. organic samples) found at depths varying between 7.3 m and 10.1 m.

AMS measurements were conducted at the Purdue Rare Isotope Measurement Laboratory (PRIME Lab). The AMS method is a modern radiocarbon dating technique that directly counts the ^{14}C atoms relative to the ^{13}C atoms (or ^{12}C, depending on the laboratory), whereas the conventional beta-counting method counts the beta particles emitted by a given sample as a result of radiocarbon decay (Muzikar et al., 2003). The main advantage of AMS over the conventional beta-counting method is that the former is relatively faster and requires a much smaller sample.

Aliquots from the carbonatic soil layer were placed in deionized water for several days to soften the sediment enough to pass through a 0.075 mm sieve (ASTM #200). Shells and pieces of wood were hand-picked from the retained fraction

and repeatedly washed with deionized water to remove all the soil that adhered to the surface. The shells were then broken and the soil lodged within the shell was removed with a small spatula. Following additional washing with deionized water the recovered shells and pieces of wood were air-dried and used for radiocarbon dating. Shells were not powdered during pretreatment to reduce the adsorption of ^{14}C from the atmosphere.

After the physical treatment, the samples were sent to the PRIME lab for a chemical treatment designed to remove any contamination from the sample surface before radiocarbon dating. For the carbonate samples identified in Table 2-3, this involved acid etching, a process in which a small amount of acid is used to remove surface carbonates, followed by reaction with excess acid to produce carbon dioxide. An acid-base-acid (ABA) treatment was instead performed on the organic samples. This treatment entails reaction with acid to remove surface carbonates, extraction of the humic acids using sodium hydroxide, and a final reaction with acid to remove carbonates introduced by the second stage of the treatment. The organic samples are then combusted with copper oxide to produce carbon dioxide. The gaseous CO_2 collected from the carbonate samples or the organic samples is then trapped and later graphitized using zinc and iron. The resulting graphite is mounted in the accelerator for AMS measurements (Muzikar et al., 2003).

Table 2-3 summarizes the nine different samples (shells or wood fragments) used for radiocarbon dating, as well as the radiocarbon ^{14}C results. The samples were collected from different depths to investigate the variation/uniformity of the deposit age with depth.

Table 2-3: Radiocarbon ^{14}C results for carbonate samples (shells) and organic samples (wood) recovered at depth ranging between 7.3 m and 10.1 m

Sample #	Depth (m)	Description	Comments	Radiocarbon Age (yrs)[a]	Cal age BP (yrs)[a,b]
1	7.3	Shell type 1 (Amnicola)	Carbonate sample	17,278 ± 252	20,864 ± 336
2	7.3	Shell type 2 (Valvata sincera)	Carbonate sample	17,060 ± 253	20,584 ± 324
6	7.3	Shell type 6 (Pisidium)	Carbonate sample	17,315 ± 252	20,912 ± 338
F	7.3	Wood	Organic sample	17,336 ± 220	20,935 ± 299
A	8.0	Shell type 4 (Gyraulus)	Carbonate sample (large shell)	17,973 ± 267	21,753 ± 357
B	8.8	Wood	Organic sample	19,557 ± 227	23,551 ± 295
C	10.1	Shells types 1 (Amnicola), 2 (Valvata sincera), 3 (Valvata tricarinata)	Carbonate sample (mixed types)	19,401 ± 238	23,361 ± 300
D	10.1	Wood	Organic sample	19,759 ± 232	23,782 ± 275
E	10.1	Shell type 6 (Pisidium)	Carbonate sample	19,607 ± 233	23,610 ± 294

[a] the ± reflects the uncertainty in the age

[b] cal age BP: calibrated age before present (referenced to 1950)

Radiocarbon ages obtained from the AMS measurements were converted to "real" calendar years by accounting for the variation in the atmospheric ^{14}C activity (Reimer et al., 2009). Calibrated ages were calculated using CALIB v. 7.1, IntCal13 database, and they are reported as the midpoint of the calibrated range in terms of years 'before present' (BP), which refers to 1950.

The calendar ages of the nine different samples are also shown in Figure 2-18. Radiocarbon dating resulted in an age of 20,800 yr BP (at 7.3 m) to 23,600 yr BP at (10.1 m), with the age increasing with depth, indicating that the formation of this portion of the deposit occurred during a period of approximately 3,000 years. For the same depth, the carbonate samples and the organic samples resulted in a very similar calendar age. This implies that the fossil shells used in this analysis were not affected by the hard water effect. This effect occurs in presence of calcium carbonate that has been dissolved into the freshwater source from limestone and carbonate rocks, causing samples to appear older

than their true age. The resulting bias in age can vary between a few decades and several hundreds years (Beta Analytic Inc., 2016).

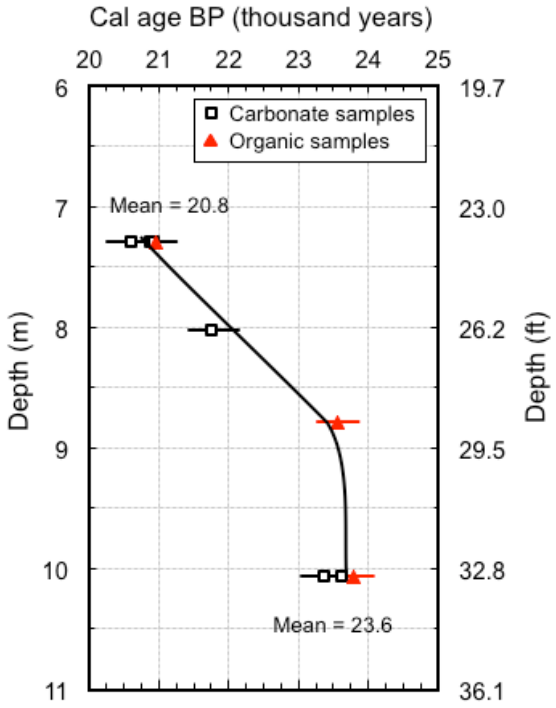

Figure 2-18: Calendar age BP of carbonate samples (shells) and organic samples (wood) recovered at depth ranging between 7.3 m and 10.1 m

2.4.2. Sediment Source and Effects of Sedimentary Environment

While the characteristics of the deposit investigated in this study are overall consistent with its hypothesized lacustrine origin and Wisconsin age, the sections above highlighted clear differences between the characteristics of the two soils – soil M and soil C – forming the deposit. In particular, the XRD analyses demonstrate differences in mineralogy, with soil M shown to be richer in calcite and smectite, minerals generally associated with a higher degree of weathering, and soil C richer in dolomite and illite. Moreover, microstructural observations indicate the presence of biological intrusions in soil M, but not in soil C.

These observations suggest not only that the sediments forming soil M and soil C originated from two different sources, which alternated over the 3,000 year-long

process of formation of the deposit, but also that this led to differences in the sedimentary environment. Specifically, it is hypothesized that soil M – the smectite-calcite rich sediment – was carried into the lake through First Creek (source 1 – see Figure 2-17), while soil C – the illite-dolomite rich sediment – was transported into the lake through the White River (source 2), as a result of occasional flooding above the valley trains (see Figure 2-17) caused by the high volume of Wisconsin-melt waters. The fact that soil M is prevalent in the deposit is consistent with the exceptional conditions that would have caused the influx of sediment from the White River. Similar hypotheses have been put forth by Frye et al. (1972) and Curry & Grimley (2006) to explain variations in the characteristics of lake sediments in Lake Saline in southeastern Illinois, and in the St. Louis Metro East area, respectively.

The observation that the mineralogy of soil M is dominated by smectite and calcite can be explained by the fact that source 1 would have likely transported into the lake locally derived sediments of Illinoian age subjected to a high degree of weathering. Source 2, on the other hand would have potentially carried much younger sediments from the northern part of Indiana. The relatively high content of illite and dolomite in soil C (associated with source 2) is consistent with the abundance of paleozoic shale and dolostone as bedrock in the northern part of Indiana and Illinois (Curry & Grimley, 2006).

The presence of gastropod fossils in soil M, documented above in Figure 2-5, Figure 2-12, and Figure 2-15, indicates that the sediments deposited under conditions that promoted a biogenic environment. Charophyte oospores were also found in samples of soil M (see Figure 2-19). These are pond-dwelling algae that live in still or slow-moving water rich calcium carbonate, and whose resistant wall structures allow them to be preserved for thousands of years.

Neither fossil shells, nor charophyte oospores were observed in soil C, indicating that at the time this soil was deposited the sedimentary environment did not promote biogenic life.

These differences are consistent with the hypotheses on sediment origin and transport postulated above, as the depositional conditions hypothesized for soil M would be expected to involve slow accumulation rates and shallow water conditions which would promote a biogenic environment. Much faster accumulation rates and deeper water would instead be consistent with the deposition of soil C sediments due to flooding of the White River.

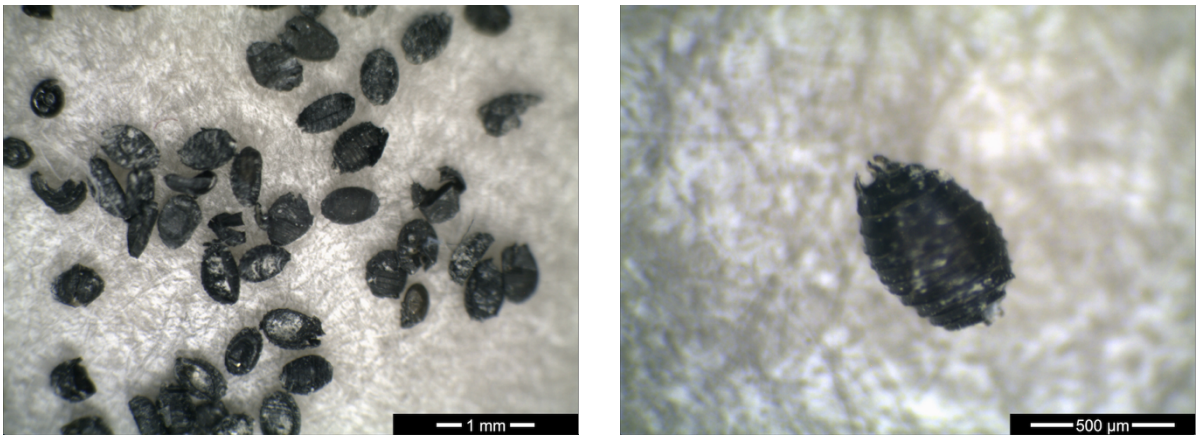

Figure 2-19: Microscopic images for charophyte oospores collected from the carbonatic soil layer

Also consistent with the hypothesis of the deposition of soil M occurring in shallower water is the higher calcite content of this soil (see Table 2-2 and Figure 2-9). Greater calcite precipitation is promoted as a result of the reduction in CO_2 and/or the consumption of CO_2 due to the growth of algae. Under conditions of deeper water the growth of algae would be instead impeded and the reduction in CO_2 limited, limiting the precipitation of calcite.

Finally, additional evidence of the different sedimentary environment present at the time of formation of soils M and C comes from a closer analysis of the

morphology of one particular mineral – pyrite - present in very small quantities in both soils. The development of iron sulfide minerals, especially pyrite (FeS_2), in lacustrine deposits has long been reported in the literature (e.g. Japanese fresh water sediments, Vallentyne 1961; Lake Michigan, Moore 1961, Little Round Lake, Ontario, Vallentyne 1963; Lake Naivasha, Kenya, Richardson & Richardson, 1972). The presence of sulfide and reactive Fe in water is essential for the formation of pyrite. Groundwater and runoff streams supply the lake with silicates and Fe (hydr)oxides, which are then reduced to hydrogen sulfide (H_2S) and Fe^{2+} with the aid of microbes (Fanning et al., 2002). The path of pyrite formation begins with the reaction of the dissolved iron and sulfide to form iron monosulfide (FeS) or mackinawite ($FeS_{0.9}$), which are then sulfurized to produce pyrite, as shown in the following equations:

$$Fe^{2+} + S^{2-} \rightarrow FeS \qquad \text{(Eq. 2-1)}$$

$$FeS + S^0 \rightarrow FeS_2 \quad \text{(simplified)} \qquad \text{(Eq. 2-2)}$$

$$FeS_x + (2\text{-}x)\, S^0 \rightarrow FeS_2 \quad \text{(general)} \qquad \text{(Eq. 2-3)}$$

In soil sediments, pyrite usually occurs as small individual well-formed euhedral microcrystals or as spheroidal aggregates of microcrystals called framboids. The term framboid derives from the French word *framboise*, which refers to their raspberry-like morphology (Rust, 1935). Pyrite framboids found in nature vary greatly in size (<1 μm up to 250 μm) but are typically of the order of 10 μm in diameter (Love & Amstutz, 1966; Rickard, 1970; Wilkin et al., 1996). Each framboid is composed of equidimensional and equimorphic discrete microcrystals that are densely packed in a spherical shape (Ohfuji & Rickard, 2005). Microcrystals that constitute natural pyrite framboids show a rather wide range in size (<0.1 μm – 20 μm) but are typically less than 2 μm in diameter.

Figure 2-20(a) and Figure 2-20(b) show the scanning electron micrographs for framboidal pyrite and non-framboidal pyrite that were found in soils M and C, respectively. The micrograph for soil M (Figure 2-20(a)) reveals the texture of framboidal pyrite in clear detail. Individual framboids are built up from equidimensional and equimorphic discrete microcrystals that are densely packed in a spherical shape. There is no apparent means of cohesion between individual microcrystals, and some authors have attributed the framboid aggregation process to van der Waals attractive forces and the ferromagnetic properties of iron sulfide (e.g., Wilkin & Barnes, 1997).

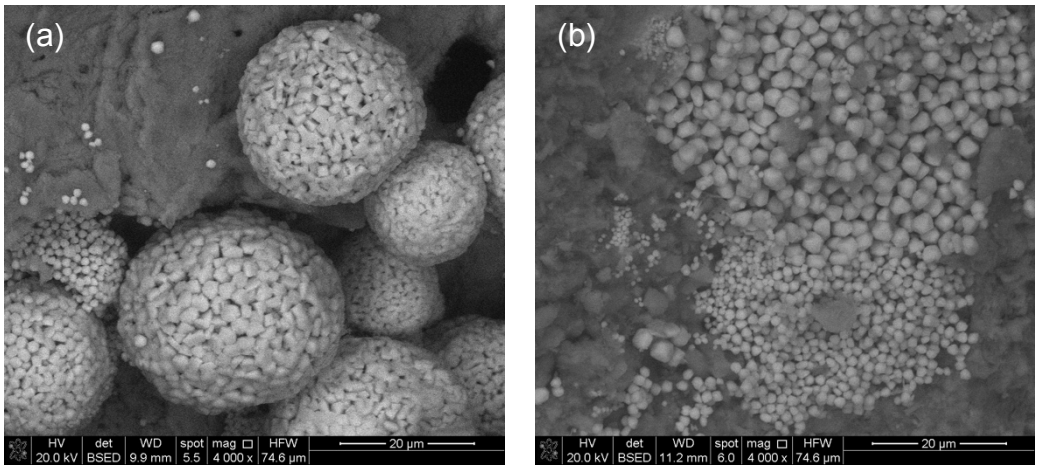

Figure 2-20: Scanning electron micrographs showing (a) framboidal pyrite found in soil M and (b) non-framboidal pyrite found in soil C

The remarkable morphology of pyrite framboids and its abundance in natural sediments compared to other pyrite textures have generated numerous studies on the laboratory synthesis of this mineral, as a means to understand the mechanism of formation of pyrite framboids, and evaluate the influence of environmental factors on its formation. Based on a review of eleven different experimental syntheses of framboidal pyrite, Ohfuji and Rickard (2005) concluded that the factors that can promote its synthesis are: (1) the addition of S^0, (2) the addition of O_2, (3) the increase of the oxidation/reduction potential (Eh) of the system, and (4) the increase in temperature. In particular, the presence of

oxygen appears to be a critical condition for formation of pyrite framboids (see also Sweeney & Kaplan (1973) and Wilkin & Barnes (1996)).
As a result of the above, the presence of well-formed framboids in soil M appears further indication of a biogenic environment during the deposition of soil M, while the presence of non-framboidal pyrite in soil C might be indicative of the absence of such an environment.

2.5. Conclusions

This paper presents the results of a detailed characterization study of a soft lacustrine carbonatic deposit formed during the Wisconsin glaciation in southwestern Indiana. The approximately 4m thick soft layer examined in this work was identified based on seismic cone penetration tests (SCPT), and the subsequent laboratory characterization study relied on samples obtained over the entire thickness of the layer using state of the art techniques aimed at preserving the integrity of the soil structure.

The laboratory experimental program was specifically designed to characterize the mineralogy and microstructure and index properties (e.g. Atterberg limits, particle size distribution, LOI, carbonate content) of the deposit as a function of depth. Alongside conventional geotechnical tests (e.g. for determination of limits and particle size distribution) the testing program relied on state-of-the-art techniques, including X-ray diffraction (XRD), optical microscopy and scanning electron microscopy (SEM) equipped with energy dispersive X-ray spectroscopy (EDX). Additionally, radiocarbon dating was performed on fossil shells and organic samples using accelerator mass spectrometry (AMS). These measurements show that the deposit is approximately 22,000 years old and was formed over a period of ~3,000 years.
The objectives of the work were to relate these results and observations to the engineering properties documented in detail through a parallel effort, as well as to the origin of the deposit.

The tests performed show that the carbonatic layer is not uniform, but is, instead, formed by the repetition of small layers of two different soils. These two soils, referred to in this paper as “soil M” and “soil C”, are both characterized by high calcium carbonate contents (over 55%, and close to 40%) but show distinct index properties (e.g. PL ~ 34.6 and 21.6; LL ~67.5 and 47.5; % clay ~ 20.2% and 36.9% for soils M and C, respectively). These differences are reflected also in the engineering properties, in particular in the measured values of the preconsolidation stress (σ'_p), which fall on two distinct bands, with the resulting values of OCR derived for soil M (average OCR~ 1.9) consistently higher than those derived for soil C (average OCR~ 1.3).

Differences in mineralogy, in particular the greater percentage of smectite measured in soil M relative to soil C, are responsible for the observed values of liquid limit and plasticity index, which are not consistent with previously observed relationships with calcium carbonate content.

While the characteristics of the deposit are overall consistent with its origin, specific discrepancies exist between soil M and soil C in terms of: their mineralogy dominated by smectite and calcite in soil M, and by illite and dolomite in soil C; and the presence of biological intrusions detected only in soil M. Also specific to soil M is the presence of pyrite framboids, whose synthesis is promoted in oxygen rich environments, further indication of a biogenic environment during the deposition of this soil. These observations lead to hypothesize that different source materials and sedimentary environments alternated during the 3,000 year long process of formation of the deposit. Specifically, it is hypothesized that soil M was formed as a result of the deposition of locally derived sediments of Illinoian age subjected to a high degree of weathering, under conditions (slow accumulation rates and shallow water) that promoted biogenic life. Soil C would, instead, have resulted from the influx of sediment from the White River under the occasional conditions associated with

flooding above the valley trains caused by the high volume of Wisconsin-melt waters.

2.6. Acknowledgments

This work was supported by the Joint Transportation Research Program administered by the Indiana Department of Transportation and Purdue University. The contents of this paper reflect the views of the authors, who are responsible for the facts and the accuracy of the data presented herein, and do not necessarily reflect the official views or policies of the Federal Highway Administration and the Indiana Department of Transportation, nor do the contents constitute a standard, specification, or regulation. The authors wish to acknowledge the help of Mr. Sriram Valavala and Ms. Mariah Schroeder, who helped perform the Atterberg limits tests; Mr. Mohammad Sasar who conducted the pH measurements; Ms. Debby Sherman who performed the SEM observations; and Prof. Paul Muzikar and Mr. Ken Mueller who performed the radiocarbon dating.

2.7. References

AASHTO T267-86. (2008). Standard method of test for determination of organic content in soils by loss on ignition. American Association of State Highway and Transportation Officials, Washington, D.C.

Alt & Witzig (2010). Geotechnical Engineering Report, I-69 Extension, Section 3 – US 50 to US 231, Segment 12 – I-69 Mainline Roadway, CR 1400N to CR 700E, Daviess County. Prepared for Indiana Department of Transportation.

ASTM D2487-11 (2011). Standard practice for classification of soils for engineering purposes (unified soil classification system). Annual Book of ASTM Standards, ASTM International, West Conshohocken, PA.

Becker, D.E., Crooks, J.H.A., Been, K., & Jefferies, M.G. (1987). Work as a criterion for determining in situ and yield stresses in clays. Canadian Geotechnical Journal, 24(4), pp. 549-564.

Beta Analytic Inc. (2016). Radiocarbon dating shell, coral, and $CaCO_3$: Reservoir effect on shells. Retrieved February 17, 2016 from http://www.radiocarbon.com/carbon-dating-shells.htm

Burch, J.B. & Tottenham, J.L. (1980). North American freshwater snails: Species list, ranges and illustrations. Walkerana 3.

Cotecchia, F. & Chandler, R.J. (1995). Geotechnical properties of the Pleistocene clays of the Pappadai Valley, Taranto, Italy. Quarterly Journal of Engineering Geology, 28, pp. 5-22.

Covarrubias-Fernandez, S. (1994). Characterization of the engineering properties of Mexico City clay. MS Thesis , Massachusetts Institute of Technology, Cambridge, MA.

Curry B.B. & Grimley, D.A. (2006). Provenance, age, and environment of mid-Wisconsinan slackwater lake sediment in the St. Louis Metro East area, USA. Quaternary Research 65, pp. 108-122.

Dawood, S. (2014). Small strain stiffness of a carbonatic fine grained soil. MS Thesis, School of Civil Engineering, Purdue University, West Lafayette, IN.

De Kimpe, C.R., Laverdiere, M.R., & Martel, Y.A. (1979). Surface area and exchange capacity of clay in relation to the mineralogical composition of gleysolic soils. Canadian Journal of Soil Science, 59(4), pp. 341-347.

DeGroot, D.J. & Lutenegger, A.J. (2003). Geology and engineering properties of Connecticut Valley Varved Clay, Proceedings of the International Workshop on Characterization and Engineering Properties of Natural Soils, 1, pp. 695-724.

Earth Exploration (2010). Geotechnical Engineering Report, I-69 Extension, Section 3 – US 50 to US 231, Segment 13 - I-69 Mainline Roadway & Access Roads CR 700E to US 231, Daviess and Greene Counties. Prepared for Indiana Department of Transportation.

Fanning, D.S., Rabenhorst, M.C., Burch, S.N., Islam, K.R., & Tangren, S.A. (2002). Sulfides and sulfates. In J.B. Dixon & D.G. Schulze (Eds.), Soil mineralogy with environmental applications (pp. 229-260). Soil Science Society of America, Madison, Wisconsin.

Fidlar, M.M. (1948). Physiography of the lower Wabash Valley. Indiana Dept. Cons., Div. Geol. Bull. 2, 112 p.

Frye, J.C., Leonard, A.B., William, H.B., & Glass, H.D. (1972). Geology and paleontology of late Pleistocene lake Saline, southeastern Illinois. Illinois State Geological Survey Circular 471, 44 p.

Gibbard, P. & Van Kolfschoten, T. (2004). The Pleistocene and Holocene Epochs. In Gradstein et al. (eds.) A Geologic Time Scale 2004. pp. 441-452. Cambridge University Press: Cambridge.

Integrating Spatial Educational Experiences Isee (2016). Retrieved February 17, 2016 from http://isee.purdue.edu/

Jung, C.M., Bobet, A., & Siddiki, N.Z. (2011). Simple method to identify marl soils. Transportation Research Record 2232, pp. 76-84.

Lamas, F., Irigaray, C., & Chacon, J. (2002). Geotechnical characterization of carbonate marls for the construction of impermeable dam cores. Engineering Geology, Elsevier, 66, pp. 283-294.

Lambe, T.W. & Whitman, R.V. (1969). Soil mechanics. New York: Wiley.

Love, L.G. & Amstutz, G.C. (1966). Review of microscopic pyrite. Fortschritte der Mineralogie, 43, pp. 273-309.

Moore, J.E. (1961). Petrography of northeastern Lake Michigan bottom sediments. J. Sed. Petrol., 3, pp. 402-436.

Muzikar, P., Elmore, D., & Granger, D.E. (2003). Accelerator mass spectrometry in geologic research. Geological Society of America Bulletin, 115, pp. 643-654.

Ohfuji, H. & Rickard, D. (2005). Experimental synthesis of framboids – a review. Earth-Science Reviews, 71, pp. 147-170.

Pigati, J.S., Rech, J.A., & Nekota, J.C. (2010). Radiocarbon dating of small terrestrial gastropod shells in North America, Quaternary Geochronology, 5, pp. 519-532.

Reimer, P., Baillie, M., Bard, E., Bayliss, A., Beck, J., Blackwell, P., Ramsey, C.B., Buck, C., Burr, G., Edwards, R., Friedrich, M., Grootes, P., Guilderson, T., Hajdas, I., Heaton, T., Hogg, A., Hughen, K., Kaiser, K., Kromer, B., McCormac, F., Manning, S., Reimer, R., Richards, D., Southon, J., Talamo, S., Turney, C., van der Plicht, J., & Weyhenmeyer, C., (2009). IntCal09 and Marine09 radiocarbon age calibration curves, 0–50,000 years cal B.P. Radiocarbon 51(4), pp. 1111-1150.

Richardson, J.L. & Richardson, A.E. (1972). History of an African Rift Lake and its climatic implications. Ecol. Mon., 42, pp. 499-534.

Rickard, D.T. (1970). The origin of framboids. Lithos, 3, pp. 269-293.

Rust, G.W. (1935). Colloidal primary copper ores at Cornwall Mines, southeastern Missouri. Journal of Geology, 43, pp. 398-426.

Stewart, K.D. & Patrick, D.M. (1990). Clay mineral composition and distribution in the Atchafalaya Basin and Terrebone Marsh areas, south-central Louisiana, Trans. Gulf Coast Assoc. Geol. Soc., 40, pp. 809-816.

Sweeney, R.E. & Kaplan, I.R. (1973). Pyrite framboid formation: Laboratory synthesis and marine sediments. Econ. Geol., 68, pp. 618-634.

Thornbury, W.D. (1950). Glacial sluiceways and lacustrine plains of southern Indiana. Indiana Geological Survey Bulletin, 4, 21 p.

Thornbury, W.D. (1940). Weathered zones and glacial chronology in southern Indiana. Jour. Geology 48(5), pp. 449-475.

Thornbury, W.D. (1937). Glacial geology of southern and south central Indiana. Indiana Dept. Cons., Div. Geol., 138 p.

Thornbury, W.D. & Deane, H.L. (1955). The geology of Miami county, Indiana. Indiana Dept. Cons., Indiana Geol. Survey Bull. 8, 49 p.

Vallentyne, J.R. (1961). On the rate of formation of black spheres in recent sediments. Verh. Int. Verein. Limnol., 14, pp. 291-295.

Vallentyne, J.R. (1963). Isolation of pyrite spherules from recent sediments. Limnol Oceanogr., 8, pp. 16-30.

Wayne, W.J. (1965). The Crawfordsville and Knightstown moraines in Indiana. Indiana Dept. Cons., Indiana Geol. Survey Report of progress 28, 15 p.

Wayne, W.J. & Thornbury, W.D. (1951). Glacial geology of Wabash County, Indiana. Indiana Dept. Cons., Indiana Geol. Survey Bull. 5, 39 p.

Wilkin, R.T. & Barnes, H.L. (1996). Pyrite formation by reactions of iron monosulfides with dissolved inorganic and organic sulphur species. Geochimica et Cosmochimica Acta, 60, pp. 4167-4179.

Wilkin, R.T. & Barnes, H.L. (1997). Formation process of framboidal pyrite. Geochimica et Cosmochimica Acta, 61, pp. 323-339.

Wilkin, R.T., Barnes, H.L., & Brantley, S.L. (1996). The size distribution of framboidal pyrite in modern sediments: an indicator of redox conditions. Geochimica et Cosmochimica Acta, 60, pp. 3897-3912.

CHAPTER 3. MICROSTRUCTURE AND CEMENTATION OF TWO CARBONATIC FINE-GRAINED SOILS[2]

3.1. Introduction

The effect of structure on the compressibility and shear strength of natural soils has been long recognized (e.g. Burland, 1990; Leroueil & Vaughan, 1990; Gens & Alonso, 1992; Cotecchia & Chandler, 1997; Chandler, 2000; Fearon & Coop, 2000, 2002). Lambe & Whitman (1969) defined the term "structure" as the combination of "fabric" (i.e., the arrangement of particles) and interparticle "bonding" (i.e., the electro-chemical forces at the inter-particle contacts). Cementation is one of the forms of interparticle bonding existing in structured soils. According to Mitchell (1993), these bonds are typically associated with crystal growth and/or chemical precipitation at the inter-particle contacts of silica, oxides, and/or carbonates from aqueous solutions.

The effects of cementation on the engineering properties of natural deposits have been widely discussed in the literature (e.g. Bjerrum & Wu, 1960; Conlon, 1966; Sangrey, 1972; Fischer et al., 1978; McGown & Ladd, 1982; Jamiolkowski et al., 1985; Allman & Poulos, 1988; Burland, 1990; Burghignoli et al. 1991; Boone & Lutenegger, 1997; Bozzano et al., 1999; Burghignoli et al., 2010). Cementation generally results in the development of an "apparent preconsolidation stress," and is also cited as a factor in increasing shear strength. For example, Kenney et al. (1967) showed that the removal of iron, using ethylenediaminetetraacetic acid (EDTA) leaching, caused a decrease in the apparent preconsolidation stress (σ'_p).

[2] This chapter is extracted from the draft manuscript "microstructure and cementation of two carbonatic fine-grained soils", to be submitted for publication.

Similarly, Loiselle et al. (1971) reported a reduction in both σ'_p and the undrained shear strength (s_u) of Quebec clays, due to the removal, using EDTA, of Fe^{3+} and Ca^{2+} cementing compounds. Fischer et al. (1978) reported that artificial cementation by calcite precipitation in Drammen clay caused an increase of s_u.

According to Mitchell (1993), carbonate is one of the most common cementing agents present in natural sediments and, as stated by Demars and Chaney (1982), it is one of the few mineral cementing agents that are capable of changing a loose aggregate into a stiff rock. It has been suggested that carbonate cementation forms over long periods of time from precipitation of calcite and/or dolomite and long-term crystal growth between grains. This process is believed to cause a physically solid link between the soil particles, bonding them together and leading to the formation of larger aggregates (e.g. Mitchell, 1993; Boone & Lutenegger, 1997). However, as noted by Boone and Lutenegger (1997), the final structure of a cemented soil "depends on the balance of deposition, stressing, and bonding rates, as well as mineralogy and pore-water chemistry." For example, It appears that the effects of carbonate cementation differ significantly in marine versus glacio-lacustrine deposits (e.g. Boone & Lutenegger, 1997). Adding further complexity is the fact that carbonates can have different origins (see Section 3.2), can exist in both detrital form and as cementing agents, and can be differently distributed across the various soil particle size fractions.

As a result of the above, and despite the prevalence of carbonatic soils around the world and the extensive literature on their engineering properties, questions still remain regarding the microstructure of these soils, the different forms in which carbonates can be present and the conditions that promote their occurrence, and their role in altering particle-level interactions at the microscopic scale.

This paper seeks to further the understanding of carbonate cementation in natural soils and of its relationship to macro behavior through the analysis of the microstructure of two fine-grained soils rich in calcium carbonate ($CaCO_3$) and calcium magnesium carbonate $CaMg(CO_3)_2$ sampled from the same glacial lacustrine deposit in southwestern Indiana, USA. The investigation is founded on: a) direct observations of the microstructure using scanning electron microscopy (SEM) equipped with energy-dispersive X-ray (EDX) spectrometry; and b) examination of the effects of carbonate dissolution on Atterberg limits and particle size distribution. While both soils examined in this study are characterized by high carbonate content (> 30%), due to different depositional environments, they show distinct index and engineering properties (see details in CHAPTER 2, APPENDIX C, and APPENDIX D). This provides the opportunity to examine effects associated with differences in both the degree of carbonate cementation and the forms of carbonates present.

3.2. The Origin of Carbonates in Lacustrine Deposits

The origin and form of deposition of carbonatic lacustrine deposits has been widely investigated (e.g. Wayne, 1971; Jones & Bowser, 1978; Boone & Lutenegger, 1997; Bozzano et al., 1999). It is generally reported that soil carbonates originate from two major sources: (i) as external to the lake (allogenic carbonates) in the form of carbonates that are eroded from the original parent material or (ii) by a solution-precipitation process occurring within the lake water mass (endogenic carbonates). The former mechanism, also referred to as mechanical sedimentation, consists of fine particles of calcium carbonate transported in suspension by ground water from limestone rock outside the lake proper; while the latter mechanism, also referred to as chemical and biochemical precipitate, involves the precipitation of calcium bicarbonates in fresh water as calcium carbonate.

Fresh water lakes can be saturated with calcium bicarbonate [$Ca(HCO_3)_2$], which exists only in aqueous solution. The removal of CO_2, as a result of evaporation, photosynthesis of aquatic plants, and/or bacterial activity, leads to the precipitation of calcium carbonate ($CaCO_3$), also known as calcite. The formation of calcite in soils follows the reaction:

$$Ca^{2+}_{(aq)} + 2HCO_3^-{}_{(aq)} = CaCO_3 + H_2O + CO_2 \qquad \text{(Eq. 3-1)}$$

The concentration of Ca^{2+} in solution depends on the partial pressure of CO_2 and temperature. Carbon dioxide dissolves in water, forming carbonic acid (H_2CO_3) and hydrated CO_2. The reaction between CO_2 and H_2O is described by the following:

$$CO_{2(g)} + H_2O = CO_{2(aq)} + H_2O \qquad \text{(Eq. 3-2)}$$

$$CO_{2(aq)} + H_2O = H_2CO_3 \qquad \text{(Eq. 3-3)}$$

$$H_2CO_3 = H^+ + HCO_3^- \qquad \text{(Eq. 3-4)}$$

$$HCO_3^- = H^+ + CO_3^{2-} \qquad \text{(Eq. 3-5)}$$

At the interface between the solution and solid $CaCO_3$ the equilibrium is:

$$CaCO_3 = Ca^{2+} + CO_3^{2-} \qquad \text{(Eq. 3-6)}$$

The reaction for the formation of calcite (Eq. 3-1) is obtained by combining equations 3-2 through 3-6.

Bozzano et al. (1999) discuss that $CaCO_3$ precipitation/dissolution equilibrium is controlled by a range of physical and chemical parameters, and that any process

that reduces the amount of CO_2 in the system will cause calcite to precipitate. In particular, the following factors come into play:

1- Temperature: while for many solids dissolved in water, the solubility of the solute increases with temperature up to 100°C, calcite exhibits the unusual characteristic of having “retrograde” or “inverse” solubility, where its solubility decreases with increasing temperature (Langmuir, 1997). This is caused by the fact that calcite dissolution/precipitation depends on the abundance of CO_2, and that the solubility of gases like CO_2 in liquids decreases with increasing temperature. Therefore, warming the water will result in a reduction in the amount of CO_2, shifting Eq. 3-1 to the right and leading to precipitation of calcite. In contrast, CO_2 is more soluble in cold water (e.g. during cold seasons and/or in deep water basins). In such conditions, calcite precipitation is less favorable.

2- Biochemical activity: Aquatic plants consume CO_2 in the process of photosynthesis. The carbonate system will buffer this loss by the precipitation of calcite until reaching an equilibrium condition.

3- Acidity (pH): Calcite solubility decreases with increasing pH. In general, calcium carbonate dissolves in an acid solution (decreasing pH) and precipitates in a basic solution (increasing pH).

4- Pressure: The solubility of gases like CO_2 in liquids increases with increasing load pressure (e.g. due to the mass of the overlying material). This causes Eq. 3-1 to shift to the left causing calcite to dissolve. Nitecki (1960) reported that the solubility of calcite is generally higher at greater depths than at lesser depths (lower pressure).

Fresh water lakes might also contain a host of soluble organic and inorganic materials that may modify the types of minerals formed (Doner & Lynn, 1989). For instance, the presence of magnesium Mg^{2+} promotes the formation of calcium magnesium carbonate [$CaMg(CO_3)_2$], also known as dolomite. Eq. 3-7 shows the reaction for the formation of dolomite. Kelts and Hsu (1978) report that

the formation of dolomite as a replacement of calcium carbonate in lacustrine deposits requires that Mg/Ca in the water is larger than the equilibrium ratio K_{dz} (= Mg^{2+}/Ca^{2+}),

$$2\ CaCO_3 + Mg^{2+} = CaMg(CO_3)_2 + Ca^{2+} \qquad \text{(Eq. 3-7)}$$

3.3. Characteristics of Deposit

3.3.1. Geographical Location, Soil Profile, and Site Geology

A soft carbonatic lacustrine deposit was studied to investigate the different forms of carbonates that are present in carbonatic deposits and their effects on soil microstructure. Figure 3-1 shows the location of the site on the map of Daviess County, Indiana, USA. The site is located at the intersection of County Road 900 E and County Road 1650 N, in Madison, Daviess County, Indiana, about 85 miles southwest of Indianapolis.

A small creek, called “First Creek” crosses the site, and controls the water table making it very close to the ground surface (1.9 m below the ground surface, corresponding to 150.8 m above mean sea level). The average soil profile obtained from field observations and from examination of the samples used for the laboratory tests is shown in Figure 3-2. A 4.3 m-thick carbonatic soil layer is found at a depth of 6.1 m, above which there is 1.9 m of silty sand, 1.5 m of clayey silt, and 2.7 m of clay. The carbonatic soil is underlain by a sand layer with occasional traces of clayey silt and sandy silt. The bedrock, mostly sandstone, highly weathered, is located at a depth of about 37 m.

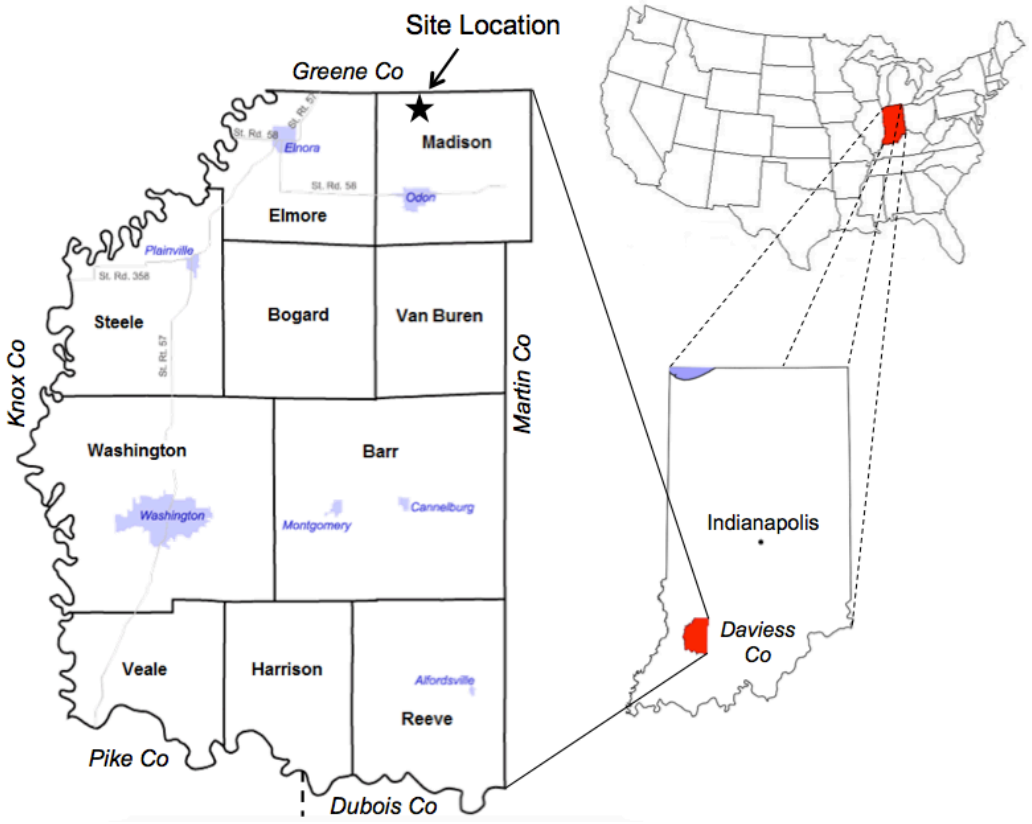

Figure 3-1: Map of Daviess County (Indiana) showing the site location

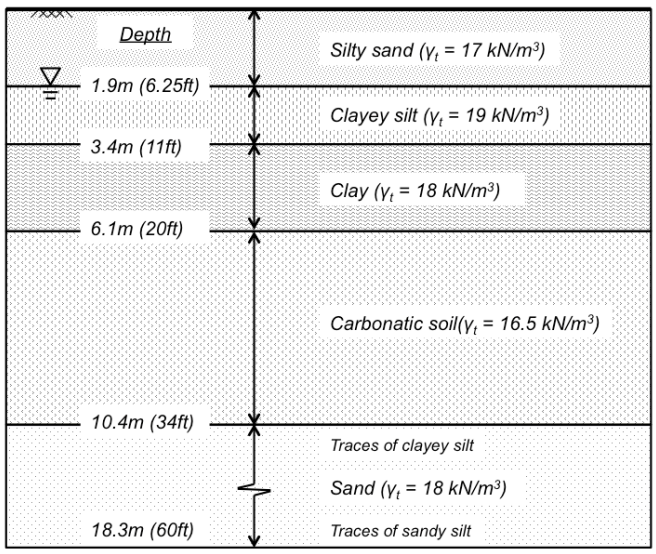

Figure 3-2: Stratigraphy of the site

CHAPTER 2 provides details on the site geology and the deposit formation. It reports that the site lies between the Wisconsin and Illinoian glacial boundary and is adjacent to the west fork of the White River. The deposit is of Wisconsin age, where the White River acted as sluiceway for Wisconsin melt-waters carrying debris that caused the formation of extensive valley trains near the site. These valley trains resulted in ponding of First Creek, one of its tributaries, leading to the formation of a lake. The presence of fossils of small freshwater gastropods as well as charophyte oospores (pond-dwelling algae) in the soil deposit at different depths confirms that the soil was deposited in a lacustrine environment. Radiocarbon dating using accelerator mass spectrometry (AMS), conducted on both fossils (shells) and plants (pieces of wood) taken from the deposit at depths varying between 7.3 m and 10.1 m, was used to accurately estimate the age of the deposit at 23,600 to 20,800 yr BP, with the age increasing with depth.

3.3.2. Index Properties

A full laboratory testing program, including both index and engineering tests, was performed on Shelby tube samples obtained from the carbonatic soil layer identified at depths between 6.1 m and 10.4 m. Examination of the soil samples obtained from the layer revealed that it is formed by alternating thin layers of two soils, which are herein referred to as “soil M” and “soil C”. This denomination was selected based on the fact that they can be classified as silt and clay, respectively (CHAPTER 2). Soil C is found in thin layers with thickness ranging between 0.5 cm and 10 cm, whereas soil M is found in thicker layers and forms the majority of the carbonatic layer. A feature specific to soil M is the presence of shells. While both soils are characterized by high calcium carbonate content (with an average value exceeding 55% for soil M and close to 40% for soil C), they show distinct mineralogy, index and engineering properties, requiring separate characterization. CHAPTER 2 linked the observed differences between soil M and soil C to the geologic history of sedimentation. Specifically, it suggests that

different source materials and sedimentary environments alternated during the formation process of the deposit leading to the formation of the two soils.

An extensive program of index tests was conducted on tube samples to characterize the variation of the index properties with depth. Key index properties for soils M and C derived from this work are summarized in Figure 3-3. The sequential loss on ignition method (Jung et al., 2011) was used to derive the $CaCO_3$ content values reported in Figure 3-3(b). In this method, a sample is placed in the furnace at 455 °C for six hours, and then at 800 °C for additional six hours. The reduction in mass measured during the second ignition stage is used to calculate the release of CO_2 associated with the decomposition of calcium carbonate (which takes place between 650 °C and 800 °C). This value is used to determine the calcium carbonate content. Given that dehroxylation of some clay minerals, such as kaolinite, illite, chlorite and smectite (e.g. see Bish & Duffy, 1990; Velde, 1992), can occur in this temperature range, this method can lead to slightly overestimating the true carbonate content. Based on a study on a variety of clayey soils with calcium carbonate contents exceeding 10%, Jung et al. (2011) found that the deviation between the double ignition method and the chemical test performed in accordance with ASTM C25-06 (ASTM 2006), did not exceed 5%, and that the double ignition method provided values consistent with measurements obtained from thermal gravimetric analyses (TGA). In spite of this limitation, the ease and rapidity of the double ignition method make it practical where numerous measurements are required (e.g. to profile calcium carbonate as a function of depth). Moreover, measurement of the loss on ignition during the first ignition stage also provides an estimate of the soil's organic content, based on AASHTO T267-86 (AASHTO, 2008).

See APPENDIX C for details on the testing procedures followed to derive all other index properties.

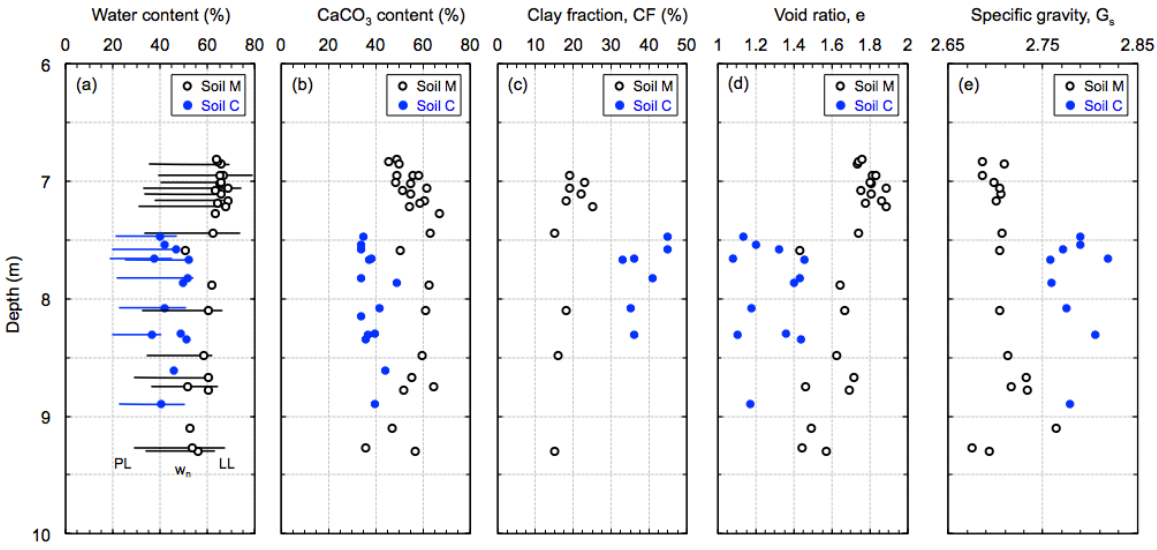

Figure 3-3: (a) Water content and Atterberg limits, (b) calcium carbonate content, (c) clay fraction, (d) void ratio, and (e) specific gravity profiles for the carbonatic soil

In general, compared to soil C, soil M has lower specific gravity, unit weight and clay content, but higher void ratio, water content, Atterberg limits, and $CaCO_3$ content. In particular, the average $CaCO_3$ content is 55% for soil M and 38% for soil C. Values of salt concentration (not shown) range from 2.1 to 5.1 g/l, with an average value throughout the layer of 3.2 g/l ± 0.8 S.D.

The initial void ratio of soil M shows a decreasing trend with depth (Figure 3-3(d)) ranging between 1.4 and 1.9 (mean e = 1.7 ± 0.2SD), which is expected due to the increase in confinement. This trend is not observed in the data for soil C, likely due to the limited number of data points and the significant scatter; however, the average void ratio of soil C is lower than that of soil M. There is no clear variation of the other index properties with depth (Atterberg limits, water content, $CaCO_3$ content, and clay content).

The difference in void ratio between the two soils can be attributed to the presence of shells in soil M, as well as the more open microstructure of soil M compared to soil C, observed by SEM (see Figures 3-8 to 3-11). The presence of internal voids within the shells likely also contributes to the lower specific gravity

of soil M (mean G_s = 2.71) relative to soil C (mean G_s = 2.78) (see Figure 3-3(e)). Another contributing factor to the difference in G_s is the mineralogy, as XRD analyses presented in CHAPTER 2 on randomly-oriented powder samples indicate that calcite, which has a specific gravity equal to 2.72 (Doner & Lynn, 1989; Mitchell, 1993), is the dominating carbonate mineral in soil M, while dolomite (with specific gravity of 2.85 Doner & Lynn, 1989; Mitchell, 1993) is the dominating carbonate mineral in soil C.

Despite the lower clay fraction and higher carbonate content (which is known to generally translate into lower values of the Atterberg limits and the plasticity – see Section 3.4.1 below), both the liquid limit and the plastic limit of soil M exceed the values measured on soil C. As discussed in CHAPTER 2, this can be explained based on the mineralogy of the clay fraction of the two soils. XRD analyses on oriented aggregates performed after different treatments allow accurate identification of the clay minerals. These analyses indicate that smectite, which is characterized by high specific surface and high water sorption capacity (e.g. De Kimpe et al., 1979), is the dominating clay mineral in soil M, contributing to 50% of the clay fraction and 10% of the bulk soil. In contrast, in soil C, smectite accounts for only 2% of the bulk soil, with illite and chlorite being the main clay minerals.

3.4. Investigation of the Microstructure

3.4.1. Insights from Decarbonation Experiments

Natural samples of soils M and C containing calcium carbonate ($CaCO_3$) and calcium magnesium carbonate ($CaMg(CO_3)_2$) and laboratory decarbonated samples were tested to investigate the influence of carbonate minerals on the Atterberg limits and particle size distribution, as well as to gain insight into the microstructure of the carbonatic soils. Two samples were analyzed: one of soil M recovered from a depth of 7.21 m; the second of soil C recovered from a depth of 7.82 m. Each sample was first completely homogenized by mixing and quartering,

and then divided into two portions: one was tested in its original state, while the other was transferred to a centrifuge bottle for decarbonation.

Several techniques have been reported in the literature for carbonate dissolution. For example, Griffiths et al. (1988) used EDTA flushing to remove cementation bonds from a structured soil; Hawkins & McDonald (1992) used acetic acid to decalcify a calcareous mudstone ($CaCO_3$ content ~ 36.3%); Bozzano et al. (1999) used hydrochloric acid (HCl) to decalcify a Pliocene lacustrine deposit ($CaCO_3$ content ~ 22%); and Musso et al. (2008) used both HCl and acetic acid to decalcify a marly clay ($CaCO_3$ content ~ 35%). Since the effects of HCl on pH are dramatic and may have significant effect on the clay minerals present in the soil, carbonate dissolution using glacial acetic acid (CH_3COOH) through buffering with sodium acetate (CH_3COONa) was adopted in this study. Acetic acid dissolves $CaCO_3$ and $CaMg(CO_3)_2$ according to the reactions:

$$CaCO_{3(s)} + 2\ CH_3COOH_{(aq)} \rightarrow Ca\ (CH_3COO)_{2(aq)} + CO_{2(g)} + H_2O_{(l)} \qquad \text{(Eq. 3-8)}$$

$$CaMg(CO_3)_{2(s)} + 4\ CH_3COOH_{(aq)} \rightarrow CaMg\ (CH_3COO)_{4(aq)} + 2\ CO_{2(g)} + 2\ H_2O_{(l)} \qquad \text{(Eq. 3-9)}$$

Carbonates were removed by adding a pH 5, 1 M sodium acetate-acetic acid solution (82.03 g of sodium acetate [CH_3COONa] + 27 ml of glacial acetic acid [CH_3COOH] + distilled water to reach a total volume of 1 liter) to the centrifuge bottle filled with the soil sample and heating to about 100 °C in a water bath for 20 min, followed by centrifuging and discarding the clear supernatant. This process was repeated 5 times to ensure a complete removal of carbonates (i.e. until vigorous bubbling was no longer observed). This decarbonation method is preferable to treatment with HCl since the pH can be maintained around 5, thus not affecting the clay minerals present in the soil. After the treatment, the samples were centrifuge-washed three times with deionized water to ensure the removal of the reagents.

X-ray diffraction (XRD) analyses were performed on randomly-oriented powder of the treated specimens and compared with those on the natural samples. The XRD patterns for soils M and C before and after decarbonation are shown in Figure 3-4. Each peak in the figures is labeled with the mineral name, the Miller index (hkl), and the d-spacing. For comparison purposes, the patterns for the decarbonated samples are shifted downward. The XRD analyses demonstrate that the treatment with acetic acid did not cause any alteration to the clay minerals, which was shown to consist predominantly of smectite, illite, chlorite, and kaolinite (see CHAPTER 2 for a detailed discussion of the mineral composition). Figure 3-4 also demonstrates the effectiveness of the acid treatment in completely removing all carbonates from the two soils, which is indicated by the disappearance of the calcite and dolomite peaks.

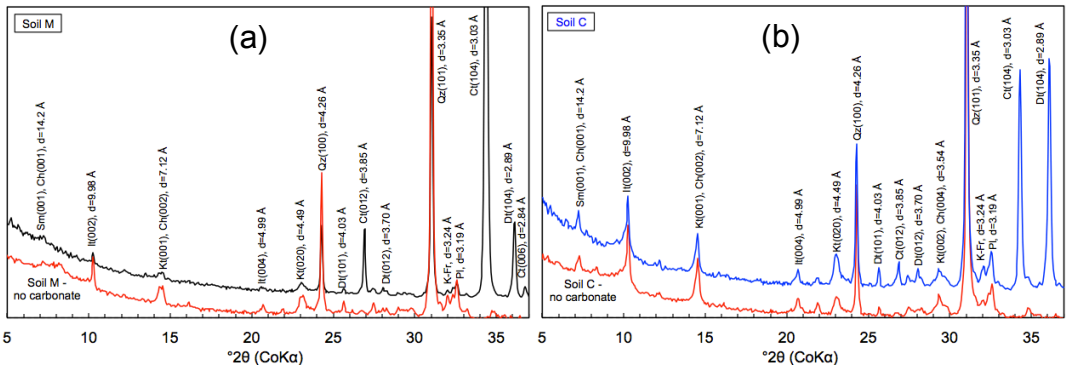

Figure 3-4: XRD patterns (randomly-oriented powder) of (a) soil M and (b) soil C in both natural state and following decarbonation. Mineral codes: Sm = smectite, Ch = chlorite, It = Illite, Kt = kaolinite, Qz = quartz, Dt = dolomite, Ct = calcite, K-Fr = K-feldspar, Pl = plagioclase feldspar

Measurements of pH were conducted on the treated specimens, since the acidity of the pore fluid is known to influence the Atterberg limits (e.g. see work by Fang & Daniels, 2006; Gronbech et al., 2010; Tajnin et al., 2014 showing a decrease in the Atterberg limits with increasing pH). Again, these data were compared with those from measurements on the untreated natural samples. The pH values for the untreated samples ranged between 7.6 and 7.7, compared to 7.7 to 7.8 for the specimens treated with CH_3COOH. These measurements demonstrate that

the acid treatment, followed by the washing with distilled water did not cause appreciable changes in the pH of the pore fluid.

The particle size distributions obtained from the hydrometer analyses and the Atterberg limits conducted on soil M and soil C before and after decarbonation are shown in Figure 3-5 and Figure 3-6, respectively. The untreated samples are labeled as M-orig and C-orig, while the treated samples are labeled M-dec and C-dec. The figures also include data reported in CHAPTER 2 for additional samples of soils M and C tested in their natural state. Table 3-1 summarizes the index properties of the original and decarbonated samples. Note that for these two samples, the percentages of $CaCO_3$, reported in Table 3-1, were derived based on the mass reduction measured using TGA between 650 °C and 1000 °C. This method was employed for these specific samples in order to obtain a more accurate estimate since it allows the separation between the loss due to the release of CO_2 associated with the decomposition of carbonates and that due to the dehroxylation of kaolinite and illite, which occurs between 400 °C and 600 °C (Bish & Duffy, 1990; Velde, 1992). However, Table 3-1 shows that the TGA results conducted on the decarbonated samples yield $CaCO_3$ values equal to 5.2% and 4.3% for soils M and C, respectively. The authors believe that these values are caused by the dehydroxylation of chlorite and smectite which occurs at temperature > 600 °C (Bish & Duffy, 1990; Velde, 1992) and cannot be separated from the decarbonation (recall that the XRD results in Figure 3-4 confirm the absence of carbonates in the soil after treatment).

Figure 3-5 shows that for both soils, decarbonation leads to an upward shift of the particle size distribution curves, reflecting the reduced size of the particles, and, in particular, an increased clay fraction. This observation provides insight on the role played by the carbonate on the soil microstructure. That is, it indicates that carbonate is acting as a cementing agent that connects clay particles together forming larger aggregates.

Decarbonation also induces a noticeable increase of the liquid limit (LL) and plasticity index (PI), whereas the plastic limit (PL) remains practically unchanged (Figure 3-6). These changes are associated with the increased surface area caused by the removal of the cementing agent through decarbonation. As seen in Figure 3-6, as a result of the changes in LL and PI (which are similar for both soils), the classification of soil M changes from MH to CH, and that of soil C from CL to CH.

These observations are in agreement with findings by Hawkins & McDonald (1992), who showed that the progressive removal of carbonates using acetic acid of a sample with 36% calcite resulted in an increase in liquid limit from 63% to 101% and in clay fraction from 52% to 82%. Contrary to this study, an increase in plastic limit from 21% to 33% was also observed. Similar observations were reported by Bozzano et al. (1999) and Lamas et al. (2002). The data obtained are also generally consistent with reports by other researchers for various carbonatic sediments (Bozzano et al., 1999; Fischer et al., 1978; Tsiambaos, 1991; Hawkins et al., 1988; Hawkins & McDonald, 1992; Hawkins, 1996; Lamas et al., 2002; and Musso et al., 2008) showing that, in general, as carbonate content increases, both Atterberg limits and clay fraction decrease.

As discussed earlier, soil M is also characterized by the presence of shells. To quantify the effect of these inclusions on the index properties, an additional set of limits and particle size analysis were performed on the original sample of soil M (from depth = 7.21 m), after elimination of the shells through wet sieving on a 0.075 mm sieve (ASTM #200). The material retained on the sieve is almost entirely composed of shells and forms ~6 % of the soil sample by dry mass. The results of these tests are included in Figure 3-5 and Figure 3-6 (M-no shells). It is seen from Figure 3-5 that the shells have minimal effect on the Atterberg limits (LL reduced from 66.3% to 63.9%). This is consistent with the findings reported in the literature for soils with small percentages of sand. For example, Fatahi et al (2011) show that the addition of 5% sand to kaolinite causes a decrease in liquid

limit from 49% to 46.7% (the LL was further reduced to 41% when the sand content increased to 20%). Similarly, a 2.9% decrease in liquid limit was reported by Shiwakoti et al. (2002) when 5% crushed Toyoura sand was mixed with kaolinite.

The table included in Figure 3-6 shows that the elimination of the shells reduces the percentage of sand-size particles from 6% to 0% and that the clay fraction remains practically unchanged. It also shows about 10% reduction in $CaCO_3$ content. Hence it can be concluded that shells make up about 6-10% of this particular soil sample. Note that the percentage of shells in soil M varies from one sample to another due to natural soil variability. A total of eight hydrometer analysis tests conducted on soil M collected from different depths indicate that the percentage of shells (estimated based on the mass retained on a #200 sieve) varies between 2% and 6%.

Table 3-1: Index properties of the carbonatic soil before and after decarbonation

	Original soil		Decarbonated soil	
	Soil M	Soil C	Soil M	Soil C
$CaCO_3$ content (%)[a]	63.1	34.2	5.2	4.3
1:1 water pH[b]	7.6	7.7	7.7	7.8
Plastic limit, PL (%)[c]	31.2	22.0	29.8	22.4
Liquid limit, LL (%)[c]	66.3	53.7	75.6	66.6
Plasticity index, PI (%)	35.1	31.7	45.8	44.2
Clay fraction, CF (%)[d]	25	41	40	53

[a] Based on the reduction in mass measured using TGA between 650 °C and 1000 °C (APPENDIX C)
[b] Based on ASTM D4972-13 (ASTM, 2013)
[c] Based on ASTM D4318-10 (ASTM, 2010)
[d] Based on ASTM D422-63 (ASTM, 2007)

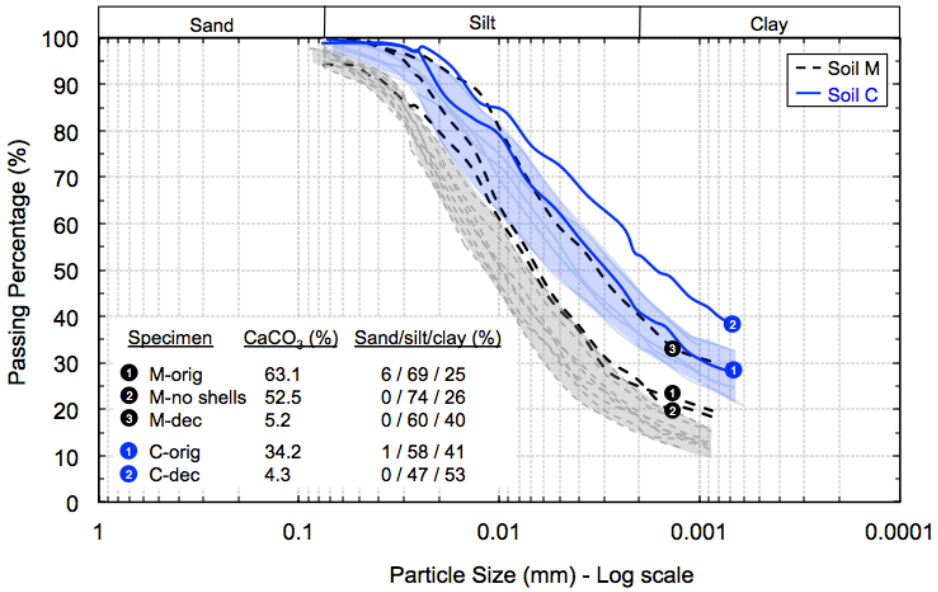

Figure 3-5: Particle size distribution of soils M and C and the changes caused by decarbonation

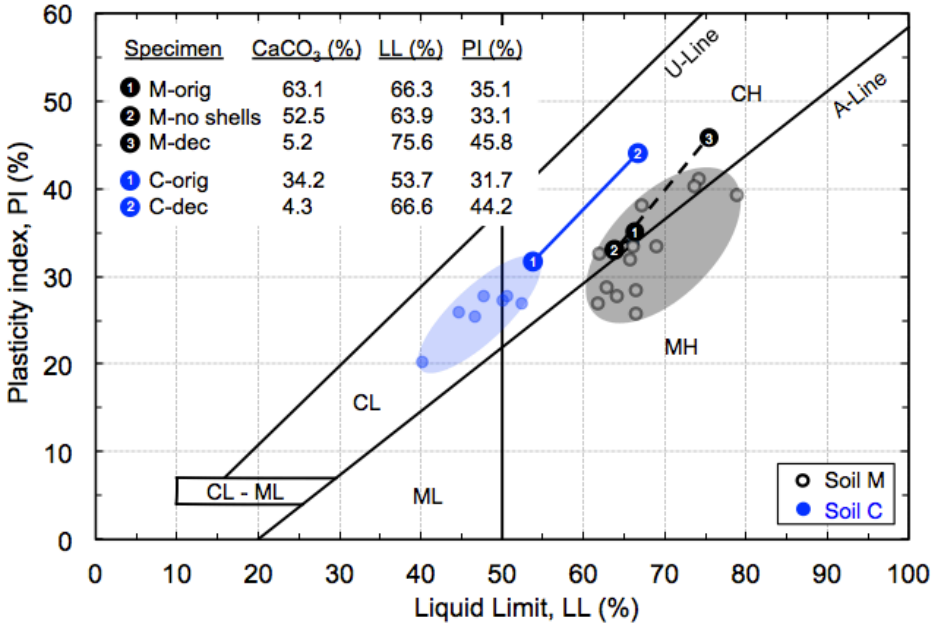

Figure 3-6: Plasticity chart showing the variation in Atterberg limits of soils M and C caused by decarbonation

It should be noted that similar observations to the ones presented above have been reported in the literature for soils characterized by the presence of other cementing agents. For example, Zhang et al. (2004) showed that in the case of a

weathered old alluvium the removal of the Fe-oxide cementing agents through remolding led to a similar increase in LL, PI and clay fraction. Note that while mechanical action alone is effective in destroying the cementation associated with Fe-oxide, chemical treatment is required in the case of carbonates. Similarly, Fearon and Coop (2000) showed that, in the case of an Italian scaly clay, a remolding process that disaggregated the micro-fabric as well as the scaly macro-fabric led to an increase in LL and PI. The data reported above are also consistent with the changes in limits and particle size distribution associated with artificially cemented soils (e.g. Kang, 2016). Finally, the presence of an aggregating agent such as organic matter has been shown to generate similar behavioral patterns in both Atterberg limits (e.g. Huang et al., 2012) and particle size distribution (e.g. Santagata et al., 2008).

3.4.2. Direct Observations using SEM

Scanning electron microscopy (SEM) was employed to gain direct insight into the microstructure of the two carbonatic soils, and investigate the role played by carbonates as cementing agents, with a special emphasis on highlighting the differences between soils M and C.

Two undisturbed samples were analyzed: one of soil M recovered at a depth of 7.28 m with $CaCO_3$ = 66.8%; the second of soil C at a depth of 8.15 m with $CaCO_3$ = 33.7%. These two specific samples were selected for the analysis since they represented the extreme conditions in terms of $CaCO_3$ content encountered in the deposit. Each sample was allowed to dry at room temperature for about 1 week and then broken to create a free fractured surface that was mounted on a sampler holder using graphite paste (Figure 3-7). Images were obtained at the Purdue University's Life Science Microscopy facility with the FEI Quanta 3D FEG SEM using the low vacuum LVSED detector as well as the backscattered BSE detector (with 20kV, Spot 6.0, and 10mm WD). Magnifications ranged between 130x and 40,000x. Qualitative elemental analysis on selected areas was

performed by energy-dispersive X-ray (EDX) spectrometry using an Oxford INCA Xstream-2 with Xmax80 detector (Oxford Instruments, Peabody, MA) with 20kV, 6.5 spot, 10mm WD, 50µm objective aperture. All samples were imaged without coating to avoid the interference of the coating material (typically gold or carbon) with the interpretation of the EDX analysis.

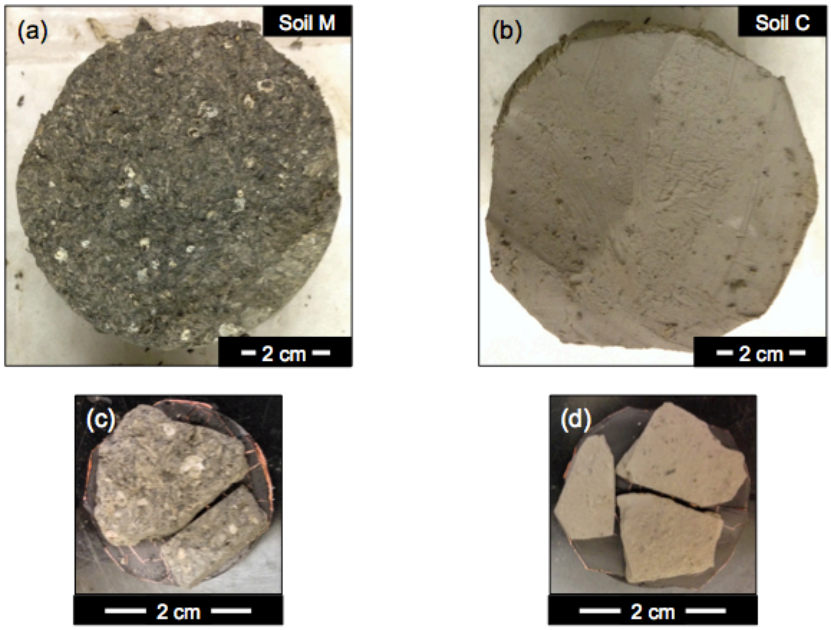

Figure 3-7: (a)-(b) Samples immediately after removal from Shelby tubes, and (c)-(d) after mounting on holders for SEM analyses

SEM micrographs of soil M obtained at low magnification (130x to 4,000x) reveal the presence of biological intrusions (fossils of snails, bivalves and diatoms) as well as framboidal pyrite. No shells are observed in soil C, but non-framboidal pyrites are observed. These observations are at the core of the hypothesis put forward in CHAPTER 2 that soils M and C were formed in different sedimentary environments, and that only the conditions during deposition of soil M promoted biogenic life.

The SEM micrographs (Figures 3-8(a-b) and Figure 3-9(a-d)) show that calcium carbonate is present in soil M in three different forms: (1) shells of gastropods; (2) calcium carbonate mesocrystals; and (3) integrated in the soil matrix. Included in

Figures 3-8 and 3-9 are spectra from EDX analyses performed at the locations identified on the micrographs, which provide location specific elemental analysis. In Figure 3-8(a), it is possible to identify part of a broken snail shell (which is shown to contain framboidal pyrite), a hypothesis confirmed by the EDX spectrum (Figure 3-8(c)), which indicates the presence of calcium, carbon, and oxygen (see CHAPTER 2 for a detailed presentation of the different types of gastropods identified in soil M). Based on the particle size analyses reported above, gastropods contribute to less than 10% of the soil's M dry mass, and thus less than 15-20% of its total carbonate content. Calcium carbonate is also found in the form of relatively large well-formed calcium carbonate crystals (Figure 3-8(b)), which the EDX spectrum (Figure 3-8(d)) confirms are composed of calcium, carbon, and oxygen. Based on their very rare occurrence in the samples examined using SEM, these crystals contribute in minimal part to the overall calcium carbonate content.

The third, and primary, form of calcium carbonate can be observed by increasing the magnification and analyzing an area of the soil matrix that is free from any biological intrusions, pyrite, and calcium carbonate mesocrystals. Figure 3-9(a-d) show the SEM micrographs for soil M at magnifications ranging between 10,000x and 40,000x, a resolution high enough to observe individual clay-size particles (<2 μm). The micrographs reveal the presence of clay platelets that are formed by groups of clay particles stacked together in a mainly 'face to face' configuration (see arrows in Figure 3-9(d)). These clay platelets appear to be covered by a continuous coating layer (Figure 3-9(b-c)) which "networks" the particles and groups of particles which, at some locations, are also interconnected by "bridges" (Figure 3-9(a)).

Note that the microstructure seen in Figure 3-8 and Figure 3-9 differs completely from that documented, for example by Bozzano et al. (1999) for an Italian carbonate deposit in which cementation occurred following consolidation of the

soil by precipitation of $CaCO_3$ inside the void space. In that case $CaCO_3$ was found to appear in form of “aggregates” of crystals of irregular shape that “filled void spaces and surrounded the clay particles.” This emphasizes how the microstructure of carbonatic soils strongly depends on depositional and geologic conditions and suggests that the interpretation of carbonate cementation resulting from “long-term crystal growth between the grains” may not accurately represent all deposits, including the one studied in this work.

In addition to the different forms of carbonate, the micrographs shown in Figure 3-8 and Figure 3-9 also suggest that there are different types of porosity: one associated with larger pore spaces around the inclusions (shells and mesocrystals) and within the shells (Figure 3-8), and one associated with the soil matrix at small scale (Figure 3-9). The rather “compact” nature of the clay matrix is consistent with the low-salinity depositional environment.

EDX analysis was performed on the surfaces of the clay platelets as well as on the “bridges” connecting the platelets. Representative examples of the results are shown in Figure 3-9(e-g) (similar spectra were obtained at other locations). The spectra reveal that calcium (Ca), magnesium (Mg) and carbon (C) exist on both the surfaces of the clay platelets, as a coating, and on the bridge connections between the clay platelets, indicating that, as expected, based on the chemical dissolution experiment, the cementing agent is carbonate. Note that the chemical elements contained in the clay and silt particles (i.e., silicon [Si], aluminum [Al], oxygen [O]) are also shown in the recorded X-ray spectra. Since the penetration depth of the electron beam into the sample is around 2 to 3 micrometers (McHardy & Birnie, 1987; Hafner, 2007), it can be concluded that the coating thickness should be less than ~3 micrometers.

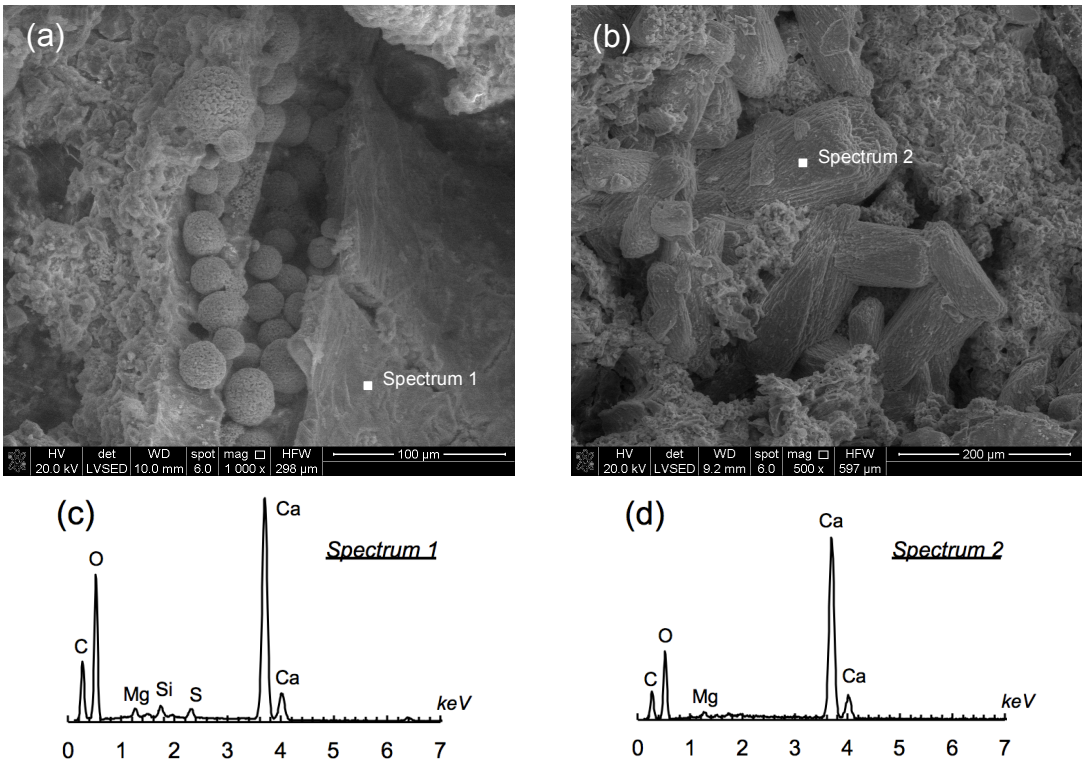

Figure 3-8: SEM micrographs of soil M showing (a) shell of a gastropod (containing framboidal pyrite) and (b) calcium carbonate mesocrystals; (c)-(d) spectra from EDX analysis at indicated locations

SEM-EDX analyses conducted at different magnifications reveal that, rather than being concentrated at the particle contacts, the carbonate coating is present in the majority of the sample, making it difficult to recognize individual clay and silt particles. This is illustrated in Figure 3-10(a-c) that show SEM micrographs of soil M at three different magnifications (1,000x, 10,000x, and 20,000x). Note that Figure 3-10(c) presents the image of the area identified by the box in Figure 3-10(b), and similarly, that Figure 3-10(b) provides the more close-up view of the area identified by the box in Figure 3-10(a). The corresponding average map spectra obtained from EDX analysis are shown in Figure 3-10(d-f). Unlike the spectra shown in Figures 3-8 and 3-9, these spectra provide the average distribution of the chemical elements detected in the entire micrograph at each magnification. The three EDX spectra show very similar results, i.e., the presence of calcium, magnesium, carbon, silicon and oxygen peaks have similar

relative intensities. This indicates that the carbonate coating is uniformly distributed across the sample.

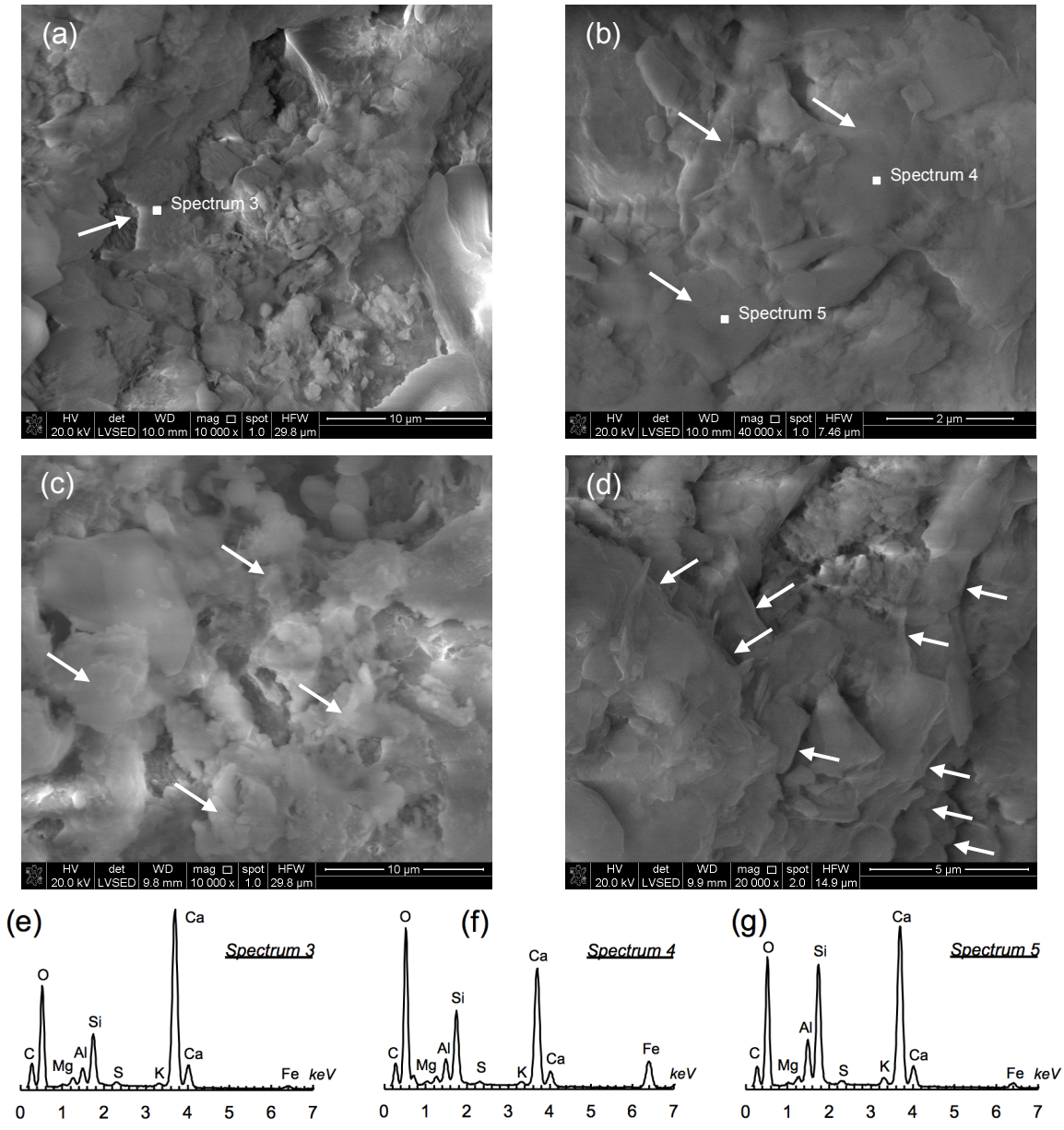

Figure 3-9: SEM micrographs of soil M showing (a) “bridge” connections between grains (indicated by arrow), (b)-(c) coating on particle surfaces (indicated by arrows), and (d) face-to-face particle orientation (indicated by arrows); (e)-(g) spectra of EDX analysis at indicated locations

Analogous images and spectra plots for soil C are shown in Figure 3-11 and similar conclusions can be drawn. The main difference observed between soil M and soil C is that the soil particles in soil C are more easily discernible as revealed by these micrographs. It can be also observed from the spectra that the carbonate (Ca/Mg) to silicon ratio in soil C is lower than that in soil M, which indicates a smaller thickness of the coating layer in soil C. This is consistent with the fact that soil C is characterized by lower $CaCO_3$ content. The micrographs shown in Figure 3-8 to Figure 3-11 also reveal that soil M has a more open microstructure compared to soil C. This observation is consistent with the void ratio values reported earlier (e ~ 1.7 for soil M versus e ~ 1.3 for soil C).

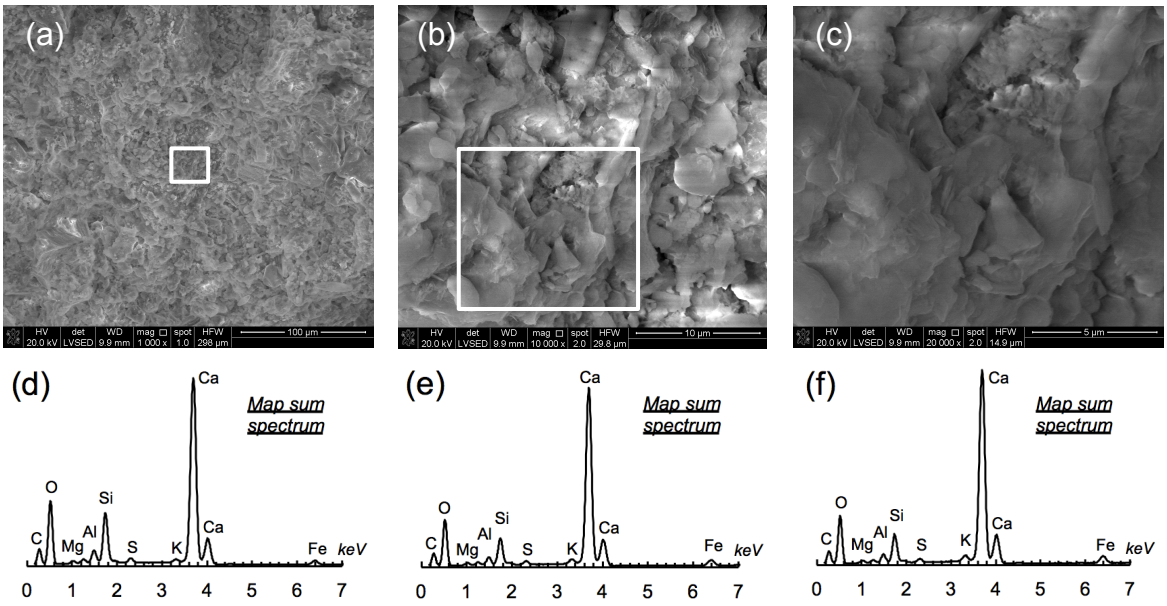

Figure 3-10: (a)-(c) SEM micrographs of soil M at different magnifications (1,000x, 10,000x, and 20,000x); (d)-(f) average map spectra from EDX analysis. Note that (c) is the area of the box in (b), and (b) is the area of the box in (a)

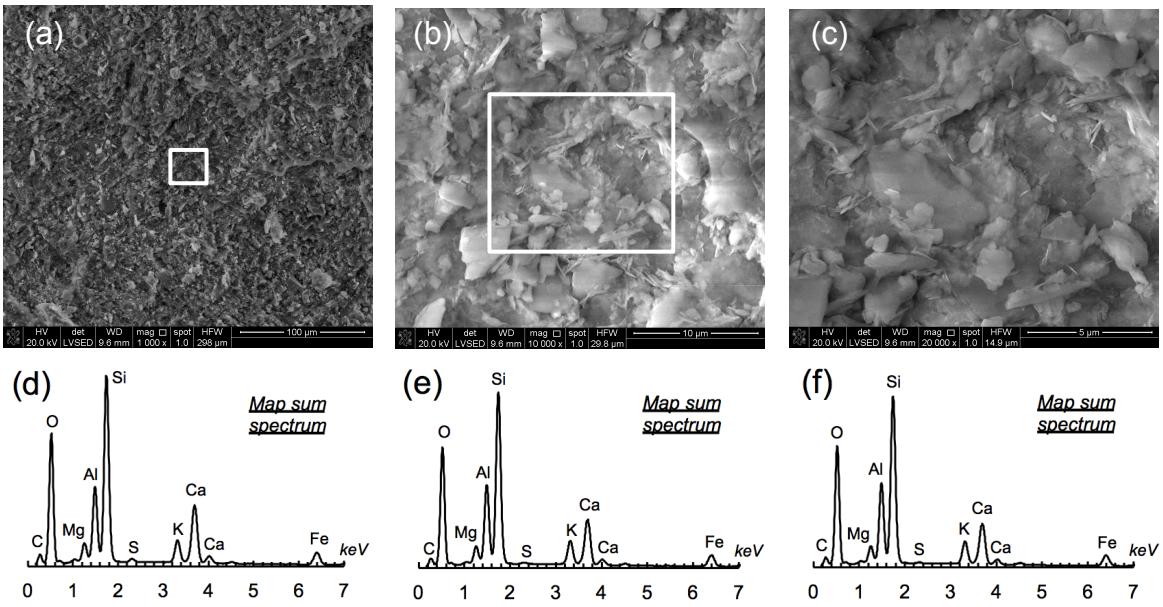

Figure 3-11: (a)-(c) SEM micrographs of soil C at different magnifications (1,000x, 10,000x, and 20,000x); (d)-(f) average map spectra from EDX analysis. Note that (c) is the area of the box in (b), and (b) is the area of the box in (a)

Further analysis was conducted on the SEM micrographs shown in Figure 3-10(c) and Figure 3-11(c) by generating EDX maps that show the distribution of calcium (Ca), magnesium (Mg), and silicon (Si). Figure 3-12 shows the distribution of these elements for the same samples of soils M and C. Each figure is composed of a SEM micrograph overlaid by EDX maps of select chemical elements with defined colors. Figure 3-12(a) plots the distribution of Ca, Mg and Si in soil M, and Figure 3-12(b) is an analogous plot for soil C. In these figures, the combined distribution of Ca and Mg is shown in cyan, and can be interpreted as a rough carbonate distribution map. Si is represented in red and is thought to be indicative of the distribution of clay and silt particles. For both soils, it can be seen that Ca/Mg and Si are evenly distributed, providing further evidence that carbonates are coating the clay and silt particles. As described earlier, since the penetration depth of the electron beam into the sample is around 2 to 3 micrometers (McHardy & Birnie, 1987; Hafner, 2007), which is larger than the estimated thickness of the carbonate coating, the chemical elements contained in the clay and silt particles (i.e., Si), as well as the elements in the carbonates (i.e., Ca and Mg) are all shown in the generated X-ray map. As reported above, the

amount of Ca/Mg relative to Si is much higher in soil M than in soil C, indicating that soil C is characterized by a thinner coating film.

A comparison between the distribution of Ca and Mg for soil M and soil C is shown in Figure 3-12(c) and Figure 3-12(d), respectively. In these figures, Ca is represented in cyan and Mg in purple. The maps reveal that the amount of Ca relative to Mg is much higher in soil M than in soil C, which can be also seen in the EDX spectra (Figure 3-10(d-f) for soil M and Figure 3-11(d-f) for soil C). This is in agreement with the mineral composition determined using XRD analyses showing that soil M has more calcite than soil C, but less dolomite (CHAPTER 2). It is also consistent with the results of TGA analyses presented in APPENDIX C showing that the carbonate breakdown for soil M occurs at relatively higher temperatures compared to soil C (~865°C for soil M and ~821°C for soil C). Since the decarbonation temperature of calcite is higher than that of dolomite (Doner & Lynn, 1989; Bish & Duffy, 1990; and APPENDIX C), the TGA test results indicate that soil M contains relatively more calcite than soil C, whereas the latter is richer in dolomite.

As discussed in detail in CHAPTER 2, the difference in the mineral composition is related to the different origin of the material and different sedimentary environments in which the two soils were deposited. Specifically, soil M is believed to have been formed from the locally derived calcite-rich sediments of Illinoian age subjected to a high degree of weathering which were transported through a small creek (First Creek); while the source of the sediments for soil C was through the White River as a result of occasional flooding above the valley trains caused by the high volume of Wisconsin-melt waters. This second source carried much younger dolomite-rich sediments from the northern part of Indiana.

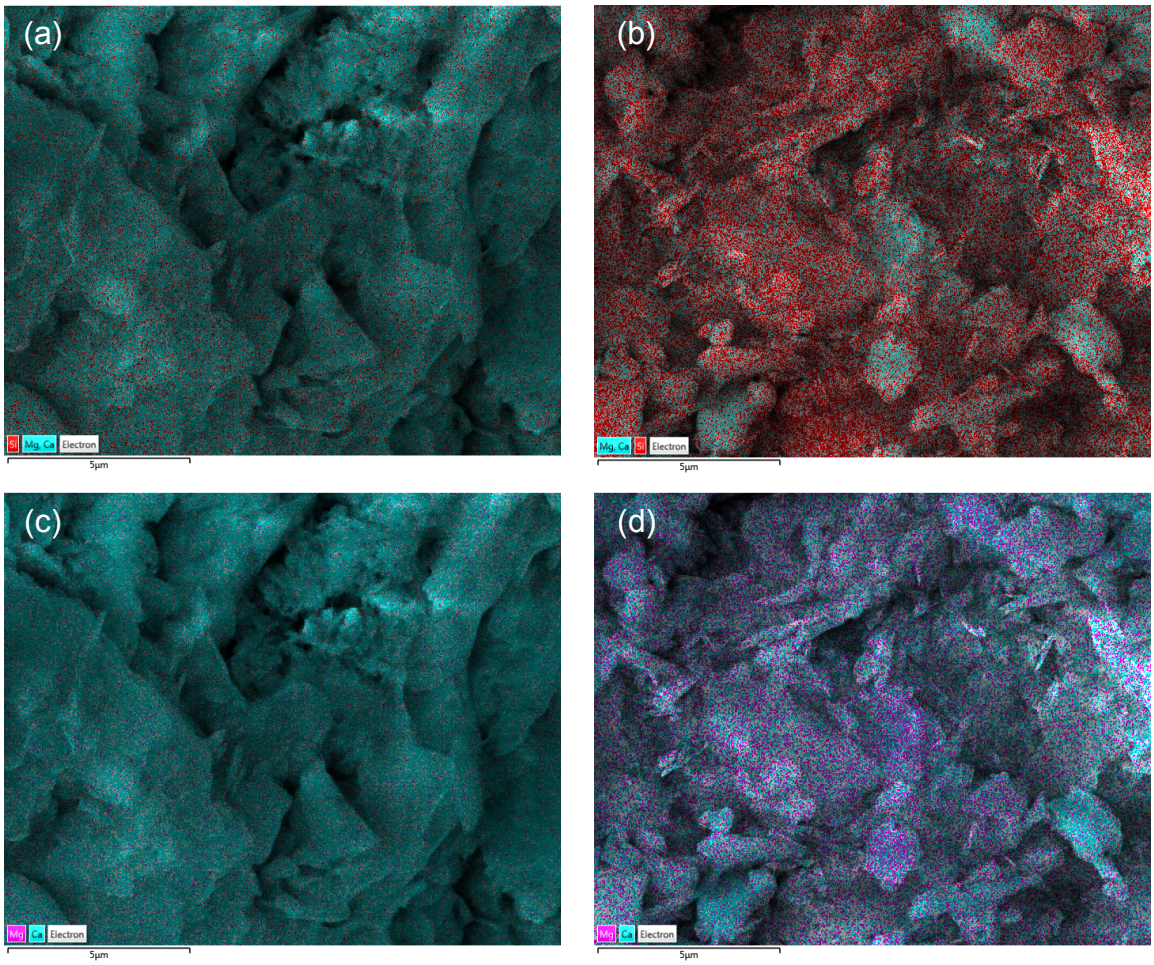

Figure 3-12: Maps from EDX analyses performed on: (a) soil M showing the distribution of Ca, Mg, and Si; (b) soil C showing the distribution of Ca, Mg, and Si; (c) soil M showing the distribution of Ca and Mg; (d) soil C showing the distribution of Ca and Mg

3.5. Discussion: Relationship Between Microstructure and Geotechnical Properties

The microstructural features identified in the previous discussion manifest themselves at the macro-scale in the results of both laboratory and field tests. In particular, the cementing action associated with the presence of carbonates is evident in the values of the preconsolidation stress (σ'_p) derived from constant rate of strain tests, incremental loading tests and the K_0-consolidation stage of triaxial tests (APPENDIX D). Figure 3-13(a) plots values of σ'_p derived using the strain energy method (Becker et al., 1987) from tests conducted on specimens of

soil M (15 tests) and soil C (8 tests) (APPENDIX D) from samples obtained over the depth of the layer examined in this work.

Although the deposit is known to be geologically normally consolidated, for both soils, σ'_p consistently exceeds the in-situ vertical effective stress (solid line in Figure 3-13(a)). Given the relatively young age of the deposit (accurately estimated in this study using radiocarbon dating as ~22,000 calendar years), this apparent OCR (Figure 3-13(b)) cannot be attributed solely to aging effects. The variable OCR profile with depth also does not support aging as the dominating preconsolidation mechanism (Jamiolkowski et al., 1985). Instead, the variation of OCR with soil type, and the greater values of σ'_p, consistently measured on soil M relative to soil C (average OCR = 1.9 for soil M versus 1.3 for soil C), indicate that interparticle bonding due to carbonate cementation is the controlling mechanism, and that the observed σ'_p profile is associated with changes in carbonate content. This is not unexpected as the preconsolidation stress is known to be impacted by structure forming processes including cementation, and similar effects on σ'_p have been reported in other studies of carbonatic deposits, including Burghignoli et al. (2010) and Boone and Lutenegger (1997).

Note that the increases in yield stress due to carbonate cementation reported by Boone and Lutenegger (1997), who compiled literature data from a large number of case histories, exceed significantly the values measured in this study (i.e. in glacio-lacustrine soils, for calcium carbonate values exceeding 30% the relationship provided by Boone and Lutenegger would predict increases in the yield stress exceeding 400 kPa – compared to a maximum value of ~100 kPa measured in this work – see Figure 3-13(a)). The data provided by Burghignoli et al. (2010) for two carbonatic lacustrine soils from the Fucino area in Italy with carbonate contents between 25% and 65%, show instead smaller increases in σ'_p, with values close to the ones reported in this study for one of the two soils investigated.

Differences in soil composition and depositional conditions (in particular pore water chemistry and the relative magnitude of sedimentation rate and cementation rate) are known to play a significant role in the structure and properties of carbonatic soils (Quigley 1980; Boone & Lutenegger 1997), and can contribute to explain the discrepancies between the different studies. For example, the sedimentation rate of the soil layer examined in this study (estimated at ~ 1 mm/year based on the layer thickness and the depositional period derived from carbon dating) is similar to that estimated for the Fucino clays, but over an order of magnitude smaller than that reported for the clays studied by Boone and Lutenegger (1997). While the discrepancies between the different studies cannot be attributed to a single factor, it is possible that the microstructure observed in this study with great part of the carbonate “distributed” on the mineral phase in form of a coating was promoted by the slow sedimentation rate. This type of microstructure may be responsible for less carbonate contributing to actual bonds at the particle contacts.

Additional insight into the nature of the microstructure and its impact on macro response can be gained examining the compression behavior. Figure 3-14(a-b) report one-dimensional compression curves for soils M and C, respectively. The data are plotted in terms of intrinsic void ratio (I_v) (Burland, 1990) versus vertical effective stress. Use of I_v in place of void ratio allows normalization of the compression data for clays of different composition. In this work, the parameters (i.e. the void ratios of the reconstituted soil at stresses of 100 and 1000 kPa) used to calculate I_v from void ratio were derived from relationships with the liquid limit provided by Burland (1990). Figure 3-14(a-b) also include two reference curves – the intrinsic compression line (ICL) and the sedimentation compression line (SCL) – which define the position of materials that are completely reconstituted (ICL) or characterized by what Burland (1990) refers to as a sedimentation structure (SCL) (i.e. a structure not significantly affected by post-depositional processes).

To start, the position of the in situ state relative to SCL provides a measure of the additional degree of structuring associated with post-depositional processes. Consistent with the relatively small values of void ratio derived from phase relations calculations (Figure 3-3) and the images reported in Figures 3-9 to 3-11, which attest to a relatively “compact” arrangement of the clay particles, the in-situ stress states fall only slightly above the SCL, evidence of limited degree of structuring. This is expected given the lacustrine origin of the deposit as deposition in a low salinity environment cannot produce the high void ratio flocculated structure typical, for example, of highly structured soils which exist significantly above the SCL (e.g. quick clays with I_v values as high as 4, Sheahan, 2005).

Comparison of the position of the compression curves of the natural soil beyond σ'_p relative to the intrinsic compression line (ICL) highlights the enhanced resistance to compression associated with the natural microstructure. As seen in Figure 3-14(a-b), beyond the yield stress, the compression curves are steeper than the SCL indicating partial destructuration, and at higher stresses they tend to become parallel to the ICL. The difference between the compression curves of the natural soil and the ICL observed at high applied stresses indicate that the specimens does not experience complete destructuration, and demonstrates the “stable” nature of the microstructure formed. Much higher stresses appear needed to damage the remaining structure. Again this appears consistent with the role of the carbonates, as observed in the SEM images, which, in addition to providing local bonds at particle contacts are distributed on the entire mineral surfaces. Similar observations on the compression behavior are reported by Soccodato (2003) for Fucino clay. The post-yield behavior observed in Figure 3-14(a-b), is also similar to that reported for artificially cemented soils (e.g. Kang & Santagata 2006, Bobet et al. 2011).

Note that Bozzano et al. (1999) also analyzed the compression behavior of an Italian Pliocene lacustrine carbonatic soil using Burland's framework. For this deposit, these authors found that the compression curves fell between the ICL and the SCL, and in some cases below the ICL. It can be hypothesized that this is due to the fact that, unlike what occurred in the soils examined in this paper, cementation occurred by precipitation of the calcium carbonate after consolidation of the soil, leading to further reduction of the void ratio.

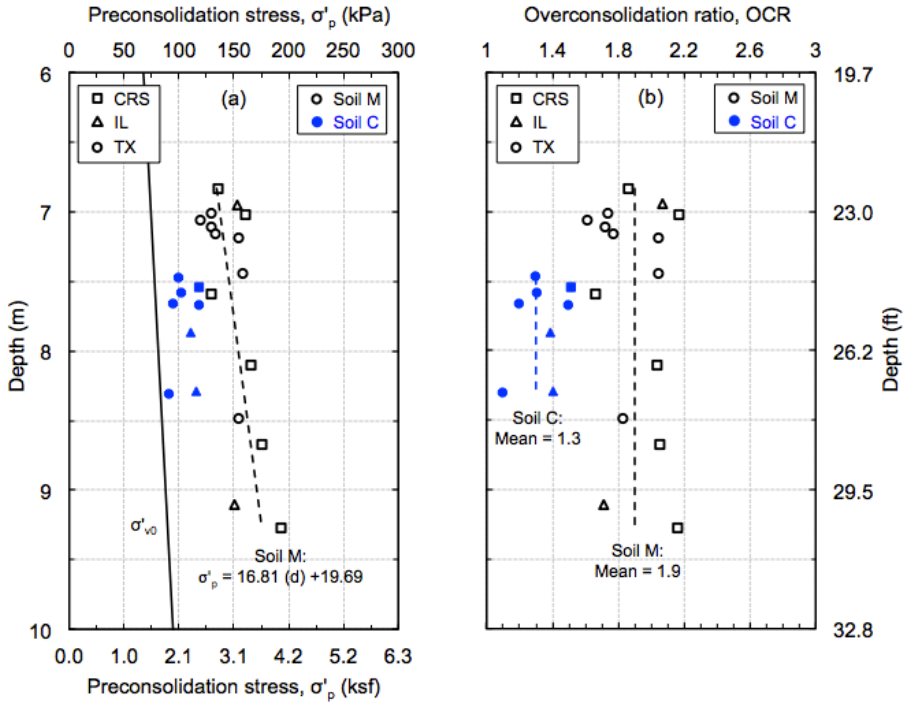

Figure 3-13: Stress history profile: variation of (a) preconsolidation stress and (b) OCR with depth

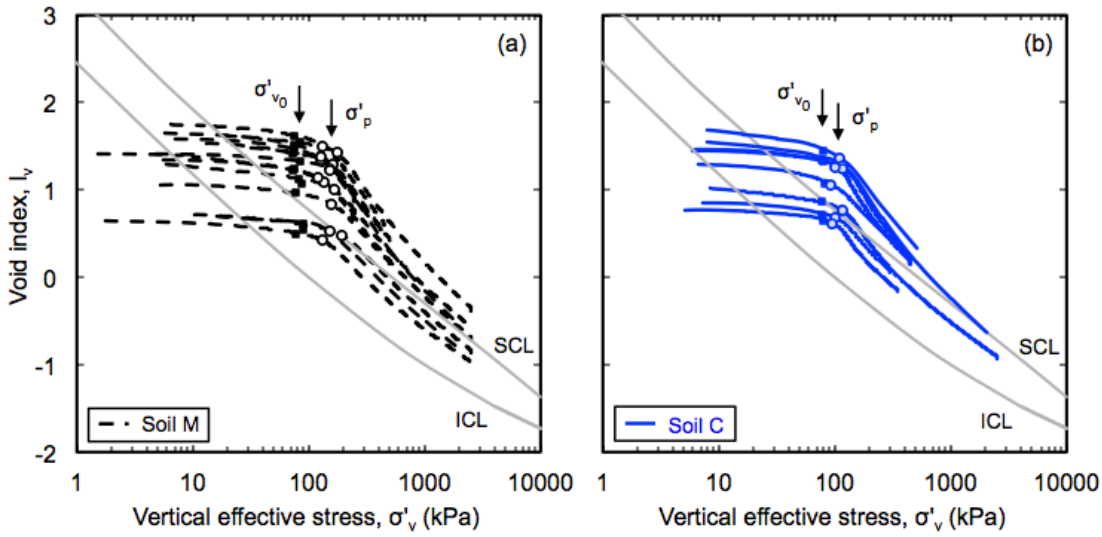

Figure 3-14: One-dimensional compression curves of (a) soil M and (b) soil C plotted using void index

The effects of cementation and the nature of the structure that characterize the deposit examined in this study are also evident when analyzing the undrained shear strength data obtained from field vane (FV) tests. Figure 3-15(a) summarizes the peak and remolded strengths computed from FV tests conducted every 0.6 m at the site, using the relationship for vanes tapered at both ends (ASTM D2573, 2008) and corrected based on Bjerrum (1972). Note that the FV measurements reflect the shear behavior of approximately a 0.3 m thick soil layer, and thus the results are influenced by the relative abundance of soils M and C at any depth. Figure 3-15(b) shows the resulting values of the peak undrained shear strength normalized by the in situ vertical effective stress, which for the most part tend to fall around 0.4. These values of the undrained strength ratio are generally consistent with the OCR of the deposit (Figure 3-13(b)), and the effects of cementation and/or the presence of the small shells identified in soil M. Figure 3-15(c) shows that the average ratio between peak and remolded undrained shear strength is about 5. This corresponds to a medium-high sensitivity (Holtz et al., 2011), which can be ascribed to the effects of carbonate cementation. Cementation is indeed the mechanism most

commonly responsible for such levels of sensitivity in clayey soils (e.g. Boone & Lutenegger 1997).

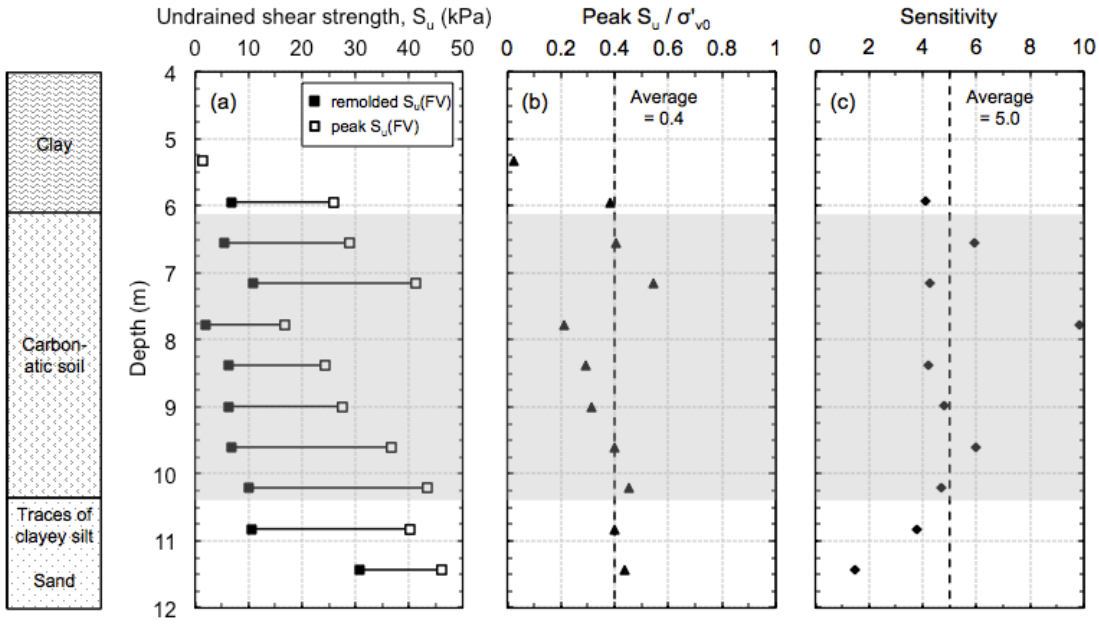

Figure 3-15: Profiles of (a) field vane undrained shear strength, (b) normalized peak undrained shear strength, and (b) soil sensitivity with depth

3.6. Conclusions

The microstructure of two carbonatic fine-grained soils (soil M with average carbonate content of ~ 55%, and soil C with average carbonate content of 38%) obtained from the same lacustrine deposit of Wisconsin age was characterized through a combination of direct microscopic observations by SEM and indirect examinations by EDX, carbonate dissolution using chemical treatment, XRD, Atterberg limits, and particle size analyses.

Particle size analyses and measurement of the Atterberg limits on both the natural soils, and on samples treated using acetic acid to remove the carbonates, show a reduction in the size of the particles and an increase in liquid limit and plasticity index following decarbonation. This is evidence that the carbonate acts

as a cementing agent that connects soil particles together to form larger aggregates.

Examination by SEM combined with EDX analyses of intact samples of both soils reveal the presence of a continuous carbonatic coating on the clay and silt particles, with carbonatic bridges connecting groups of particles. The thickness of the coating appears to be less than 2-3 micrometers and decreases in the sample with lower total carbonate content (soil C). Especially in the soil with higher carbonate content, the presence of the coating inhibits identification of individual soil particles in the SEM images.

EDX analyses also highlight another difference in the cementation microstructure of the two soils, as carbonates in soil M are mostly composed of calcium carbonate, while in soil C both calcium carbonate and calcium magnesium carbonate are present. Additionally, in soil M, approximately 15% of the carbonate content is ascribed to the presence of 1-2 mm size gastropods. This fraction has negligible effect on the limits.

Carbonate cementation impacts the engineering properties of both soils, leading, as previously shown for other soils, to the development of an apparent OCR. The OCR profile, derived from consolidation tests on high quality undisturbed samples, clearly reflects changes in carbonate content, with tests on soil M yielding OCR values greater than for soil C (average of 1.9 versus 1.3). These values of OCR fall at the very low end of what would be expected for soils having carbonate contents as high as those of soils M and C. This suggests that, in the soils examined, great part of the carbonate is in form of the coating layer identified in the SEM images, with only a fraction contributing to interparticle bonding.

In the I_v-σ'_v space proposed by Burland (1990), the in-situ stress states for both soils plot just above the sedimentation compression line (SCL), evidence of limited degree of structuring. Moreover, one-dimensional compression tests indicate that the cementation structure is stable, with no complete destructuration occurring even after the effective stress level exceeds ten times the preconsolidation stress. Consistent with this, in situ measurements of the peak and remolded undrained strength conducted at the site using the field vane indicate a medium-high sensitivity (S_t=5) of both soils.

3.7. Acknowledgments

This work was supported by the Joint Transportation Research Program administered by the Indiana Department of Transportation and Purdue University. The contents of this paper reflect the views of the authors, who are responsible for the facts and the accuracy of the data presented herein, and do not necessarily reflect the official views or policies of the Federal Highway Administration and the Indiana Department of Transportation, nor do the contents constitute a standard, specification, or regulation. The authors wish to acknowledge the help of Ms. Mariah Schroeder, who helped perform the Atterberg limits tests and Ms. Debby Sherman who performed the SEM observations and EDX analyses.

3.8. References

AASHTO T267-86 (2008). Standard method of test for determination of organic content in soils by loss on ignition. American Association of State Highway and Transportation Officials, Washington, D.C.

Allman, M.A. & Poulos, H.G. (1988). Stress-strain behaviour of an artificially cemented calcareous soil. Proceedings of International Conference on Calcareous Soil (Perth), Balkema, 1, pp. 51-60.

ASTM C25-06 (2006). Standard Test Methods for chemical analysis of limestone, quicklime, and hydrated lime. Annual Book of ASTM Standards, ASTM International, West Conshohocken, PA.

ASTM D2573-08 (2008). Standard Test Method for Field Vane Shear Test in Cohesive Soil. Annual Book of ASTM Standards, ASTM International, West Conshohocken, PA.

ASTM D422-63 (2007). Standard test method for particle-size analysis of soils. Annual Book of ASTM Standards, ASTM International, West Conshohocken, PA.

ASTM D4318-10 (2010). Standard test methods for liquid limit, plastic limit, and plasticity index of soils. Annual Book of ASTM Standards, ASTM International, West Conshohocken, PA.

ASTM D4972-13 (2013). Standard test method for pH of soils. Annual Book of ASTM Standards, ASTM International, West Conshohocken, PA.

Becker, D.E., Crooks, J.H.A., Been, K., & Jefferies, M.G. (1987). Work as a criterion for determining in situ and yield stresses in clays. Canadian Geotechnical Journal, 24(4), pp. 549-564.

Bish, D.L. & Duffy, C.J. (1990). Thermogravimetric Analysis of Minerals. In J.W. Stucki, D.L. Bish, & F.A. Mumpton (Eds.), Thermal analysis in clay science (pp. 96-157). Clay Minerals Society Workshop Lectures, Boulder, Colorado.

Bjerrum, L. (1972). Embankments on soft ground. Proceedings of the ASCE Conference on Performance of Earth-Supported Structures, Purdue University, 2, pp. 1-54.

Bjerrum, L. & Wu, T.H. (1960). Fundamental shear strength properties of the Lilla Edet clay. Geotechnique, 10, pp. 101-109.

Bobet, A., Santagata, M.C., Johnston, C., & Hwang, J.H. (2011). Effects of cement treatment on the one-dimensional compression behavior of a highly organic soil. Canadian Geotechnical Journal, 48(7), pp. 1100-1115.

Boone, S.J. & Lutenegger, A.J. (1997). Carbonates and cementation of glacially derived cohesive soils in New York State and southern Ontario. Canadian Geotechnical Journal, 34, pp. 534-550.

Bozzano, F., Marcoccia, S., & Barbieri, M. (1999). The role of calcium carbonate in the compressibility of Pliocene lacustrine deposits. Quarterly Journal of Engineering Geology, 32, 271-289.

Brindley, G.W. & Lemaitre, J. (1987). Thermal, oxidation and reduction reactions of clay minerals. In: A.C.D. Newman (Ed.), Chemistry of Clays and Clay Minerals (pp. 319-370). Mineralogical Society Monograph No.6, Mineralogical Society, London.

Burghignoli, A., Cavalera, L., Chieppa, V., Jamiolkowski, M., Mancuso, C., Marchetti, S., Pane, V., Paoliani, P., Silvestri, F., Vinale, F., & Vittori, E. (1991). Geotechnical characterization of Fucino clay. 10th European Conference on Soil Mechanics and Foundation Engineering (Florence), 1, pp. 27-40.

Burghignoli, A., Miliziano, S., & Soccodato, F. M. (2010). Cementation effects in two lacustrine clayey soils. Geotech Geol Eng 28. pp 815-833.

Burland, J.B. (1990). On the compressibility and shear strength of natural clays. Geotechnique, 40, pp. 329-378.

Chandler, R.J. (2000). Clay sediments in depositional basins: the geotechnical cycle. Q. J. Engng Geol. Hydrogeol., 33(1), pp. 7–39.

Conlon, R.J. (1966). Landslide on the Toulnustouc River, Quebec. Canadian Geotechnical Journal, 3, pp. 113-144.

Cotecchia, F. & Chandler, R.J. (1997). The influence of structure on the pre-failure behaviour of a natural clay. Geotechnique, 47(3), pp. 523–544.

De Kimpe, C.R., Laverdiere, M.R., & Martel, Y.A. (1979). Surface area and exchange capacity of clay in relation to the mineralogical composition of gleysolic soils. Canadian Journal of Soil Science, 59(4), pp. 341-347.

Demars, K.R. & Chaney, R.C. (Eds). (1982). Geotechnical properties, behavior, and performance of calcareous soils. American Society for Testing and Materials, Special Technical Publication STP 777. ASTM Philadelphia.

Doner, H.E. & Lynn, W.C. (1989). Carbonate, halide, sulfate, and sulfide minerals. In J.B. Dixon & S.B. Weed (Eds.), Minerals in Soil Environments (pp. 279-330). Soil Science Society of America, Madison, Wisconsin.

Fang, H.Y. & Daniels, J. (2006). Introductory geotechnical engineering: An environmental perspective. Taylor & Francis, London New York, pp. 109.

Fanning, D.S., Keramidas, V.Z., & El-Desoky, M.A. (1989). Micas. In J.B. Dixon & S.B. Weed (Eds.), Minerals in Soil Environments (pp. 551-634). Soil Science Society of America, Madison, Wisconsin.

Fatahi, B., Khabbaz, H., & Basack, S. (2011). Effects of salinity and sand content on liquid limit and hydraulic conductivity. Australian Geomechanics Journal, 46(1), pp. 67-76.

Fearon, R.E. & Coop, M.R. (2000). Reconstitution: what makes an appropriate reference material? Geotechnique, 50(4), 471–477.

Fearon, R.E. & Coop, M.R. (2002). The influence of landsliding on the behaviour of a structurally complex clay. Q. J. Engng Geol. Hydrogeol., 35(1), pp. 25–32.

Fischer, K.P., Andersen, K.H., & Moum, J. (1978). Properties of an artificially cemented clay. Canadian Geotechnical Journal, 15, pp. 322–331.

Gens, A. & Alonso, E.E. (1992). A framework for the behavior of unsaturated expansive clays. Can. Geotech. J., 29, pp. 1013–1032.

Griffiths, F.J., Ramesh, C.J., & Tumkur, S.N. (1988). Removal of cementation bonds in stressed overconsolidated clays, Geotech. Test. Journal, 4, pp. 227-232.

Gronbech, G., Nielsen, B.N., & Ibsen, L.B. (2010). Chloride concentration and pHs influence on the Atterberg limits of Sovind Marl. Aalborg: Department of Civil Engineering, Aalborg University. (DCE Technical Reports; No. 88).

Hafner, B. (2007). Scanning electron microscopy primer. Characterization facility, University of Minnesota-Twin Cities.

Hawkins, A.B. (1996). Observation and analysis of the ground conditions in the Jurassic landslide terrain of southern Britain. Proceedings of the 7th International Symposium on Landslides (17 21 June 1996), 1, pp. 3-16.

Hawkins, A.B., Lawrence, M.S., & Privett, K.D., (1988). Implication of weathering on the engineering properties of the Fuller's Earth formation. Geotechnique, 38, pp. 517-532.

Hawkins, A.B. & Mcdonald, C. (1992). Decalcification and residual strength reduction in Fuller's Earth formation. Geotechnique, 42, pp. 453-464.

Holtz, R.D., Kovacs, W.D., & Sheahan, T.C. (2011). An introduction to geotechnical engineering. New Jersey: Pearson, Inc.

Huang, P.T., Bobet, A., & Santagata, M.C. (2012). Identification of low organic content soils: an engineering approach, ASTM Geotechnical Testing Journal, 35(4), pp. 596-606.

Jamiolkowski, M., Ladd, C.C., Germaine, J.T., & Lancellotta, R. (1985). New developments in field and laboratory testing of soils. Proceedings of the 11th International Conference on Soil Mechanics and Foundation Engineering (San Francisco), 1, pp. 57-153.

Jones, B.F. & Bowser, C.J. (1978). The mineralogy and related chemistry of lake sediments. In A. Lerman (Ed.), Lakes: Chemistry, Geology, Physics. Springer, New York, pp. 179-235.

Jung, C.M., Bobet, A., & Siddiki, N.Z. (2011). Simple method to identify marl soils. Transportation Research Record 2232, pp. 76-84.

Kang, Y.I. (2016). Stress-strain-strength behavior of a cement treated clay. PhD Thesis in progress, School of Civil Engineering, Purdue University, West Lafayette, IN.

Kang, Y.I. & Santagata, M.C. (2006). One-dimensional compression behavior of cement-treated clay. Ground Modification and Seismic Mitigation, ASCE GSP 152, Proceedings of Sessions of GeoShanghai 2006, Shanghai, China, June 6-8, 2006.

Kelts, K. & Hsu, K. (1978). Freshwater carbonate sedimentation. In A. Lerman (Ed.), Lakes: Chemistry, Geology, Physics. Springer, New York, pp. 295-323.

Kenney, T.C., Moum, J., & Berre, T. (1967). An experimental study of bonds in a natural clay. Proceedings of the Geotechnical Conference (Oslo), 1, pp. 65-69.

Lamas, F., Irigaray, C., & Chacon, J. (2002). Geotechnical characterization of carbonate marls for the construction of impermeable dam cores. Engineering Geology, Elsevier, 66, pp. 283-294.

Lambe, T.W. & Whitman, R.V. (1969). Soil mechanics. New York: Wiley.

Langmuir, D. (1997). Aqueous Environmental Geochemistry, Prentice-Hall, Inc., upper Sanddle River, NJ.

Leroueil, S. & Vaughan, P.R. (1990). The general and congruent effects of structure in natural soils and weak rocks. Geotechnique, 40(3), pp. 467-488.

Leroueil, S. (1997). Critical state soil mechanics and the behaviour of real soils. Int Symp. On Recent Developments in Soil and Pavement Mechanics, Rio de Janeiro, pp. 41-80.

Loiselle, A., Massiera, M., & Sainani, U.R. (1971). A study of the cementation bonds of the sensitive clays of the Outardes River region. Canadian Geotechnical Journal, 8, pp. 479-498.

McGown, A.F. & Ladd, C.C. (1982). Effects of cementation on the compressibility of Pierre shale. In: K.R. Demars & R.C. Chaney (Eds.). Geotechnical properties, behaviour and performance of calcareous soils. ASTM Special Technical Publication, pp. 320-339.

McHardy, W.J. & Birnie, A.C. (1987). Scanning electron microscopy. In M.J. Wilson (Ed.), A handbook of determinative methods in clay mineralogy, pp. 174-208. London: Blackie.

Mitchell, J.K. (1993). Fundamentals of soil behavior. 2nd edition. John Wiley & Sons, Inc.: New York.

Musso, G., Chighini, S., & Romero, E. (2008). Mechanical sensitivity to hydrochemical processes of Monastero Bormida clay. Water Resources Research, 44.

Nitecki, M.H. (1960). A carbonate vein in limestone. J. Sediment. Petrol., 30, pp. 624-625.

Quigley, R.M. (1980). Geology, mineralogy, and geochemistry of Canadian soft soils: a geotechnical perspective. Canadian Geotechnical Journal, 17, pp. 261-285.

Sangrey, D.A. (1972). On the causes of natural cementation in sensitive soils. Canadian Geotechnical Journal, 9, pp. 117-119.

Santagata, M.C., Bobet, A., Johnston, C., & Hwang, J.H. (2008). One-dimensional compression behavior of a highly organic soil. Journal of Geotechnical and Geoenvironmental Engineering, ASCE 134 (1), pp. 1-13.

Sheahan, T.C. (2005). A soil structure index to predict rate dependence of stress-strain behavior. In Testing, Modeling and Simulation in Geomechanics, ASCE GSP No. 143, J.A. Yamamuro & J. Koseki (Eds.), pp. 81-97.

Shiwakoti, D.R., Tanaka, H., Tanaka, M., & Locat, J. (2002). Influences of diatom microfossils on engineering properties of soils. Soils and Foundations, 42(3), pp. 1-17.

Soccodato, F.M. (2003). Geotechnical properties of Fucino clayey soil. In proceedings on characterization and engineering properties of natural soils, Singapore. Tan et al. (Eds.) 1, pp. 791-808.

Tajnin, R., Abdullah, T., & Rokonuzzaman M. (2014). Study on the salinity and pH and its effect on geotechnical properties of soil in south-west region of Bangladesh. International Journal of Advanced Structures and Geotechnical Engineering ISSN 2319-5347, 3(2), April 2014.

Tsiambaos, G. (1991). Correlation of mineralogy and index properties with residual strength of Iraklion marls. Engineering Geology, 30, pp. 357-369.

Velde, B. (1992). Introduction to clay minerals: Chemistry, origins, uses and environmental significance. London: Chapman & Hill.

Wayne, W.J. (1971). Marl resources of Indiana. Indiana Dept. of Natural Resources, Indiana Geol. Survey Bull. 42-G, 16 p.

Zhang, G., Germaine, J.T., Whittle, A.J., & Ladd, C.C. (2004). Soil structure of a highly weathered old alluvium. Geotechnique, 54(7), pp. 453-466.

Zhu, L. (2009). An integrated study of steam-induced property changes of clay minerals. PhD Thesis, Department of Geological Sciences, Indiana University, IN.

CHAPTER 4. GEOTECHNICAL PROPERTIES OF A FINE-GRAINED CARBONATIC DEPOSIT[3]

4.1. Introduction

Fine-grained carbonatic soils are commonly found in glaciated regions of the northern United States and throughout Canada (Boone & Lutenegger, 1997; IDOT, 1999; INDOT, 2010; MDOT, 2009; ODOT, 2010) and Europe (Bozzano et al., 1999; Jamiolkowski et al., 1995; Hawkins et al., 1988; Tsiambaos, 1991; Anagnostopoulos et al., 1991; Paaza et al., 1998; and Lamas et al., 2002). They are typically characterized by high carbonate content (e.g. Boone & Lutenegger, 1997) and alternating layers of silts and clays (e.g. Thornbury, 1950; DeGroot & Lutenegger, 2003; and Long, 2003).

From a geotechnical perspective, these deposits are often considered challenging soils, since they are prone to excessive settlement and slope instability caused by their high compressibility, high creep potential, and low shear strength. Moreover, the heterogeneity caused by the alternating layers of carbonatic silts and carbonatic clays creates difficulties when relating laboratory test results to anticipated field behavior. Additional challenges are caused by the presence of carbonates, which typically precipitate at the inter-particle contacts resulting in a form of cementation (bonding) between the individual particles (e.g. Mitchell, 1993; Boone & Lutenegger, 1997). Carbonate cementation typically increases the sensitivity of the soil (e.g. Boone & Lutenegger, 1997) and makes it more susceptible to decalcification induced by groundwater flow and/or intense

[3] This chapter is extracted from the draft manuscript “geotechnical properties of a fine-grained carbonatic deposit”, to be submitted for publication.

rainfall events, which can lead into the degradation of the mechanical properties and enhance slope instability (e.g. Musso et al., 2008).

The objective of the present work is to contribute to the understanding of the mechanical behavior of natural carbonatic soils by reporting the results from an extensive experimental program of constant rate of strain (CRS), incremental loading (IL), and triaxial tests carried out on two soft fine-grained carbonatic soils with distinct composition and engineering properties that are found as alternating layers in a glaciolacustrine carbonatic deposit formed about 22,000 calendar years ago in the southwestern part of the State of Indiana, USA. The paper discusses in detail the differences in index and engineering properties between these two soils and highlights the effects of carbonate cementation.

4.2. Soil Characterization

The soil used in this study was obtained from the northern part of Daviess County, Indiana, USA. The site is located at the intersection of County Road 900 E and County Road 1650 N, in Madison, about 85 miles southwest of Indianapolis. As mentioned in CHAPTER 2, the deposit formed 22,000 calendar years ago during the Wisconsin glaciation where glacial meltwater flowing through the White River carried detritus near the site creating extensive valley trains that led to the ponding of First Creek, one of its tributaries, and the formation of a lake that became filled with sediment over time. This body of water was eventually drained due to natural drainage, evaporation and/or other geophysical processes leaving the deposited sediment behind. Today, the site is used for farming.

Data from boreholes drilled at the site and examination of the results of seismic cone penetration tests with pore pressure measurements (SCPTu) and standard penetration tests performed in proximity to the sampling location indicate that the 4.3 m thick carbonatic soil layer from which the samples were obtained is found

at a depth of 6.1 m, and is underlain by a sand layer with occasional traces of clayey silt and sandy silt. Above the carbonatic layer are about 1.9 m of silty sand, 1.5 m of clayey silt and 2.7 m of clay. Sandstone, highly weathered, is found at a depth of ~37 m. The average groundwater table monitored over a period of 16 days in November-December 2011 was found to be 1.9 m below the ground surface. This is illustrated in Figure 4-1, which shows the variation with depth of the tip resistance, skin friction and pore water pressure measured immediately behind the cone tip (u_2), obtained from the seven CPTs conducted at the site. The soft carbonatic soil layer examined in this work is highlighted in gray. The CPT results indicate that this layer is very soft (q_t ~ 500 kPa and f_s ~ 7 kPa), and has low permeability (high u_2).

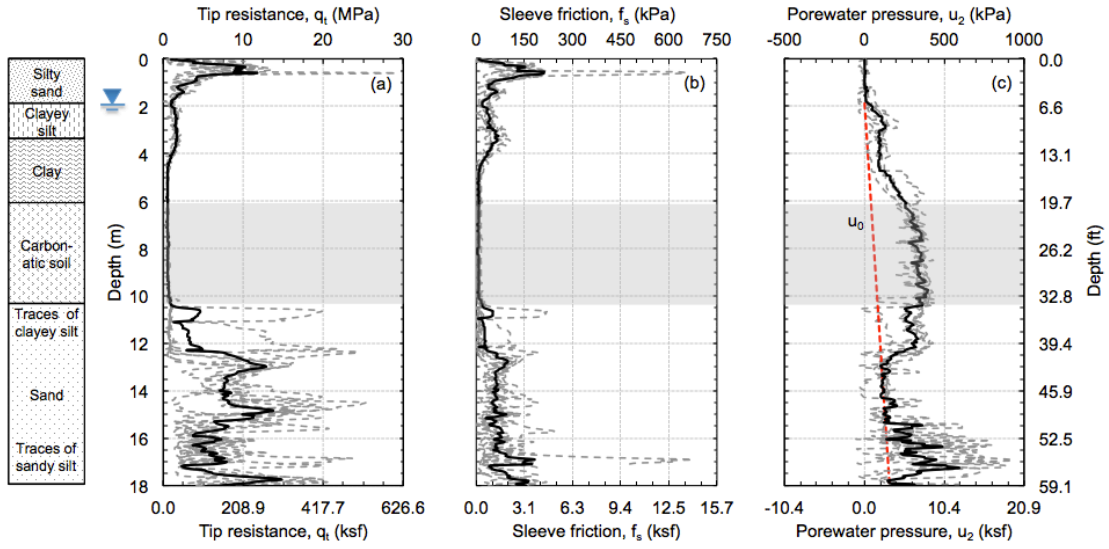

Figure 4-1: CPT results: (a) tip resistance, (b) skin friction, and (c) porewater pressure versus depth

The extensive series of laboratory tests to be described in this paper was performed on high-quality undisturbed soil samples retrieved in November 2011 using Shelby tubes from four boreholes drilled using mud rotary, which is considered one of the best practices for sampling in soft soil (Ladd & DeGroot, 2003). All the Shelby tubes had a modified edge geometry (i.e. sharp edged with an inside clearance ratio (ICR) of zero) to reduce the shear-induced strains

during sampling (Baligh et al., 1987; Clayton et al., 1998), and they were pushed with a fixed piston sampler to minimize sample disturbance (Ladd & DeGroot, 2003). Sampling was performed in a relatively small area (7 m x 9 m) to minimize the effects of spatial variability. After retrieval from the ground, the Shelby tubes were waxed and sealed with plastic caps, duct-taped on both ends and transported in a vertical position to Purdue's geotechnical laboratory. They were stored vertically in a humid room at a constant temperature of 10°C and 100% relative humidity to prevent drying.

The carbonatic soil layer identified at depths between 6.1 m and 10.4 m was characterized in the laboratory relying on the collected Shelby tube samples. This effort revealed that the carbonatic soil layer was formed by the repetition of small layers of two different soils with distinct composition, index and engineering properties, which required separate characterization. The two soils were classified according to the Unified Soil Classification System (ASTM D2487-11, 2011) as elastic silt (MH) and lean clay (CL); hence they are herein referred to as "soil M" and "soil C". As mentioned in CHAPTER 2, the observed differences between soil M and soil C could be attributed to the geologic history of sedimentation. The authors suggested that the two soils were formed in different sedimentary environments and from different source materials, which promoted the formation of the two types of soils. Soil M was found more frequently in the deposit and was characterized by the presence of shells, whereas soil C was found in relatively thinner layers, ranging between 0.5 cm and 10 cm and had no shells.

Select index properties of soils M and C are reported in Table 4-1. Soil M is characterized by higher $CaCO_3$ content, water content, Atterberg limits, and void ratio, but lower clay fraction, specific gravity, and total unit weight. CHAPTER 3 reported that the observed difference in void ratio between the two soils was

caused by the presence of shells in soil M as well as a more open microstructure of soil M compared to soil C.

Table 4-1: Select index properties of soils M and C

	Soil M[f]	Soil C[f]
$CaCO_3$ content (%)[a]	55.2 ± 7.6	38.1 ± 4.5
Water content, w_n (%)[b]	61.6 ± 5.8	44.3 ± 5.7
Plastic limit, PL (%)[c]	34.4 ± 3.4	21.6 ± 2.1
Liquid limit, LL (%)[c]	67.4 ± 5.0	48.3 ± 4.4
Liquidity index, LI	0.8 ± 0.2	0.8 ± 0.1
Clay fraction, CF (%)[d]	19.0 ± 3.4	38.7 ± 4.9
Specific gravity, G_s ,[e]	2.71 ± 0.02	2.78 ± 0.02
Void ratio, e	1.7 ± 0.2	1.3 ± 0.1
Total unit weight, γ_t (kN/m^3)	15.9 ± 0.4	17.5 ± 0.5

[a] Based on sequential loss on ignition method (Jung et al., 2011)
[b] Based on ASTM D2216-10 (ASTM, 2010)
[c] Based on ASTM D4318-10 (ASTM, 2010)
[d] Based on ASTM D422-63 (ASTM, 2007)
[e] Based on ASTM D854-14 (ASTM, 2014)
[f] the ± reflects the standard deviation

The mineral composition of soils M and C was analyzed both qualitatively and semi-quantitatively using X-ray diffraction (XRD) (CHAPTER 2; APPENDIX C). Table 4-2 summarizes the major minerals existing in soils M and C in decreasing order of predominance. For both soils the dominant non-clay mineral components are calcite, dolomite, and quartz, with small quantities of feldspars. A characteristic specific to soil M is the presence of aragonite, which is the mineral of the shells. Smectite, illite, chlorite, and kaolinite are the minerals making up the clay size fraction of both soils.

Despite the similarities in the identified minerals (with the exception of aragonite present only in soil M), CHAPTER 2 reported that there is significant difference between the quantities of each mineral. In particular, (1) soil M has more calcite

than soil C but less dolomite; (2) the predominant clay minerals in soil M are smectite (50%) and illite (27%), while those in soil C are Illite (62%) and chlorite (30%).

Table 4-2: Summary of the major minerals existing in soils M and C (in decreasing order of predominance)

Soil	Mineral type	Minerals Identified
Soil M[a]	Non-clay minerals	Calcite, quartz, dolomite, aragonite
	Clay minerals (19%)[b]	Smectite (50%), illite (27%), chlorite (12%), kaolinite (11%)[c]
Soil C[a]	Non-clay minerals	Quartz, dolomite, calcite
	Clay minerals (39%)[b]	Illite (62%), chlorite (30%), smectite (5%), kaolinite (3%)[c]

[a] Plagioclase feldspar and K-feldspar are trace minerals
[b] Based on particle size analysis – see Table 4-1
[c] Based on XRD semi-quantitative analysis

4.3. Experimental Methods

Specimens were prepared for all the engineering tests using the following procedure: the Shelby tube was cut using a horizontal band into segment lengths appropriate for each test, either consolidation or triaxial, to reduce disturbance due to extrusion. The remaining portions of the tube were resealed with wax and plastic caps and stored in the humid room for later use. The specimen was extruded following the method described by Ladd & DeGroot (2003). In summary, a piano wire was penetrated through the soil along the inside of the tube with the help of a thin hypodermic needle. The wire was used to debond the soil by rotating the tube about 3 to 4 times. The specimen was then gently pushed by hand out of the tube. The resulting specimen, ~7.4 cm in diameter, was then trimmed to its final dimension.

The consolidation behavior of the soil was measured through one-dimensional constant rate of strain (CRS) and incremental loading (IL) consolidation tests. All

tests were completed under single drainage conditions with measurements of the excess pore-water pressure at the base. The specimen was first backpressure-saturated to 200 kPa for a period of 24 hours. The saturation pressure and time were chosen based on the work reported by Black and Lee (1973), and confirmed by satisfactory B-value's measurements in the triaxial tests. Consolidation was performed by imposing a constant rate of displacement equivalent to a strain rate varying between 1%/hr and 3%/hr. For IL tests, the consolidation was performed by doubling the applied load, i.e. load increment ratio (LIR) equal to one, with each load increment maintained for 24 hours.

For the triaxial (TX) tests, porous stones and filter papers were placed at each end of the specimen and vertical drains (eight 6-mm wide filter strips) were used to provide lateral drainage. Data were corrected for the change in the specimen area during deformation, membrane and filter drains resistance (Germaine & Ladd, 1988). The specimens were all backpressure saturated to 200 kPa for 24 hours before consolidation, which resulted in an average B value of 0.99 ± 0.01SD for all triaxial tests.

Triaxial compression tests were conducted following both recompression (Bjerrum, 1972) and SHANSEP (Ladd & Foott, 1974) techniques. The recompression tests were performed by anisotropically reconsolidating the specimen along a predetermined stress path to the estimated in-situ stresses. The in-situ horizontal effective stress was calculated as the product between the in-situ vertical effective stress and the in-situ K_0 derived from the SHANSEP test results. The reconsolidation stage was carried out at strain rate of 0.5%/hr, allowed to creep for a period of 24 hours and then sheared under undrained conditions at a strain rate of 0.5%/hr. All SHANSEP triaxial tests were K_0-consolidated and sheared under undrained conditions in compression loading ($CK_0UTC(L)$), except for one test which was sheared drained ($CK_0DTC(L)$). After backpressure, the specimens were K_0-consolidated to stresses higher than $2\sigma'_p$,

at a constant strain rate varying between 0.5%/hr and 2%/hr. The specimens were allowed to creep for a period of 24 hours to dissipate the excess pore pressure. They were either sheared normally consolidated (OCR = 1) or swelled to the desired OCR, where they were sheared following a second creep stage. Undrained and drained shearing were carried out at constant rates of axial strain of 0.5%/hr and 0.2%/hr, respectively.

4.4. Results and Discussion

4.4.1. One-dimensional Compression Behavior

A total of 22 one-dimensional compression tests obtained from both IL, CRS and K_0-consolidated triaxial tests, performed on soils M and C are presented in Figure 4-2(a) and Figure 4-2(b), respectively. Both soils show similar compressibility properties that fall in the range of soft clays. The results show a consistent behavior, with compression curves characterized by a clear break at the preconsolidation stress σ'_p (derived using the method by Becker et al., 1987) and by an S-shape (i.e., a decrease in the virgin compression index (C_c) along the virgin compression line (VCL)), which evidences the soil's structure. Soil M is characterized by a higher maximum virgin compression index (derived between $2\sigma'_p$ and $3\sigma'_p$), with C_c=0.72±0.08, compared to soil C with C_c=0.52±0.11.

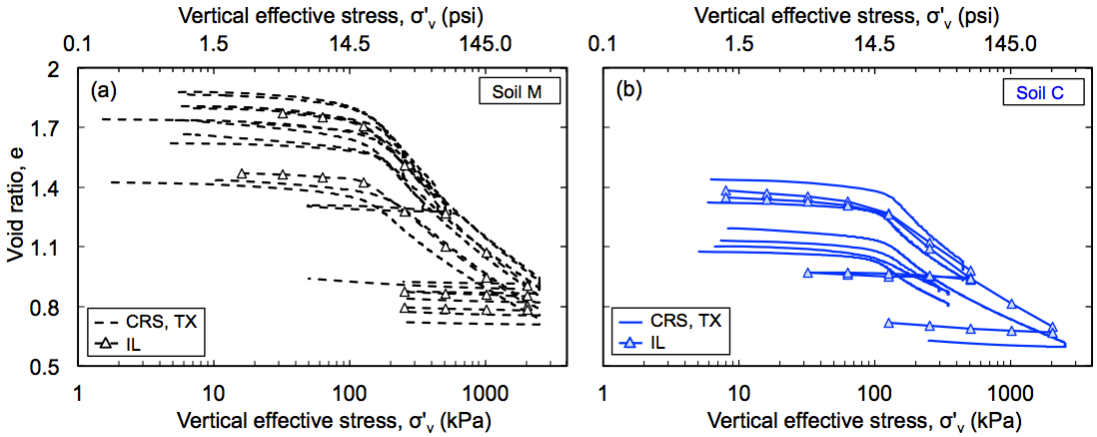

Figure 4-2: Compression curves from IL, CRS consolidation and SHANSEP CK_0UTC(L) tests on (a) soil M, and (b) soil C.

Figure 4-3(a) is a plot of σ'_p. Different symbols are used to indicate different types of tests (square, triangle and circle for CRS, IL and TX tests, respectively), while different colors are used to indicate the different types of soils (hollow black symbols for soil M and solid blue symbols for soil C). In general, there is no clear difference between the results obtained from the different tests (CRS, IL, and TX). However, a clear difference can be observed between soil M and soil C. Figure 4-3(a) shows that the data fall on two distinct bands, with soil M consistently exhibiting a higher σ'_p, and thus higher OCR (Figure 4-3(b)), at any given depth. In addition to the difference between the two soils, the oedometer compression tests yield σ'_p values higher than the in-situ vertical effective stresses (σ'_{v0}), even though the latter have never been exceeded during the geological history of the deposit (CHAPTER 2). This apparent overconsolidation is evidence of the soil's structure caused by interparticle carbonatic cementation (Leroueil & Vaughan, 1990). The higher values of OCR (averaging 1.9 for soil M and 1.3 for soil C) for soil M are attributed to the higher carbonate content present in soil M resulting in a higher degree of interparticle bonding.

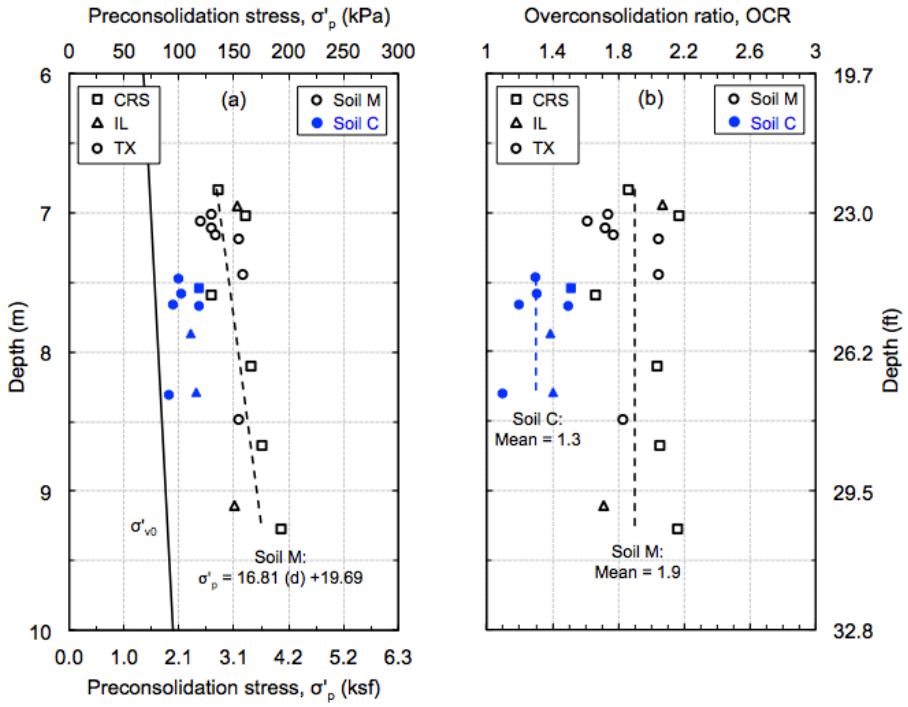

Figure 4-3: Stress history profile: (a) preconsolidation stress; and (b) OCR with depth

Values of the lateral stress ratio (or coefficient of earth pressure) at rest, K_0, were derived from the K_0-consolidation stage of the triaxial tests. Figure 4-4(a) presents the variation of K_0 with vertical effective stress for each of the tests performed. The figure shows that K_0 decreases as the specimen is loaded, reaches a minimum and then increases again reaching a constant value in the normally consolidated region. This behavior is typical of structured soils. The normally consolidated value of K_0 for soil C (0.55) exceeds that of soil M (0.48). This is consistent with the friction angle values measured on these two soils (see below). Upon unloading, K_0 increases once again. From the data shown in Figure 4-4(a) it is possible to derive a relationship between K_0 and OCR (see Figure 4-4(b)), which has similar form for both soils. Note that the values of K_0 shown in Figure 4-4(b) are obtained at the end of the unloading phase and before shear. The relationship between K_0 and OCR is:

$$K_0 = K_{0NC} (OCR)^n \qquad \text{(Eq. 4-1)}$$

Where K_{0NC} = 0.48, n = 0.40, and r^2 = 1.00 for soil M; and K_{0NC} = 0.55; n = 0.37; and r^2 = 0.99 for soil C.

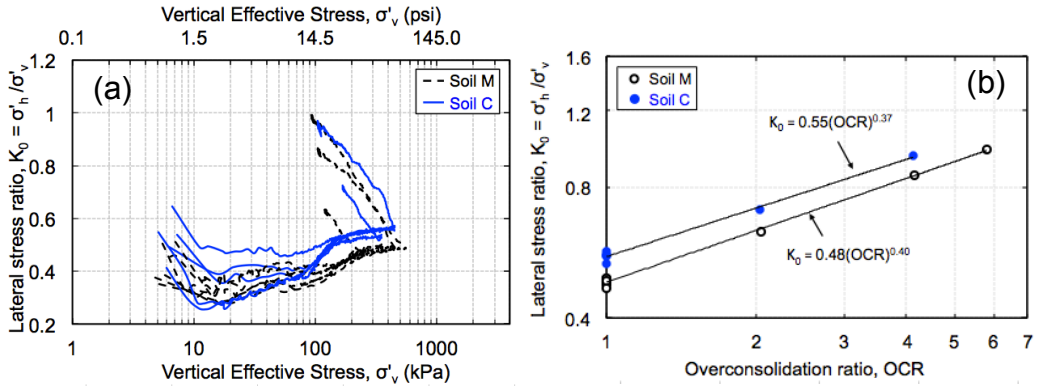

Figure 4-4: Results of K_0-consolidation from triaxial tests: lateral stress ratio vs. (a) σ'_v; and (b) OCR

Figure 4-5 shows how the coefficient of consolidation C_v obtained from CRS (denoted by lines) and IL (denoted by triangles) consolidation tests. For the CRS consolidation tests, the values of C_v are calculated based on the CRS consolidation theory developed by Wissa et al. (1971). For the IL consolidation tests, the values of C_v represent the average of the logarithm of time (Casagrande, 1936) and the square root of time (Taylor, 1948) curve fitting methods. The results show a decrease in C_v during loading followed by a slight increase in the normally consolidated region. For all tests, the results are characterized by an increasing value of C_{vNC}, with similar trends reported by Berman (1993) and Abdulhadi (2009). This is a result of the fact that the increase in the constrained modulus D occurring at higher stresses overrides the reduction in the hydraulic conductivity associated with loading.

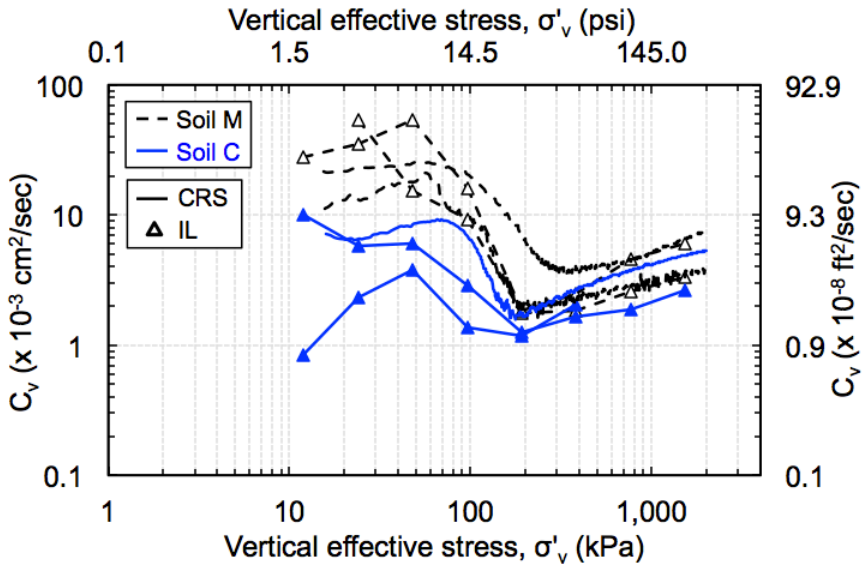

Figure 4-5: Coefficient of consolidation versus vertical effective stress from CRS and IL consolidation tests

Key consolidation properties for soil M and soil C are summarized in Table 4-3. The Table lists the ratio $C_{\alpha e}/C_c$ calculated for soil M and soil C using four IL consolidation tests. The ratio is equal to 0.041 for soil M (r^2 = 0.99) and 0.036 for soil C (r^2 = 0.97), which falls in the range of soils with relatively high creep rate (Mesri & Godlewski, 1977). Moreover, the quality of the soil samples was assessed by calculating the normalized change in void ratio ($\Delta e/e_0$; where Δe is the change of the void ratio associated with reconsolidation of the soil to the in situ stress, and e_0 is the initial void ratio) obtained from the consolidation (CRS and IL) tests, and the K_0 consolidation phase of the triaxial tests. All the data fall below 0.055, indicating that the samples can be classified as “excellent” to “good” based on the sample quality designation suggested by Lunne et al. (1997).

Table 4-3: Summary of consolidation properties

	Soil M		Soil C	
	Range	Mean ± SD[a]	Range	Mean ± SD[a]
Overburden stress, σ'_{v0} (kPa)	73.1 – 89.4	78.9 ± 5.7	77.3 – 82.9	79.5 ± 2.2
Preconsolidation stress, σ'_p (kPa)	120 – 193	149 ± 20.8	91.0 – 118	106 ± 10.9
Overconsolidation ratio, OCR	1.6 – 2.2	1.9 ± 0.2	1.1 – 1.5	1.3 ± 0.1
Maximum virgin compression index, C_{cmax}	0.56 – 0.81	0.72 ± 0.08	0.34 – 0.67	0.52 ± 0.11
Maximum virgin compression ratio, CR_{max}	0.23 – 0.29	0.26 ± 0.02	0.16 – 0.28	0.23 ± 0.04
Permeability change index, C_k	0.648 – 0.709	0.671 ± 0.029	0.529	0.529
Normally consolidated lateral stress ratio, K_{0NC}	0.469 – 0.495	0.484 ± 0.010	0.532 – 0.569	0.555 ± 0.014
$K_0 = K_{0NC}\,(OCR)^n$	K_{0NC} = 0.48; n = 0.40		K_{0NC} = 0.55; n = 0.37	
$C_{\alpha e}/C_c$	0.041		0.036	
$\Delta e/e_0$	0.016 – 0.049	0.033 ± 0.009	0.027 – 0.055	0.041 ± 0.009

[a] SD: Standard Deviation

4.4.2. Undrained Shear Strength

A total of eleven K_0-consolidated SHANSEP triaxial compression tests ($CK_0UTC(L)$) were performed. Six tests were sheared at OCR 1, and five at OCR ranging from 2 to 6.

The triaxial tests results are summarized in Figure 4-6(a-d) (black lines for soil M and blue for soil C). Figure 4-6(a) shows the normalized shear stress-strain behavior. It can be observed that for both soils, increasing OCR results in: (i) transition from ductile to strain-softening behavior; (ii) an increase of the peak normalized shear stress (q_f/σ'_{vc}); and (iii) an increase of the axial strain at failure (ε_{af}). The results also show that for the same value of OCR, the soil with the higher $CaCO_3$ content, soil M, has higher normalized undrained shear strength than soil C, which has a lower $CaCO_3$ content (e.g. for OCR=1, q_f/σ'_{vc} ~ 0.33 vs. 0.28). This is attributed to the reinforcement provided by the shells as well as the cementation caused by the higher carbonate content present in soil M.

Figure 4-6(b) presents the effective stress paths normalized by the maximum vertical consolidation stress (σ'_{vm}) for soils M and C. The MIT stress path convention was used, where the shear stress is calculated as $q = (\sigma'_v - \sigma'_h) / 2$ and the average effective stress is calculated as $p' = (\sigma'_v + \sigma'_h) / 2$. The results show that the effective stress paths approach a common failure envelope at large strains. The p'-q effective stress failure envelope (ESFE) is defined by a linear regression through the shear stress and average effective stress at maximum obliquity, which are represented by hollow black diamonds for soil M and solid blue diamonds for soil C. The linear regression on the data yields a friction angle at maximum obliquity (ϕ'_{mo}) of 39° for soil M and 30° for soil C and a negligible cohesion intercept ($c' \sim 0$) for both soils.

The change in normalized excess pore pressure ($u_e/\sigma'_{vc} = [\Delta u - \Delta\sigma_h] / \sigma'_{vc}$) versus axial strain ($\varepsilon_a$) is shown in Figure 4-6(c). In all normally consolidated (NC) tests, u_e/σ'_{vc} increases with increasing axial strain. However, in the overconsolidated (OC) tests, u_e/σ'_{vc} initially increases and then gradually decreases when q_f is approached; after the peak, large positive excess pore pressures develop. This behavior was also observed for Boston blue clay BBC (Berman, 1993), resedimented Boston blue clay RBBC (Santagata, 1998), and Avezzano (AZ) silt in the Fucino basin (Burghignoli et al., 2010). For the NC cases, no clear difference was observed between soil M and soil C. However, for the OC cases, Soil M has slightly higher u_e/σ'_{vc} than soil C.

Figure 4-6(d) illustrates the change in normalized shear stress with OCR. Overall, the triaxial data are repeatable and the results show that the soil exhibits normalized behavior. The SHANSEP (Stress History and Normalized Soil Engineering Properties; Ladd & Foott, 1974) parameters link stress history to undrained shear strength through the following equation:

$$S_u / \sigma'_{vc} = S\,(OCR)^m \qquad \text{(Eq. 4-2)}$$

where S_u is the undrained shear strength, σ'_{vc} is the vertical effective stress, OCR is the overconsolidation ratio, and S and m are the two SHANSEP parameters (S = 0.34; m = 0.85; r^2 = 1.00 for soil M; and S = 0.28; m = 0.72; and r^2 = 0.99 for soil C). Although these values fall in the range of soft soils (e.g. BBC: S = 0.28 and m = 0.70, Sheahan 1991; Taipei clay: S = 0.32 and m = 0.82, Chin et al. 2007), it is important to note the significant difference between soils M and C.

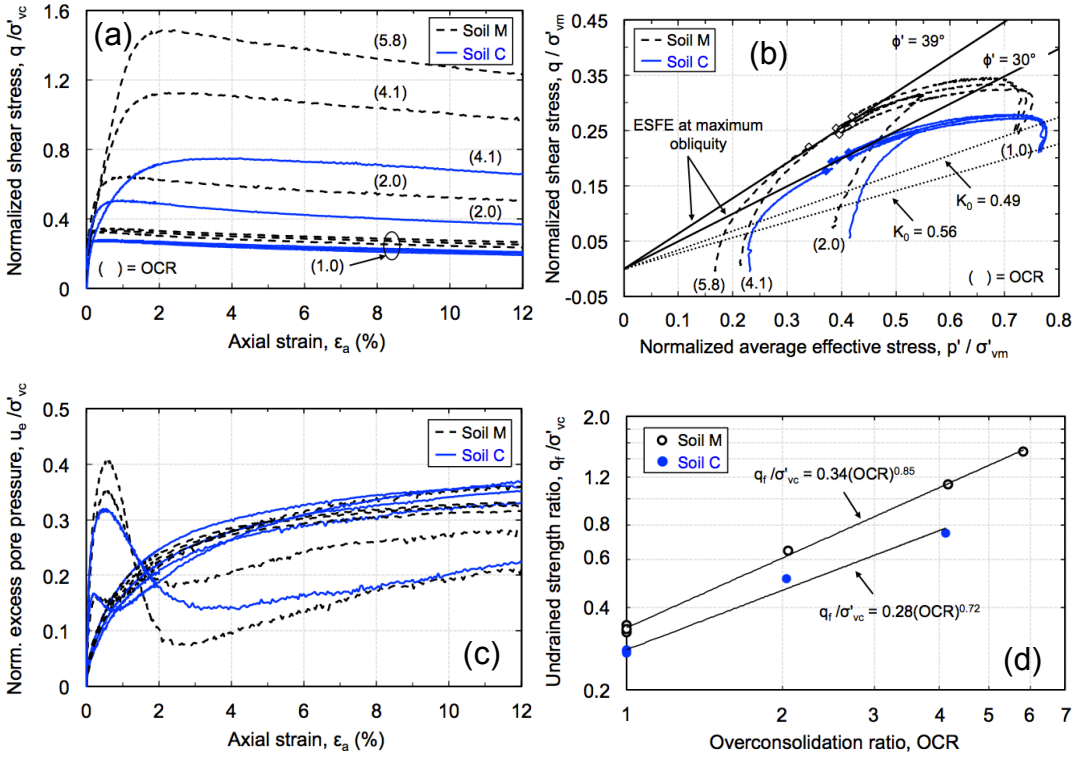

Figure 4-6: Results of triaxial tests: (a) normalized shear stress vs. axial strain, (b) normalized effective stress paths, (c) normalized change in excess pore pressure, and (d) normalized shear stress vs. OCR.

The normalized undrained secant Young's modulus (E_u/σ'_{vc}) is plotted versus the axial strain in Figure 4-7. The degradation of the modulus with increasing axial strain is apparent. In general, soil M has slightly higher values of E_u/σ'_{vc} compared with soil C. The figure also shows that the values of E_u/σ'_{vc} increase

with OCR for the same ε_a. The E_u/σ'_{vc} for the NC soil is consistently smaller than the OC soil at all strain levels.

Table 4-4 lists the key properties of soils M and C obtained from the triaxial tests.

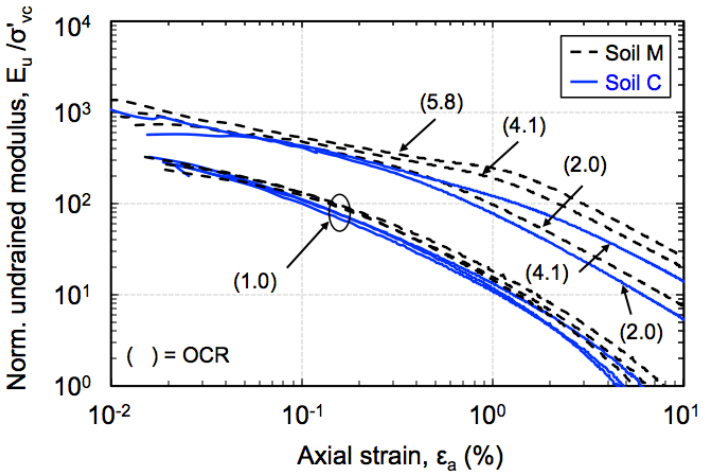

Figure 4-7: Normalized undrained modulus degradation for SHANSEP $CK_0UTC(L)$ tests of soils M and C

Table 4-4: Summary of undrained shear strength properties

OCR		Soil M				Soil C		
		1.0[a]	2.0	4.1	5.8	1.0[a]	2.0	4.1
At peak	q/σ'_{vc}	0.334	0.646	1.127	1.489	0.277	0.509	0.749
	p'/σ'_{vc}	0.683	1.109	1.805	2.401	0.729	1.098	1.580
	ε_{af}	0.528	1.298	2.460	2.092	0.394	1.005	4.217
	ϕ'	29.4	35.6	38.6	38.3	22.3	27.6	28.3
	A_f	0.721	0.173	0.084	0.027	0.764	0.179	0.091
At maximum obliquity	q/σ'_{vc}	0.260	0.520	1.052	1.281	0.203	0.395	0.730
	p'/σ'_{vc}	0.411	0.798	1.658	1.978	0.407	0.777	1.531
	ε_a	10.42	10.26	7.17	1.11	11.71	8.81	6.45
	ϕ'	39.2	40.6	39.4	40.4	30.0	30.5	28.5
$E_{0.1}/\sigma'_{vc}$		128.7	425.3	479.4	531.3	106.7	411.4	431.5
$E_{u,\,max}/\sigma'_{vc}$		36.2	76.2	89.3	143.8	33.9	78.2	36.3
$S_u/\sigma'_{v0} = S\,(OCR)^m$		S = 0.34; m = 0.85				S = 0.28; m = 0.72		
ϕ'_{mo}		39°				30°		

[a] Average of three NC tests.

One SHANSEP triaxial test was conducted on soil M and sheared drained ($CK_0DTC(L)$) to ensure that the relatively high values of ϕ'_{mo} (39° for soil M) are not caused by experimental errors. The drained test yielded a friction angle at maximum obliquity of ϕ'_{mo} = 37°, similar to that reported from the undrained tests.

4.4.3. Effect of Soil Structure

The effects of soil structure can be determined using the framework proposed by Burland (1990), which relies on the normalization of the compression curves through the use of the void index (I_v), a normalizing parameter defined as:

$$I_v = \frac{e - e^*_{100}}{e^*_{100} - e^*_{1000}} = \frac{e - e^*_{100}}{C^*_c} \qquad \text{(Eq. 4-3)}$$

where e = void ratio of the soil in its natural state; and e^*_{100} and e^*_{1000} = void ratios of the soil in its reconstituted-remolded state at vertical effective stresses (σ'_v) of 100 kPa and 1000 kPa, respectively.

Burland (1990) showed that, when plotted in terms of I_v-log(σ'_v), the compression curves of reconstituted soils all fall around a reasonably unique line that defines the intrinsic compression line (ICL; the term intrinsic refers to the inherent properties of the soil which are independent of its natural state and serve as reference to evaluate the effects of structure); see Figure 4-8. When plotted in the same space, the in-situ stress state of a large range of normally consolidated natural sedimentary clays fall in a very narrow band with a reasonably unique line termed the sedimentation compression line (SCL) (Figure 4-8). The SCL falls above the ICL due to the fabric and soil structure developed during sedimentation and postdepositional processes. Over the range of σ'_v = 10 kPa to 1000 kPa, the SCL is approximately parallel to the ICL. At the same void ratio, the SCL lies at a vertical effective stress five times greater than that of the ICL.

Several researchers have shown that the in situ state of some soils can fall substantially above the SCL (e.g. freshwater glacial lake clay, Burland 1990; quick and carbonate clays, Chandler et al. 2004). This fact can be attributed to differences in the depositional environments and post-depositional processes such as cementation, ageing, and leaching (Kavvadas, 2000). Hence, the two lines proposed by Burland (i.e., ICL and SCL) can be used as reference to evaluate the degree of structuring of natural soils by comparing the soil's current I_v -σ'_v state with the intrinsic and sedimentary lines. Plotting the compression data of natural soils in these coordinates requires the intrinsic void ratios e^*_{100} and e^*_{1000}, which can be measured from oedometer tests on the reconstituted soil. Burland (1990) proposed empirical correlations between the void ratio at the liquid limit (e_L) and the e^*_{100} and C_c^* as follows:

$$e_{100}^* = 0.109 + 0.679e_L - 0.089{e_L}^2 + 0.016{e_L}^3 \qquad \text{(Eq. 4-4)}$$

$$C_c^* = 0.256e_L - 0.04 \qquad \text{(Eq. 4-5)}$$

Using these correlations for the carbonatic soil investigated in this study, e^*_{100} and C_c^* were determined as 1.15 and 0.426, respectively for soil M and 0.877 and 0.293, respectively for soil C.

Figure 4-8(a) and Figure 4-8(b) present the one-dimensional compression curves of soils M and C in the normalized I_v-log(σ'_v) space. The figures also show that the points corresponding to σ'_p fall slightly above the SCL. After preconsolidation, the compression curves are steeper than the SCL indicating a progressive collapse of the soil structure, while at higher stresses they tend to become parallel to the ICL. Note that this behavior is different than what Burland (1990) reported, i.e. that at high stresses the compression curves slowly converge to the ICL. Soccodato (2003) reported observations similar to those discussed here for Fucino clay and suggested that the specimens did not experience a complete

destructuration and that higher stresses were needed to damage the remaining structure.

Sheahan (2005) introduced the concept of a “structure number” (SN) to quantify the soil’s state in Burland’s (1990) I_v-log(σ'_v) space, relative to the ICL and the SCL:

$$SN = (I_v - I_{v,ICL}) / (I_{v,SCL} - I_{v,ICL}) \qquad \text{(Eq. 4-6)}$$

where I_v, $I_{v,ICL}$, and $I_{v,SCL}$ are obtained at the preconsolidation stress of the soil since it best represents the natural soil’s bonding. Overall the data in Figure 4-8 shows that the SN for soil M varies between 0.7 and 2.2 (mean SN = 1.6) and for soil C between 0.8 and 1.8 (mean SN = 1.3). This indicates that on average, soil M has higher degree of structuring than soil C, which agrees with the higher carbonate content of soil M reported earlier. In addition, the relatively low SN values are evidence of limited degree of structuring. CHAPTER 3 reported that this is expected given the lacustrine origin of the deposit as deposition in a low salinity environment cannot produce the high void ratio flocculated structure typical, for instance, of highly structured soils which fall markedly above the SCL (e.g. quick clays with SN values as high as 4.4, Sheahan, 2005)

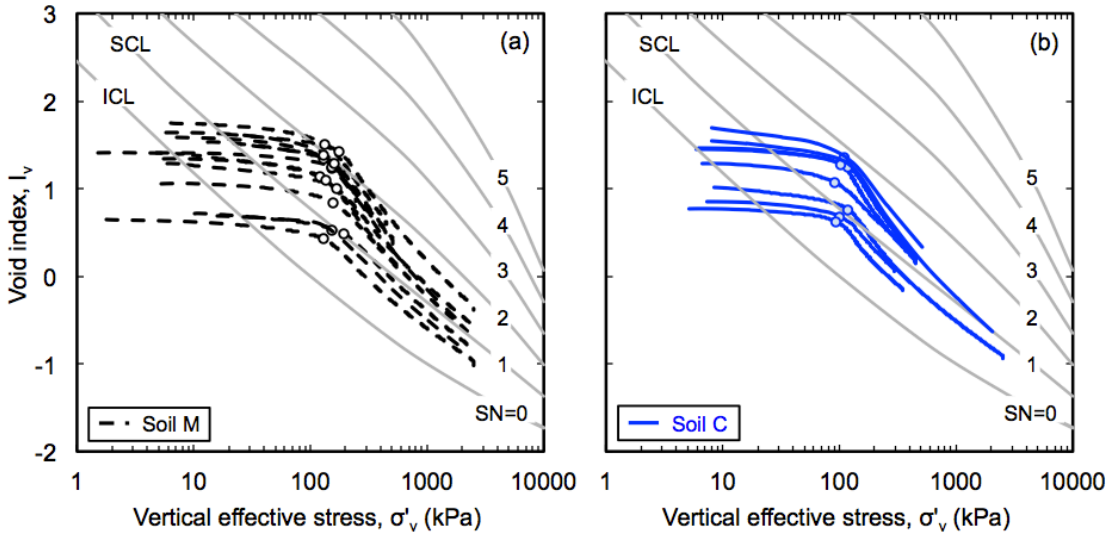

Figure 4-8: One-dimensional compression curves of (a) soil M and (b) soil C, represented in the normalized I_v-log(σ'$_v$) space

The post-yield structure degradation of intact soils, also known as "destructuration" in the normally consolidated (NC) region, can be described using the model proposed by Liu and Carter (1999, 2000), which expresses the virgin compression behavior of a structured soil by the following equation:

$$e = e^* + \Delta e = e^* + \Delta e_i \left(\frac{\sigma'_p}{\sigma'_v}\right)^b \quad \text{for} \quad \sigma'_v \geq \sigma'_p \qquad \text{(Eq. 4-7)}$$

where e = void ratio of the intact structured soil in the NC region; e* = void ratio of the reconstituted soil at the same vertical effective stress; Δe = difference between the void ratio of the structured soil and that of the reconstituted soil at a given σ'$_v$ in the NC region (σ'$_v$>σ'$_p$); Δe$_i$ = difference in void ratio at σ'$_p$; and b is the compression destructuring index (0 ≤ b < ∞)

This equation was based on the observation that the additional void ratios sustained by the soil structure during virgin compression (Δe) are inversely proportional to the current mean effective stress (or vertical effective stress in 1-D consolidation) (Liu & Carter, 1999). The rate of reduction in Δe increases with the index b, which has two extremes: (i) for b = 0 the value of Δe is constant

during virgin compression ($\Delta e = \Delta e_i$) and so no destructuring takes place; and (ii) for $b = \infty$, the value of Δe is zero immediately after preconsolidation ($\Delta e = 0$, for $\sigma'_v > \sigma'_p$), indicating an immediate collapse of the soil structure. Data presented by Liu and Carter (2000) shows that for natural soft clays, b generally lies between 0.3 and 1 (although values as high as 30 have been reported, e.g. Fontana et al. 1998). The values of b for the carbonatic soil are within the range 0.2-0.3, which fall on the low side and, as mentioned earlier, support the notion of limited damage to the soil structure and confirm the conclusion that much higher stresses are needed to completely damage the structure.

The effects of the soil structure can be also highlighted by comparing the undrained shear strength results obtained using the SHANSEP and Recompression methods. A number of researchers (e.g. Mesri, 1975; Ladd & Foott, 1974; Seah & Lai, 2003; Amorosi & Rampello, 2007) have reported that consolidating soil specimens beyond the preconsolidation stress, as in the SHANSEP method, could result in a mechanical bond degradation of the soil. Hence, a comparison between the SHANSEP and the Recompression results can provide an additional assessment to the degree of structuring of the carbonatic soils investigated.

Figure 4-9(a) and Figure 4-9(b) show the normalized effective stress paths during the triaxial tests for soils M and C, respectively. Dashed lines refer to the SHANSEP results while the Recompression test is represented as a solid line. At the same OCR (1.9 for soil M and 1.4 for soil C), the undrained shear strength obtained from the Recompression test is higher than the one estimated from SHANSEP tests by ~1% and ~9% for soil M and soil C, respectively. This difference is thought to be caused by soil destructuring during the SHANSEP tests. Similar observations, with much larger differences between SHANSEP and Recompression results, were reported in soils with a high degree of structuring

(e.g. ~28% for Bangkok clay, Seah & Lai (2003); ~36% for Vallericca clay, Amorosi & Rampello, 2007).

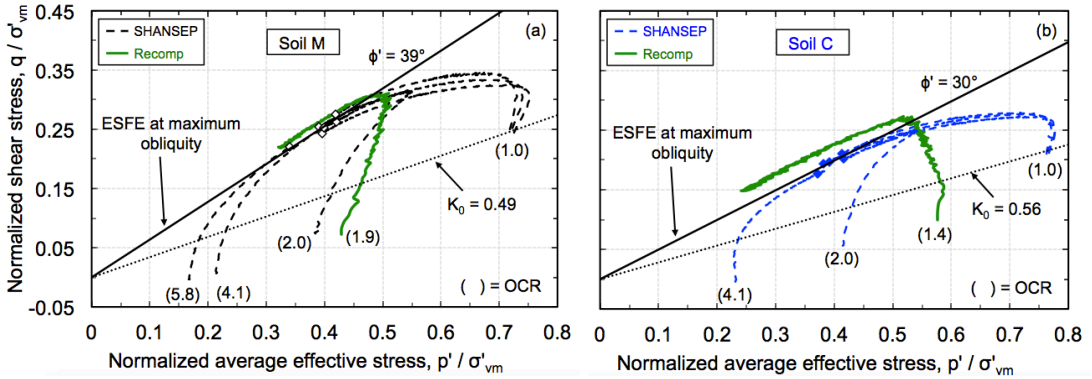

Figure 4-9: normalized effective stress paths from SHANSEP and Recompression tests for (a) soil M and (b) soil C

4.5. Summary and Conclusions

The paper presents the results of a laboratory investigation of the mechanical behavior of two soft fine-grained carbonatic soils from a lacustrine deposit formed during the Wisconsin glaciation in southwestern Indiana. The two soils (soil M and soil C), found as alternating layers in the deposit, are characterized by the presence of 40-60% calcium carbonate, but show distinct mineral composition in that the dominant minerals are calcite and smectite in soil M, and dolomite and illite in soil C. The index properties of the soils are PL ~ 34.4 and 21.6; LL ~ 67.4 and 48.3; % clay ~ 19.0% and 38.7% for soils M and C, respectively. These differences are reflected also in the engineering properties, which is the main focus of the present paper.

The 1D compression behavior of the two soils was investigated by conducting constant rate of strain (CRS) and incremental loading (IL) consolidation tests on specimens obtained from high quality Shelby tube samples. The measured values of σ'_p fall on two distinct bands, with OCR values for soil M (average OCR ~ 1.9) consistently higher than those for soil C (average OCR ~ 1.3). This suggests that the degree of cementation in soil M is larger than in soil C, which is

consistent with its higher carbonate content (average $CaCO_3$ ~ 55% for soil M and 38% for soil C). Such cementation provides a moderate degree of structuring (Burland, 1990), that is only partially destroyed beyond the preconsolidation pressure.

K_0-consolidated triaxial tests showed that both soils exhibit normalized behavior between undrained shear strength, OCR and effective stress, as described by the SHANSEP framework. However, there was a significant differences between the two soils, with SHANSEP parameters S = 0.34 and m = 0.85 for soil M and S = 0.28 m = 0.72, for soil. Consistent with this observation, are the findings that the maximum obliquity friction angle of soil M, ϕ'_{mo} = 39°, was larger than that of soil C, ϕ'_{mo} = 30°, and that the value of the normally consolidated K_0 was smaller for soil M (K_0 = 0.48) than for soil C (K_0 = 0.55). For both soils the cohesion intercept was found to be negligible.

The effect of soil structure was also highlighted by comparing the undrained shear strength obtained using SHANSEP and Recompression methods. The test results indicate that the Recompression test yield slightly higher undrained shear strength than SHANSEP (~1% higher for soil M and ~9% higher for soil C). This difference is attributed to soil destructuration during SHANSEP and supports the notion that the carbonatic soil possesses some sort of cementation that enhances its shear strength.

4.6. Acknowledgments

This work was supported by the Joint Transportation Research Program administered by the Indiana Department of Transportation and Purdue University. The contents of this paper reflect the views of the authors, who are responsible for the facts and the accuracy of the data presented herein, and do not necessarily reflect the official views or policies of the Federal Highway Administration and the Indiana Department of Transportation, nor do the contents

constitute a standard, specification, or regulation. The authors wish to acknowledge the support of Ms. Francesca Palmieri who helped with the Recompression triaxial tests.

4.7. References

Abdulhadi, N.O. (2009). An experimental investigation into the stress-dependent mechanical behavior of cohesive soil with application to Wellbore instability. PhD Thesis, Department of Civil and Environmental Engineering, Massachusetts Institute of Technology, Cambridge, MA.

Amorosi, A., & Rampello, S. (2007). An experimental investigation into the mechanical behaviour of a structured stiff clay. Geotechnique, 57(2), pp. 153-166.

Anagnostopoulos, A.G., Kalteziotis, N., Tsiambaos, G.K., & Kavvadas M. (1991). Geotechnical properties of the Corinth Canal marls. Geotechnical and Geological Engineering, 9, pp. 1-26.

ASTM D2216-10 (2010). Standard test methods for laboratory determination of water (moisture) content of soil and rock by mass. Annual Book of ASTM Standards, ASTM International, West Conshohocken, PA.

ASTM D2487-11 (2011). Standard practice for classification of soils for engineering purposes (unified soil classification system). Annual Book of ASTM Standards, ASTM International, West Conshohocken, PA.

ASTM D422-63 (2007). Standard test method for particle-size analysis of soils. Annual Book of ASTM Standards, ASTM International, West Conshohocken, PA.

ASTM D4318-10 (2010). Standard test methods for liquid limit, plastic limit, and plasticity index of soils. Annual Book of ASTM Standards, ASTM International, West Conshohocken, PA.

ASTM D854-14 (2014). Standard test methods for specific gravity of soil solids by water pycnometer. Annual Book of ASTM Standards, ASTM International, West Conshohocken, PA.

Baligh, M.M., Azzouz, A., & Chin, C.T. (1987). Disturbances due to "ideal" tube sampling. Journal of Geotechnical Engineering, ASCE, 113(7), pp. 739-757.

Becker, D.E., Crooks, J.H.A., Been, K., & Jefferies, M.G. (1987). Work as a criterion for determining in situ and yield stresses in clays. Canadian Geotechnical Journal, 24(4), pp. 549-564.

Berman, D.R. (1993). Characterization of the engineering properties of Boston blue clay. MS Thesis, School of Civil Engineering, MIT, Cambridge, MA.

Bjerrum, L. (1972). Embankments on soft ground. Proceedings of the ASCE Conference on Performance of Earth-Supported Structures, Purdue University, 2, pp. 1-54.

Black, D.K., & Lee, K.L. (1973). Saturating laboratory samples by back pressure. Journal of the Soil Mechanics and Foundations Division, ASCE 1, pp. 75-93.

Boone, S.J., & Lutenegger, A.J. (1997). Carbonates and cementation of glacially derived cohesive soils in New York State and southern Ontario. Canadian Geotechnical Journal, 34, pp. 534-550.

Bozzano, F., Marcoccia, S., & Barbieri, M. (1999). The role of calcium carbonate in the compressibility of Pliocene lacustrine deposits. Quarterly Journal of Engineering Geology, 32, pp. 271-289.

Burghignoli, A., Miliziano, S., & Soccodato, F.M. (2010). Cementation effects in two lacustrine clayey soils. Geotech Geol Eng 28, pp. 815-833.

Burland, J.B. (1990). On the compressibility and shear strength of natural clays. Geotechnique, 40, pp. 329-378.

Casagrande, A. (1936). The determination of the pre-consolidation load and its practical significance. Proceedings of the 1st International Conference on Soil Mechanics and Foundation Engineering. Cambridge, MA 3, pp. 60-64.

Chandler, R.J., de Freitas, M.H., & Marinos, P. (2004). Geotechnical characterisation of soils and rocks: A geological perspective, In: R.J. Jardine, D.M. Potts, & K.G. Higgins (Eds.), Advances in Geotechnical Engineering, The Skempton Conference, Thomas Telford, London, 1, pp. 67-102.

Chin, C.-T., Chen, J.-R., Hu, I.-C., Yao, D.T.C., & Chao, H.-C. (2007). Engineering characteristics of Taipei clay. In Proceedings International Workshop on Characterization and Engineering Properties of Natural Soils ("Natural Soils 2006"). NUS Singapore, December. Tan, T. S. et al. (eds.) 3, pp. 1755-1804. London: Taylor & Francis.

Clayton, C.R.I., Siddique, A., & Hopper, R.J. (1998). Effects of sampler design on tube sampling disturbance – numerical and analytical investigations. Geotechnique, 48(6), pp. 847-867.

DeGroot, D.J., & Lutenegger, A.J. (2003). Geology and engineering properties of Connecticut Valley Varved Clay, Proceedings of the International Workshop on Characterization and Engineering Properties of Natural Soils. 1, pp. 695-724.

Fontana, P., Lagioia, R., & Nova, R. (1998). Subsidence and wellbore stability during the excavation of oil wells. In: A. Evangelista & L. Picarelli (Eds), the geotechnics of hard soils – soft rocks, pp. 519-527.

Germaine, J.T., & Ladd, C.C. (1988). Triaxial testing of saturated cohesive soils. Advanced Triaxial Testing of Soil and Rock, ASTM STP 977. In R. T. Donaghe, R. C. Chaney, & M. L. Silver (Eds.), ASTM (pp. 421-459). Philadelphia.

Hawkins, A.B., Lawrence, M.S., & Privett, K.D. (1988). Implication of weathering on the engineering properties of the Fuller's Earth formation. Geotechnique, 38, pp. 517-532.

IDOT (1999). Geotechnical Manual. Illinois Department of Transportation. Springfield.

INDOT (2010). Geotechnical Manual. Indiana Department of Transportation. Indianapolis.

Jamiolkowski, M., Lancellotta, R., & Lo Presti, D.C.F. (1995). Remarks on the stiffness at small strains of six Italian clays. Pre-failure Deformations of Geomaterials, 2, pp. 817-836.

Jung, C.M., Bobet, A., & Siddiki, N.Z. (2011). Simple method to identify marl soils. Transportation Research Record 2232, pp. 76-84.

Kavvadas, M.J. (2000). General report: Modelling the soil behavior – selection of soil parameters. Proc 2nd Int. Conf. Geotech. Hard Soils-Soft Rocks, 2, pp. 1441-1481.

Ladd, C.C., & DeGroot, D.J. (2003). Recommended practice for soft ground site characterization: Arthur Casagrande Lecture. Proc. 12th Panamerican Conf. on Soil Mechanics and Geotech. Eng. MIT, 1, pp. 3-57.

Ladd, C.C., & Foott, R. (1974). New design procedure for stability of soft clays. Journal of Geotechnical Engineering, ASCE, 100(GT7), pp. 763-786.

Lamas, F., Irigaray, C., & Chacon, J. (2002). Geotechnical characterization of carbonate marls for the construction of impermeable dam cores. Engineering Geology, Elsevier, 66, pp. 283-294.

Leroueil, S. & Vaughan, P.R. (1990). The general and congruent effects of structure in natural soils and weak rocks. Geotechnique 40, (3), pp. 467-488.

Liu, M.D., & Carter, J.P. (1999). Virgin compression of structured soils. Geotechnique, 49(1), pp. 43-57.

Liu, M.D., & Carter, J.P. (2000). Modelling the destructuring of soils during virgin compression. Geotechnique, 50(4), pp. 479-483.

Long, M., & Lunne, T. (2003). Stiffness of Onsoy clay. In Deformation Characteristics of Geomaterials, Di Benedetto et al. (Eds.), Swete & Zeitlinger, Lisse, pp. 151-158.

Lunne, T., Berre, T., & Strandvik, S. (1997). Sample disturbance effect in soft low plasticity Norwegian clay. Proceedings of the Conference on Recent Developments in Soil Mechanics, Rio de Janeiro, pp. 81-102.

MDOT (2009). Uniform Field Soil Classification System (Modified Unified Description). Michigan Department of Transportation. Lansing.

Mesri, G. (1975). Discussion of new design procedure for stability of soft clays. J. of Geotech. Engrg., 101(GT4), pp. 409-412.

Mesri, G., & Godlewski, P.M. (1977). Time- and stress-compressibility interrelationship. Journal of Geotechnical Engineering, ASCE, 103(5), pp. 417-430.

Mitchell, J.K. (1993). Fundamentals of soil behavior. 2nd edition. John Wiley & Sons, Inc.: New York.

Musso, G., Chighini, S., & Romero, E. (2008). Mechanical sensitivity to hydrochemical processes of Monastero Bormida clay. Water Resources Research, 44.

ODOT (2010). Specifications for Geotechnical Explorations. Ohio Department of Transportation. Columbus.

Paaza, E.A., Lamas, F., Irigaray, C., & Chacon, J. (1998). Engineering geological characterization of Neogene marls in the southeastern Granada basin, Spain. Engineering Geology 50, pp. 165-175.

Santagata, M.C. (1998). Factors affecting the initial stiffness and stiffness degradation of cohesive soils. PhD Thesis, Department of Civil and Environmental Engineering, Massachusetts Institute of Technology, Cambridge, MA.

Seah, T.H. & Lai, K.C. (2003). Strength and deformation behavior of soft Bangkok clay. Geotechnical Testing Journal, 26(4).

Sheahan, T.C. (1991). An experimental study of the time-dependent undrained shear behavior of resedimented Boston blue clay using automated stress path triaxial equipment. PhD Thesis, Department of Civil and Environmental Engineering, Massachusetts Institute of Technology, Cambridge, MA.

Sheahan, T.C. (2005). A soil structure index to predict rate dependence of stress–strain behavior. In: J.A. Yamamuro, & J. Koseki (Eds.), Testing, Modeling and Simulation in Geomechanics, ASCE GSP No. 143, pp. 81-97.

Soccodato, F.M. (2003). Geotechnical properties of Fucino clayey soil. In proceedings on characterization and engineering properties of natural soils, Singapore. Tan et al. (Eds.) 1, pp. 791-808.

Taylor, D.W. (1948). Fundamentals of soil mechanics. New York: John Wiley & Sons, Inc.

Thornbury, W.D. (1950). Glacial sluiceways and lacustrine plains of southern Indiana. Indiana Geological Survey Bulletin, 4, 21 p.

Tsiambaos, G. (1991). Correlation of mineralogy and index properties with residual strength of Iraklion marls. Engineering Geology, 30, pp. 357-369.

Wissa, A.E.Z., Christian, I.T., & Davis, E.H. (1971). Consolidation at constant rate of strain. Journal of Soil Mechanics and Foundation Division, 97(10), pp. 1393-1413.

CHAPTER 5. SUMMARY, CONCLUSIONS, AND RECOMMENDATIONS

5.1. Introduction

The research presented in this thesis aimed at furthering the current knowledge of the behavior of natural carbonatic fine-grained soils. The specific objectives of the work completed were to: a) characterize the geotechnical properties of a glaciolacustrine carbonatic fine-grained soil deposit, b) investigate the relationship between soil characteristics, geologic origin and geological depositional environment, c) gain a fundamental understanding of the cementation microstructure of carbonatic soils and its relationship with observed macro-behavior, and d) integrate the laboratory and field data to develop recommendations for the interpretation of geotechnical properties from field results.

This chapter attempts to answer whether the objectives of this research work were satisfied based on the experimental findings. An overview of the experimental program is provided in Section 5.2, while the main conclusions drawn from the results gathered are presented in Section 5.3. Section 5.4 provides recommendations for future work.

5.2. Overview of the Experimental Program

This thesis presents the results of a detailed characterization study of a soft lacustrine carbonatic deposit formed during the Wisconsin glaciation in the southwestern part of the State of Indiana, USA. The experimental program was specifically designed to characterize the geology, mineralogy, microstructure, index properties, and engineering properties of the deposit as a function of depth.

This was achieved through extensive field tests and laboratory experiments. The field testing program included (1) seismic cone penetration tests with pore pressure measurements (SCPTu); (2) standard penetration tests (SPTs) for soil profiling and collection of disturbed samples; (3) field vane shear tests; and (4) the installation of an open pipe piezometer. High-quality Shelby tubes samples were obtained for laboratory tests using mud rotary drilling and a fixed piston sampler. The laboratory testing program involved: (1) assessment of the index properties, namely Atterberg limits, natural water content, LOI, $CaCO_3$ content, pH, salinity, specific gravity, and particle size distribution analysis, over the entire thickness of the deposit; (2) characterization of the stress history profile and measurement of the consolidation and creep properties of the soil through incremental and constant rate of strain consolidation tests; and (3) investigation of the undrained shear behavior, including derivation of the SHANSEP parameters through K_0-consolidated undrained triaxial tests. Additionally, the mineralogy and the microstructure of the soil were studied in detail using state-of-the-art techniques, including X-ray diffraction (XRD), thermogravimetric analysis (TGA), and scanning electron microscopy (SEM) equipped with energy dispersive X-ray (EDX) spectroscopy. Radiocarbon dating was performed on fossil shells and organic samples using accelerator mass spectrometry (AMS).

5.3. Conclusions

This section discusses the conclusions drawn for this research work. The presentation is organized in three main subsections, outlining the conclusions that pertain to: (1) the geotechnical properties; (2) the origin of the deposit and sedimentary environment; and (3) cementation microstructure

5.3.1. Geotechnical Properties

The tests performed show that the carbonatic layer is not uniform, but is, instead, formed by the repetition of layers of two different soils. These two soils, referred to in this thesis as “soil M” and “soil C”, are both characterized by high calcium

carbonate contents (over 55%, and close to 40% for soils M and C, respectively) but show distinct index properties. In general, soil M is characterized by lower specific gravity, unit weight and clay content, and higher void ratio, water content, Atterberg limits, and $CaCO_3$ content (e.g. PL ~ 34.6 and 21.6; LL ~ 67.5 and 47.5; % clay ~ 20.2% and 36.9% for soils M and C, respectively). Additionally, soil M is characterized by a higher percentage of smectite minerals (~ 10% and 2% for soils M and C, respectively). A clear difference between the two sublayers was also observed in terms of color and texture, with shells identified in soil M. Soil C was found in thin layers of thickness ranging between 0.5 cm and 10 cm, whereas soil M was found in thicker layers and represented the majority of the carbonatic layer. The observed differences between soil M and soil C could be attributed to the geologic history of sedimentation. It was suggested in this research that the two soils were formed in different sedimentary environments and from different source materials, which promoted the formation of the two types of soils, as described in more details in Section 5.3.2.

These differences are reflected also in the engineering properties. The consolidation tests showed that the measured values of σ'_p fall on two distinct bands, with the resulting values of OCR derived for soil M (average OCR ~ 1.9) consistently higher than those derived for soil C (average OCR ~ 1.3). Both soils exhibit S-shaped compression curves, with compressibility parameters markedly dependent on stress level.

K_0-consolidated tests performed varying the pre-shear effective stress showed that both soils exhibit normalized behavior with the relationship between undrained shear strength, OCR and effective stress being well described by the SHANSEP equation. However, there was a significant difference in the SHANSEP parameters measured on the two soils (S = 0.34 and 0.28, and m = 0.85 and 0.72, for soils M and C, respectively). Consistent with this observation, the maximum obliquity friction angle for soil M (ϕ'_{mo} = 39° [likely affected by the

presence of shells]) exceeded that measured on soil C (ϕ'_{mo} = 30°), and the value of the normally consolidated K_0 was smaller for soil M (K_0 = 0.48) relative to soil C (K_0 = 0.55). For both soils the cohesion intercept was found to be negligible.

The sampling and specimen preparation techniques used in this study (drilling using mud rotary, sampling using fixed piston sampler, extrusion using a piano wire, trimming using wire saw) were found to generate samples of high quality and reliable laboratory test data. The quality of the soil samples was assessed by calculating the normalized change in void ratio ($\Delta e/e_0$) obtained from the consolidation (CRS and IL) tests and the K_0 consolidation phase of the triaxial tests. All the data fall below 0.055, indicating that the samples can be classified as “excellent” to “good” based on the sample quality designation suggested by Lunne et al., 1997).

Comparison of the field data and laboratory results provided the means to validate existing correlations for interpretation of the geotechnical properties of carbonatic fine-grained soils from field results. The piezocone tests results were analyzed and correlations to estimate shear wave velocity, stress history, and undrained shear strength that provided the best match to the laboratory results were identified. For the site examined it was found that, of the 13 relationships examined, only the one developed by Andrus et al. (2007) for soils with a Pleistocene geologic age provides a prediction of V_s from the CPT data consistent with the in-situ seismic measurements. The preconsolidation stress of the deposit is best estimated from the CPT data using the correlation provided by Mayne (1995). The undrained shear strength, S_u, is best estimated from the CPT tip resistance data using the equation $S_u = (q_t - \sigma_{v0})/N_{kt}$, although for the same shear mode (triaxial compression) N_{kt} varies from 10 to 17 for soil M and soil C, respectively.

5.3.2. Origin of Deposit and Sedimentary Environment

Radiocarbon dating using accelerator mass spectrometry (AMS) performed on fossil shells and organic samples obtained from the carbonatic layer, at depths varying between 7.3 m and 10.1 m, showed that the deposit is approximately 22,000 years old and was formed over a period of ~3,000 years. Radiocarbon dating of nine different samples resulted in an age of 20,800 yr BP (at 7.3 m) to 23,600 yr BP at (10.1 m), with the age increasing with depth. For the same depth, the carbonate samples and the organic samples resulted in a very similar calendar age. This implies that the fossil shells used in this analysis were not affected by the hard water effect.

While the characteristics of the deposit are overall consistent with its hypothesized lacustrine origin and Wisconsin age, clear differences exist between soil M and soil C. In particular, soil M is dominated by smectite and calcite, while the dominant minerals in soil C are illite and dolomite. Moreover, microstructural observations indicate the presence of biological intrusions (fossil shells & charophytes oospores) and pyrite framboids detected only in soil M, which indicates that this soil was deposited in a biogenic environment.

The observed discrepancies between the two soils lead to hypothesize that different source materials and sedimentary environments alternated during the formation of the deposit. Specifically, it is hypothesized that soil M was formed as a result of the deposition of locally derived sediments of Illinoian age subjected to a high degree of weathering under conditions (slow accumulation rates and shallow water) that promoted biogenic life. Soil C would, instead, have resulted from the influx of sediment from the White River under the occasional conditions associated with flooding above the valley trains caused by the high volume of Wisconsin-melt waters. These occasional flooding occurred during relatively short period of time resulting in thin layers compared with soil M.

5.3.3. Cementation microstructure

The microstructure of the two soils was characterized through a combination of direct microscopic observations by SEM and indirect examinations by EDX, carbonate dissolution using chemical treatment, XRD, Atterberg limits, and particle size analyses.

The SEM-EDX analyses on intact samples of both soils suggest that carbonate is providing a continuous coating layer (less than 2-3 micrometers thick) on the clay and silt particles, with carbonatic bridges connecting groups of particles to form larger aggregates. This was confirmed by particle size analyses and measurements of the Atterberg limits conducted on both the natural soils and on samples treated using acetic acid to remove the carbonates. The results show a reduction in the size of the particles and an increase in liquid limit and plasticity index following decarbonation. These observations provide insight on the role played by the carbonate on the soil microstructure. That is, it indicates that carbonate is acting as a cementing agent that connects clay particles together forming larger aggregates.

The microstructural observations highlighted clear differences in the cementation microstructure of the two soils: (1) the thickness of the coating layer appears to be smaller in soil C; and (2) the carbonates in soil M are mostly calcium carbonate, while in soil C both calcium carbonate and calcium magnesium carbonate are present.

Carbonate cementation impacts the engineering properties of both soils, leading, as previously shown for other soils, to the development of an apparent OCR. The OCR profile, derived from consolidation tests on high quality undisturbed samples, clearly reflects changes in carbonate content, with tests on soil M yielding OCR values greater than for soil C (average of 1.9 versus 1.3). These values of OCR fall at the very low end of what would be expected for soils having

carbonate contents as high as those of soils M and C. This suggests that, in the soils examined, great part of the carbonate is in form of the coating layer identified in the SEM images, with only a fraction contributing to interparticle bonding.

5.4. Recommendations for Future Work

Although the experimental program performed for this thesis involved an extensive study on the mineralogy, microstructure, and engineering tests of the carbonatic deposit and has contributed fundamentally to the understanding of its micro and macro behavior, there are still some opportunities for additional work that would complement and enhance the research completed. The primary recommendations for future work can be summarized as follows:

1- Implement the acquired knowledge in a constitutive model;
2- Investigate the relative role of calcite versus dolomite on the macro-behavior and link the presence of these minerals to the depositional environment;
3- Extend the work to reconstituted material, to quantify the degree of structuring associated with carbonate cementation and the presence of shells;
4- Provide further validation of the proposed correlations for CPT interpretation through testing at different sites.
5- Extend the work to other soft carbonatic clay deposits to investigate if the observations and conclusions reached can be generalized.

5.5. References

Andrus, R.D., Mohanan, N.P., Piratheepan, P., Ellis, B.S., & Holzer, T.L. (2007). Predicting shear-wave velocity from cone penetration resistance, Proc., 4th Inter. Conf. on Earthq. Geotech. Eng., Thessaloniki, Greece.

Lunne, T., Berre, T., & Strandvik, S. (1997). Sample disturbance effect in soft low plasticity Norwegian clay. Proceedings of the Conference on Recent Developments in Soil Mechanics, Rio de Janeiro, pp. 81-102.

Mayne, P.W. (1995). CPT determinations of overconsolidation ratio and lateral stresses in clean quartz sands, Proceedings, International Symposium on Cone Penetration Testing (CPT '95), Vol. 2, Swedish Geotechnical Society Report No.3:95, Linkoping, pp. 215-220.

APPENDICES

Appendix A. Literature Review

A.1 Introduction

Many researchers have investigated the effect of structure on the compressibility and shear strength of natural soils and showed that they generally differ from reconstituted soils (e.g. Burland, 1990; Leroueil & Vaughan, 1990; Gens & Alonso, 1992; Cotecchia & Chandler, 1997; Chandler, 2000; Fearon & Coop, 2000, 2002). These differences can be attributed to the soil structure. Lambe & Whitman (1969) defined the term “structure” as the combination of “fabric” (i.e., the arrangement of particles) and interparticle “bonding” (i.e., the electro-chemical forces at the inter-particle contacts). Extensive experimental work has shown that most natural soft clays are structured (Tavenas & Leroueil, 1990; Burland, 1990; Burland et al., 1996; Leroueil, 1997).

Cementation is one of the interparticle bonds existing in most structured soils. These bonds have significant influences on the macroscopic engineering properties of soils (Leroueil & Vaughan, 1990). Mitchell (1993) points out that cementation is typically caused by crystal growth or chemical precipitation of silica, oxides, and/or carbonates from aqueous solutions at the inter-particle contacts forming bonding between soil particles. It is well know that cementation has significant impact on the mechanical properties of soils, such as compressibility, shear strength, and sensitivity. Boone and Lutenegger (1997) provided an extensive summary of various cementing agents that have been reported in literature and their suspected effect on geotechnical engineering properties of soils (see Table A-1).

The effect of cementation on the compressibility characteristics of natural deposits has been widely discussed in literature (e.g. Bjerrum & Wu, 1960; Conlon, 1966; Sangrey, 1972; Fischer et al., 1978; McGown & Ladd, 1982; Jamiolkowski et al., 1985; Allman & Poulos, 1988; Burland, 1990; Burghignoli et

al., 1991; Boone & Lutenegger, 1997; Bozzano et al., 1999; Burghignoli et al., 2010). They all reported that cementation typically results in an increase in the preconsolidation stress, which is also called “apparent preconsolidation stress” and is different than the geological preconsolidation stress. Kenney et al. (1967), Loiselle et al. (1971), and Rosenqvist (1975) reported that the removal of cementing agent causes a decrease in the apparent preconsolidation stress.

According to Mitchell (1993), carbonate is one the most common cementing agents present in natural sediments, and as stated by Demars and Chaney (1982), it is one of the few mineral cementing agents that are capable to change a loose aggregate into stiff rock. Despite the prevalence of carbonatic soils around the world and the extensive literature on the effect of carbonates on the macroscopic engineering properties of soils,

Table A-1: cementing agents and suspected effect on geotechnical engineering properties of soils (Boone & Lutenegger, 1997)

Cementing agent	Suspected effect on geotechnical engineering properties	Deposit location	Deposit type[a]	Source
Unspecified	Particle bonding; increases strength, σ'_p	Lilla Edet, Sweden	GM	Bjerrum & Wu 1960
Carbonates, iron oxides, silicates, aluminates, and organic matter	Aggregation of fines; increases in shear strength	---	---	Lambe 1960; Soderblom 1966
Unspecified	Particle bonding; increases S_u; decreases strain at failure (ε_f)	Skabo, Sweden	GM	Bjerrum & Lo 1963
Carbonates	Particle bonding	New Liskeard, Ont.	GL	Townsend 1965
Organics, carbonates, gypsum, Al and Fe compounds	Particle bonding, increases σ'_p, strength	---	---	Bjerrum 1967
Iron oxides, salt	Increases σ'_p	Labrador	GM	Kenney et al. 1967
Aluminum and iron hydroxides	Particle bonding; increases strength	Toulnustouc River, Que.	GM	Conlon 1966; Quigley 1968
Carbonates	Cementation bonding	St. Jean de Vianney, Que.	GM	Moum & Zimmie 1972
Salt, carbonates, iron oxides	Increases σ'_p, strength; decreases ε_f	Outardes region, Que.	GL	Loiselle et al. 1971
Salt, carbonates, Al and Fe hydroxides	Increases strength at low stresses	St. Lawrence River valley	GM	Sangrey 1972a
Salt, carbonates, Al and Fe hydroxides	Increases strength at low stresses	Mattagami, Que.	GL	Sangrey 1972a
Amorphous Al and Fe; Mg and Ca; salt	Increases S_u and sensitivity (S_t); Mg decreases S_t	Drammen, Norway	GM	Moum et al. 1971
Carbonates, amorphous Si, Al, Fe oxides	Results in cementation and related to S_t	Canadian glacial and glacial-marine clays	GL, GM	Quigley 1980
Carbonates	Increases strength, brittle behavior	Northampton, Mass.	GL	Bemben 1982
Carbonates	Directly related to S_t	Hawkesbury, Ont.	GL	Quigley et al. 1985
Carbonates	Affects σ'_p, S_u	James Bay, Canada; Taranto, Italy	GM; L	Jamiolkowski et al. 1985
Carbonates	Variation in S_u and compressibility	Hertfordshire, U.K.	TILL	Little 1989
Carbonates	Affects σ'_p, S_u, G_0, OCR, K_0	Fucino, Italy	L	Burghignoli et al. 1991

[a]GL, glaciolacustrine; GM, glacial marine; L, lacustrine; TILL, basal or water-laid glacial till or lacustrotill.

A.2 The Origin of Carbonates in Lacustrine Deposits

Several researchers (e.g. Wayne, 1971; Jones & Bowser, 1978; Boone & Lutenegger, 1997; Bozzano et al., 1999) reviewed extensively the origin and the form of deposition of carbonatic lacustrine deposits, sometimes referred to as marls. They reported that soil carbonates originate from two major sources: either as external to the lake (allogenic carbonates) in the form of carbonates that are eroded from the original parent material or by a solution-precipitation process occurring within the lake water mass (endogenic carbonates). The former mechanism, also referred to as mechanical sedimentation, consists of fine particles of calcium carbonate transported in suspension by ground water from limestone rock outside the lake proper; while the latter mechanism, also referred to as chemical and biochemical precipitate, hypothesized that spring water saturated with calcium bicarbonates loses CO_2 when it emerges through a spring into lake water and due to the presence of aquatic plants that consume CO_2 in the process of photosynthesis. The loss of CO_2 causes the precipitation of calcium carbonate.

A.2.1 Formation of Calcium Carbonate

Fresh water lakes can be saturated with calcium bicarbonate [$Ca(HCO_3)_2$], which exists only in aqueous solution. The removal of CO_2, as a result perhaps of evaporation or photosynthesis of aquatic plants, results in the precipitation of calcium carbonate ($CaCO_3$), also known as calcite.

The formation of calcite in soils follows the reaction:

$$Ca^{2+}_{(aq)} + 2HCO_3^-{}_{(aq)} = CaCO_3 + H_2O + CO_2 \qquad \text{(Eq. A-1)}$$

According to the above equation, the concentration of Ca^{2+} in solution depends on the partial pressure of CO_2 and the temperature. Carbon dioxide dissolves in water, forming carbonic acid (H_2CO_3) and hydrated CO_2. The reaction between CO_2 and H_2O can be described by:

$$CO_{2(g)} + H_2O = CO_{2(aq)} + H_2O \quad \text{(Eq. A-2)}$$

$$CO_{2(aq)} + H_2O = H_2CO_3 \quad \text{(Eq. A-3)}$$

$$H_2CO_3 = H^+ + HCO_3^- \quad \text{(Eq. A-4)}$$

$$HCO_3^- = H^+ + CO_3^{2-} \quad \text{(Eq. A-5)}$$

At the interface between the solution and solid $CaCO_3$ the equilibrium is:

$$CaCO_3 = Ca^{2+} + CO_3^{2-} \quad \text{(Eq. A-6)}$$

Note that the reaction for the formation of calcite (Eq. A-1) is obtained by combining equations A-2 through A-6.

Bozzano et al. (1999) showed that the $CaCO_3$ precipitation/dissolution equilibrium is controlled by a range of physical and chemical parameters, any process that reduces the amount of CO_2 in the system will cause calcite to precipitate:

5- Temperature: For many solids dissolved in water, the solubility of the solute increases with temperature up to 100°C. However, calcite exhibits an unusual characteristic referred to as “retrograde” or “inverse” solubility, where its solubility product decreases with increasing temperature (Langmuir, 1997). This is mainly caused by the fact that calcite dissolution/precipitation depends on the abundance of CO_2. The solubility of gases like CO_2 in liquids decreases with increasing temperature. Therefore, warming the water will result in a reduction in the amount of CO_2, hence, shifting Eq. A-1 to the right and calcite will precipitate. In contrast, CO_2 is more soluble in cold water (e.g. during cold seasons

and/or in deep water basins). In such conditions, calcite precipitation is less favorable.

6- Biochemical activity: Aquatic plants consume CO_2 in the process of photosynthesis. The carbonate system will buffer this loss by the precipitation of calcite until reaching an equilibrium condition.

7- Acidity (pH): The calcite solubility product decreases with increasing pH. In general, calcium carbonate dissolves in an acid solution (decreasing pH) and precipitates in a basic solution (increasing pH).

8- Pressure: The solubility of gases like CO_2 in liquids increases with increasing load pressure (e.g. due to the mass of the overlying material). This causes Eq. A-1 to shift to the left causing calcite to dissolve. In general, calcite precipitates at relatively low pressure.

A.2.2 Formation of Calcium Magnesium Carbonate

Fresh water lakes might also contain a host of soluble organic and inorganic materials that may modify the types of minerals formed (Doner & Lynn, 1989). For instance, the presence of magnesium Mg^{2+} promotes the formation of calcium magnesium carbonate [$CaMg(CO_3)_2$], also known as dolomite. Kelts and Hsu (1978) reported that the formation of dolomite as a replacement of calcium carbonate in lacustrine deposits requires that Mg/Ca in the water is larger than the equilibrium ratio K_{dz} (= Mg^{2+}/Ca^{2+}),

$$2\ CaCO_3 + Mg^{2+} = CaMg(CO_3)_2 + Ca^{2+} \qquad \text{(Eq. A-7)}$$

A.3 Structured Soils

Many researchers have investigated the effect of structure on the compressibility and shear strength of natural soils, and showed that they generally differ from reconstituted soils. These differences can be attributed to the soil structure. Mitchell (1993) defined the term “structure” as the combination of “fabric” (i.e., the arrangement of particles) and interparticle “bonding” (i.e., the electro-chemical forces at the inter-particle contacts). Burland (1990) adopted this definition of soil structure and proposed so-called “intrinsic properties” to describe the properties of reconstituted clays and use them as reference for understanding the behavior of natural clays. Extensive experimental work has shown that most natural soft clays are structured (Tavenas & Leroueil, 1990; Burland, 1990; Burland et al., 1996; Leroueil, 1997).

Structured soils are typically characterized by:

(i) A distinct transition from stiff to softer response when the preconsolidation stress, σ'_p (or vertical yield stress) is reached during compression tests;

(ii) At stresses immediately greater than σ'_p, compressibility increases abruptly indicating a collapse in the soil structure;

(iii) S-shape compression curves with varying compression index (C_c), that decreases with the vertical effective stress (σ'_v);

(iv) Higher preconsolidation stress, undrained shear strength, and stiffness compared to the same soil unstructured and at the same void ratio.

Kavvadas and Anagnostopoulos (1998) extended the definition of “soil structure” and postulated that soils can exist in two states: “intrinsic” and “structured”. Intrinsic state exists when the soil is reconstituted from a slurry (i.e., at high water content) and then consolidated, preferably under one-dimensional conditions in order to avoid rotation of principal stress axes and simulate the conditions

experienced by in-situ sedimentary soils. On the other hand, a soil is in its structured state when its properties deviate from the intrinsic properties.

Kavvadas (2000) observed similarities between the engineering characteristics of overconsolidated clays, partially saturated soils, and natural soils structured by diagenetic bonding (cementation and thixotropy), and he proposed an extended approach to soil structure in soils, which can be classified into three major categories:

1- Stress-history-induced structure, which is related to the geological pre-consolidation of the soil. Overconsolidated clays can be treated as structured materials because their properties are different than the properties of the reconstituted material. In general, all clays consolidated along a radial stress path and then loaded or unloaded along a different stress path (e.g. overconsolidation caused by unloading) possess such extended structure.
2- Bond-induced structure, which can be related to several different lithification (or bonding) processes that typically occur in geological timescale and can be associated with:
    a- *Cementation* due to the deposition of adhesive agents such as carbonates, hydroxides, organic matter at the inter-particle contacts. Cementation-type bonding is the most common type of structure in carbonatic soils;
    b- *Ageing* due to secondary compression (or creep) and thixotropic hardening. This type of structure can be found in most natural clays and it has very large impact on the engineering behavior of soils (e.g., Leonards & Ramiah, 1959; Leroueil et al., 1985; Perret, 1995). Ageing, which can develop even in very short time periods (i.e. days), increases the strength and the stiffness of the soil and prevents the onset of yielding. Although secondary compression and thixotropic hardening occur concurrently, they are two distinct phenomena.

Secondary compression is associated with a reduction in void ratio and structural readjustments that take place under constant effective stress conditions owing to the viscous nature of soil structures. However, thixotropic hardening is associated with reorganization of particles and water-cation system (Mitchell, 1993). Mitchell (1993) defined thixotropy as an isotherm, reversible, time-dependent process occurring under conditions of constant composition and volume. Thixotropic material stiffens when at rest and flows upon shear.

Cementation and thixotropic ageing typically result in an increase in the preconsolidation stress, which is also called "apparent preconsolidation stress" and is different than the geological preconsolidation stress.

c- *Leaching* of soft sensitive clays and removal of dissolved salts tend to shift the compression line of the reconstituted soil (or the intrinsic compression line ICL as defined by Burland (1990)) away from that of the intact soil, resulting in a higher degree of structure (Figure A-1).

d- *Heating and cooling* of clays. It is well known that one-dimensional compression curve and the entire limit state surface are temperature dependent. Many researchers (e.g. Horseman et al., 1987; Leroueil and Marques, 1996) reported that cooling has effects similar to diagenetic bonding while heating has opposite effects (Figure A-2).

3- Suction-induced structure, which is associated with partially saturated soils. Alonso and Gens (1994) reported that the matric suction (u_a - u_w) creates attractive inter-particle forces that causes the development of apparent preconsolidation stress resulting in a behavior similar to soils structured by diagenetic bonds.

In general, natural soils experience all the above types of structure concurrently and only the combined effects can be analyzed. For instance, Cotecchia and Chandler (1997) reported that, in most cases, geological overconsolidation and

bonding occur concurrently and separating their effects is not possible unless the geology of the deposit is very well known.

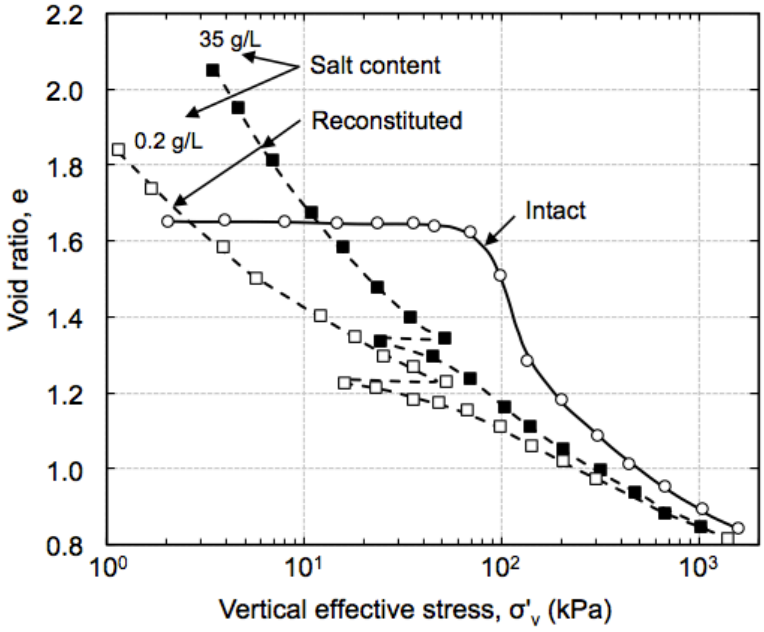

Figure A-1: Effect of leaching of a Canadian (Grande Baleine) marine clay on the position of the ICL (Locat & Lefebvre, 1985).

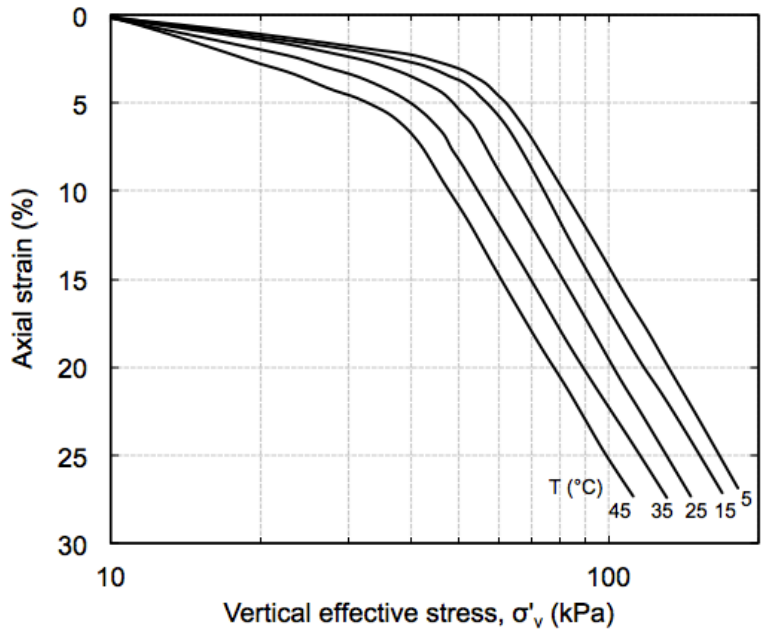

Figure A-2: Oedometer tests performed on Lulea clay at different temperatures (Eriksson, 1989)

A.3.1 Burland's (1990) Framework

Burland (1990) introduced the term "intrinsic properties" to describe the properties of clays which have been reconstituted at water content equal to 1 – 1.5 times the liquid limit. These properties, which are inherent to the soil and independent of the natural state, are used as reference against which natural clays are compared. In order to examine the characteristics of natural sedimentary clays and assess the influence of structure on properties, Burland (1990) proposed the concept of void index (I_v), a normalizing parameter defined as:

$$I_v = \frac{e - e^*_{100}}{e^*_{100} - e^*_{1000}} = \frac{e - e^*_{100}}{C^*_c} \qquad \text{(Eq. A-8)}$$

Where e = void ratio of the soil

e^*_{100} = intrinsic void ratio (i.e. void ratio on the intrinsic compression line (ICL)) under vertical effective stress σ'_v of 100 kPa

e^*_{1000} = intrinsic void ratio under σ'_v of 1000 kPa

C_c^* = intrinsic compression index

Figure A-3 shows schematics for the intrinsic compressions curves in (a) e-log σ'_v space and (b) I_v-log σ_v' space. When $e = e^*_{100}$, $I_v = 0$ and when $e = e^*_{1000}$, $I_v = -1$. Burland (1990) analyzed various reconstituted clays with a wide range of plasticities and normalized their one-dimensional compression curves using the void index. He concluded that this normalization produces a reasonably unique line, termed the intrinsic compression line (ICL) and may be expressed by the following equation:

$$I_v^* = I_{v,ICL} = 2.45 - 1.285(\log\sigma'_v) + 0.015(\log\sigma'_v)^3 \qquad \text{(Eq. A-9)}$$

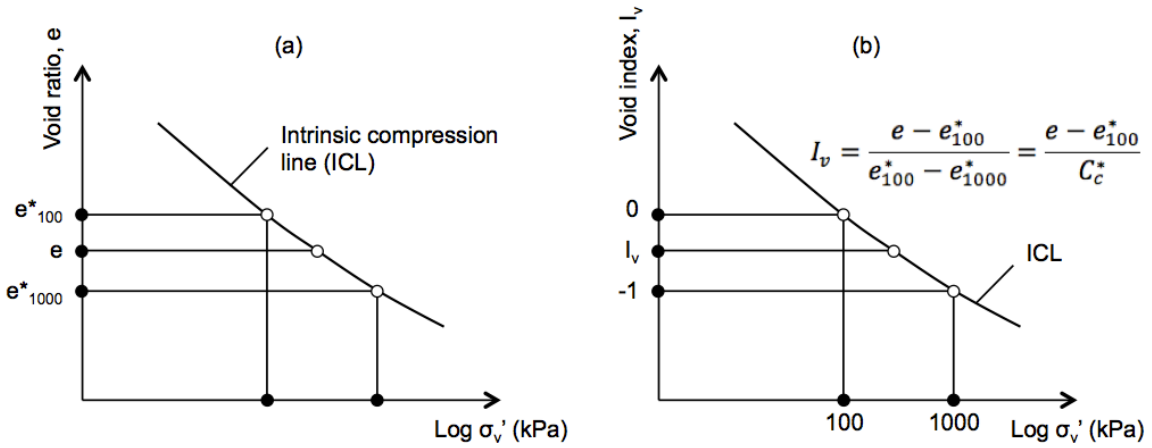

Figure A-3: The intrinsic compression line (ICL) in (a) e-log σ'$_v$ and (b) I_v-log σ'$_v$ space (Burland, 1990)

Using the void index I_v as a normalizing parameter, Burland (1990) plotted the in-situ stress state of a large range of normally consolidated natural sedimentary clays in I_{v0}-log σ'$_{v0}$ space (Figure A-4). It was found that the various sedimentation curves fall in a very narrow band with a reasonably unique line termed the sedimentation compression line (SCL) and may be expressed by the following equation:

$$I_{v,SCL} = 3.2436 - 0.6239(\ln\sigma'_v) + 0.0244(\ln\sigma'_v)^2 - 0.0012(\ln\sigma'_v)^3 \qquad \text{(Eq. A-10)}$$

The SCL is observed to fall clearly above the ICL owing to the fabric and soil structure developed during sedimentation and postdepositional processes. Over the range of σ'$_v$ = 10 kPa to 1000 kPa, the SCL is approximately parallel to the ICL. At the same void ratio, the SCL lies at a vertical effective stress five times greater than that of the ICL.

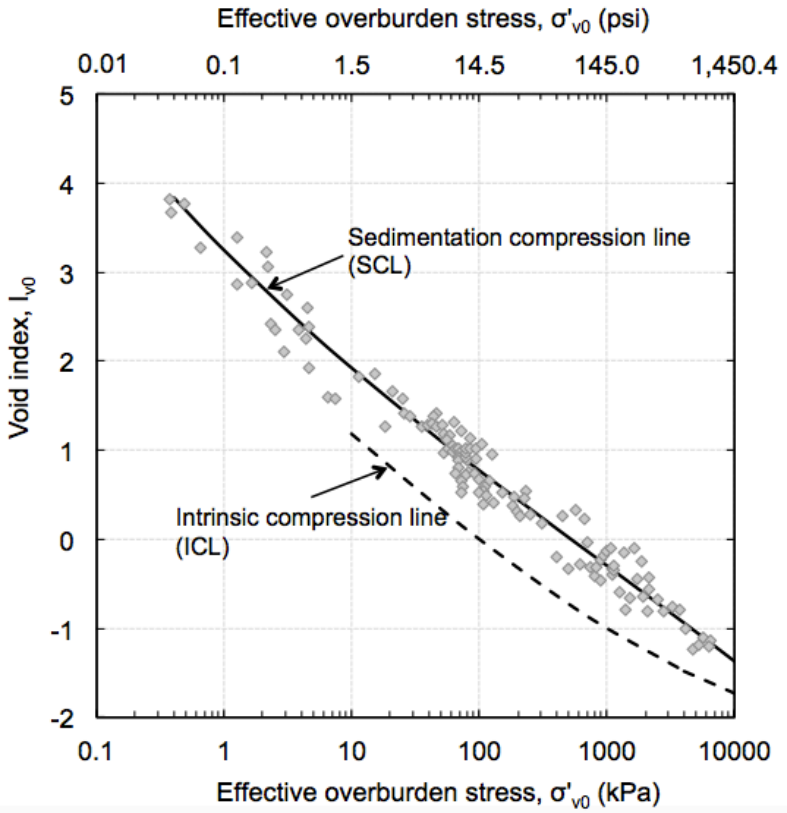

Figure A-4: The sedimentation compression line (SCL) for various normally consolidated clays (Burland, 1990)

Burland (1990) as well as others have shown that the in situ state of some clays can fall substantially above the SCL which can be attributed to differences in the depositional environments and post-depositional processes such as cementation, ageing, and leaching. Hence, the two lines proposed by Burland (i.e., ICL and SCL) can be used as reference to evaluate the degree of structuring of natural soils by comparing the soil's current e-σ'_v state with the intrinsic and sedimentary conditions. Plotting the compression data of natural soils in these coordinates requires the knowledge of the intrinsic void ratios e^*_{100} and e^*_{1000}, which can be measured by means of oedometer test on the reconstituted soil. Burland (1990) proposed empirical correlations between the void ratio at the liquid limit (e_L) and the intrinsic constants of compressibility e^*_{100} and C_c^* as follows:

$$e^*_{100} = 0.109 + 0.679e_L - 0.089{e_L}^2 + 0.016{e_L}^3 \qquad \text{(Eq. A-11)}$$

$$C_c^* = 0.256e_L - 0.04 \qquad \text{(Eq. A-12)}$$

These correlations are valid only for soils with Atterberg limits lying above the A-line and for values of e_L within the range of 0.6 to 4.5 (equivalent to w_L= 25% to 160%).

Using the void index I_v as a normalizing parameter (in conjunction with the proposed empirical correlations to determine the intrinsic constants of compressibility e^*_{100} and C_c^*), Burland compared the results of oedometer tests on freshwater glacial lake clay with the ICL and the SCL (Figure A-5). It can be seen that the post-yield compression curves are markedly steeper than the SCL, and at high stresses they slowly converge on the ICL as a result of soil "destructuration" (Leroueil, 1997).

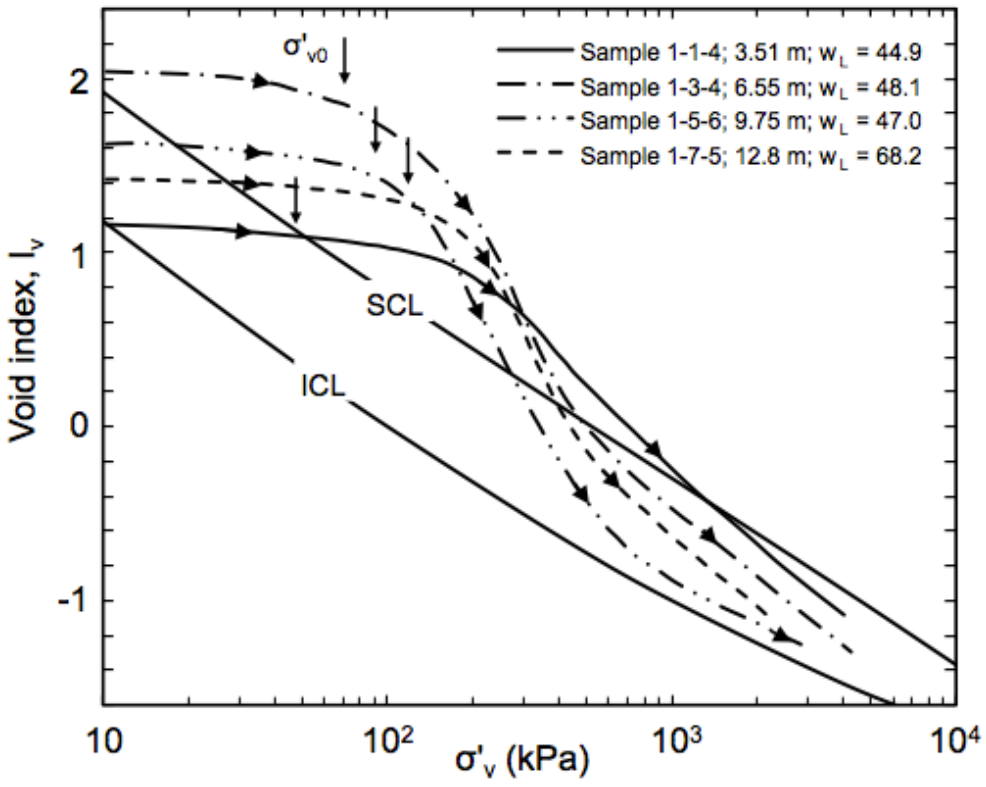

Figure A-5: Oedometer compression curves for freshwater glacial lake clay (Burland, 1990)

Figure A-6 shows a generalized view of in-situ states of various natural soils and their relative position compared to the ICL and SCL. Note that carbonate clays lies substantially above the SCL, which is typically caused by cementation and thixotropy at inter-particle contacts.

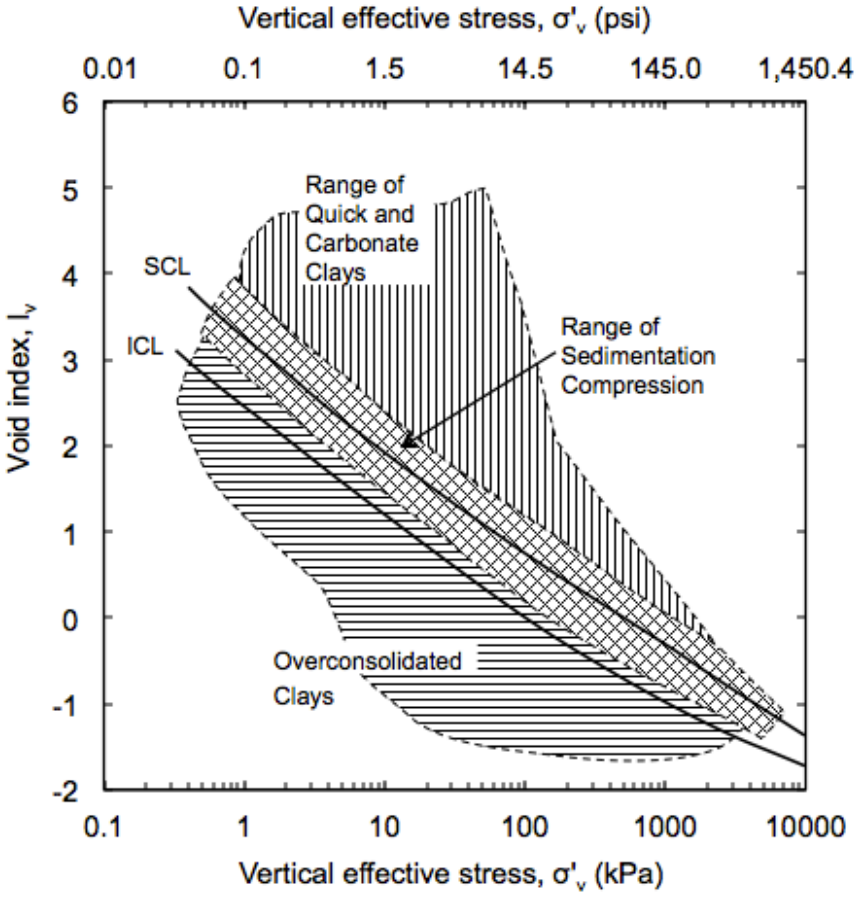

Figure A-6: I_v-σ'_v states for various clay types compared with the ICL and SCL (Chandler et al. 2004)

A.3.2 Destructuration

The post-yield structure degradation of intact soils, also known as "destructuration" in the normally consolidated (NC) region can be described using the model proposed by Liu and Carter (1999, 2000), which expresses the virgin compression behavior of a structured soil by the following equation:

$$e = e^* + \Delta e = e^* + \Delta e_i \left(\frac{\sigma_p'}{\sigma_v'}\right)^b \quad \text{for} \quad \sigma_v' \geq \sigma_p' \qquad \text{(Eq. A-13)}$$

Where e = void ratio of the intact structured soil in the NC region

e* = void ratio of the reconstituted soil at the same vertical effective stress

Δe = difference between the void ratio of the structured soil and that of the reconstituted soil at a given vertical effective stress in the NC region ($\sigma'_v > \sigma'_p$)

Δe_i = difference in void ratio at the preconsolidation pressure (σ'_p)

b = the compression destructuring index ($0 \leq b < \infty$)

This equation was proposed based on the observation that the additional void ratios sustained by soil structure during the virgin compression (Δe) is inversely proportional to the current mean effective stress (or vertical effective stress in 1-D consolidation) (Liu & Carter, 1999). An idealization for the compression behavior of structured and reconstituted soils is shown in Figure A-7.

Figure A-8 illustrates the destructuring process of soils during compression with a special emphasis on the influence of the compression destructuring index, b. The figure shows that the rate of reduction in Δe increases with the index b, with two extreme cases: (i) for b = 0, the value of Δe is constant during the virgin compression ($\Delta e = \Delta e_i$), hence no destructuring takes place during virgin compression; and (ii) for b = ∞, the value of Δe goes to zero immediately after the preconsolidation stress (Δe = 0, for $\sigma'_v > \sigma'_p$), indicating an immediate collapse of the soil structure.

Data presented by Liu and Carter (2000) shows that for natural soft clays, b generally lies between 0.3 and 1 (although values as high as 30 are reported).

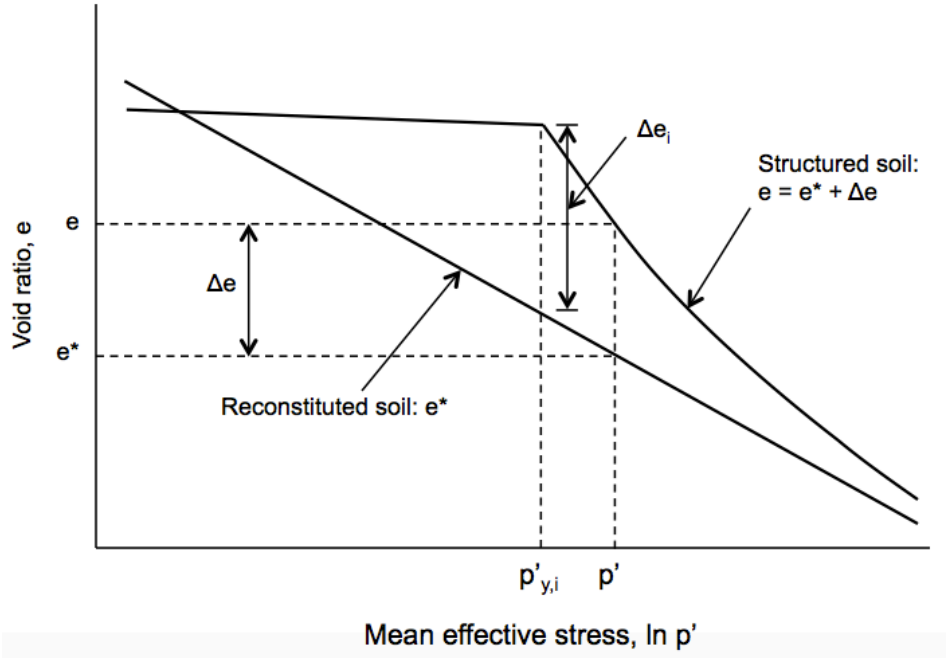

Figure A-7: Idealized compression behavior of structured and reconstituted soils (Liu & Carter 2000)

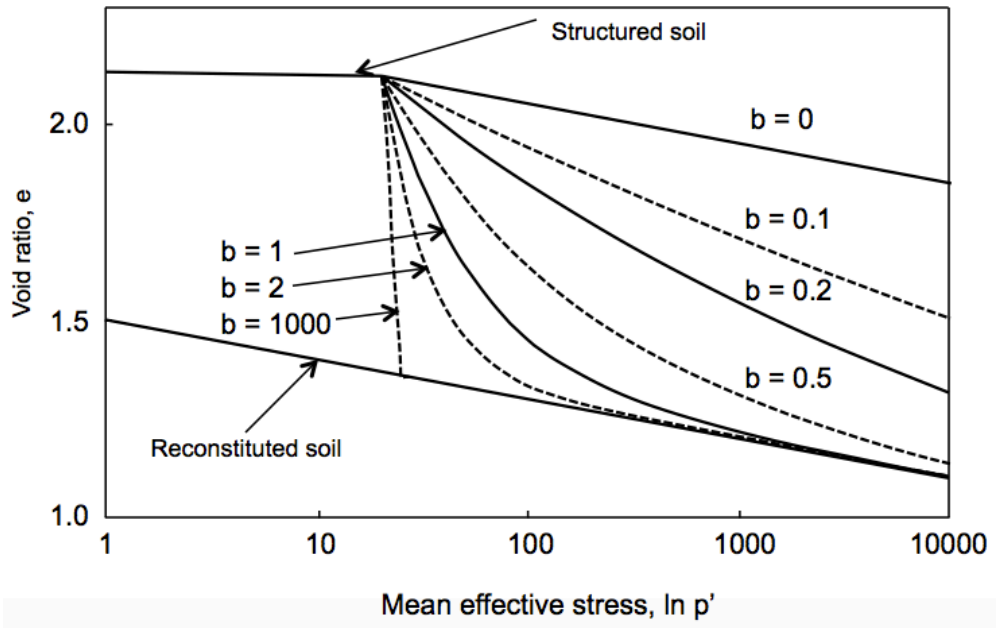

Figure A-8: Soil destructuration during compression (Liu & Carter, 2000)

Appendix B. Site Characteristics and Field Program

B.1 Introduction

Deposits of marl are encountered in the State of Indiana with layers as thick as 20', at relatively shallow depths (10-15') below the ground surface (Alt & Witzig, 2010; Earth Exploration, 2010). A site was selected in southwestern Indiana along the interstate I-69. The choice was based on the presence of marl deposits at shallow depths, the percentage of calcium carbonate present in the soil, as well as the accessibility to the site. This appendix provides the site characteristics and describes the field testing program that were conduced as part of this research effort. Section B.2 describes the geographical location and soil profile, while Section B.3 focuses on the site geology. Section B.4 and Section B.5 deal with the sampling operations and sampling program. The appendix concludes with a description of the field testing program (Section B.6) and of the field tests results (Section B.7).

B.2 Geographical Location and Soil Profile

The site is located at the intersection of County Road 900 E and County Road 1650 N, Madison, Daviess County, Indiana, about 85 miles southwest of Indianapolis (see Figure B-1).

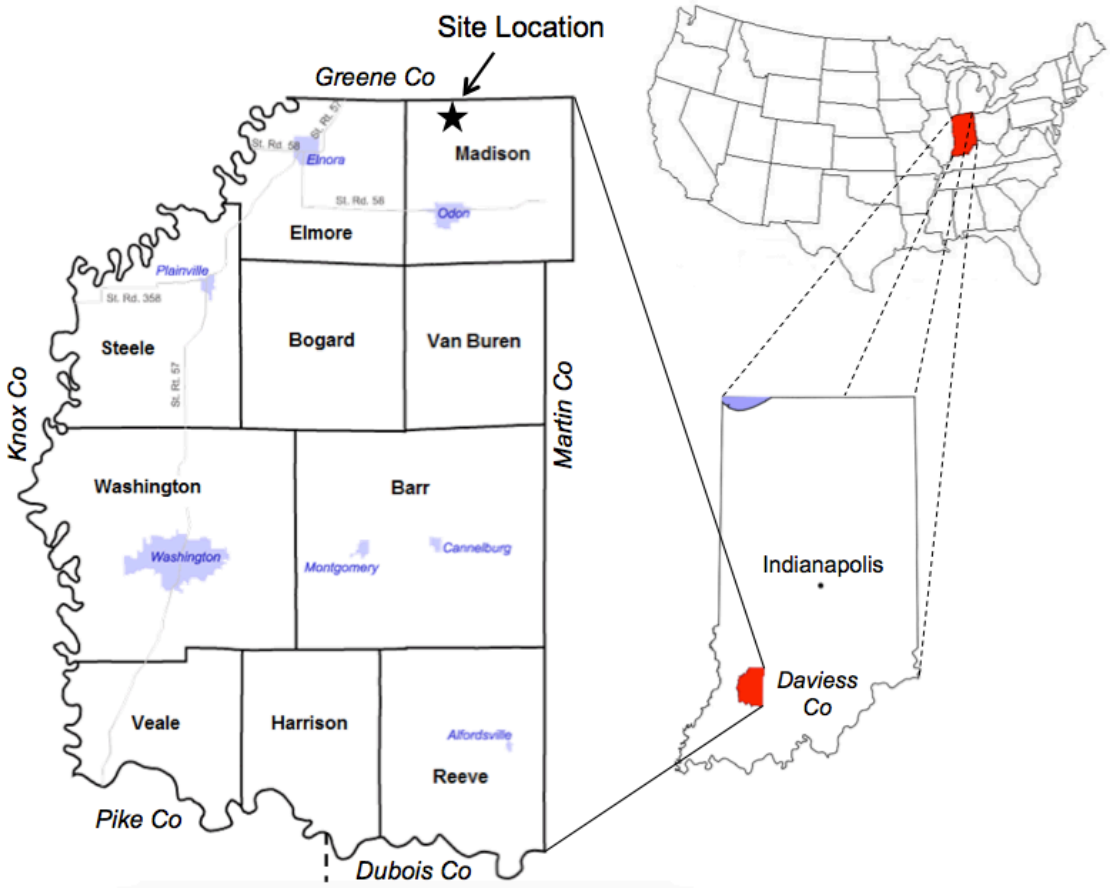

Figure B-1: Map of Daviess County (Indiana) showing the site location

The average ground elevation of the site was determined using a leveler as 150.84 m (494.88 ft). The site is adjacent to a creek (First Creek), which controls the water table, and produces frequent flooding (Isee, 2016). Monitoring of the water table level in a 50.8 mm (2 in) diameter open pipe piezometer over a period of 16 days showed an average depth of the water table of 1.9 m (6.25 ft) below the ground surface. Groundwater conditions are hydrostatic. Figure B-2 illustrates the average soil profile determined based on observations made in the field as well as examination of the samples used for the laboratory tests, which comprises about 1.9 m (~6.25 ft) of silty sand underlain by 1.5 m (~4.75 ft) of clayey silt and 2.7 m (~9 ft) of clay. At a depth of 6.1 m (~20 ft) the marl layer starts and has a thickness of 4.3 m (~14 ft). A sand layer is encountered below the marl layer with thin layers of clayey silt and sandy silt. The bedrock, mostly

sandstone, is located at a depth of about 37 m (120 ft) (see more discussion in Section B.3).

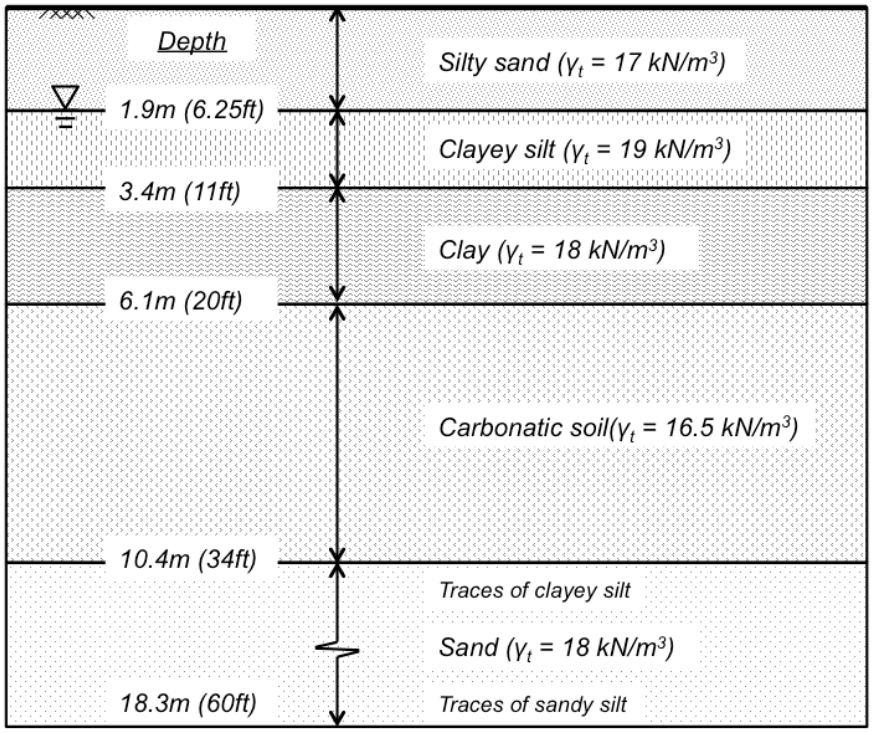

Figure B-2: Stratigraphy of the site

B.3 Site Geology and Age of Deposit

Glacial sluiceways and lacustrine plains are commonly encountered in the states of Indiana, Illinois, and Ohio. These plains are caused by the advance and retreat of the ice sheets that extended into the northern part of the Midwest during glaciation. During the Pleistocene geological period, North America experienced several glacial and interglacial periods. The most two recent glacial periods are Illinoian glaciation and Wisconsin glaciation (Wayne & Thornbury, 1951). The former occurred from approximately 300,000 to 130,000 years ago, whereas the latter occurred during the last years of the Pleistocene, from approximately 85,000 to 11,000 years ago (Fidlar, 1948; Gibbard & van Kolfschoten, 2004). The Illinoian ice sheet advanced into Indiana as two large lobes covering most of the state. The southeastern lobe advanced to the Ohio River at Louisville, Kentucky,

and the southwestern lobe covered nearly all Indiana crossing in the middle of Posey County, Indiana. The Wisconsin ice sheet covered most of central Indiana reaching as far south as Johnson County (South of Indianapolis). Figure B-3 shows the glacial lobes and sublobes that extended into Indiana during the Wisconsin age, as well as the Wisconsin and Illinoian glacial boundaries. The figure also shows the location of the site investigated in this research, which lies between the Wisconsin and Illinoian glacial boundary.

Figure B-3: Map showing site location relative to the Wisconsin and Illinoian glacial boundaries (modified from Thornbury & Deane, 1955 and Wayne 1965)

Thornbury (1937, 1940, and 1950) conducted an extensive research on the lacustrine plains in southern Indiana and reported that these plains are generally formed under two different systems of distinct ages and origins. The first system of lakes came into existence during the Illinoian glaciation period as a result of the ponding of the southwest drainage along the ice front of the southwestern glacial lobe. The second and more extensive system of lakes occurred during the Wisconsin glaciation period south of the Wisconsin glacial boundary, and thus deposition here is an indirect rather than direct effect of glaciation. The major streams acted as glacial sluiceways for Wisconsin melt-waters carrying detritus that caused the formation of extensive valley trains. The streams in the tributary valleys were ponded, which resulted in the formation of an extensive system of lakes. Lacustrine plains of this origin are widely developed along the tributaries of the Wabash, Ohio, and White Rivers.

As shown in Figure B-3, the site investigated in this research lies between the Wisconsin and Illinoian glacial boundary and is adjacent to the west fork of the White River. The deposit is most probably of Wisconsin age (85,000 to 11,000 years ago), where a large lake was created as a result of the ponding of the tributary stream (i.e. plains of First creek) by the extensive valley trains built down the west fork of the White River which acted as sluiceway for Wisconsin melt-waters (Thornbury, 1950). This was confirmed by radiocarbon dating conducted on both fossils (shells) and plants (pieces of wood) taken from the deposit at depths varying between 23.9 ft and 33 ft. The analysis resulted in an age of 23,600 to 20,800 yr BP (see more details below).

In order to better understand the ponding phenomenon of the tributary streams by the valley trains and appreciate the extent of the glacial lake that might have been formed during the Wisconsin age, Figure B-4 shows the elevation contour map of the site with elevations varying between ~152 m (500 ft) and ~198 m (650 ft). The First Creek flows northwest at an elevation of ~152 m (500 ft), passes

through the site and eventually joins the west fork of the White River. During Wisconsin age, the White River acted as glacial sluiceways for melt-waters carrying detritus that caused the formation of valley trains. The detritus deposited created a natural damn for the First Creek, which was ponded leading to the formation of a lake. Figure B-4 also illustrates a hypothesized lake that might have been generated at an elevation of ~152 m (500 ft), covering an area of about 2.5 km^2 (~1 mi^2). Due to natural drainage, evaporation and/or other geophysical processes that occurred over time, the water was drained from the lake, leaving the deposited sediments behind.

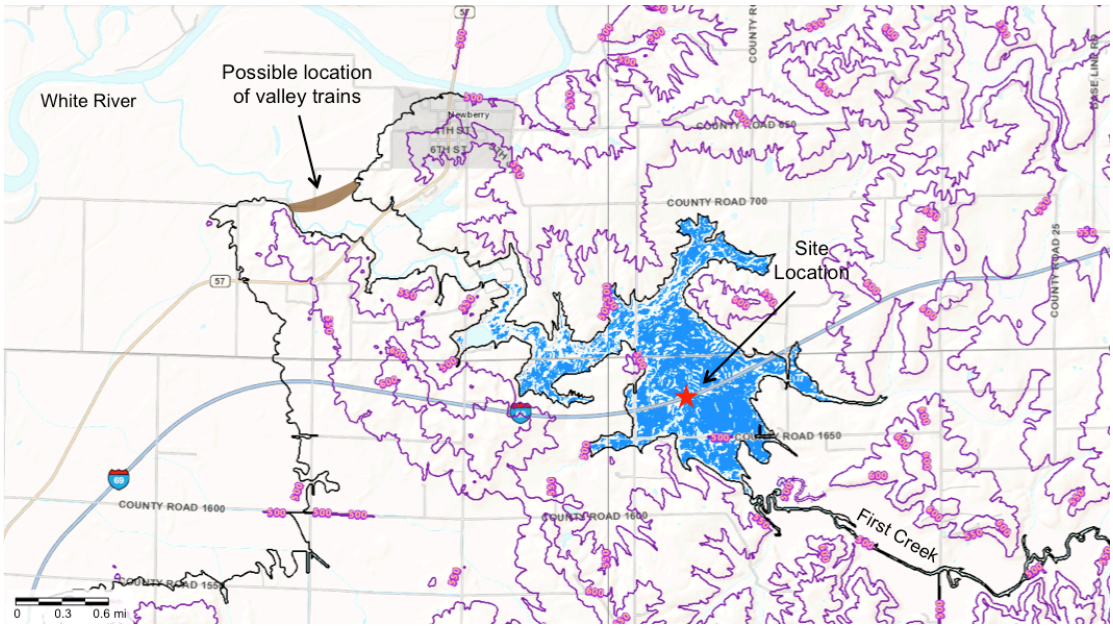

Figure B-4: Topographic map of the site showing the possible location of the glacial lake and the valley trains along the White River

A total of 69 boreholes, drilled as part of the construction of the interstate I-69 (Alt & Witzig, 2010; Earth Exploration, 2010), were used to develop the geotechnical crossection at the site shown in Figure B-5. The bedrock, mostly sandstone with highly weathered surface, is located as deep as ~37 m (120 ft) in the middle of the site and as shallow as ~3 m (10 ft) on the sides. The bedrock exists in a basin shape, which favors the formation of glacial lake in which the soil was deposited. The carbonatic soil deposit is found in the middle of the basin with a

width of approximately 1,150 m (~3770 ft) and a thickness of approximately 10 m (~33 ft).

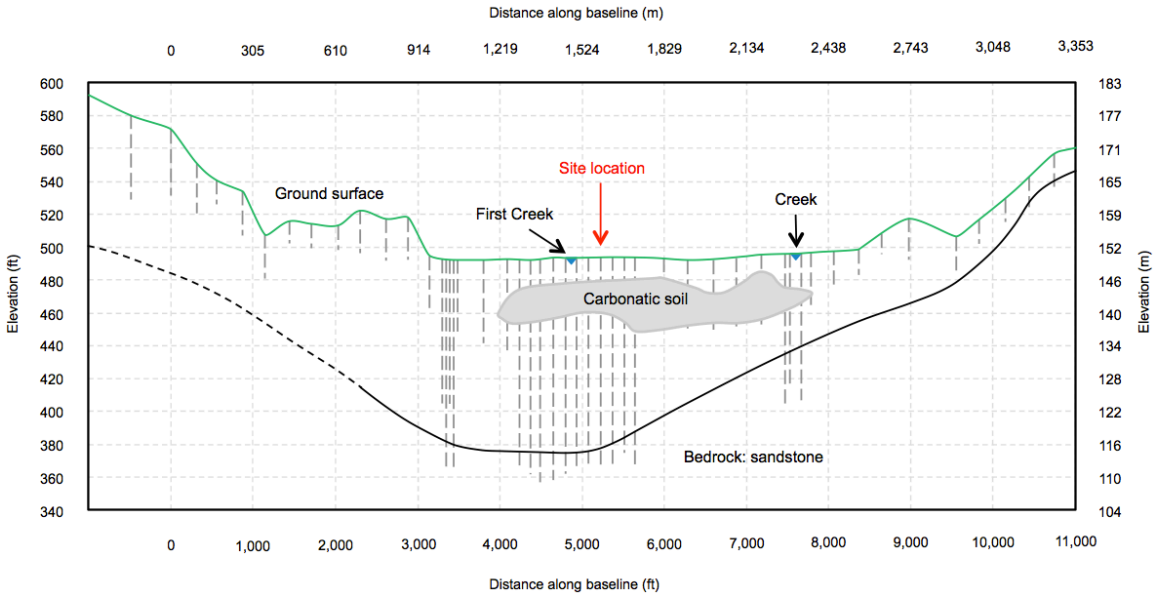

Figure B-5: Geotechnical crossection of the lacustrine deposit

Fossil shells of small gastropods that were found in the carbonatic soil layer, at depths varying between 23.9 ft and 33 ft, were collected and analyzed using an optical light microscope. All shells collected are < 5 mm in maximum dimension and are classified as minute (2-5 mm) and micro (< 2 mm) gastropods (Pigati et al. 2010).

Based on the extensive study conducted by Burch and Tottenham (1980) on the different species of freshwater snails that are found in North America, the six different species identified in this study (see Figure B-6) were found to be freshwater snails. The name, family, and subfamily of each type are summarized below:

Type 1: Amnicola (family: Hydrobiidae, subfamily: Amnicolinae)
Type 2: Valvata sincera (family: Valvatidae)
Type 3: Valvata tricarinata (family: Valvatidae)

Type 4: Gyraulus (family: Planorbidae, subfamily: Planorbinae)

Type 5: Cincinnatia (family: Hydrobiidae, subfamily: Nymphophilinae)

Type 6: Pisidium (family: Sphaeriidae, subfamily: Pisidiinae)

Charophyte oospores were also found in the carbonatic soil layer (see Figure B-7). These are pond-dwelling algae that live in still or slow-moving water with calcium carbonate. The presence of freshwater snails and charophyte oospores in the soil deposit at different depth confirms that the soil is deposited under lacustrine condition.

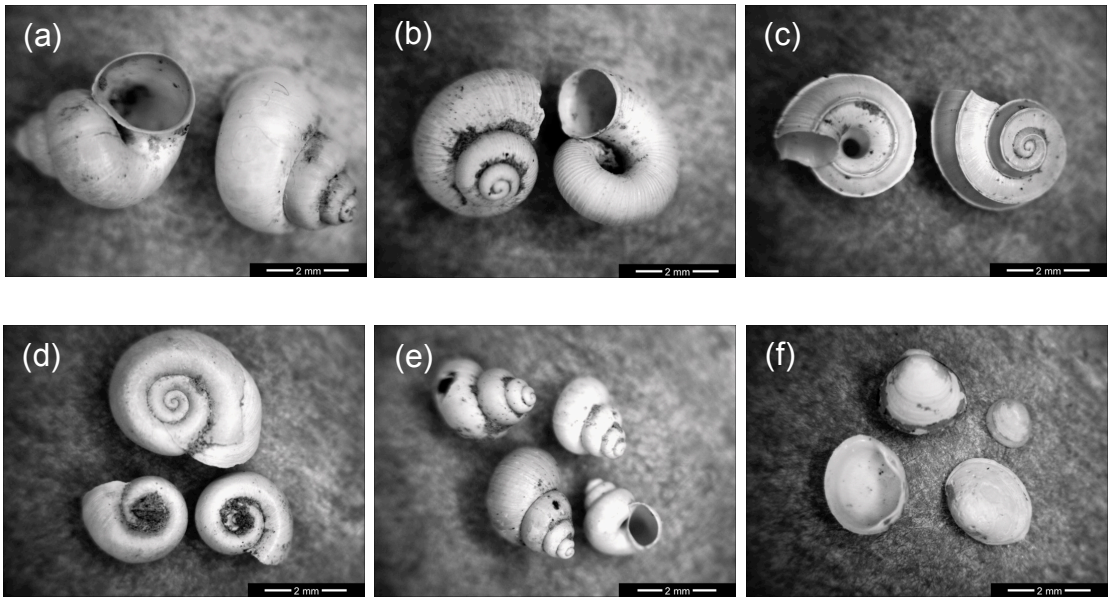

Figure B-6: Microscopic images for the different types of gastropods collected from the carbonatic soil layer. (a) Amnicola (Hydrobiidae), (b) Valvata sincera (Valvatidae), (c) Valvata tricarinata (Valvatidae), (d) Gyraulus (Planorbidae), (e) Cincinnatia (Hydrobiidae), and (f) Pisidium (Sphaeriidae)

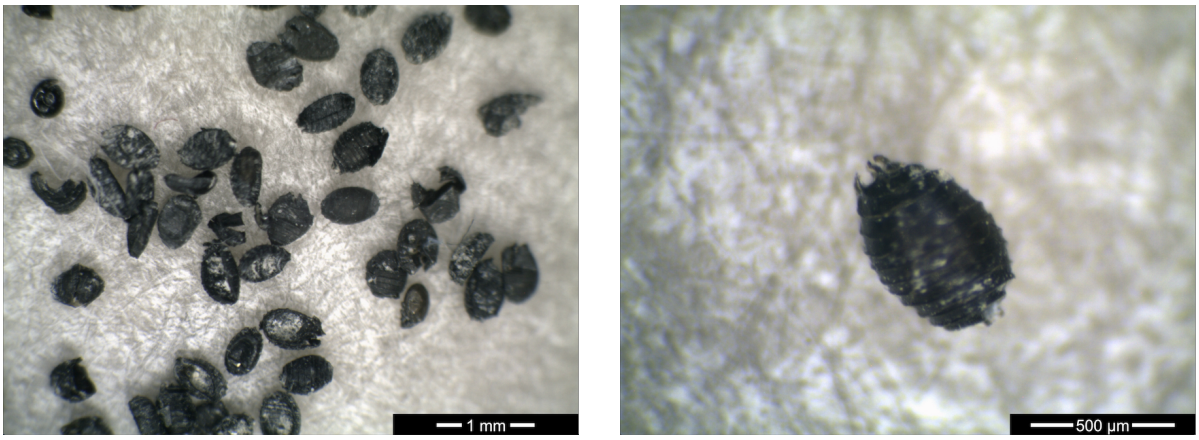

Figure B-7: Microscopic images for charophyte oospores collected from the carbonatic soil layer

To support the above outlined hypotheses on the geology and the age of the deposit, radiocarbon dating using accelerator mass spectrometry (AMS) was conducted on the fossil shells summarized above as well as plants (pieces of wood) (i.e. organic samples) found in the carbonatic soil layer at depths varying between 7.3 m (23.9 ft) and 10.1 m (33 ft). AMS measurements were conducted at Purdue Rare Isotope Measurement Laboratory (PRIME Lab). The AMS method is a modern radiocarbon dating technique that directly counts the ^{14}C atoms relative to the ^{13}C atoms (or ^{12}C, depending on the laboratory), whereas the conventional beta-counting method counts the beta particles emitted by a given sample as a result of radiocarbon decay (Muzikar et al., 2003). The main advantage of AMS over the conventional beta-counting method is that the former is relatively faster and requires a much smaller sample.

Aliquots from the carbonatic soil layer were placed in deionized water for several days to soften the sediment enough to pass through a 0.075 mm sieve (ASTM #200). Shells and pieces of wood were hand-picked from the retained fraction and repeatedly washed with deionized water to remove all the soil that adhered to the surface. The shells were then broken and the soil lodged within the shell was removed with a small spatula. Following additional washing with deionized water the recovered shells and pieces of wood were air-dried and used for

radiocarbon dating. Shells were not powdered during pretreatment to reduce the adsorption of ^{14}C from the atmosphere.

After the physical treatment, the samples were sent to PRIME lab for chemical treatment to remove any contamination from the sample surface before radiocarbon dating. For carbonate samples, acid etching is applied. This process involves reaction with a small amount of acid to remove surface carbonates, followed by reaction with excess acid to produce carbon dioxide. For organic samples, acid-base-acid (ABA) treatment is applied, which involves reaction with acid to remove surface carbonates, extraction with sodium hydroxide (base) to remove humic acids, and reaction with acid to remove carbonates introduced by the base treatment. The organic samples are then combusted with copper oxide to produce carbon dioxide. The gaseous CO_2 collected from the carbonate samples or the organic samples is then trapped and later graphitized using zinc and iron. The resulting graphite is mounted in the accelerator for AMS measurements (Muzikar et al., 2003). Sample preparation was performed with great care to avoid sample contamination with extraneous carbon.

Table B-1 summarizes the nine different samples (shells or wood fragments) used for radiocarbon dating, as well as the radiocarbon ^{14}C results. The samples were collected from different depths to investigate the variation/uniformity of the deposit age with depth.

Radiocarbon ages obtained from the AMS measurements were converted to “real” calendar years by accounting for the variation in the atmospheric ^{14}C activity (Reimer et al., 2009). Calibrated ages were calculated using CALIB v. 7.1, IntCal13 database, and they are reported as the midpoint of the calibrated range in terms of years ‘before present’ (BP), which refers to 1950. Calibration curves are attached in APPENDIX J.

Table B-1: Radiocarbon ^{14}C results for carbonate samples (shells) and organic samples (wood) recovered at depth ranging between 7.3 m and 10.1 m

Sample #	Depth (m)	Description	Comments	Radiocarbon Age (yrs)[a]	Cal age BP (yrs)[a,b]
1	7.3	Shell type 1 (Amnicola)	Carbonate sample	17,278 ± 252	20,864 ± 336
2	7.3	Shell type 2 (Valvata sincera)	Carbonate sample	17,060 ± 253	20,584 ± 324
6	7.3	Shell type 6 (Pisidium)	Carbonate sample	17,315 ± 252	20,912 ± 338
F	7.3	Wood	Organic sample	17,336 ± 220	20,935 ± 299
A	8.0	Shell type 4 (Gyraulus)	Carbonate sample (large shell)	17,973 ± 267	21,753 ± 357
B	8.8	Wood	Organic sample	19,557 ± 227	23,551 ± 295
C	10.1	Shells types 1 (Amnicola), 2 (Valvata sincera), 3 (Valvata tricarinata)	Carbonate sample (mixed types)	19,401 ± 238	23,361 ± 300
D	10.1	Wood	Organic sample	19,759 ± 232	23,782 ± 275
E	10.1	Shell type 6 (Pisidium)	Carbonate sample	19,607 ± 233	23,610 ± 294

[a] the ± reflects the uncertainty in the age

[b] cal age BP: calibrated age before present (referenced to 1950)

The calendar ages of the nine different samples are also shown in Figure B-8. Radiocarbon dating resulted in an age of 20,800 yr BP (at 7.3 m) to 23,600 yr BP at (10.1 m), with an increasing trend with depth. For the same depth, the carbonate samples and the organic samples resulted in a very similar calendar age, which implies that the fossil shells used in this analysis were not affected by the hard water effect (i.e., the age of carbonate samples can appear older than their true age due to the presence of calcium carbonate that has been dissolved into the freshwater source from limestone and carbonate rocks. This bias in age can vary between few decades and several hundreds years (Beta Analytic Inc., 2016), which can be neglected since it falls within the same order of magnitude for the age uncertainty obtained from the AMS method – See Table B-1)

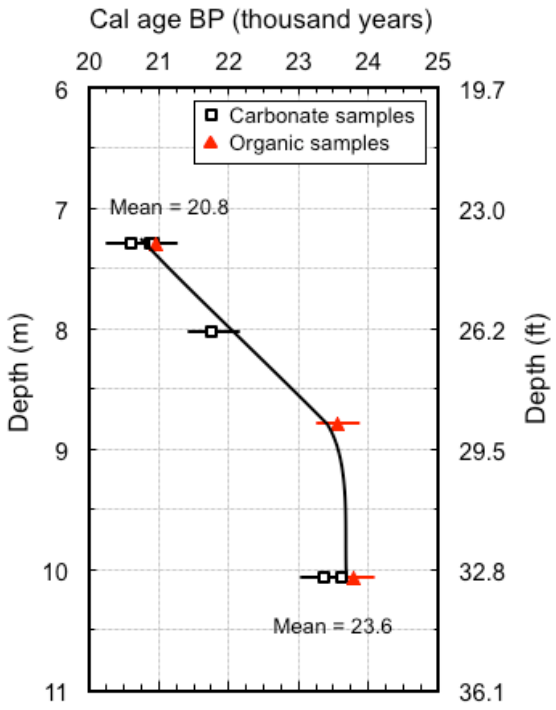

Figure B-8: Calendar age BP of carbonate samples (shells) and organic samples (wood) recovered at depth ranging between 7.3 m and 10.1 m

B.4 Sampling Operations

A total of five boreholes were performed to collect undisturbed marl samples. Four boreholes were drilled using mud rotary, while the fifth was drilled using a hollow stem auger (see more details below). The first represents the best practice for sampling in soft soil (Ladd & DeGroot, 2003), while the latter was carried out as an example of the sampling practice that is routinely used in Indiana. Comparison of laboratory test results on samples obtained using these two methods provides an opportunity to explore the effect of the drilling method on sample disturbance. Figure B-9 shows the location of the borings with MR# denoting the borehole drilled using mud rotary and HSA# denoting the borehole drilled using hollow stem auger. The figure also shows the locations where field vane shear tests (FV#) and cone penetration tests (CPT#) were performed (see more details in Section B.6). Field testing and sampling were performed in close proximity to each other in order to minimize the effects of spatial variability and

facilitate the comparison between field and laboratory results (the site is about 9 m x 7 m (30 ft x 23 ft)). Table B-2 summarizes the location of all the borings, field vane, piezometer and piezocones that were conducted in this research. Boring logs are attached in APPENDIX F.

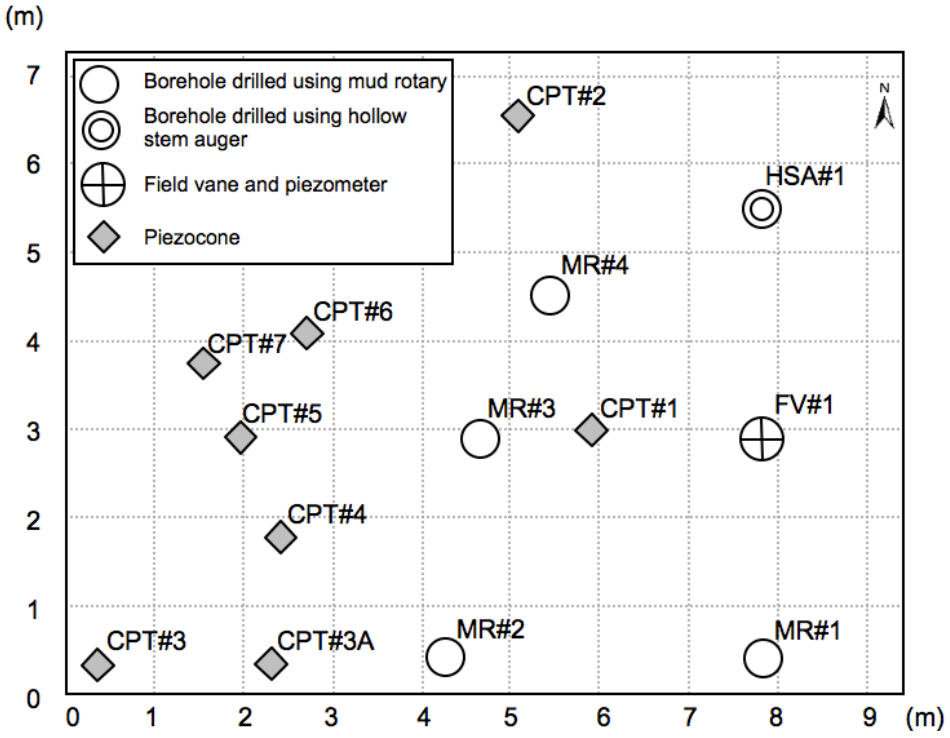

Figure B-9: Location of borings, piezometer, field vane, and piezocone tests (to scale)

Table B-2: Coordinates of borings, field vane, piezometer and piezocones

Boring no.	Latitude	Longitude
MR#1	38.898745	-86.990570
MR#2	38.898745	-86.990615
MR#3	38.898770	-86.990610
MR#4	38.898785	-86.990600
FV#1*	38.898770	-86.990570
HSA#1	38.898795	-86.990570
CPT#1	38.898770	-86.990595
CPT#2	38.898805	-86.990605
CPT#3+	38.898745	-86.990640
CPT#3A	38.898745	-86.990665
CPT#4	38.898759	-86.990640
CPT#5	38.898770	-86.990645
CPT#6	38.898781	-86.990635
CPT#7	38.898777	-86.990650

* FV#1 was also used to install an open pipe piezometer

+ CPT#3 was directly aborted due to the presence of some gravel below the piezocone

Continuous sampling was conducted from the ground surface to a depth of 15.24 m (50 ft). From 0 to 4.88 m (16 ft), a standard penetration test SPT was done and disturbed samples were collected from the split spoons and preserved in sealed containers and plastic bags. SPT plastic spring core catchers were used to retain the samples during retrieval. Shelby tubes were pushed between 4.88 m (16 ft) and 11.58 m (38 ft) where marl was found. For the last 3.66 m (12 ft) below the marl layer, the SPT was again performed and samples were collected and preserved in sealed containers and plastic bags. The purpose of conducting continuous sampling was to analyze the stratigraphy at the site and characterize the soil that is present above and below the marl layer. Figure B-11 shows the truck mounted drilling rig that was used to carry out the sampling and in-situ tests. All the Shelby tubes were pushed with a fixed piston sampler to minimize sample disturbance. For very soft soils, it is very hard to collect undisturbed soil samples because they tend to fall out of the sampler. Under such conditions fixed piston sampler should be used which consists of a thin wall tube (i.e. Shelby tube) with a piston (shown in Figure B-12). The piston is first positioned at the bottom end

of the thin wall tube and the sampler is lowered to the bottom of the borehole. The thin wall tube is pushed into the soil, past the piston. When the Shelby tube is filled, both tube and piston are pulled up. During the sampling process, the soil is in direct contact with the piston head, which, through a rubber packing (see Figure B-12(a)), applies a vacuum, keeping the sample from falling out of the sampler. Moreover, tubes with modified geometry were used to reduce the shear-induced strains during sampling. The modified Shelby tubes are 76.2 cm (30 in) long and have a diameter of 76 mm (3 in) with sharp edge (tapered from the outside) and an inside clearance ratio (ICR) of zero (shown in Figure B-10). Baligh et al. (1987) showed that during tube sampling, the soil at the centerline experiences shear in compression ahead of the tube, shear in extension while entering the tube and compression again when moving upward within the tube. The strain amplitude is dependent on the geometry of the tube increasing as the diameter to thickness ratio decreases. It is also affected by the geometry of cutting, and can be minimized using Shelby tubes with an ICR equal to zero because it prevents lateral expansion of the soil once inside the tube (e.g. Clayton et al., 1998).

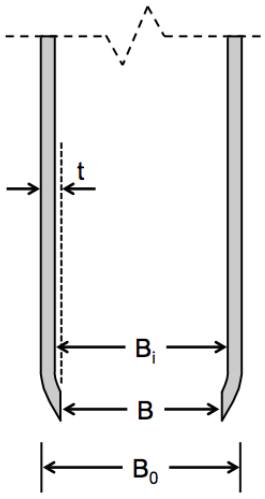

- External tube diameter:
  B_0 = 7.6 cm (3 in)
- Internal tube diameter:
  B_i = 7.29 cm (2.87 in)
- Cutting edge diameter:
  B = B_i = 7.29 cm (2.87 in)
- Effective wall thickness of tube:
  t = (B_0 – B) / 2 = 0.165 cm (0.065 in)
- B / t = 44
- Inside clearance ratio: ICR = (B_i – B) / B = 0

Figure B-10: The geometry of Shelby tube used for sampling

Two methods were used for advancing the borehole: 1) hollow stem auger and 2) mud rotary. In both cases the power for drilling is delivered by the truck mounted drilling rig (Figure B-11). Four boreholes were drilled with mud rotary whereas the fifth one was drilled using a hollow stem auger. For the first method, hollow stem augers with diameter equal to 82.55 mm (3.25 in) and length of 1.52 m (5 ft) were used. A cutter head (Figure B-13(c)) is attached to the tip of the auger (also referred to as “lead auger”) while the other end is connected to the drive cap of the drilling rig (Figure B-13(b)). During the drilling operation (Figure B-13(a)), section after section of auger (1.52 m (5 ft) each) is added and the hole extends downward. A center bid is attached to the bottom of the auger by means of a center rod which helps keep the inside of the hollow augers clean, and loose soil from the bottom of the hole is brought to the surface by the flights of the augers. When soil samples are needed, the center rod is raised with the auger in place and the center bid is replaced by the sampler. Drilling mud (bentonite slurry) was used at all time to avoid heave of the soil at the bottom of the borehole caused by the upward water flow. The second method of advancing boreholes is mud rotary. In this method, the soil is drilled by means of rotary blades, also referred to as drilling bits, (Figure B-14(b)) attached to a drilling rod. Drilling mud (a slurry of water and bentonite) is forced down the drilling rods and the return flow forces the soil cuttings to rise in the drill hole and overflow at the top of the casing through a T connection (Figure B-14(a)). When soil samples are needed, the drilling rod is raised and the rotary blade is replaced by the sampler.

The first 4.27 m (14 ft) of soil was drilled the same way for all the five boreholes. Hollow stem augers (82.55 mm (3.25 in) diameter) were used to form the casing for the borehole. Three augers were inserted (1.52 m (5 ft) each) until reaching a depth of 4.27 m (14 ft) (0.3 m (1 ft) was left above the ground surface). At a depth of 4.88 m (16 ft), the fixed piston was positioned at the bottom end of the Shelby tube and then inserted in the borehole (see Figure B-12). Once the desired sampling depth was reached, the sampling tube was advanced ahead of

the piston followed by a waiting period of ten minutes; which is necessary to improve sample recovery for soft saturated clays as reported by ASTM D6519-08 (ASTM, 2008). The tube was then rotated several times to ensure shearing along the bottom surface, and the sampler was retracted, initially at a very slow rate to allow the sample to break from the ground; this is also consistent with ASTM D6519-08 (ASTM, 2008). The tubes were then waxed and sealed with plastic caps and duct tape at both ends and transported in vertical position to Purdue's geotechnical laboratory. They were stored vertically in a humid room at a constant temperature of 10°C and 100% relative humidity to prevent soil drying.

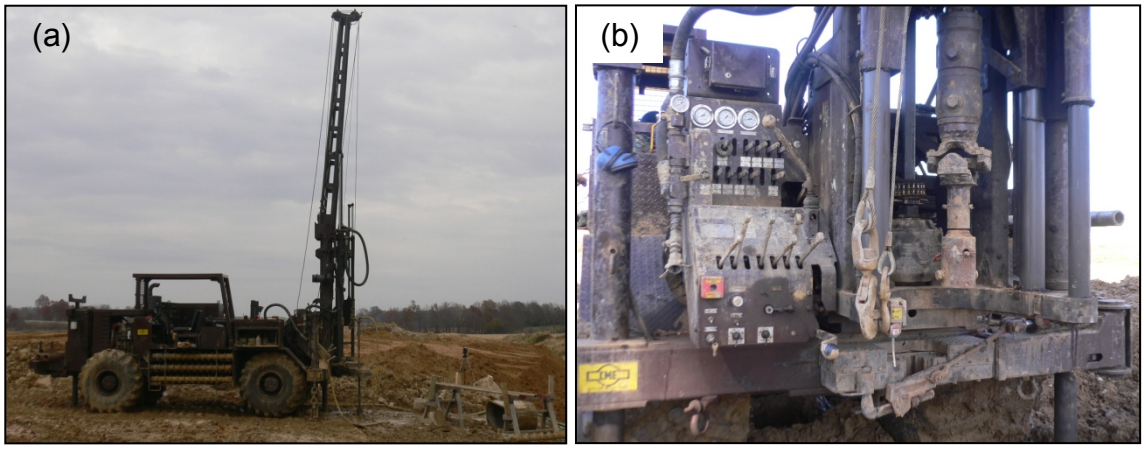

Figure B-11: (a) Truck mounted drilling rig and (b) rig control panel

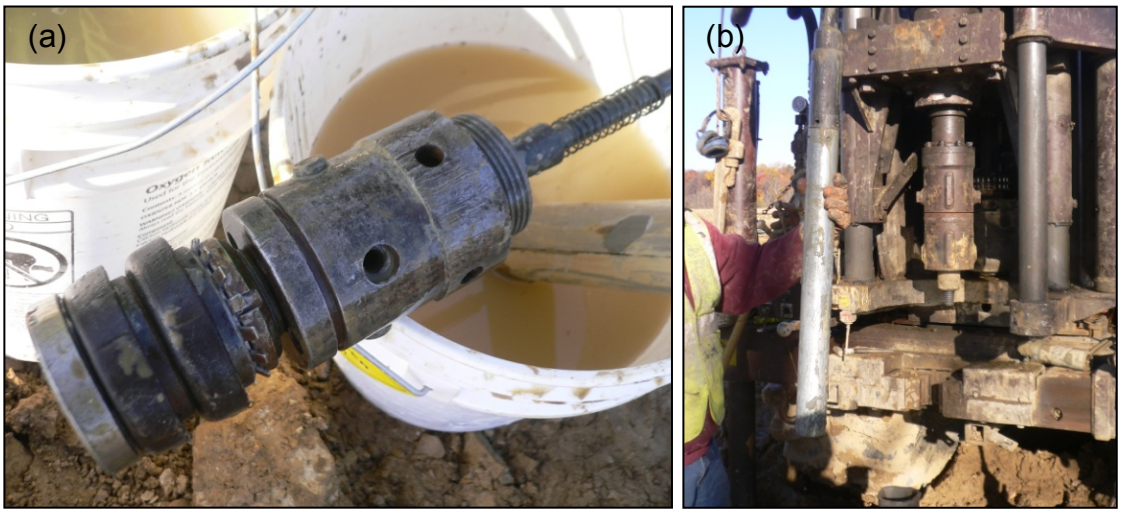

Figure B-12: Fixed piston sampler: (a) fixed piston and (b) piston mounted on Shelby tube

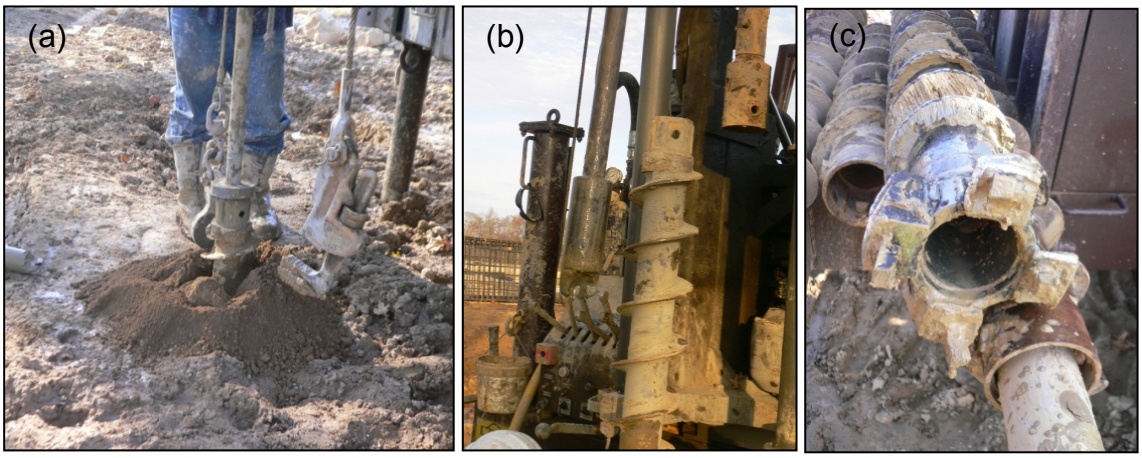

Figure B-13: Hollow stem auger: (a) drilling with continuous-flight augers, (b) auger flight and drive cap of the drilling rig and (c) cutter head

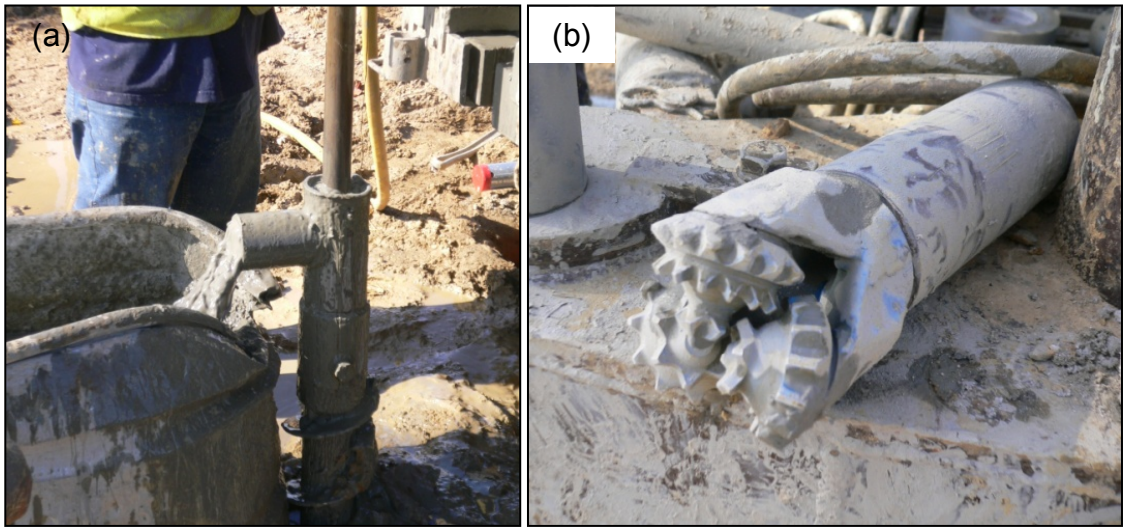

Figure B-14: Mud rotary: (a) T connection (b) rotary blades

B.5 Sampling Program

A total of 53 Shelby tubes (ST) (76.2 cm (30 in) long and 76 mm (3in) in diameter) were obtained from the sampling operations for depths ranging between 4.9 m (16 ft) and 11.6 m (38 ft). The soil samples retrieved are ~61 cm (24 in) long since the fixed piston occupies the first top 15.2 cm (6 in) of the ST. Table B-3 summarizes the samples collected in each boring. Different symbols are used to indicate differences in the sampling operations. Specifically, ellipses denote ST with machined edges, i.e. zero inside clearance ratio (ICR – see Section B.4),

while dashed ellipses identify the two samples obtained using the two non-machined tubes, which were pushed at depths between 4.3 m (14 ft) and 4.9 m (16 ft) [MR#3 ST1] and between 9.1 m (30 ft) and 9.8 m (32 ft) [MR#4 ST8]. These samples were obtained in order to examine the effect of the ICR on sample disturbance. Finally, a double ellipse is used for the single sample [MR#4 ST7], which was pushed without a fixed piston. Note that this procedure resulted in zero recovery, demonstrating the importance of using a fixed piston when sampling soft soils.

Table B-3 also provides an indication of the degree of disturbance of all ST, based on the degree of recovery, and observations made during sampling and transportation (a quantitative assessment of disturbance was also performed from the results of laboratory tests and is presented in Section D.3.8). Specifically, as described in the legend of the table, different colors are used to indicate different degrees of recovery (green, yellow and red for full, incomplete and no recovery, respectively), whereas samples that incurred disturbance during sampling due to problems with the piston (fixed piston was stuck because of the usage of the wrong screw) or during transportation (ST was bent because of the wire that was used to fix it during transportation) are identified with the colors brown and blue.

The table also shows the location of the split spoon (disturbed) samples (SS), which were collected from the soil above and below the marl layer. Between 0 and 4.9 m (16 ft), a total of 30 SS samples were obtained from MR#1, MR#2, HAS#1 and FV#1. From 11.6 m (38 ft) to 15 m (50 ft), a total of 16 SS samples were obtained from MR#1, MR#2, and MR#4. 1 SS sample was obtained from 10.4 m (34 ft) to 11 m (36 ft) [MR#1 SS8]. The locations of the vane shear tests conducted in boring FV#1 are included in the last column of Table B-3 and are denoted by hexagons.

Table B-3: Quality of samples collected

Depth (m)	Depth (ft)	MR#1	MR#2	MR#3	MR#4	HSA#1	FV#1
		SS1	SS1	-	-	SS1	SS1
0.6	2	SS2	SS2	-	-	SS2	SS2
1.2	4	SS3	SS3	-	-	SS3	SS3
1.8	6	-	SS4	-	-	SS4	SS4
2.4	8	SS4	SS5	-	-	SS5	SS5
3	10	SS5	SS6	-	-	SS6	SS6
3.7	12	SS6	SS7	-	-	SS7	SS7
4.3	14	SS7	SS8	ST1	-	SS8	FV0
4.9	16	ST1	ST1	ST2	ST1	ST1	FV1
5.5	18	ST2	ST2	ST3	ST2	ST2	FV2
6.1	20	ST3	ST3	ST4	ST3	ST3	FV3
6.7	22	-	ST4	ST5	ST4	ST4	FV4
7.3	24	ST4	ST5	-	ST5	ST5	FV5
7.9	26	ST5	ST6	ST6	ST6	-	FV6
8.5	28	ST6	ST7	ST7	ST7	ST6	FV7
9.1	30	ST7	ST8	ST8	ST8	ST7	FV8
9.8	32	ST8	ST9	ST9	ST9	ST8	FV9
10.4	34	SS8	ST10	ST10	ST10	ST9	FV10
11	36	ST9	-	ST11	ST11	ST10	FV11
11.6	38	SS9	ST11	-	ST12	-	-
12.2	40	SS10	SS9	-	SS1	-	-
12.8	42	SS11	SS10	-	SS2	-	-
13.4	44	SS12	SS11	-	SS3	-	-
14.0	46	SS13	SS12	-	SS4	-	-
14.6	48	SS14	SS13	-	SS5	-	-

SS	Split spoon		Undisturbed - full recovery
ST	Shelby tube		Undisturbed - incomplete recovery
ST	Shelby tube (not machined)		No recovery
FV	Field vane shear test		Disturbed (fixed piston stuck)
	Fixed piston was not used		Disturbed (ST bent during transportation)

B.6 Field Testing Program

One of the major tasks in this project was to conduct field tests that would complement the laboratory testing program. The in-situ testing program included: (i) seven seismic cone penetration tests with pore pressure measurements (SCPTu); (ii) forty six standard penetration tests (SPT) for soil profiling and collection of disturbed samples; (iii) eleven field vane (FV) shear tests to determine the undrained shear strength and soil sensitivity profile; and (iv) the installation of an open pipe piezometer to locate the groundwater table.

B.6.1 Seismic Cone Penetration Tests (SCPTu)

A total of seven CPTs were conducted at the site for profiling the stratigraphy, and deriving tip resistance, skin friction, shear wave profiles with depth and measuring pore pressure dissipation. Three CPTs (CPT#1, CPT#2 and CPT#7) were conducted continuously up to a depth of 18.3 m (60 ft) at a constant rate of 20 mm/sec. Two CPTs (CPT#4 and CPT#5) were used to obtain the shear wave profiles with depth. At one-meter intervals, a surface shear wave was generated using a hammer (see Figure B-15) and the shear wave arrival times were recorded by a geophone in the cone. The last two CPTs (CPT#3A and CPT#6) were performed to conduct porewater dissipation tests. For each hole, four dissipation tests were conducted in the marl layer (increments of 1.5m (5ft)). Figure B-16 shows the assembly of the penetrometer before running the CPT; silicone gel was used for saturating the pressure transducer.

Figure B-15: Generation of a surface shear wave using a hammer

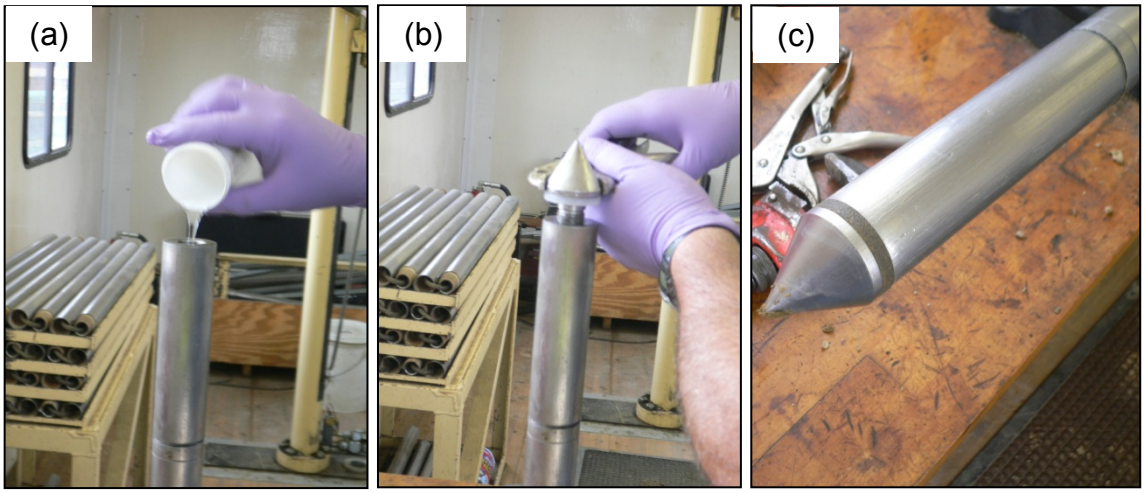

Figure B-16: (a) Saturation of pressure transducer, (b) piezocone head, and (c) piezocone filter

B.6.2 Standard Penetration Test (SPT)

SPTs were performed in the soil above and below the marl layer and were used for soil profiling, as described in Section B.4 (see Figure B-17). Disturbed samples retrieved from the split spoons were collected and preserved in sealed containers and plastic bags for index testing. All the samples were stored in a

humid room at a constant temperature of 10°C and 100% relative humidity. Plastic spring core catchers were used to retain the sample during retrieval (Figure B-18). In order to have continuous sampling with 609.6 mm (2 ft) long split spoons, the sample tube was driven 609.6 mm (2 ft) into the ground and the number of blows needed for the tube to penetrate each 152.4 mm (6 in) was recorded. Thus, consistent with ASTM D1586-11 (ASTM, 2011), four intervals are obtained but only the top three are used to calculate the standard penetration resistance (N-value).

Figure B-17: Standard penetration test (SPT)

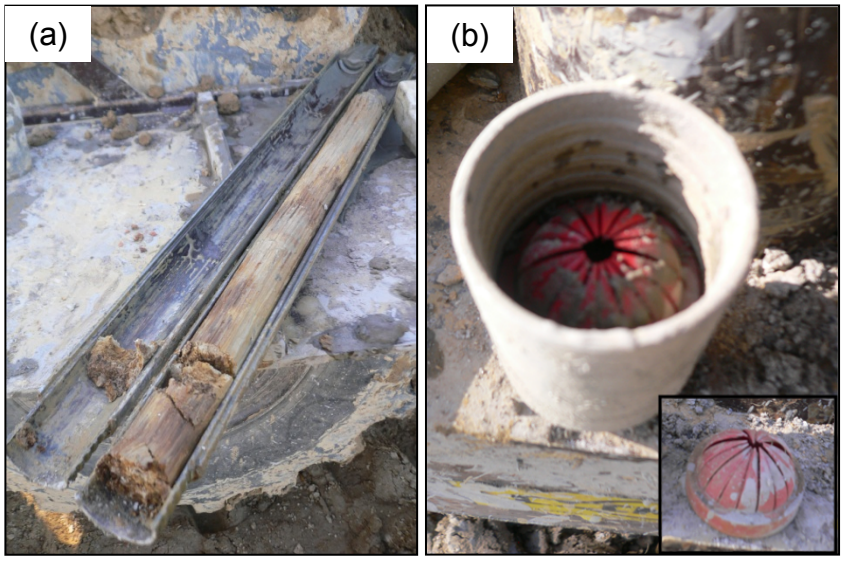

Figure B-18: (a) Split-spoon sampler (b) plastic spring core catcher

B.6.3 Field Vane Shear Test

In addition to the CPT, the field vane (FV) shear test is commonly used to determine the undrained shear strength of soft soil deposits. A separate borehole was drilled for the field vane shear test. Hollow stem augers (107.95 mm (4.25 in) diameter) were used to form the casing for the borehole. Note that an auger diameter larger than the one used for the other tests described in Section B.4 was utilized so that the vane shear blades could fit in the borehole. Figure B-19 shows the geometry of the field vane (both ends tapered) as well as the minimum and maximum dimensions required by ASTM D2573-08 (ASTM, 2008). Three augers were inserted (1.52 m (5 ft) each) to form the casing until reaching a depth of 4.27 m (14 ft) (0.3 m (1 ft) was left above the ground surface which is needed to install the sub and the force arm of the vane shear, see Figure B-20(a)). Drilling mud (bentonite slurry) was used at all time to avoid heave of the soil at the bottom of the borehole caused by the upward water flow. Ball bearing guide couplings, shown in Figure B-20(b), were used every 3 m (10 ft) to keep the drilling rod and vane in the center of the borehole. Figure B-21 summarizes the steps that were followed during the test. At a depth of 4.88 m (16 ft), the vane shear was inserted 0.6 m (2 ft) into the undisturbed soil; this is consistent with

ASTM D2573-08 (ASTM, 2008), in which it is recommended that the depth of penetration be at least 5 times the hole diameter, 5 x 0.11 m = 0.54 m (5 x 4.25 in = 21.25 in); also consistent with ASTM D2573-08 (ASTM, 2008), the vane shear test was conducted by rotating the vane at 0.1 °/sec to obtain the peak strength. Ten full revolutions were then performed at high rate to free the vane; an additional test was conducted to determine the remolded undrained shear strength, which was used later to calculate the soil's sensitivity. Following the second measurement, the center rod was raised and the vane replaced by a split spoon sampler to collect the disturbed soil at the depth of the test. The marl layer was tested every 0.61 m (2 ft) from 4.88 m (16 ft) to 11.58 m (38 ft).

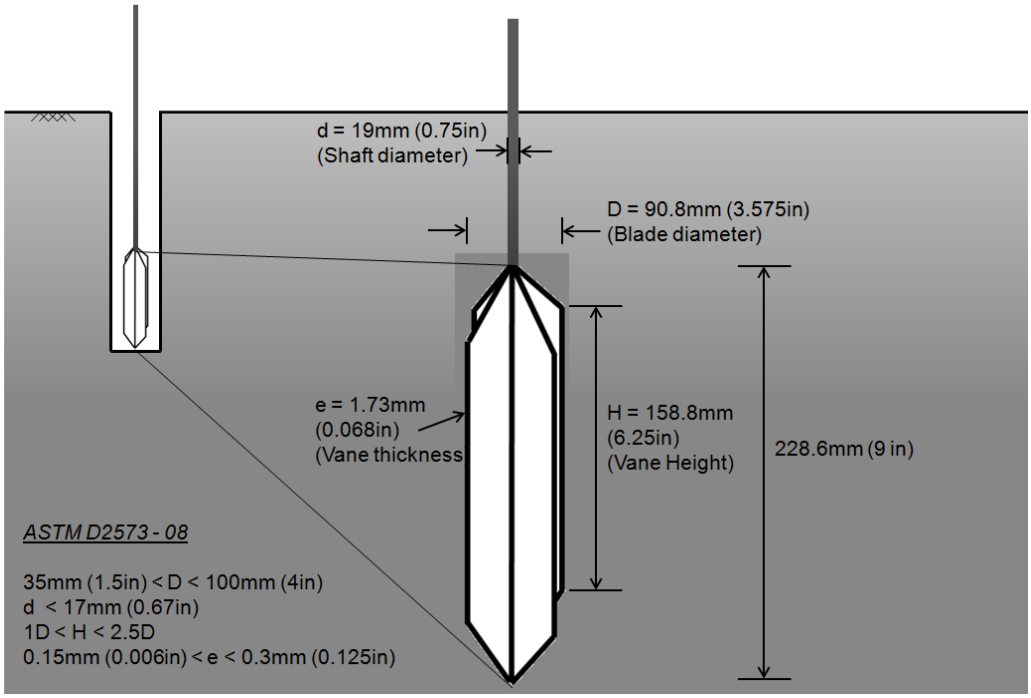

Figure B-19: Field vane geometry

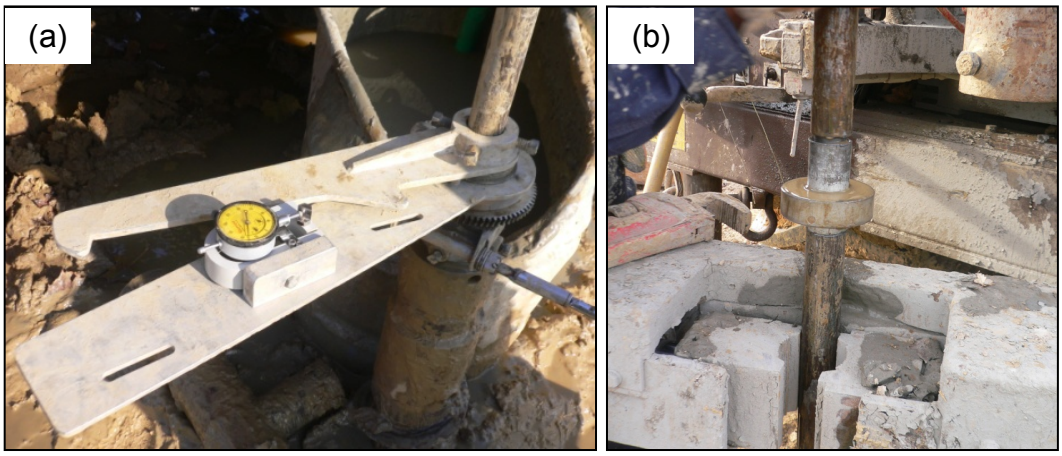

Figure B-20: (a) Force arm and sub mounted on the casing (b) ball bearing guide coupling

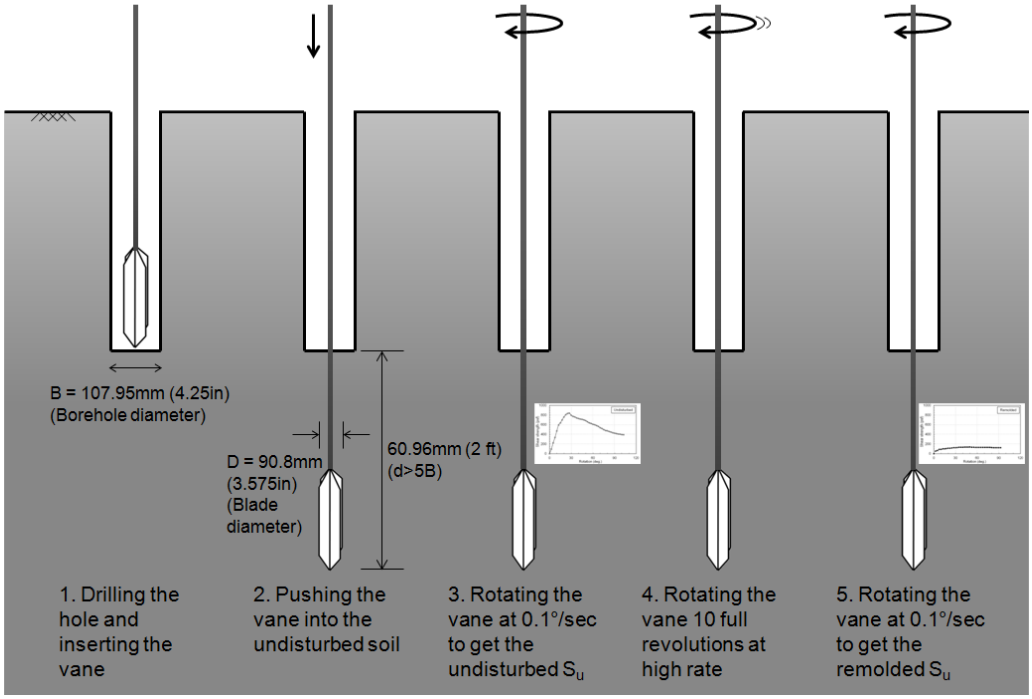

Figure B-21: Stages of the field vane shear test

B.6.4 Location of Groundwater Table

At the end of the field vane shear test, a 50.8 mm (2 in) diameter open pipe piezometer was installed with the perforated pipe located at the bottom of the marl layer between 9.1 m (30 ft) to 10.7 m (35 ft). Figure B-22 shows all the

details about the pipe installation, sand filter and bentonite sealant. The water was pumped twice from the tube and the water level was measured at different time intervals while rising in the tube to measure the hydraulic conductivity. A final reading was taken when the water level returned to the hydrostatic conditions (after two weeks), which was then monitored over a period of 16 days resulting in an average depth of the water table of 1.9 m (6.25 ft) below the ground surface.

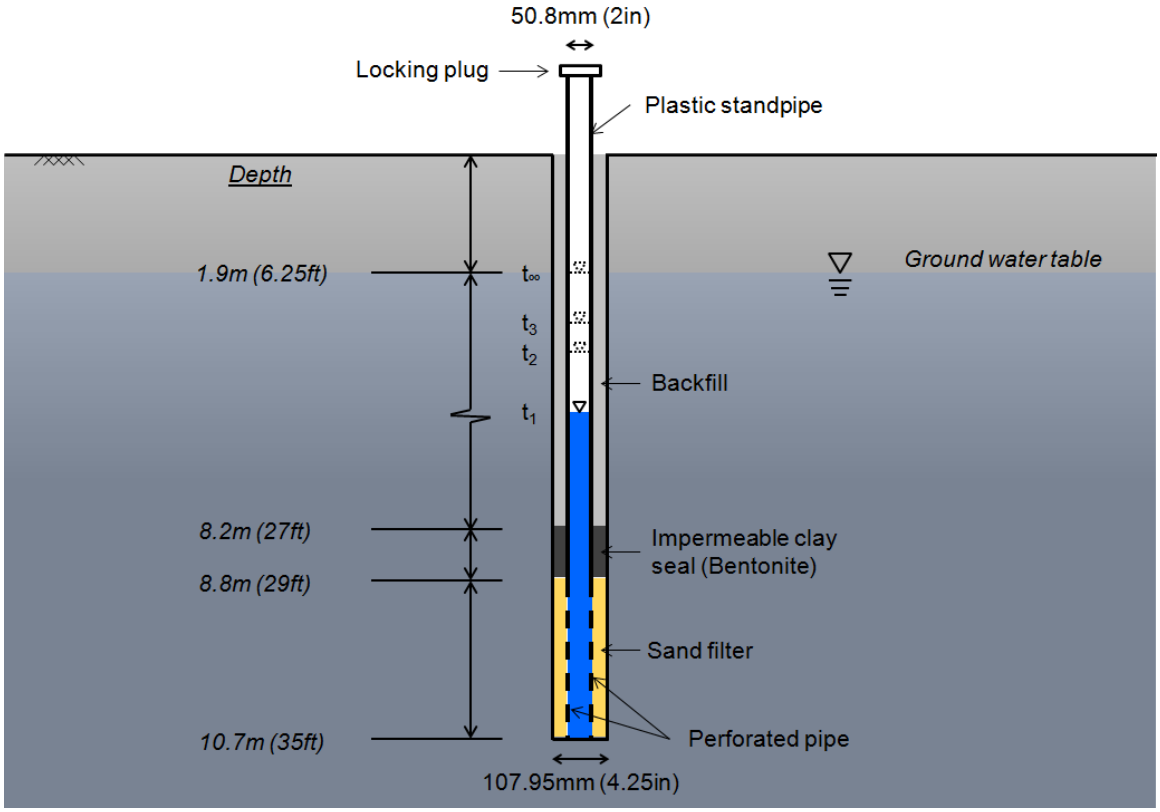

Figure B-22: Details of installation of open pipe piezometer

B.7 Field Tests Results

The following section presents the basic results for the field tests described in Section B.6. Further analysis of the field results is provided in APPENDIX E, which deals with integration of laboratory and field data.

B.7.1 Seismic Cone Penetration Test (SCPTu)

B.7.1.1 Seismic Piezocone Tests

The tip resistance, the skin friction and the pore water pressure variation with depth obtained from the CPT tests are summarized in Figure B-23. The figure shows the data for a total of seven CPTs (dashed gray lines) as well as the average values (continuous black line). Refer to APPENDIX G for the Piezocone penetration profiles obtained at different locations. High permeability layers, such as sand and silty sand layers, are characterized by a high tip resistance (q_t) and sleeve friction (f_s), and porewater pressure (u_2) close to the hydrostatic value (u_0). Low permeability layers, such as marl and soft clay layers, are characterized by low q_t and f_s, and high u_2. The average CPT results show that there is a very soft layer (q_t ~ 500 kPa and f_s ~ 7 kPa) at a depth ranging between 4.9 m (16 ft) and 11.6 m (38 ft). This is the marl layer from which undisturbed Shelby tubes were obtained.

B.7.1.2 Shear Wave Tests

Two CPTs (#4 and #5) were performed to derive the shear wave profiles with depth. At one-meter intervals, a shear wave was generated at the surface and the shear wave arrival times were recorded by a geophone located in the piezocone. Figure B-24 and Figure B-25 show the shear wave arrival traces for CPT#4 and CPT#5, respectively. The shear wave velocity was calculated from the arrival times as described in ASTM D7400-14 (ASTM, 2014), and the shear modulus was derived using the relation $G_{max} = \rho V_s^2$; where G_{max} is the shear modulus, ρ is the density of the soil (shown in Figure B-2), and V_s is the shear wave velocity. The resulting profiles are shown in Figure B-26. The figure shows that the marl layer (between 4.9 m (16 ft) and 11.6 m (38 ft)) has an average shear wave velocity equal to 155 m/s. Based on this value of V_s, the average shear modulus of the deposit is estimated to be approximately 40 MPa. These are values typical of soft clays (e.g. Boston Blue Clay (Weiler, 1988), Bothkennar clay (Shibuya et al., 1997), and Onsoy clay (Long & Lunne, 2003)).

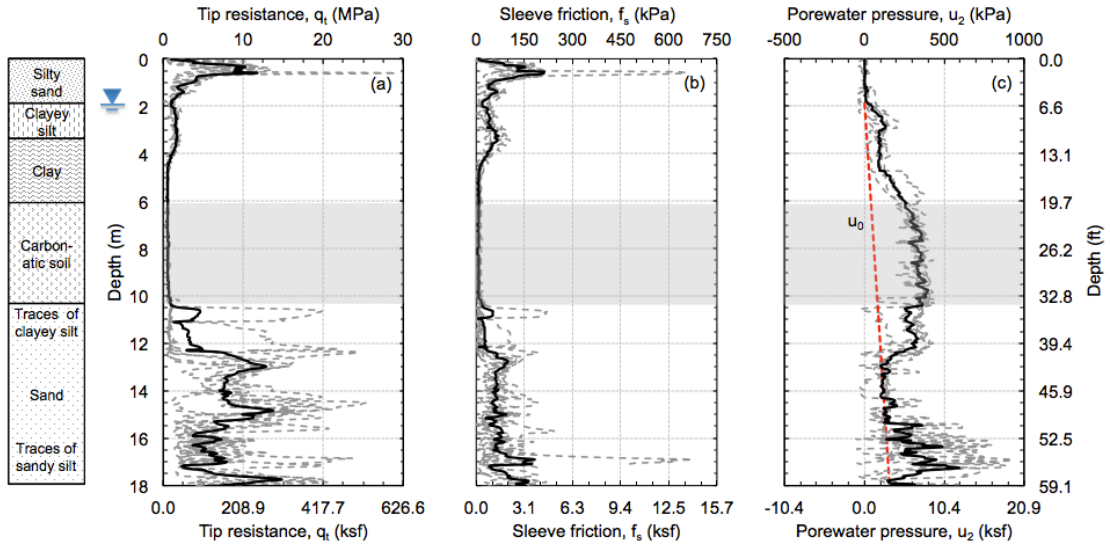

Figure B-23: CPT results: (a) tip resistance, (b) skin friction, and (c) porewater pressure versus depth

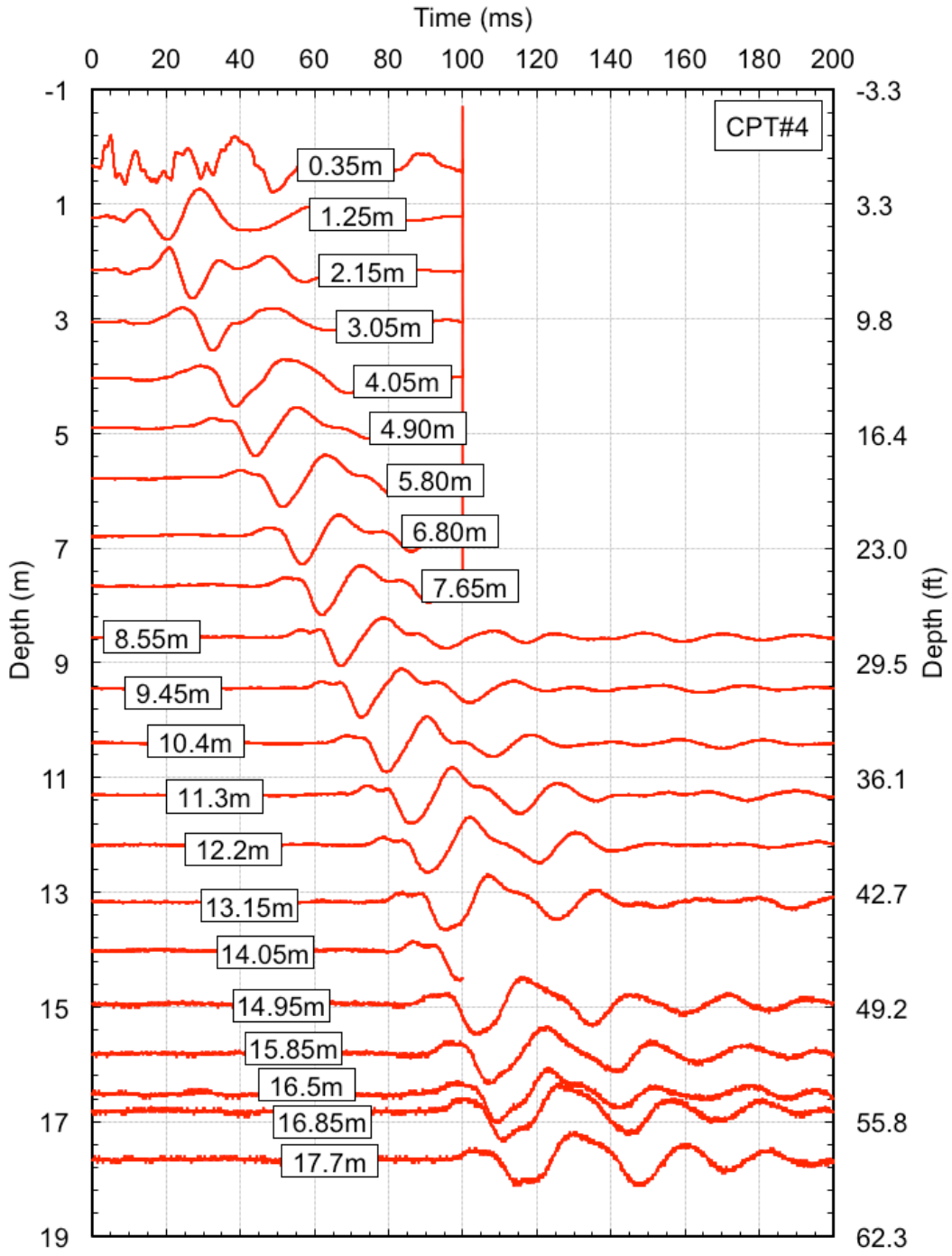

Figure B-24: Shear wave arrival traces for CPT#4

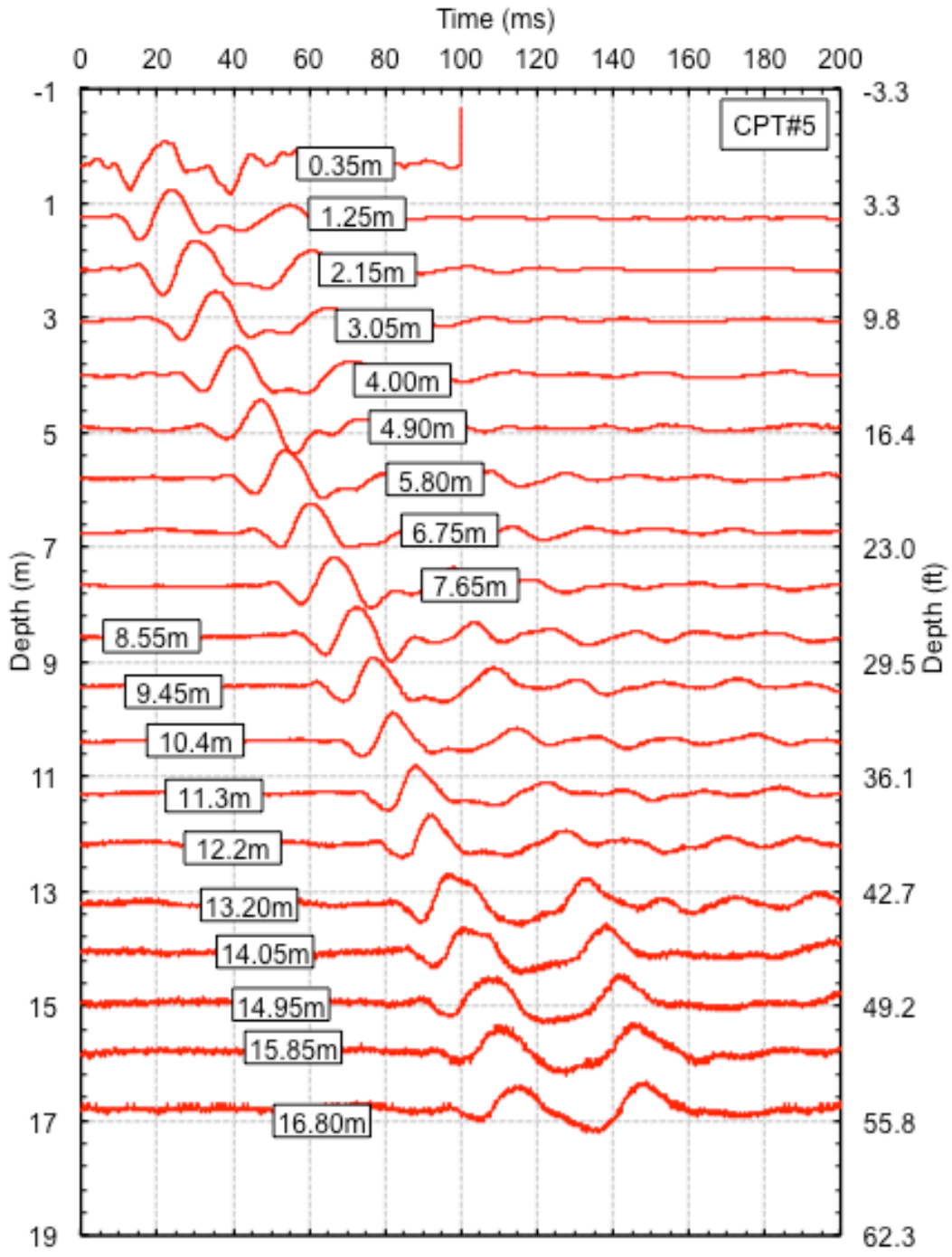

Figure B-25: Shear wave arrival traces for CPT#5

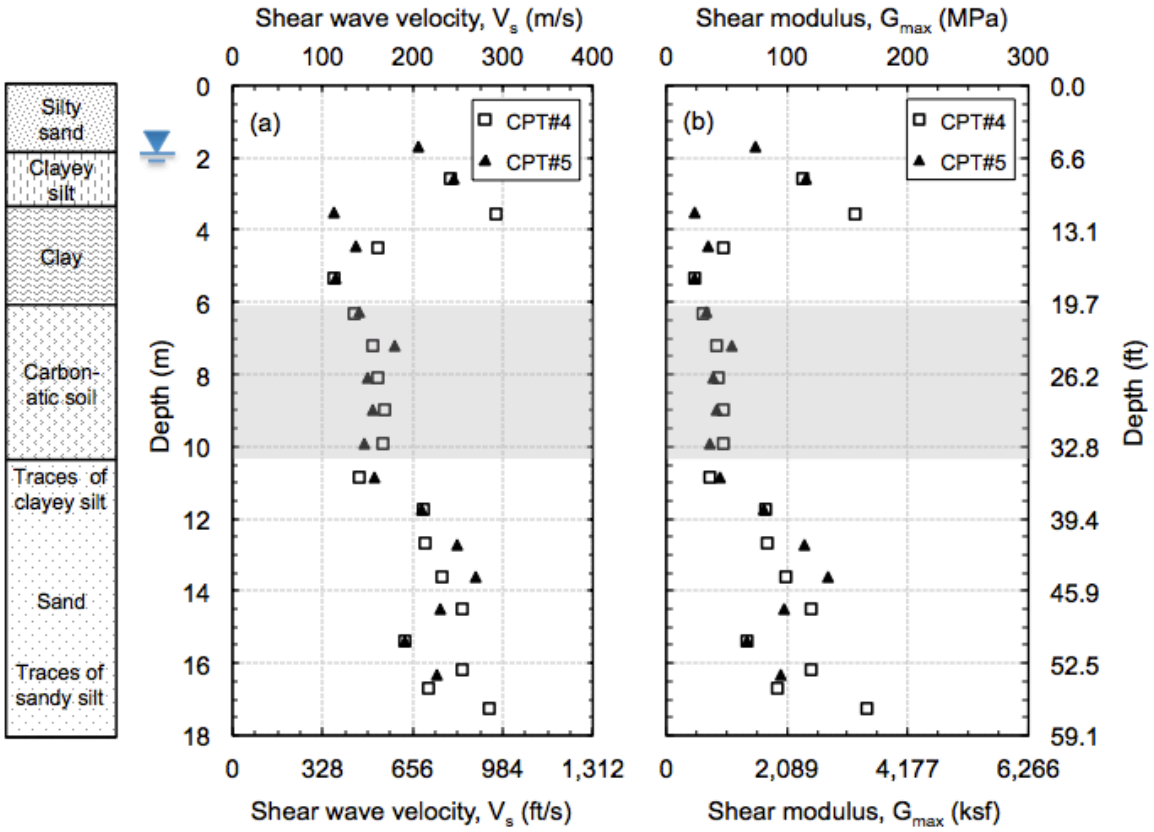

Figure B-26: (a) Shear wave velocity, and (b) shear modulus profiles with depth

B.7.2 Standard Penetration Test (SPT)

SPTs were performed on the soil above and below the marl layer for soil profiling. Figure B-27 summarizes the values of the standard penetration resistance (N-values) obtained as a function of depth based on ASTM D1586-11 (ASTM, 2011). The figure shows the SPT N-values obtained from five boreholes. The top silty sand layer (described in Figure B-2) has N-values ranging between 5 and 15; N-values decrease to 0-5 for the clayey silt layer and clay layer below. For the sand layer beneath marl, N-values range between 5 and 25.

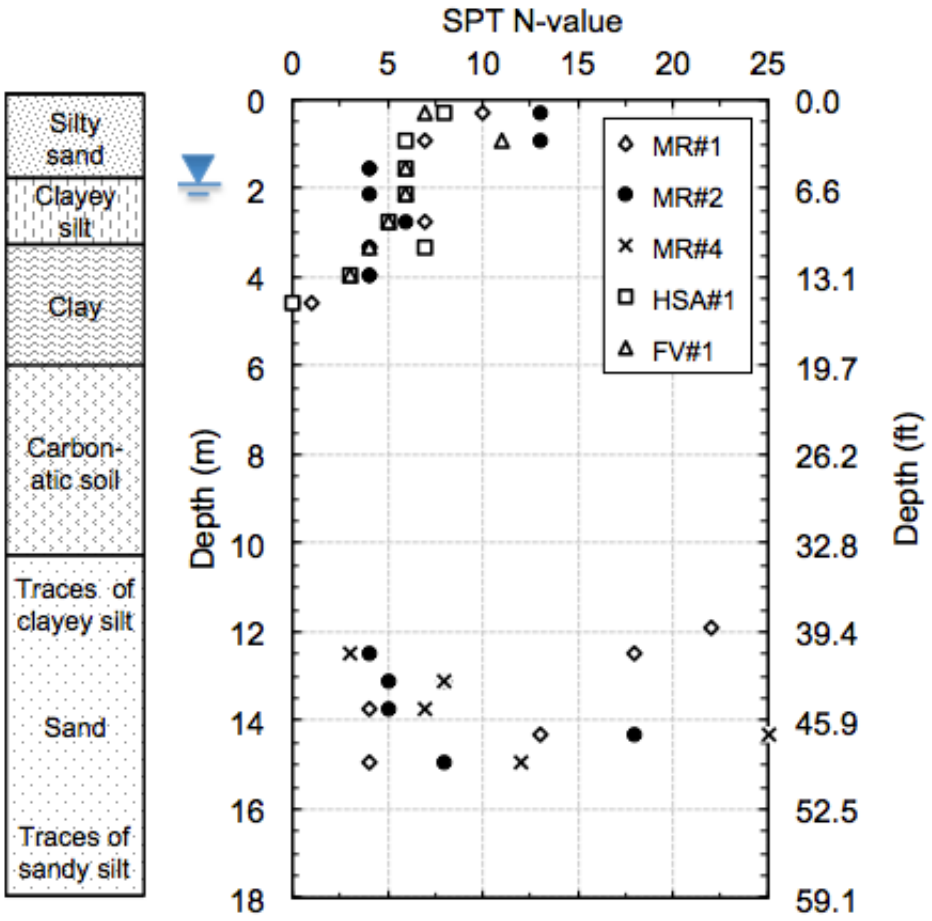

Figure B-27: Standard penetration resistance (N-values) with depth

B.7.3 Field Vane Shear Test

The field vane (FV) is widely used in-situ test for evaluating the undrained shear strength of soft soil deposits. Figure B-28 shows the curves of shear stress versus rotation for the test conducted at a depth between 6.7 m (22 ft) and 7.3 m (24 ft). The figure shows two curves: one for the first measurement from which the peak undisturbed shear strength is derived (presented in hollow squares); the second used to obtain the remolded shear strength (presented in solid squares). The peak and remolded strengths are computed using the relationship for both ends tapered vanes reported in ASTM D2573-08 (ASTM, 2008):

$$S_u(FV) = \frac{12\ T_{max}}{\pi\ D^2\ \left(\frac{D}{\cos(i_T)} + \frac{D}{\cos(i_B)} + 6\ H\right)} \qquad \text{(Eq. B-1)}$$

where S_u(FV) is the undrained shear strength from the vane (peak or remolded); T_{max} is the maximum value of measured torque; D is the vane diameter; H is the height of vane; and i_T and i_B are the angle of taper at vane top and bottom respectively (Figure B-19). The marl layer was tested every 0.6 m (2 ft) from 4.9 m (16 ft) to 11.6 m (38 ft). The data of undisturbed shear strength and remolded strength are summarized in Figure B-29(a). Refer to APPENDIX H for the complete results of all field vane tests conducted at various depths. Note that results of FV tests are not corrected for strain rate and anisotropy effects (Bjerrum, 1972); refer to Section E.2 for such correction.

Figure B-29(a) shows that the undrained shear strength varies between 25 kPa and 50 kPa, which is typical for soft clays. The soil sensitivity with depth is shown in Figure B-29(b); this parameter is calculated from the ratio between the peak and the remolded undrained shear strength measurements. The figure shows that the sensitivity value of marl is about 5.0 on average, with the exception of one test (FV5) conducted at depth ~7.8 m (25.5 ft); it is believed that the lower S_u(FV) ~18 kPa and the higher sensitivity ~10 at this depth are caused by the presence of a more sensitive soil within the marl layer (further discussion about this is presented in Section E.2). Thus the marl deposit can be considered a “sensitive” soil based on the sensitivity scale reported by Skempton and Northey (1952) or a “very sensitive” soil based on Bjerrum (1954). Note that field vane test is not applicable for sandy soils and the last two tests conducted in the bottom sand layer should be regarded with caution.

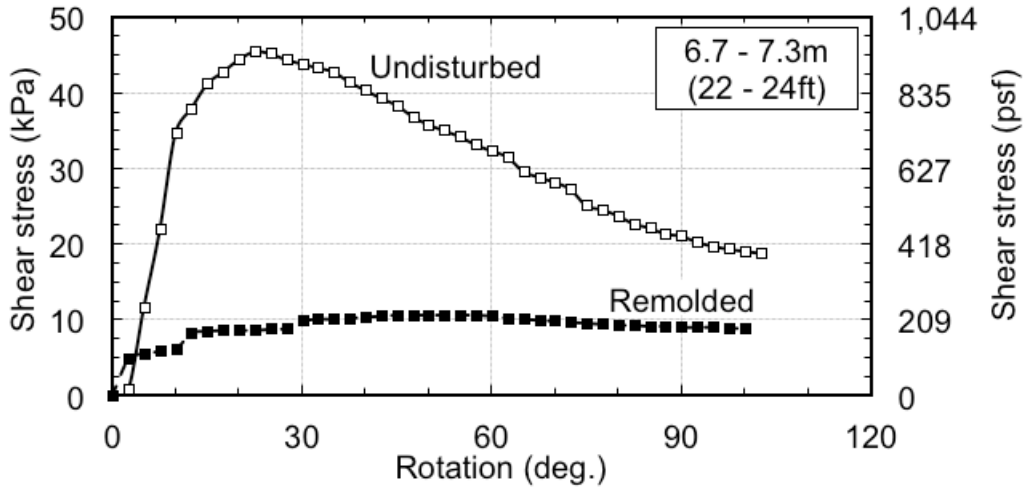

Figure B-28: Results of field vane shear test (FV4) conducted at ~7.2 m (23.5 ft)

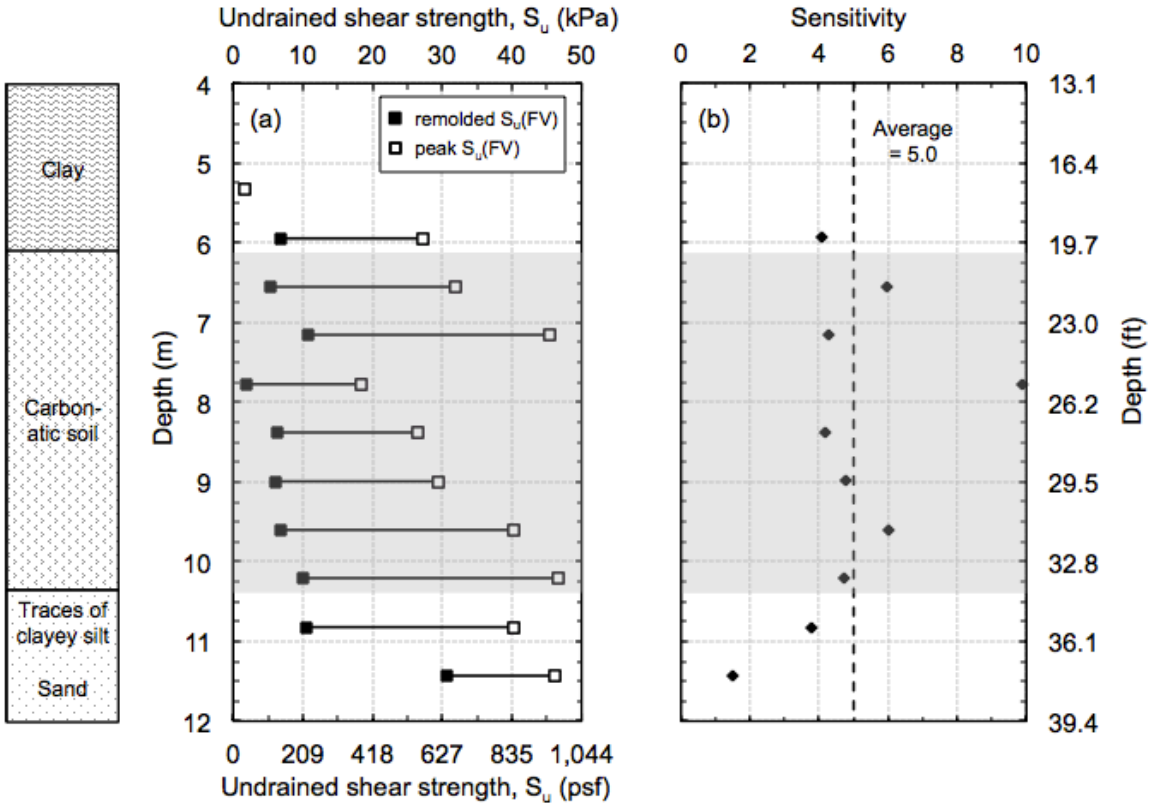

Figure B-29: Profiles of (a) field vane undrained shear strength and (b) soil sensitivity with depth

Appendix C. Index Properties, Mineralogy, and Microstructure

C.1 Introduction

From the interpretation of the field data collected, marl was identified at depths between 6.1 m (20 ft) and 10.4 m (34 ft). A full laboratory testing program was performed on Shelby tube samples obtained from this layer. The program consisted of tests aimed at characterizing: (i) the index properties; (ii) the mineralogy and microstructure; and (iii) the consolidation, and (iv) shear strength behavior of this layer. The first two are presented in this appendix whereas the last two are discussed in APPENDIX D. The soil samples obtained from the marl layer were not homogenous as was initially anticipated, but were composed of two types of soils. A brief description of these two soils is provided in Section C.2. Section C.3 presents and discusses the various index tests performed for this investigation. Section C.4 provides a detailed evaluation of the results from mineralogical analysis and microstructure.

C.2 Description of Soils Within the Marl Deposit

Examination of the soil samples obtained from the marl layer revealed that the marl layer was not homogenous as was initially anticipated, but was formed by two types of soils with distinct properties that repeated in horizontal thin layers. These two soils were identified after starting the laboratory tests, and are herein referred to as “soil M” and “soil C”. This denomination was selected based on the fact that soil M has relatively more silt, hence the letter “M”; whereas soil C has relatively more clay, hence the letter “C” (as reported in Section C.3.2). These two types of soils showed distinct index and engineering properties, which created the necessity to carefully characterize each soil separately and examine the fundamental difference(s) between them. Moreover, as discussed below, both soils are characterized by very high calcium carbonate contents (over 55%,

and close to 40%). Soil M was found to be more prominent throughout the depth of the deposit.

Although the field exploration showed the presence of a very soft layer between 6.1 m (20 ft) and 10.4 m (34 ft), it failed to detect the presence of the two types of soils (i.e. soil M and soil C). A more detailed description of the two soils is presented in Section C.3.

Figure C-1 shows soil samples composed from both soil M and soil C, with a clear difference between the color, texture and presence of shells. Soil C was found in thin layers of thicknesses ranging between a fraction of an inch (< 2.54 cm) and few inches, whereas soil M was found in thicker layers and it formed the majority of the marl deposit.

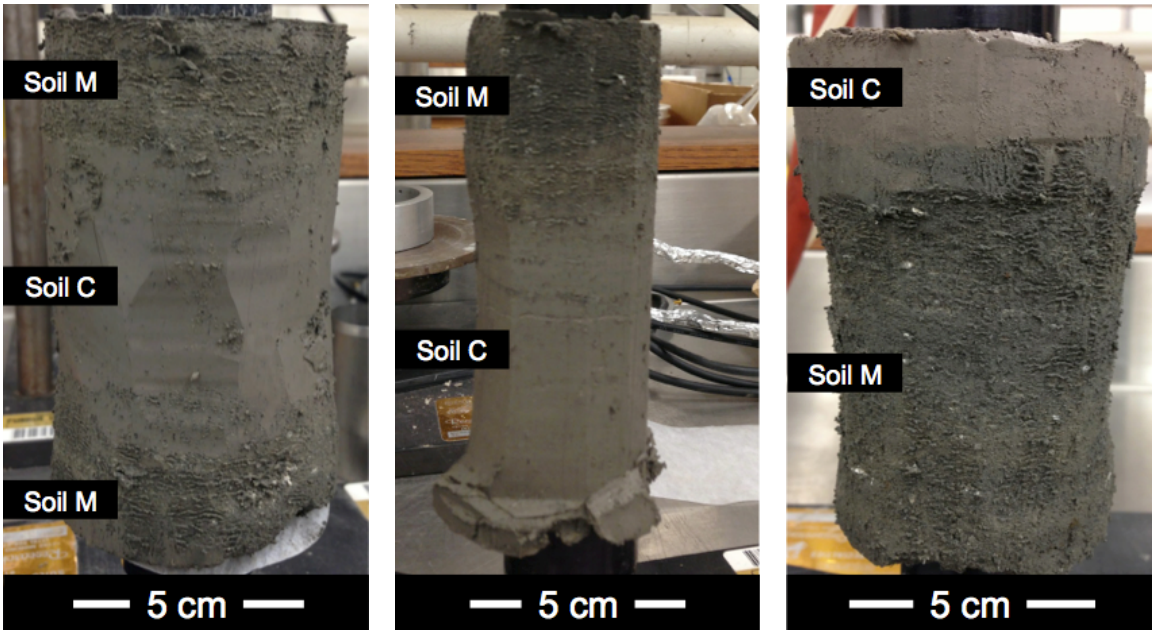

Figure C-1: Soil samples showing layers of soil M and soil C

C.3 Index Properties

Index tests were conducted on a total of 28 soil samples obtained from different depths to classify the soil present in the marl deposit and derive parameters that correlate with the engineering behavior. Index properties measured included: organic content, calcium carbonate content, Atterberg limits, natural water

content, particle size distribution, specific gravity, void ratio, total unit weight, degree of saturation, salt concentration, and pH. In most cases the index tests were performed on trimmings from engineering tests. Key index properties for soils M and C are summarized in Table C-1**.** The table shows that soil M is characterized by a lower specific gravity and unit weight, but has higher porosity, water content, silt content, and $CaCO_3$ content. In particular, the average $CaCO_3$ content exceeds 55% for soil M and is close to 40% for soil C. Based on these values the two soils would be considered carbonatic soils. A characteristic specific to soil M is the presence of shells, which, as discussed below, is responsible for a higher void ratio.

Table C-1: Summary of index properties

	Soil M		Soil C	
	Range	Mean ± SD[1]	Range	Mean ± SD
Organic content (%)	2.0 – 4.3	3.0 ± 0.6	1.7 – 3.2	2.5 ± 0.4
$CaCO_3$ content (%)	35.9 – 66.8	55.2 ± 7.6	33.7 – 48.8	38.1 ± 4.5
Water content, w_n (%)	50.5 – 68.5	61.6 ± 5.8	36.6 – 52.2	44.3 ± 5.7
Plastic limit, PL (%)	29.0 – 40.6	34.4 ± 3.4	18.8 – 25.5	21.6 ± 2.1
Liquid limit, LL (%)	61.7 – 78.8	67.4 ± 5.0	40.1 – 53.7	48.3 ± 4.4
Silt content (%)	69.0 – 82.0	76.7 ± 3.9	54.0 – 66.0	60.6 ± 5.2
Clay content (%)	15.0 – 25.0	19.0 ± 3.4	33.0 – 45.0	38.7 ± 4.9
Specific gravity, G_s	2.68 – 2.76	2.71 ± 0.02	2.76 – 2.82	2.78 ± 0.02
Void ratio, e	1.4 – 1.9	1.7 ± 0.2	1.1 – 1.5	1.3 ± 0.1
Total unit weight, γ_t (kN/m^3)	15.4 – 16.8	15.9 ± 0.4	16.8 – 18.3	17.5 ± 0.5
Degree of saturation, S_i (%)	95.3 – 100	97.9 ± 1.4	93.2 – 100	97.9 ± 1.8
Salt concentration (g/l)	2.1 – 3.8	3.0 ± 0.5	2.2 – 5.1	3.6 ± 1.2
Salt concentration (g/kg)	1.4 – 2.2	1.9 ± 0.2	0.9 – 1.9	1.5 ± 0.4
pH	7.5 – 7.9	7.8 ± 0.1	7.6 – 7.9	7.8 ± 0.1

[1]SD: Standard Deviation

Overall, the presence of these two soil types provides the opportunity to essentially study two types of marls, and explore, in particular, the effect of shells, mineral composition, and carbonate content on both index and engineering properties. The following subsections will discuss the results of the various index tests in greater detail.

C.3.1 Organic Content and Calcium Carbonate Content

The organic content and calcium carbonate content were determined using the "sequential" loss on ignition (LOI) method proposed by Jung et al. (2011). This method consists of heating the soil up to 455°C for six hours, in accordance with AASHTO T267-86 (AASHTO, 2008); the corresponding mass loss is used to estimate the organic content. The soil is then heated up to 800°C for six hours and the corresponding mass loss is used to determine the calcium carbonate content. The measurement is based on the fact that calcium carbonate decomposes into calcium oxide (CaO) and carbon dioxide (CO_2) in the range of 650°C to 800°C. The reduction in mass due to the release of CO_2 can be used to infer the calcium carbonate content. Note that the value obtained with the above method is not the percentage of calcium carbonate ($CaCO_3$), but the percentage of calcium carbonate equivalent (C.C.E.). This is due to the fact that other types of carbonates might be present in the soil such as dolomite ($CaMg(CO_3)_2$), as illustrated by the mineralogical analysis (Section C.4.1.3), which also decomposes in the range of 650°C to 800°C. In other words, the $CaCO_3$ presented in this thesis represents the amount of all carbonates in terms of C.C.E.

Figure C-2(a) and Figure C-2(b) show the organic content and the calcium carbonate content profiles for the marl deposit, respectively. Hollow black circles correspond to soil M whereas solid blue circles correspond to soil C. Low values of organic content were measured for all the soils tested. The LOI generally falls below 4% (Figure C-2 (a)), with no clear difference between soil M and soil C. Huang et al. (2012) reported that the LOI often overestimates the true organic

content when applied to soils with organic content matter content less than ~10%. Hence, the low values of LOI (< 4%) obtained in this study did not warrant further testing to refine the organic content.

All specimens have relatively high calcium carbonate content ranging between 34% and 67%, which is typical for marl soils. The calcium carbonate content was the basis for distinguishing between soil M and soil C. As shown in Figure C-2(b), soil C has an average calcium carbonate content of 38.1% ± 4.5SD, while soil M has an average calcium carbonate content of 55.2% ± 7.6SD. The higher calcium carbonate content in soil M could be partially caused by the presence of shells; which are composed of aragonite ($CaCO_3$) as well as the higher carbonate content present in the soil matrix of soil M, as illustrated by the mineralogical analysis (Section C.4.1.3).

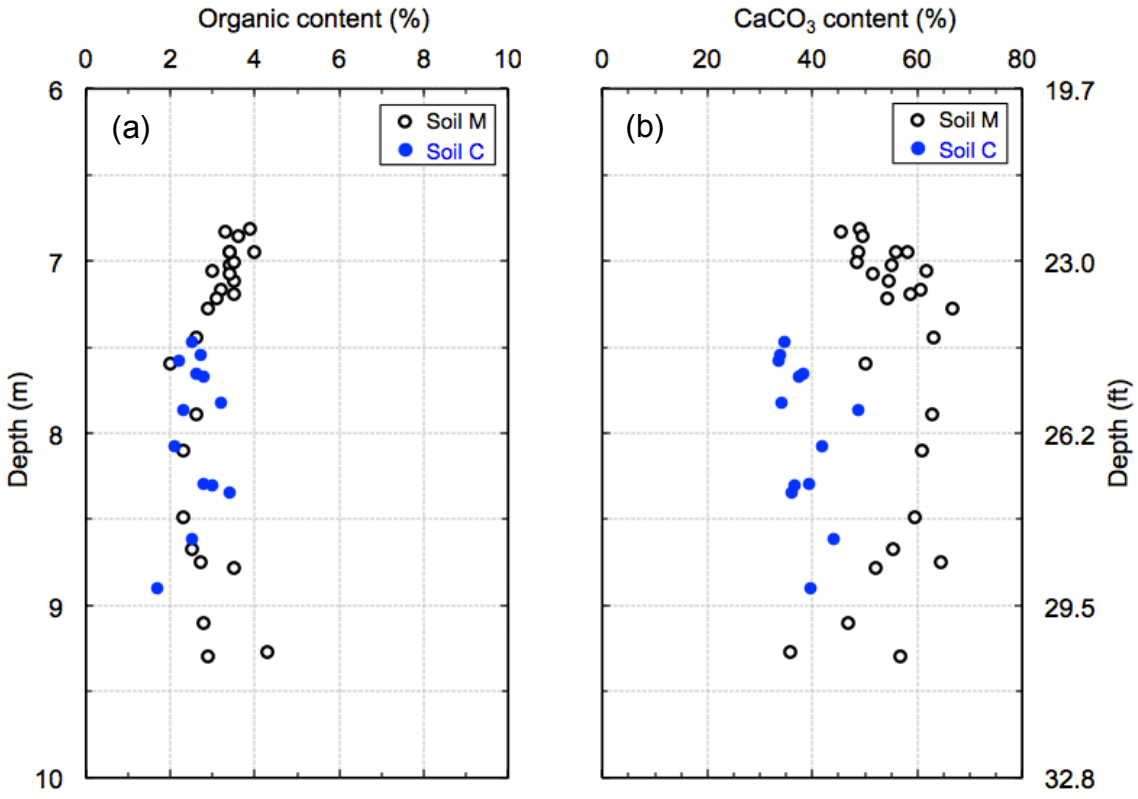

Figure C-2: (a) Organic content and (b) calcium carbonate content profiles for marl

C.3.2 Atterberg Limits, Natural Water Content and Particle Size Distribution

Atterberg limit tests were performed in accordance with ASTM D4318-10 (ASTM, 2010). The only deviation from the standard is the order of performing the determination of the blow counts at various water contents: while the standard suggests a dry to wet procedure (i.e. water is added to the soil before each blow count determination), a wet to dry procedure (using a fan to dry the soil) is instead recommended. It is acknowledged that the two procedures may cause slight differences in the results of liquid limit; however, the use of the latter procedure is reported to generate more repeatable data (Germaine & Germaine, 2009). Most of the tests were performed on trimmings from engineering tests.

The natural water contents are calculated, at the end of each engineering test, for the entire test specimen based on phase relationships, which use the initial wet mass and the final mass of solids. Water contents were also measured from the trimmings of each engineering test as part of the procedure for Atterberg limits testing. During the trimming process, sufficient trimmings were immediately collected for water content determination prior to storage of the soil for subsequent Atterberg limit tests in order to avoid soil drying. There was no significant difference between the water contents measured from the trimmings of the engineering tests and those calculated at the end of the test.

Figure C-3 plots depth versus plastic limit (PL), natural water content (w_n), and liquid limit (LL). The water contents are shown as data points (hollow black circles correspond to soil M and solid blue circles correspond to soil C) and the Atterberg limits are represented by lines (plastic limit represented by the left end of the line; liquid limit represented by the right end of the line). The data in Figure C-3 show the following:

1) In general, soil M has a natural water content higher than soil C. The average water content is 61.6% ± 5.8SD for soil M and 44.3% ± 5.7SD for soil C.

2) The Atterberg limits for soil M are consistently higher than the ones for soil C (soil M: mean PL = 34.4% ± 3.4SD and mean LL = 67.4% ± 5.0SD; soil C: mean PL = 21.6% ± 2.1SD and mean LL = 48.3% ± 4.4SD)
3) Marl has liquidity index (LI) values typically close to one (mean LI = 0.8 ± 0.2SD), which is evidence of the soil's high sensitivity, with no clear difference between soil M and soil C.
4) There is no clear variation of Atterberg limits or water contents with depth.

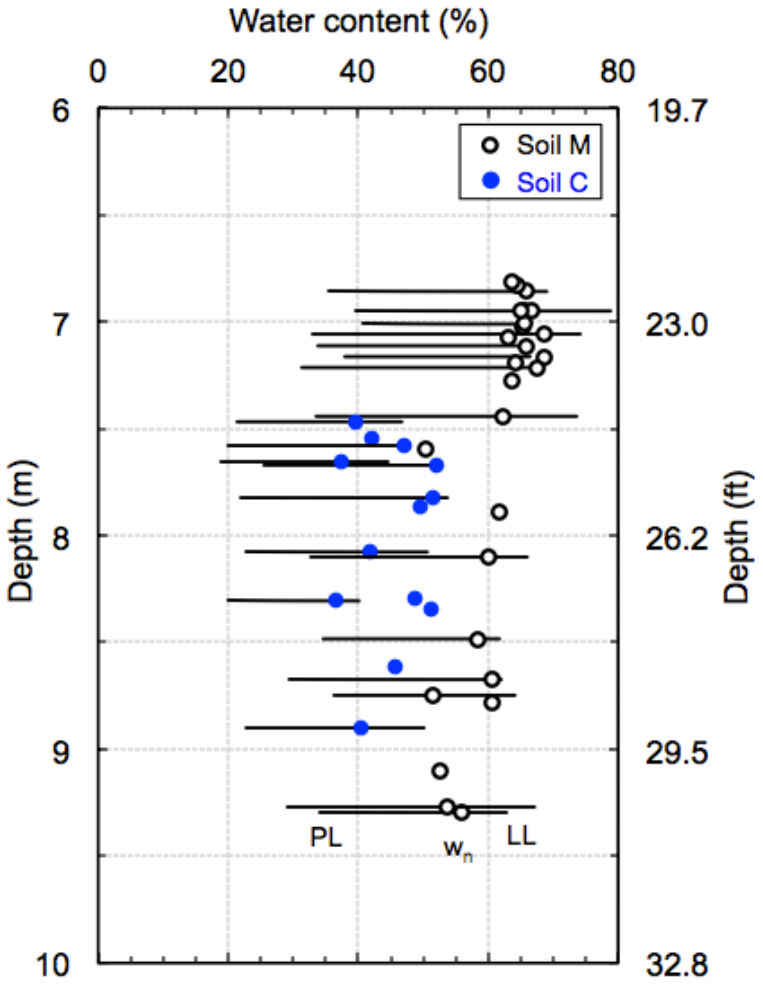

Figure C-3: Results of Atterberg limits for marl

The liquid limit and the plasticity index of all the specimens from the marl layer are plotted on the plasticity chart in Figure C-4. For the most part, Soil M plots

below the A-line and is thus classified as an elastic silt (MH) according to the unified soil classification system (USCS), whereas soil C plots above the A-line and is classified as a lean clay (CL).

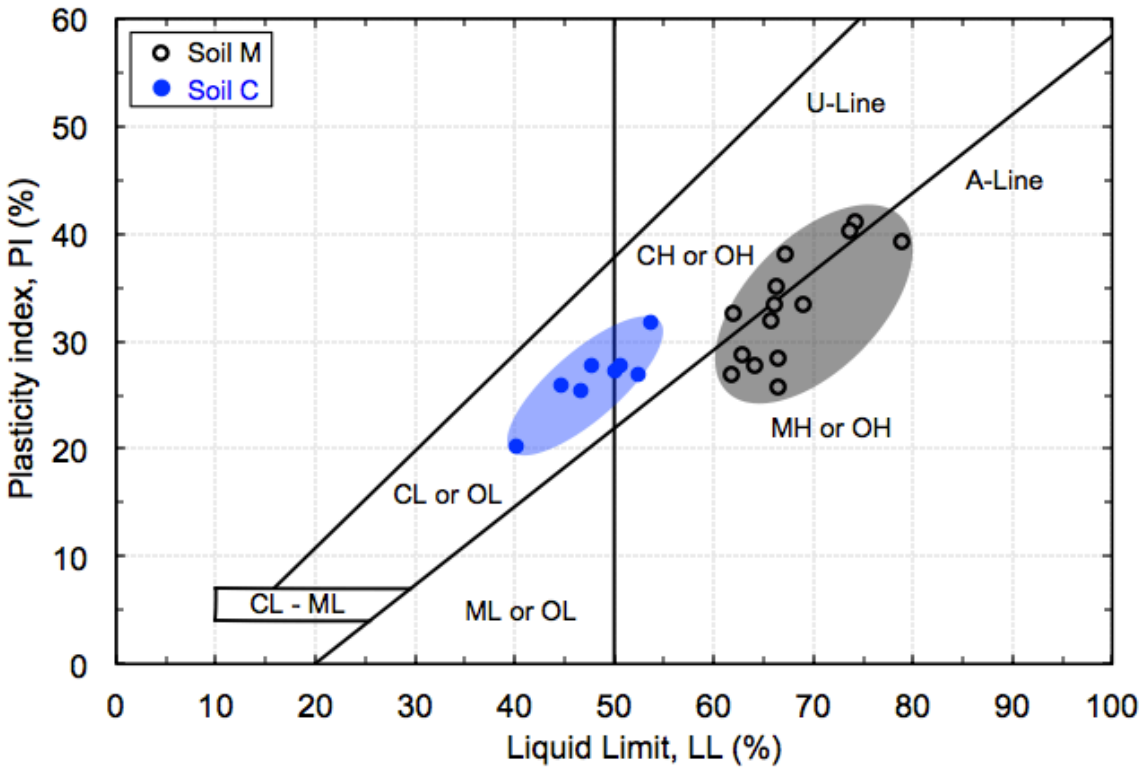

Figure C-4: Plasticity chart with data from marl

Figure C-5 shows the particle size distribution curves obtained from hydrometer tests performed in accordance with ASTM D422-63 (ASTM, 2007). Both soils have a fine fraction (less than 75 μm) greater than 96%. The small percentage of sand-size particles (greater than 75 μm) found in soil M (< 4%) consists mainly of shells. The figure shows that soil M and soil C fall on two distinct bands. The average percentage of clay size particles (less than 2 μm) is 19.0% ± 3.4SD for soil M, which is lower than soil C (38.7% ± 4.9SD).

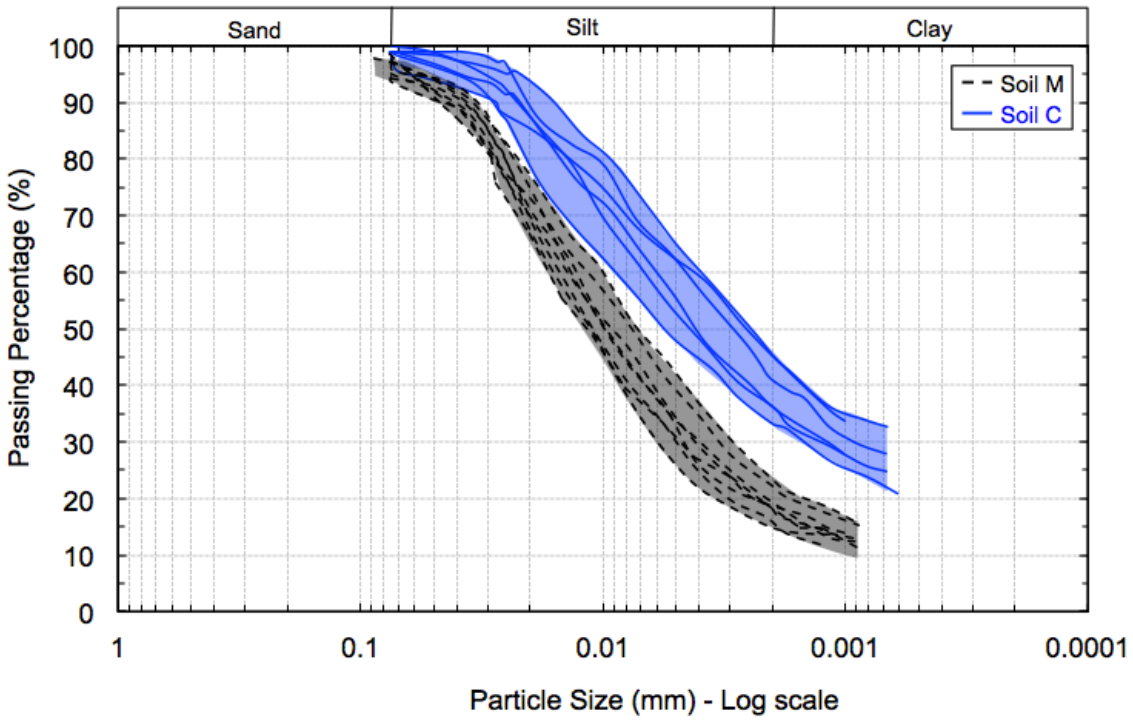

Figure C-5: Results of particle size analyses on marl

The higher plasticity of soil M is not consistent with the typical trends reported in the literature of increasing LL and PI with higher clay content. It is also inconsistent with the data reported by Lamas et al. (2002) for other carbonatic fine-grained soils, which show that LL and PI decrease with increasing calcium carbonate. This difference can be ascribed to variations in the mineralogy of the clay fraction of the two soils, as both the type and amount of clay in a soil influence the Atterberg limits. The mineralogical analysis presented in Section C.4.1 shows that the smectite content in the bulk soil is about 10% for soil M and about 2% for soil C. The large difference in the smectite content between soil M and soil C may explain the discrepancy observed in the Atterberg limits, as soils rich in smectite have higher LL and PI, due to their higher water sorption capacity caused by the higher specific surface area (De Kimpe et al., 1979).

C.3.3 Specific Gravity and Void Ratio

Specific gravity tests were performed based on ASTM D854-14 (ASTM, 2014) on trimmings from engineering tests. The void ration was calculated for the entire test specimen based on phase relationships.

Figure C-6 shows the variation with depth of specific gravity (G_s) and void ratio (e) for marl. For most part, soil M shows a specific gravity value lower than soil C (Figure C-6(a)). The average specific gravity for soil M is 2.71% ± 0.02SD, while for soil C it is 2.78% ± 0.02SD.

The initial void ratio for soil M show a decreasing trend with depth (Figure C-6(b)) ranging between 1.4 and 1.9 (mean e = 1.7 ± 0.2SD), which is expected due to the increase in confinement. This trend was not observed for soil C due to the limited number of data points and the significant scatter; however, its average void ratio (mean e = 1.3 ± 0.1SD) is lower than that of soil M.

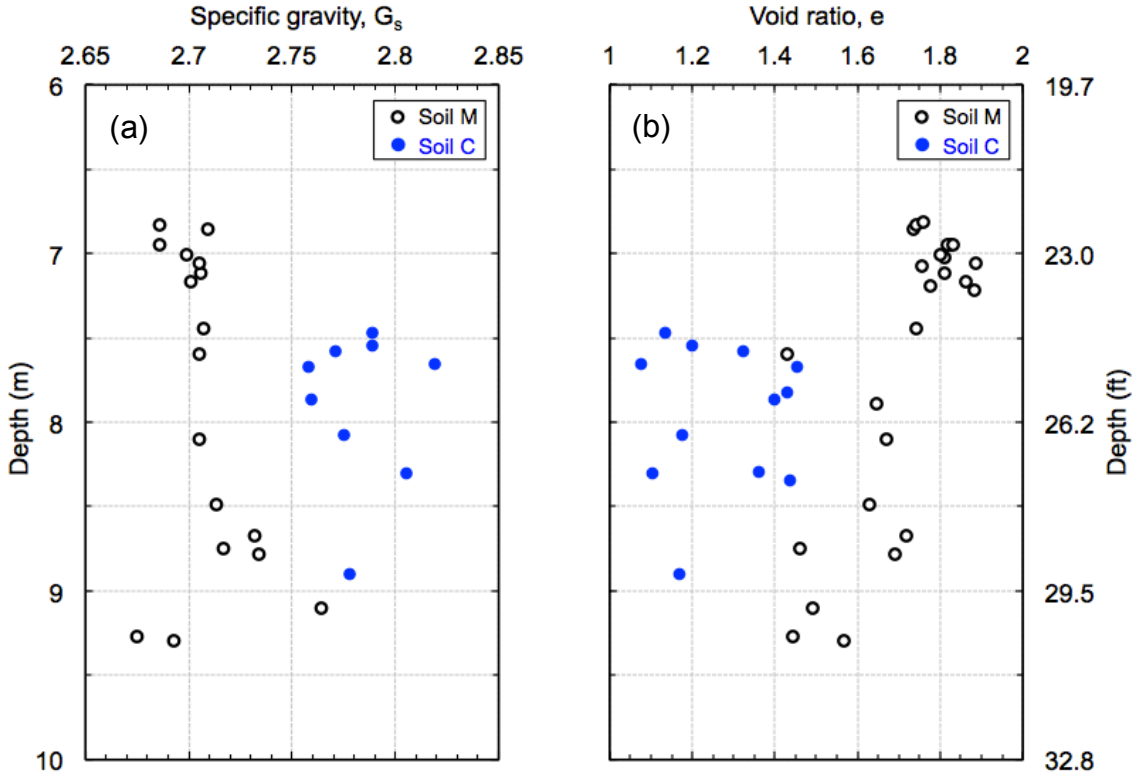

Figure C-6: (a) Specific gravity and (b) void ratio profiles for marl

C.3.4 Total Unit Weight and Degree of Saturation

The total unit weight (γ_t) of the marl layer was measured for specimens used for laboratory consolidation and triaxial test programs. At the end of each engineering test, the initial degree of saturation (S_i) is calculated for the entire test specimen based on phase relationships, which use the initial mass and volume of the test specimen.

Figure C-7 shows the variation with depth of the total unit weight (γ_t), and the initial degree of saturation (S_i). Again a clear difference can be observed between soil M and soil C. As shown in Figure C-7(a), the values of the total unit weight for soil M increase with depth (γ_t = 15.4-16.8 kN/m^3; mean γ_t = 15.9 kN/m^3 ± 0.4SD) and are at the low end of the range typically reported for fine grained soils (Germaine & Germaine, 2009), while the values for soil C are higher (γ_t = 16.8-18.3 kN/m^3; mean γ_t = 17.5 kN/m^3 ± 0.5SD)). This is in agreement with the observation of a lower void ration for soil C than for soil M. In general, S_i was greater than 93% (Figure C-7(b)) with an average of 97.9% ± 1.6SD indicating that the in situ marl deposit can be treated as fully saturated.

The average values of total unit weight for soil M and soil C are consistent with the average natural water contents determined from phase relationships at the end of each engineering test. For soil M, the average natural water content was 61.6% ± 5.8SD (Figure C-3), which translates into a total unit weight of 15.9 kN/m^3. For soil C, the average natural water content was 44.3% ± 5.7SD (Figure C-3), which translates into a total unit weight of 17.4 kN/m^3. These calculations used a degree of saturation of 98% and a specific gravity of 2.71 and 2.78 for soil M and soil C, respectively.

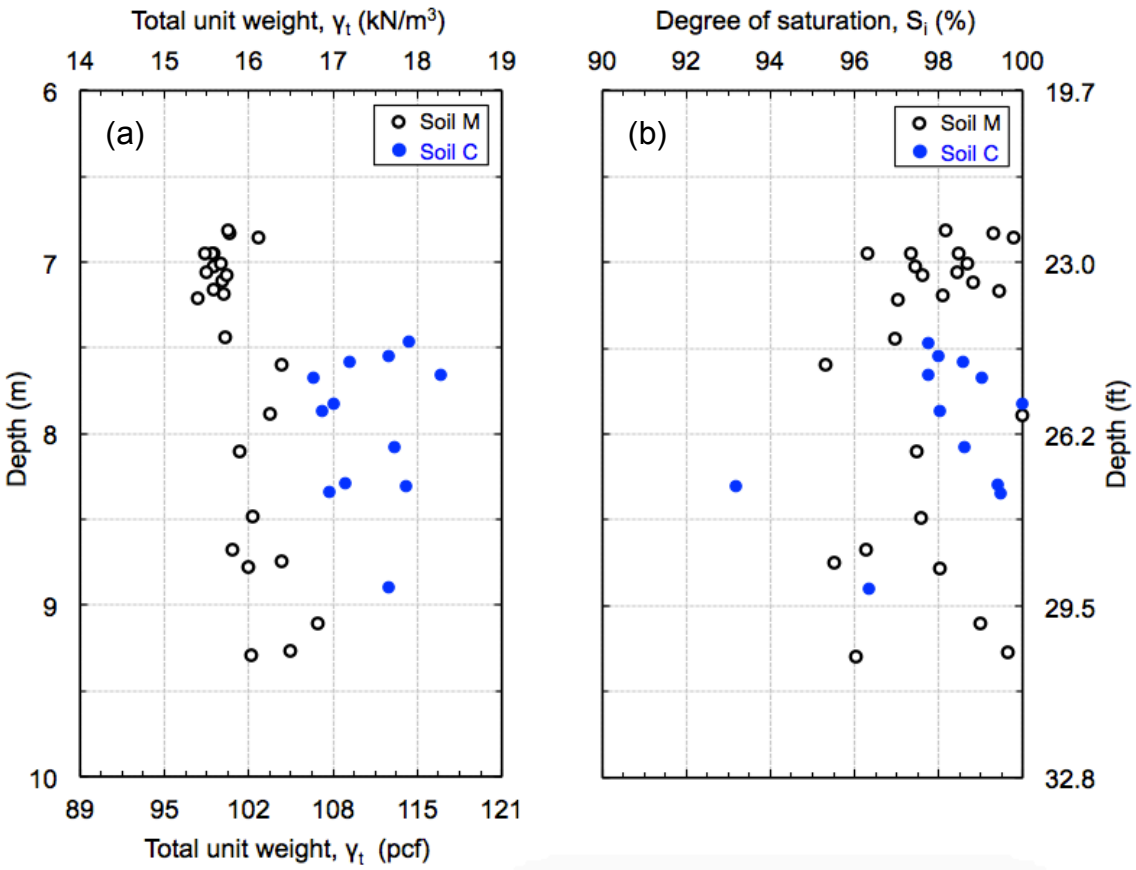

Figure C-7: (a) Total unit weight and (b) initial degree of saturation profiles for marl

C.3.5 Salt Concentration and pH

The pH analysis was performed in general accordance with ASTM D4972-13 (ASTM, 2013) on trimmings from engineering tests. Each sample was tested using a distilled water solution and a dilute salt solution of 0.01 M calcium chloride ($CaCl_2$). The premise of using a salt solution is to minimize the effect of natural salts in the soil on the pH measurements (Germaine & Germaine, 2009). For each soil, two 10 gr air dried samples were prepared for pH measurements. One of the samples were mixed with 10 mL of water and the other with 10 mL of the 0.01 M $CaCl_2$ solution and the mixture was shaken with a reciprocating shaker (~228 excursions per minute) for 20 minutes. The samples were then placed in a centrifuge and ran at about 2500 rpm for 20 minutes.

The clear supernatant liquid was decanted from the centrifuge tube into a 10 ml glass beaker and the pH was measured while the extract was being mixed using

a magnetic jar mixer. All measurements were performed at room temperature (21 to 25°C) with an Accumet™ Excel XL50 pH/mV/Temperature/ISE/Conductivity Meter. This device has the ability to account for temperature changes (i.e. Automatic temperature correction). Calibration of the measuring system was done every 8 hours using the buffer solutions with pH values of 4, 7, and 10.

The salt concentration was measured following the procedure provided by Germaine and Germaine (2009). The method estimates the soluble salts present in the soil pore fluid from the measurement of the electrical conductivity of the supernatant liquid. All tests were conducted on wet samples from trimmings of the engineering tests. The test should not be performed on dried material, because drying will transport salts to the boundaries of the specimen, making it difficult to obtain representative samples (Germaine & Germaine, 2009). An equivalent of 13 g dry mass of the soil was mixed with 15 ml of distilled water and the mixture was shaken with a reciprocating shaker (~228 excursions per minute) for 20 minutes. The samples were then placed in a centrifuge and ran at about 2500 rpm for 20 minutes.

The electrical conductivity (EC) of the supernatant liquid was measured at room temperature (21 to 25°C) with an Accumet™ Excel XL50 pH/mV/Temperature/ISE/Conductivity Meter. Calibration of the measuring system was done every 8 hours using the buffer solution of KCl (single point calibration). The soluble salt concentration present in the supernatant was estimated from the measured EC using a sodium chloride (NaCl) calibration curve. The salt concentration is then corrected to account for the difference between the water content of the soil in the centrifuge tube and the natural water content w_n.

Figure C-8 plots depth versus salt concentration and pH. The salt concentration is expressed as equivalent NaCl concentration both in grams per liter of pore fluid and grams per kilogram of dry soil. The pH values obtained using a distilled water solution and a dilute salt solution of 0.01 M calcium chloride ($CaCl_2$)

yielded very similar results and the data points shown in Figure C-8 correspond to the average values.

In general, there is no clear variation of salt concentration or pH with depth. The pH remains neutral, ranging from 7.5 to 7.9 (mean pH = 7.8 ± 0.1SD), through the marl deposit, with no clear difference between soil M and soil C.

The salt concentration shows some scatter in the data with values ranging from 2.1 g/l to 5.1 g/l and a collective average value equals to 3.2 g/l ± 0.8SD; significantly lower than that of seawater (35 g/l). These values are very close to the ones obtained by Fernandez (1994) on Mexico City Clay: pH ranges from 7.2 to 9.1 and salinity ranges from 1 g/l to 6 g/l. However, when comparing the salt concentration in grams per kilogram of dry soil, soil M has slightly higher values than soil C (soil M: mean salt concentration = 1.9 g/kg ± 0.2SD and soil C: mean salt concentration = 1.5 g/kg ± 0.4SD), which might be due to the fact that soil M has higher water content.

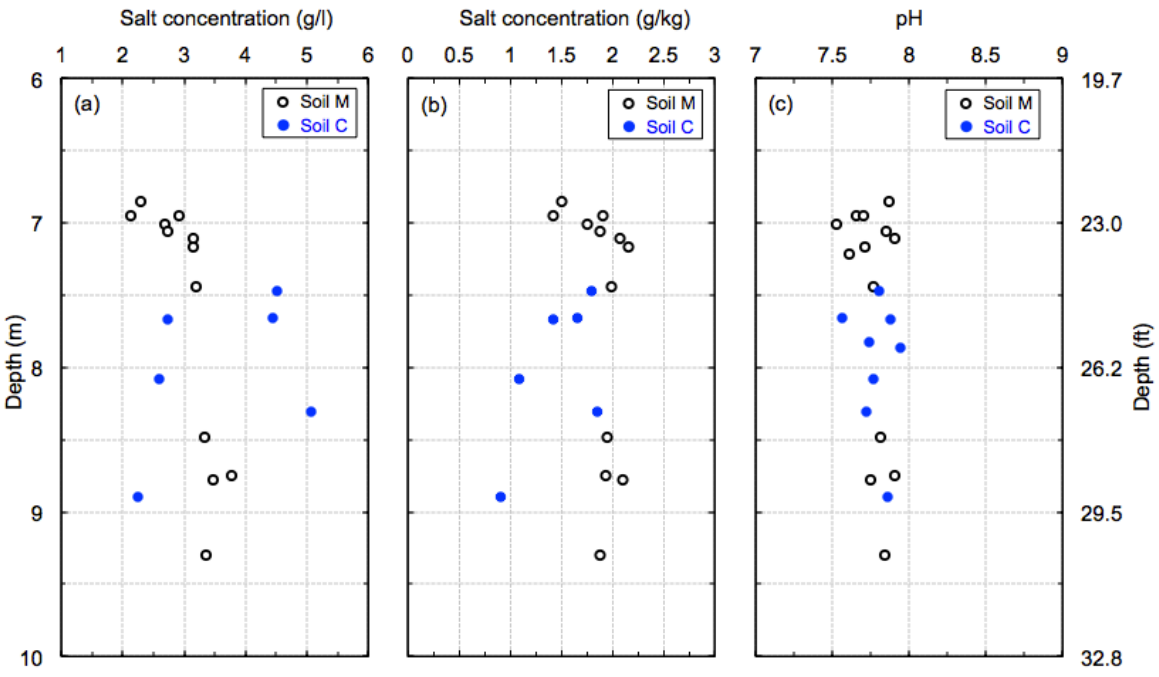

Figure C-8: Salt concentration in (a) g/l of pore fluid and (b) g/kg of dry soil, and (c) pH profiles for marl

C.4 Mineralogy and Microstructure

The mineralogy and microstructure of the two soils identified in the marl deposit were investigated using state of the art techniques that included: X-ray diffraction (XRD), thermogravimetric analysis (TGA), and scanning electron microscopy (SEM) equipped with energy dispersive X-ray (EDX) spectroscopy, which can provide useful information on microstructure and chemical composition of individual particles. The following subsections provide the detailed procedures, analyses, and results, as well as the dominant mineralogical composition and the microstructure of the soils. In this portion of the work specific emphasis was placed on understanding the fundamental differences between soil M and soil C.

C.4.1 X-ray Diffraction (XRD)

X-ray diffraction (XRD) is generally used to study crystalline minerals, including the minerals in soil environments. There are two common methods used to conduct XRD tests: the random powder method and the oriented aggregates method. The former requires a random orientation of the particles and is typically used to identify the non-clay minerals found in the soil (e.g. quartz, feldspars, and carbonates), while the latter requires all platy particles to have preferred orientation in the XRD samples and is generally used to identify clay minerals.

C.4.1.1 Sample Preparation for XRD

Randomly-oriented powder

Self-supporting powder mounts of air-dried bulk soil samples were prepared as described by Schulze (1984). First, the sample was grinded using mortar and pestle to break up large aggregates. Then, about 300 mg of material was mounted into an Aluminum sample holder (15 x 20 mm sample area) and gently pressed against a glass slide attached to an unglazed paper to minimize preferred orientation. The sample holder is flipped over and the glass slide and the paper are removed. Samples prepared using this method had a flat surface that looked smooth and homogenous to the naked eye.

Oriented aggregates

With the presence of sand- and silt-size particles in the soil sample, it is usually hard to identify clay minerals (especially for peaks with higher order n) since their corresponding peaks are masked by the relatively high intensity ones from the larger size particles (e.g. quartz). Thus, it is critical to separate the coarse fraction (i.e. particle size > 2 μm) before running the XRD analysis.

Oriented aggregates were prepared by depositing the clay fraction (<2 μm) of the soil on 32 mm (1.27 inch) diameter alumina porous disks with 1 bar air entry value. Obura (2008) showed that the mass of clay needed to obtain 95% of the theoretical diffraction at 35° 2θ is ~11 mg/cm^2. Therefore 88 mg of clay was needed to cover each porous disk that has an average surface of 8 cm^2. Determination of the optimum amount of clay is essential to ensure that the relative intensities of the diffraction peaks are representative of the right amount of the different minerals in the sample (Rich & Barnhisel, 1977).

The procedures described by Jackson (1973) were followed for sample pretreatment and clay fractionation. In summary, sufficient amount of air-dried bulk soil (~3 g for soil M and ~1 g for soil C) was weighed out and placed into 50 mL conical-bottom centrifuge tubes. The amount of soil needed was estimated based on the particle size analysis (Section C.3.2) and the carbonate content (Section C.3.1), in order to provide ~350 mg of clay. Carbonates were removed by adding ~25 mL of pH 5, 1 M sodium acetate-acetic acid solution (82.03 g of sodium acetate [CH_3COONa] + 27 ml of glacial acetic acid [CH_3COOH] + distilled water until reaching a total volume of 1 liter) to the tubes and heating to about 100°C in a water bath for 20 min, followed by centrifuging and discarding the clear supernatant. This process was repeated 5 times to ensure a complete removal of carbonates (no vigorous bubbling was observed).

Glacial acetic acid dissolves $CaCO_3$ according to the reaction:

$$CaCO_{3(s)} + 2\ CH_3COOH_{(aq)} \rightarrow Ca\ (CH_3COO)_{2(aq)} + CO_{2(g)} + H_2O_{(l)} \quad \text{(Eq. C-1)}$$

About 25 mL of 1 M sodium chloride (NaCl) was added and the samples were shaken overnight on a reciprocating shaker (~228 excursions per minute). The samples were then centrifuge washed 3 times with ~25 mL of 1 M NaCl to saturate the exchange complex with Na^+ ions. Saturating the soil with lower valence ions (i.e. Na^+) results in an increase of the double layer thickness, which facilitates the clay dispersion. Sufficient deionized water was added to the samples to bring the suspension level up to 7 cm from the bottom of the centrifuge tube. The suspensions were then shaken thoroughly and centrifuged at 5000 rpm for 7 minutes (time calculated to extract the clay fraction by sedimentation according to Stoke's law). This step was repeated 5 times while decanting the supernatant into a beaker.

The clay suspensions collected were divided into two portions containing 88 mg of clay each, and saturated with either K^+ by adding 1 M KCl or Mg^{2+} by adding 0.5 M $MgCl_2$. The suspensions were then poured onto the porous disks under suction and repeatedly washing with either KCl or $MgCl_2$, followed by washing off the excess salts with deionized water. (Note that all the excess salt should be completely removed since it might crystallize and affect the diffraction pattern). The samples were then covered at an angle with watch glass and allowed to dry slowly (2-3 days) at room temperature before XRD analysis. Because of the inherent nature of the clay fraction in soil M to crack and peel on drying (as shown in Figure C-9), oriented aggregates of the clay fraction of soil M had to be repeated with much slower drying rate (6-7 days) by completely covering with watch glass and once the soil started to dry (~24 hours), the disks samples were covered with clean disks to avoid cracking and peeling.

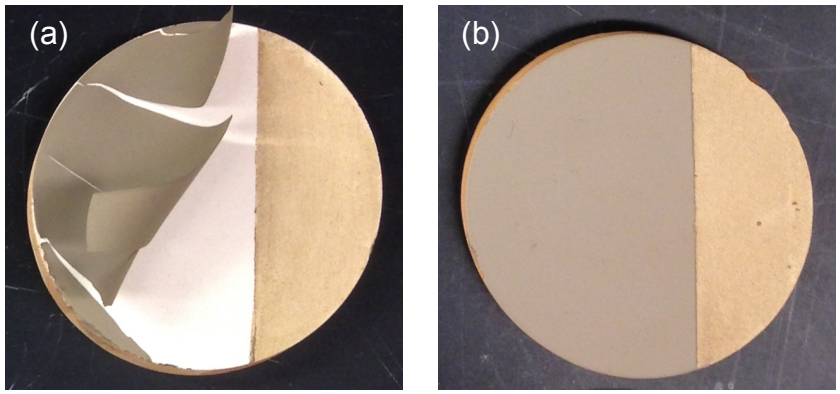

Figure C-9: Oriented clay aggregates of (a) soil M (showing cracking and peeling) and (b) soil C

C.4.1.2 X-ray Diffraction Analysis

The Mg saturated samples were scanned at room temperature before and after solvating with ethylene glycol (EG) in a sealed desiccator heated at 60°C for about 24 hours. The K saturated samples were scanned at room temperature and after successive heating to 100, 300, and 550°C for 2 hours (Note that samples should not be heated longer than 2 hours because chlorite slowly dehydroxylises between 300°C and 550°C resulting in false interpretation). Diffractograms were obtained using a PANalytical X'Pert PRO MPD x-ray diffraction system (PANalytical, Almelo, The Netherlands) equipped with a PW3050/60 θ-θ goniometer and uses Co-Kα (λ = 1.79 Å) radiation generated at 45 KeV and 40 mA. Figure C-10 shows the different components of the diffractometer used in this research. The incident beam optics consisted of an Fe beta filter, 0.04 radian Soller slit, a programmable divergence slit, and a beam mask set to illuminate a 15 × 20 mm sample area. A fixed, 1° anti-scatter slit was used at diffraction angles smaller than 12° 2θ. The diffracted beam optics consisted of a programmable diffracted beam anti-scatter slit, a 0.04 radian Soller slit, and a PW3015/20 X'Celerator detector configured for an active length of 2.12° 2θ. The XRD data were obtained by step-scanning the sample (powder mounts or oriented clay aggregates) from 2.1 to 80° 2θ at 0.05° steps using a counting time of 60 sec per step. The data were analyzed with the X'Pert High

Score Plus software package (PANalytical, Almelo, The Netherlands) and were converted to a fixed 1° divergence slit prior to phase analysis and plotting.

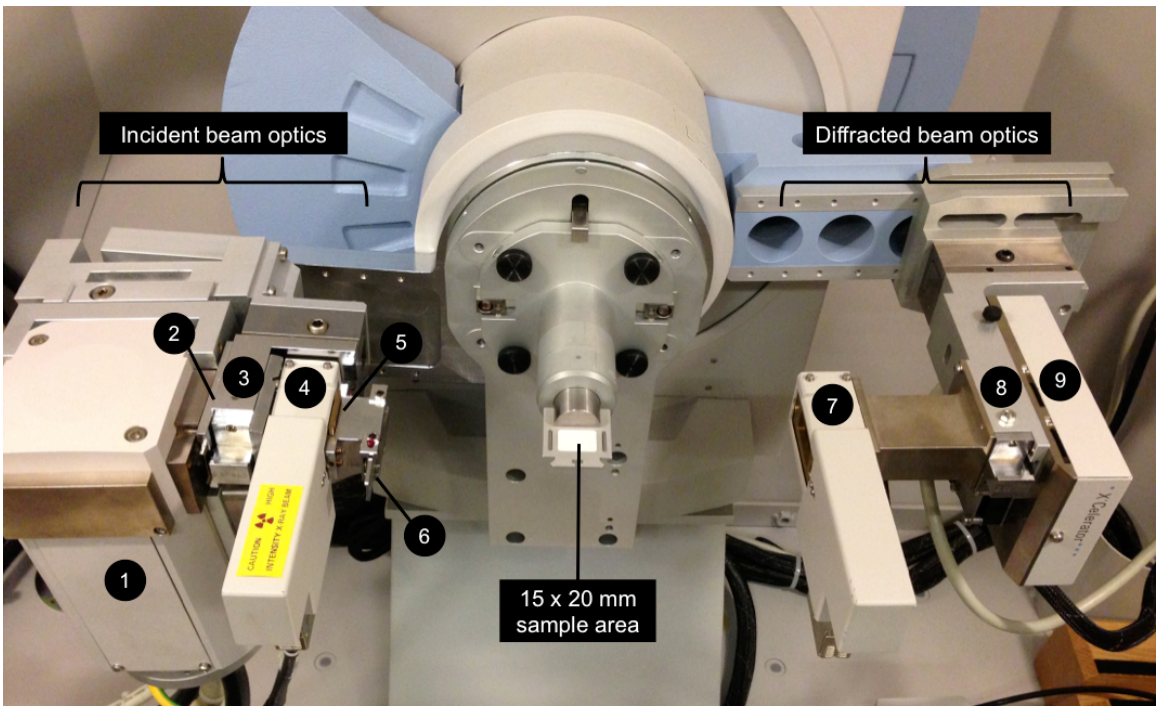

1- X-ray tube	4- Programmable divergence slit	7- Programmable diffracted slit
2- Fe beta filter	5- Beam mask	8- Soller slit
3- Soller slit	6- 1° anti-scatter fixed slit	9- X'Celerator detector

Figure C-10: X-ray diffraction system (PANalytical B.V. diffractometer)

C.4.1.3 Results and discussion

The mineral composition was determined using XRD analysis on both randomly-oriented powder and oriented aggregates. A total of 5 specimens were obtained from different boreholes at various depths (3 specimens from soil M and 2 specimens from soil C) and analyzed using XRD. Table C-2 presents basic information about the XRD samples examined:

Table C-2: Location and depth of the XRD samples examined

Specimen Number	Sample Location	Depth	Soil Type
TX112	MR#3 – ST5	7.16 m (23.5 ft)	Soil M
TX114	MR#4 – ST5	7.44 m (24.4 ft)	Soil M
SEM1	MR#4 – ST4	7.28 m (23.9 ft)	Soil M
TX102	MR#3 – ST6	8.31 m (27.2 ft)	Soil C
TX103	MR#1 – ST4	7.47 m (24.5 ft)	Soil C

The XRD patterns (randomly-oriented powder and oriented aggregates) of soil M specimens (TX112, TX114, and SEM1) were almost identical, hence the results of only one specimen (i.e. TX114) is presented in this section. Similarly, the two specimens from soil C (TX102 and TX103) have similar mineral composition and the results of only one specimen (i.e. TX102) is presented. While no variations in mineral composition were observed with depth, the mineralogy varied significantly between soil M and soil C; which might be one of the fundamental reasons of the differences observed in the geotechnical index and engineering properties. The different minerals identified in the samples are shown in Table C-3 in order of predominance (from largest to smallest).

Table C-3: The mineralogy of marl (in order of predominance) as observed by XRD analysis (from randomly-oriented powder and oriented aggregates)

Soil type	Mineral type	Identified minerals
Soil M	Non-clay minerals	Calcite, quartz, dolomite, aragonite, plagioclase feldspar, K-feldspar
	Clay minerals	Smectite, illite, chlorite, kaolinite
Soil C	Non-clay minerals	Quartz, dolomite, calcite, plagioclase feldspar, K-feldspar
	Clay minerals	Illite, chlorite, smectite, kaolinite

Non-clay minerals

All soil samples yielded similar results. The dominant non-clay mineral components are calcite, dolomite, and quartz. Figure C-11 and Figure C-12 show the XRD patterns for a randomly-oriented powder sample obtained from soil M and soil C, respectively. Each peak in the figures is labeled with the mineral name, the Miller index (hkl), and the d-spacing. Quartz is identified by distinctive peaks at 4.26 Å, 3.35 Å, 2.46 Å, 2.13 Å, and 1.98 Å; with the strongest peak observed at 3.35 Å (101). The carbonate minerals, calcite and dolomite, are found prominently in the bulk samples with the strongest (104) peak observed at 3.03 Å and 2.89 Å, respectively. Calcite is also identified from 3.85 Å, 2.84 Å, 2.49 Å, 2.28 Å, and 2.09 Å peak; whereas dolomite is identified from 4.03 Å, 3.70 Å, 2.56 Å, 2.19 Å, and 2.02 Å peak.

Soil M and soil C contain small quantities of feldspars; K-feldspar is identified by a small peak at 3.24 Å and plagioclase feldspar is identified by a peak at 3.19 Å. The latter peak is differentiated from the (012) magnesite peak by conducting XRD analysis on randomly-oriented powder samples prepared with soil M and soil C treated with pH 5, 1 M sodium acetate-acetic acid solution (described in Section C.4.1.1) to remove carbonates (including magnesite). XRD pattern for both soils show that the 3.19 Å peak persists even after treatment. Thus, it is concluded that this peak corresponds to plagioclase feldspar.

In addition, the XRD pattern for soil C shows a few additional peaks at lower angles, indicating the presence of clay minerals (e.g. smectite, chlorite, vermiculite, illite, and/or kaolinite). These peaks can be hardly identified in the pattern for soil M most likely due to its lower clay content (~20% compared to ~37% for soil C). Identification of the clay minerals in soil M and soil C were achieved by conducting XRD analysis on oriented aggregates obtained from <2 μm fractions and the results are discussed in the next subsection entitled “clay minerals”.

Aragonite ($CaCO_3$) is identified in soil M by a peak at 2.71 Å, which was found to be attributed to the presence of shells. This component is not identified in soil C due to the absence of shells. To support this hypothesis, XRD analysis was conducted on randomly-oriented powder samples prepared using shells collected from soil M. Aliquots of soil M was placed in deionized water for several days to soften the sediment enough to pass through a 0.075 mm sieve (ASTM #200). Shells were hand-picked from the retained fraction and repeatedly washed with deionized water to remove all the soil that adhered to the shell surface. The shells were then broken and the soil that was lodged within the shell was removed with small spatula and washed repeatedly with deionized water. The recovered shells were air-dried and randomly oriented powder samples were prepared according to the procedure described in Section C.4.1.1. A total of three samples were scanned using X-ray, and the patterns were identical. Figure C-13 shows the typical XRD pattern for the shells. Aragonite is the predominant mineral and is identified by distinctive peaks at 4.21 Å, 3.39 Å, 3.27 Å, 2.87 Å, 2.70 Å, 2.48 Å, 2.41 Å, 2.37 Å, 2.33 Å, 2.19 Å, 2.11 Å, and 1.98 Å; with the strongest peak observed at 3.39 Å (111). This principal peak could not be identified in the pattern of soil M (Figure C-11) as because of the principal peak of quartz (3.35 Å) of about the same position. However, the second largest peak of aragonite was observed at 2.70 Å. Note that the aragonite (012) peak observed in soil M at 2.71 Å is very small and this is because the calcite (104) peak is so robust that is typically much larger than the aragonite peaks.

The XRD patterns shown in Figure C-11 and Figure C-12 reveal the following differences between the matrix of soil M and that of soil C:

1. Soil M is richer in carbonates than soil C, which is confirmed by the thermogravimetric analysis presented in Section C.4.2;
2. Soil M has more calcite than soil C, which might be attributed to the presence of calcite mesocrystals that were precipitated more in soil M during the soil deposition. This is confirmed by the calcite crystals

identified with the scanning electron microscope (presented in Section C.4.3). These crystals are identified in soil M but are not found in soil C;

3. Soil M has less dolomite than soil C, as shown by the relative peak intensities in the XRD patterns. This is in agreement with the observation made during the removal of carbonates for oriented aggregates samples preparation. It was observed that soil C reacts much slower with acid addition than soil M, and fizzing is observed for much longer time in soil C despite the fact that it has lower carbonate content. Doner and Grossl (2002) reported that dolomite reacts slower with acid addition than calcite. Hence, it can be concluded that soil C has more dolomite than soil M;
4. Aragonite is identified in soil M but is absent in soil C. This is expected due to the presence of shells in soil M and their absence in soil C;
5. Soil M has a smaller clay content than soil C, which is consistent with the results of particle size analysis (Section C.3.2).

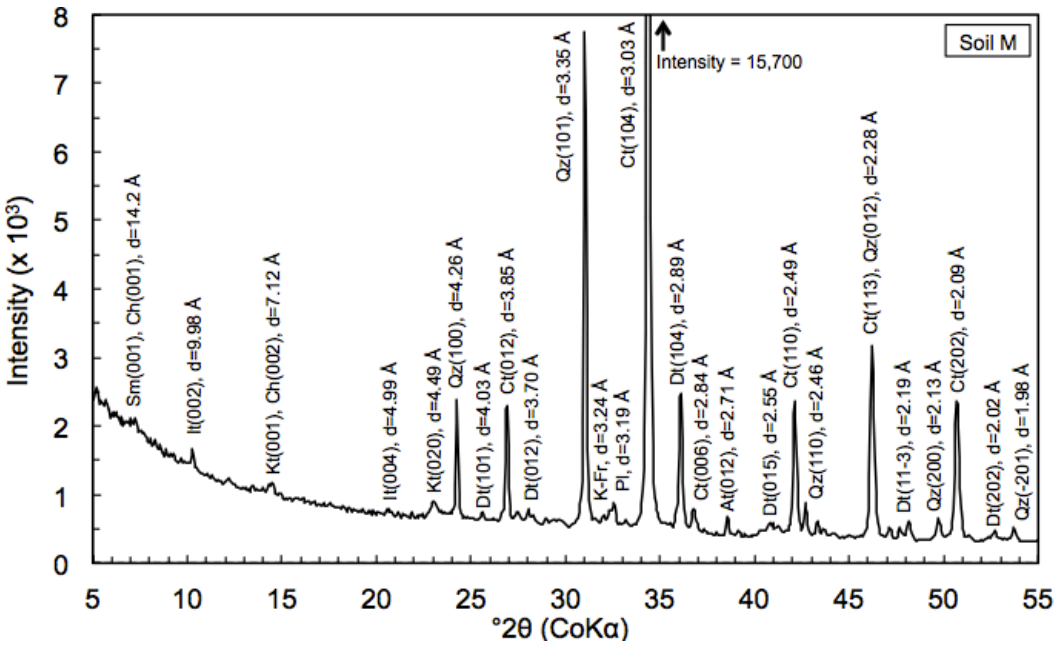

Figure C-11: XRD patterns (randomly-oriented powder) of soil M. Mineral codes: Sm = smectite, Ch = chlorite, It = Illite, Kt = kaolinite, Qz = quartz, Dt = dolomite, Ct = calcite, K-Fr = K-feldspar, Pl = plagioclase feldspar, At = aragonite

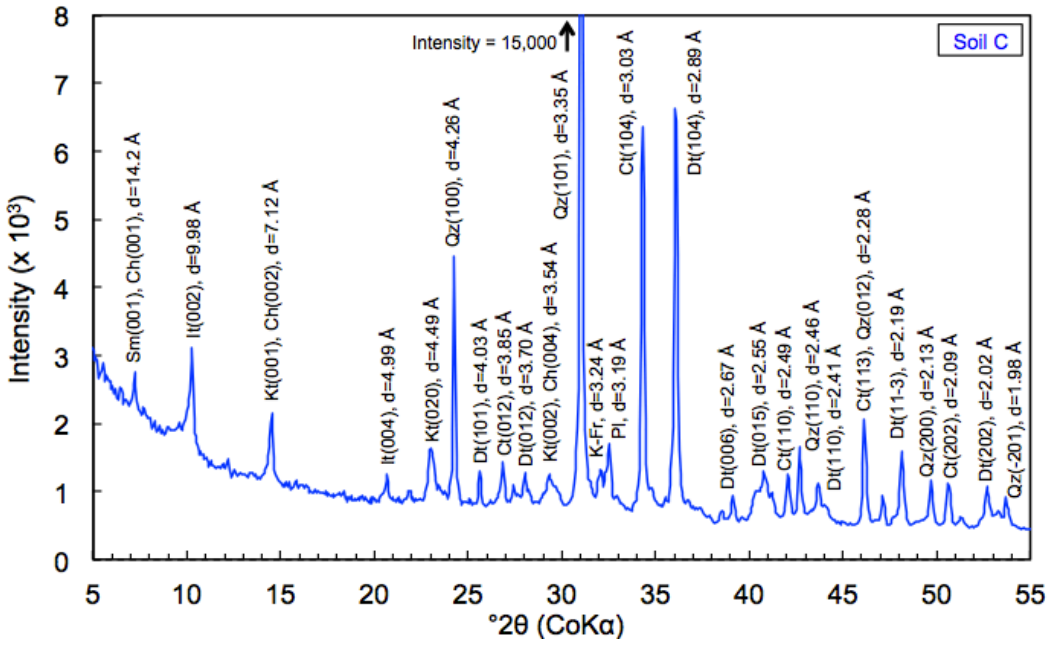

Figure C-12: XRD patterns (randomly-oriented powder) of soil C. Mineral codes: Sm = smectite, Ch = chlorite, It = Illite, Kt = kaolinite, Qz = quartz, Dt = dolomite, Ct = calcite, K-Fr = K-feldspar, Pl = plagioclase feldspar

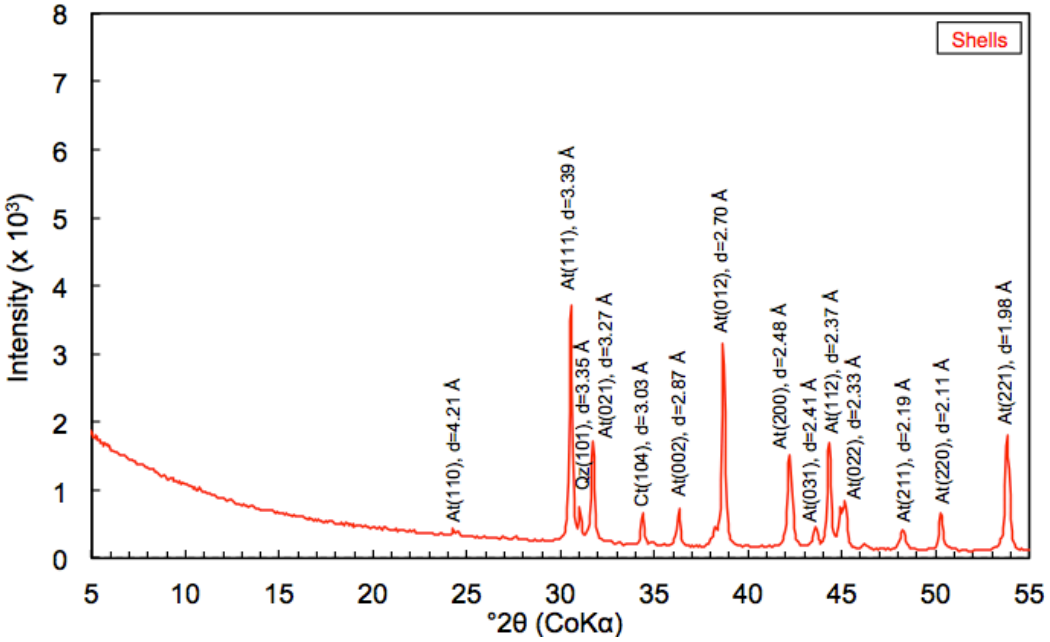

Figure C-13: XRD patterns (randomly-oriented powder) of shells collected from soil M. Mineral codes: At = aragonite, Qz = quartz, Ct = calcite

The three predominant minerals calcite, dolomite and quartz were each analyzed separately using XRD analysis on randomly-oriented powder samples prepared using pure minerals. The premise of analyzing these pure minerals is to better identify the minerals found in the marl deposit and to compare them to the shell aragonite. Table C-4 shows the results from the XRD patterns for a randomly-oriented powder sample obtained from each pure mineral. The table also includes the source from which the mineral was obtained as well as a photo. TGA was also conducted on these three minerals and the results are discussed in Section C.4.2.

Table C-4: XRD analysis of the three predominant minerals: calcite, dolomite, and quartz

Name	Source	Photo	XRD patterns (randomly-oriented powder)
Calcite	Chisos Mountain, Brewster County, Texas (Ward's Natural Science Establishment, Inc., Rochester, N.Y.)		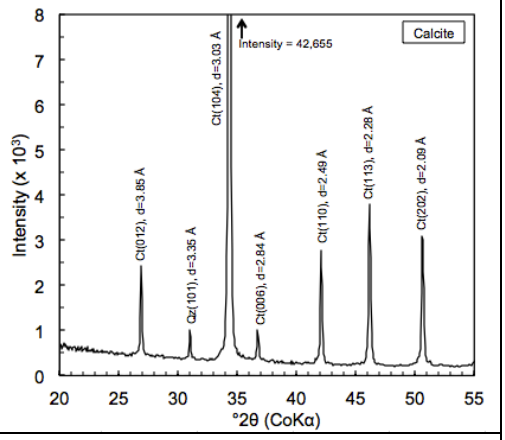
Dolomite	Thornwood, New York (Ward's Natural Science Establishment, Inc., Rochester, N.Y.)		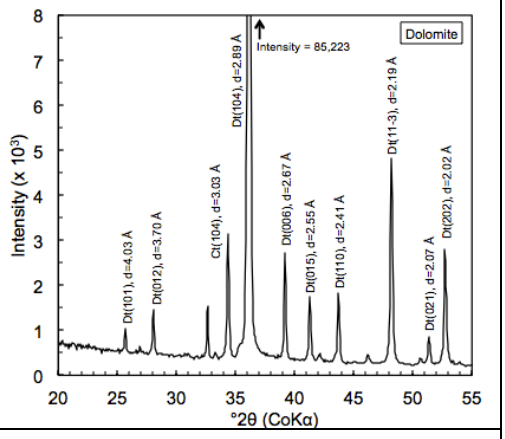
Quartz	Commission of the European Communities, Community Bureau of Reference BCR, Reference material Nr. 66 (#0788)		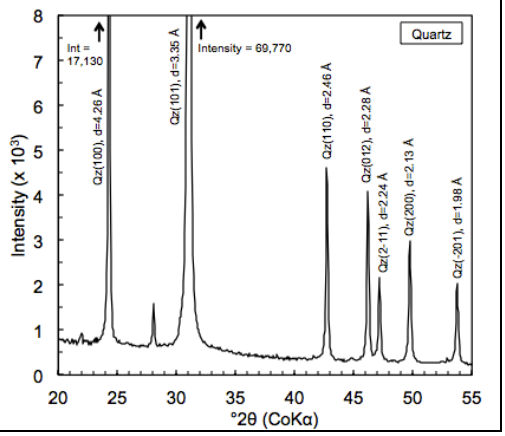

Clay minerals

Figure C-14 and Figure C-15 summarize the XRD patterns of oriented clay aggregate subjected to different treatments for soil M and soil C, respectively. Each figure shows six patterns: Mg^{2+}-saturated (Mg), ethylene glycol-solvated sample (MgEG), K^{+}-saturated sample x-rayed after air-drying at room temperature (K-23ºC), K^{+}-saturated sample x-rayed after heating at 100ºC for 2 hours (K-100ºC), 300ºC for 2 hours (K-300ºC), and 550ºC for 2 hours (K-550ºC). All XRD patterns are corrected for position shifts using corundum as a standard (corundum disks were used as sample holders). These results show that smectite, illite, chlorite, and kaolinite are present in both soils (M and C), but with different proportions.

As shown in Figure C-14, smectite and illite are the predominant minerals in soil M, while chlorite and kaolinite occur in smaller quantities.

Smectite is identified by a strong peak at ~14.2 Å in the sample saturated with Mg^{2+}, which shifts to 16.9 Å when solvated with ethylene glycol (EG), and collapses to ~11 Å and ~10 Å with K^{+} saturation and heating at 100ºC and 550ºC, respectively. The smectite probably has appreciable hydroxy-interlayering because it does not collapse completely to ~ 10 Å upon K^{+} saturation and heating up to 100ºC (Marques et al., 2002).

Illite is identified by peaks at 9.96 Å, 4.98 Å, and 3.33 Å that do not change position with K^{+} or Mg^{2+} saturation, or with ethylene glycol solvation and persist in K^{+}-saturated samples heated up to 550ºC. The pattern also shows an increase in the (002) peak at 9.96 Å with K^{+} saturation and heating to 550ºC, which is attributed to the collapse of smectite. The sharp peaks of illite indicate that illite of all the samples are well crystallized (Brindley & Brown, 1980).

Chlorite is also found in soil M and is identified by peaks at 14.2 Å, 7.06 Å, 4.71 Å, and 3.53 Å. Chlorites are differentiated from vermiculites in that, unlike

vermiculite which expands to 14 Å with ethylene glycol and collapses to 10 Å when saturated with K^+ (Malla, 2002), chlorite maintains a 14.2 Å basal spacing with glycolation and 550ºC heat treatment. When chlorite is heated to temperatures as high as 550ºC, the peak intensity of the 001 reflection (14.2 Å) increases, and at the same time, the peak intensities of higher-order (00l) reflections decrease in intensity (Barnhisel & Bertsch, 1989)

The MgEG pattern in Figure C-14 also shows the presence of some kaolinite, which is identified by peaks at 7.14 Å and 3.57 Å. All kaolinite are found to be unaffected on glycolation and 300ºC heat treatment. On heating to 550ºC, kaolinite tends to lose its crystalline character causing the two peaks at 7.14 Å and 3.57 Å to disappear.

Soil C, on the other hand, is mainly composed of Illite and chlorite (Figure C-15), while smectite and kaolinite are found in very small amount. Illite, chlorite, and kaolinite present in soil C are identified at d-spacing values similar to the ones found in soil M, hence the reader is referred to the description provided above. However, the relative peak intensities are different between the two soils indicating the difference in the mineral proportions.

Soil C also contains small amount of smectite that is identified by a peak at ~14.2 Å in the sample saturated with Mg^{2+}, which shifts to 16.3 Å when solvated with ethylene glycol (EG), and collapses to 9.95 Å with K^+ saturation. The peak disappears completely and the 9.95 Å peak becomes stronger (Figure C-15), indicating the collapse of smectite into illite. The charge on these smectite layers is quite high and there is very little hydroxy-interlayering because collapse is complete at 23ºC (Marques et al., 2002).

Fine quartz in the < 2 μm fraction can be identified by its (100) peak observed at 4.25 Å presented in both soil M and soil C. However, this peak is very weak, indicating that quartz is present in negligible amount in the clay fraction.

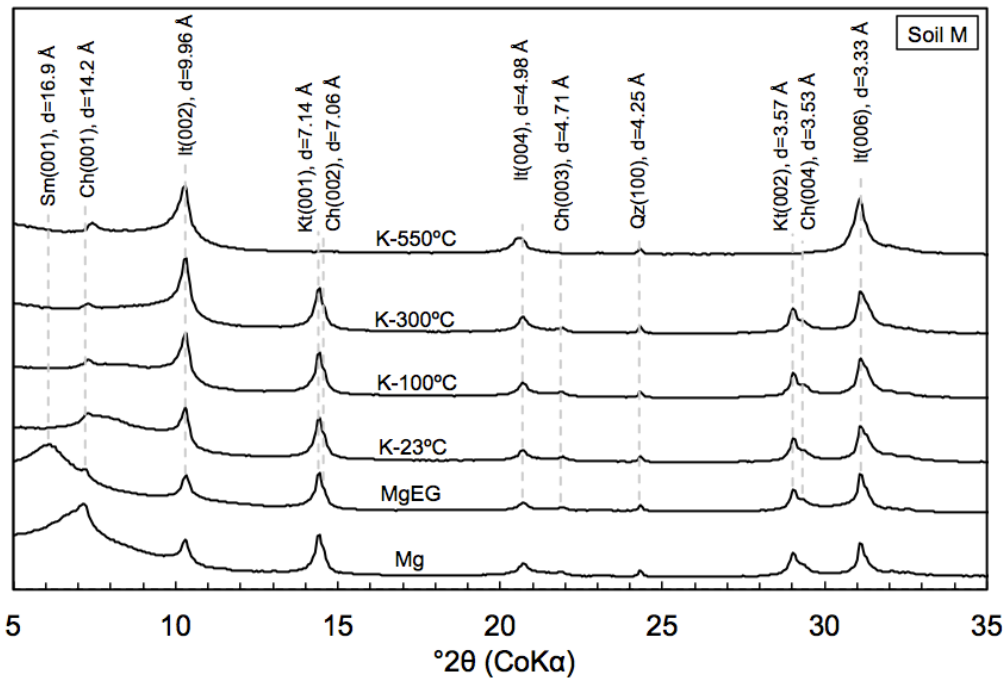

Figure C-14: XRD patterns (oriented samples) of the clay fraction (<2 µm) of soil M. Mineral codes: Sm = smectite, Ch = chlorite, It = Illite, Kt = kaolinite, Qz = quartz

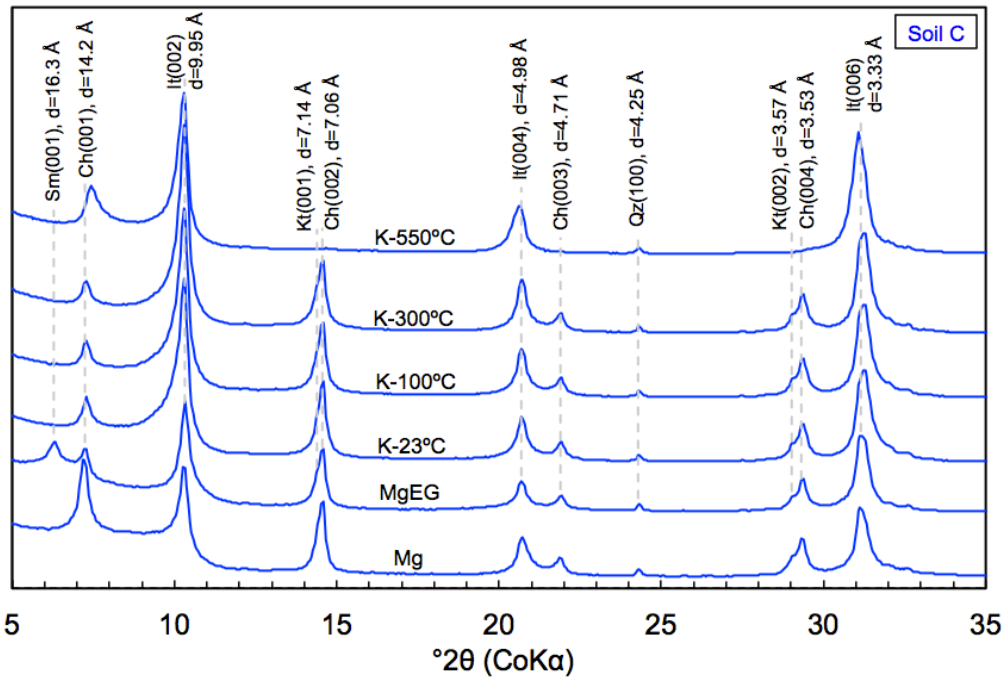

Figure C-15: XRD patterns (oriented samples) of the clay fraction (<2 µm) of soil C. Mineral codes: Sm = smectite, Ch = chlorite, It = Illite, Kt = kaolinite, Qz = quartz

C.4.1.4 Semi-quantitative analysis using XRD

A semi-quantitative mineralogical composition in the clay fractions was determined based on relative peak intensities. The peak intensities were calculated by multiplying the maximum peak height with the full width at half maximum (FWHM). These two parameters were estimated from the XRD patterns after subtracting the baseline and correcting for position shifts using corundum as a standard (corundum disks were used as sample holders). The intensities for the different patterns were also adjusted (normalized) by simple proportion to equalize the ~7 Å peak area, using the ~7 Å peak area for the K-300ºC pattern as the basis for comparison (Weir et al., 1975, Islam & Lotse, 1986). Note that the ~7 Å peak area was almost the same for all patterns and only slight adjustment was needed. The peak intensities at each d-spacing were represented with the characters a to e in Table C-5**.**

Table C-5: d-spacing of detected clay minerals for different treatment (modified after Ohtsubo et al., 2002)

Treatment	d-spacing (Å)	Minerals indicated	Peak intensity
Mg air-dried	1.4 – 1.5	Sm, Ch	a
	1.0	It	b
	0.7	Kt, Ch	c
Mg glycol	1.7	Sm	d
	1.4	Ch	e

Mineral codes: Sm = smectite, Ch = chlorite, It = Illite, Kt = kaolinite

Islam and Lotze (1986) and Egashira et al. (1999) estimated the peak intensity ratios of the respective clay minerals to illite when the minerals are present in an equal amount in the soil: Sm(001)/It(002) = 3.0; Ch(002)/It(002) = 1.5; Ch(001)/It(002) = 1.0; Kt(001)/It(002) = 2.0. The following equations were formulated to estimate the relative weight equivalent to the peak intensities for the respective clay minerals:

Smectite: $W_{Sm} = 1/3 [a \times d/(d+3e)]$

Illite: $W_{It} = b$

Chlorite: $W_{Ch} = a \times 3e/(d+3e)$

Kaolinite: $W_{Kt} = c/2 - W_{Ch}$

The percentage of the clay minerals was calculated by dividing the relative weight of each clay mineral (W_i) by the total of the relative weight of the clay minerals (ΣW_i). The results for both soils (M and C) are summarized in Table C-6.

Table C-6: Clay mineral composition of soil M and soil C

Mineral	Soil M	Soil C
Smectite	50%	5%
Illite	27%	62%
Chlorite	12%	30%
Kaolinite	11%	3%

The large difference in the smectite content between soil M and soil C may explain the discrepancy observed in the Atterberg limits results (Section C.3.2). Soil M has lower clay content than soil C yet higher LL and PI, which is not consistent with the typical trends reported in the literature of increasing LL and PI with higher clay content. However, both the type and amount of clay in a soil influence the Atterberg limits. Generally, soils rich in smectite have higher LL and PI, which is attributed to the higher water sorption capacity caused by the higher specific surface area (De Kimpe et al., 1979). The smectite content in bulk soil is calculated by multiplying the smectite content in the clay fraction with its percentage. Hence, the smectite content in bulk soil is about 10% for soil M and about 2% for soil C.

C.4.2 Thermogravimetric Analysis (TGA)

Thermogravimetric analysis (TGA) is used primarily to characterize the hydration status of some materials and study their thermal stability at elevated temperatures (up to 1,000°C). In the context of this research, the results of TGA are useful to complement the XRD data in detecting the different minerals present in marl deposit and understand the fundamental differences between soil M and soil C. The standard testing procedure for this test is summarized in ASTM E1131-08 (ASTM, 2014). TGA was performed in the Soil Chemistry laboratory of Purdue University's Agronomy Department. Air-dried samples were ground into powder using a mortar and a pestle, and ~50 mg were loosely loaded into a 70 µL aluminum oxide (Al_2O_3) ceramic crucibles. The crucibles were placed in the thermogravimetric analyzer (Model - TGA/SDTA851e, Mettler Toledo, OH, USA) and gradually heated from 25°C to 1,000°C at a rate of 20°C/min. During the test, dry nitrogen (N_2) was used as the purge gas at a flow rate of 20 mL/min. The purpose of employing a flowing gas in the TGA analyzer is to purge the thermobalance of any gas emitted from the sample during the experiment, thus minimizing its interaction with the sample powder (Bish & Duffy, 1990). Results were normalized so that all final masses (at 1,000°C) are equal to 10 mg, and first derivatives were calculated digitally from the raw TGA data.

TGA was used to analyze the thermal reactions of the same 5 samples analyzed using XRD (see Table C-2). All samples were tested twice for repeatability. A total of ten TGA curves were obtained and are presented in Figure C-16, where the dashed black lines represent soil M and the continuous blue lines represent soil C. The TGA curves for both samples show a major mass-loss event at temperatures > 700°C, which likely reflects the breakdown of carbonates. As expected, soil M has a greater mass loss compared with soil C due to its higher carbonate content. In addition, within the same soil type, samples with higher $CaCO_3$ content result in higher mass losses: SEM1 > TX114 > TX112 and TX102 > TX103.

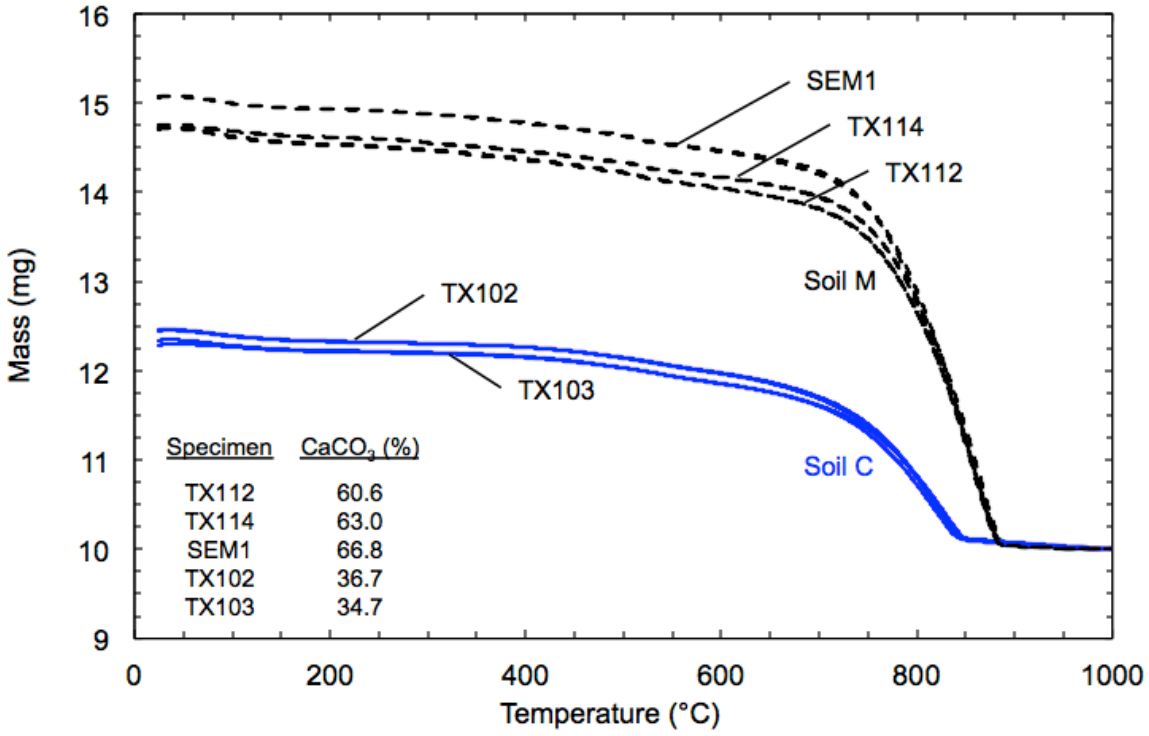

Figure C-16: Normalized thermogravimetric analysis curves of soil M (black dashed line) and soil C (blue continuous line) (~50 mg samples, 20°C/min heating rate, 20 mL/min N_2 purge)

In order to better detect the mass-loss events, the derivative mass-loss curve, also known as the derivative TGA (DTG) curve, was computed for soil M (TX114) and soil C (TX102), and plotted with the corresponding TGA curve in Figure C-17 and Figure C-18, respectively. The results for soil M and soil C show four distinctive mass loss stages when the samples were heated from 25°C to 1,000°C, with the fourth being the largest. The four mass loss events were observed at 25 - 200°C, 200 - 300°C, 400 - 600°C, and >600°C, resulting in a total mass loss of ~32% for soil M and ~20% for soil C. A mass loss plateau is reached at ~880°C and ~840°C for soil M and soil C, respectively. Table C-7 summarizes the percentage mass loss at various temperature ranges. The mass losses at temperatures <200°C are due to the loss of the adsorbed water on clay surfaces, whereas the ones at 200 to 300°C are due to the removal of interlayer bound water in the clay structure (dehydration of smectite and illite, as reported

by Velde (1992)). The third mass loss event (400 to 600°C) is related to the dehydroxylation of kaolinite and illite (Brindley & Lemaitre (1987), Fanning et al. (1989), Velde (1992)), the presence of which was detected through XRD analyses, and the fourth large mass loss at temperatures >600°C is due to a combination of carbonate breakdown and dehydroxylation of chlorite and smectite (Bish & Duffy (1990); Velde (1992), Zhu (2009)). Note that the majority of the mass loss occurs at temperatures >600°C, which is expected due the elevated carbonate content present in marl.

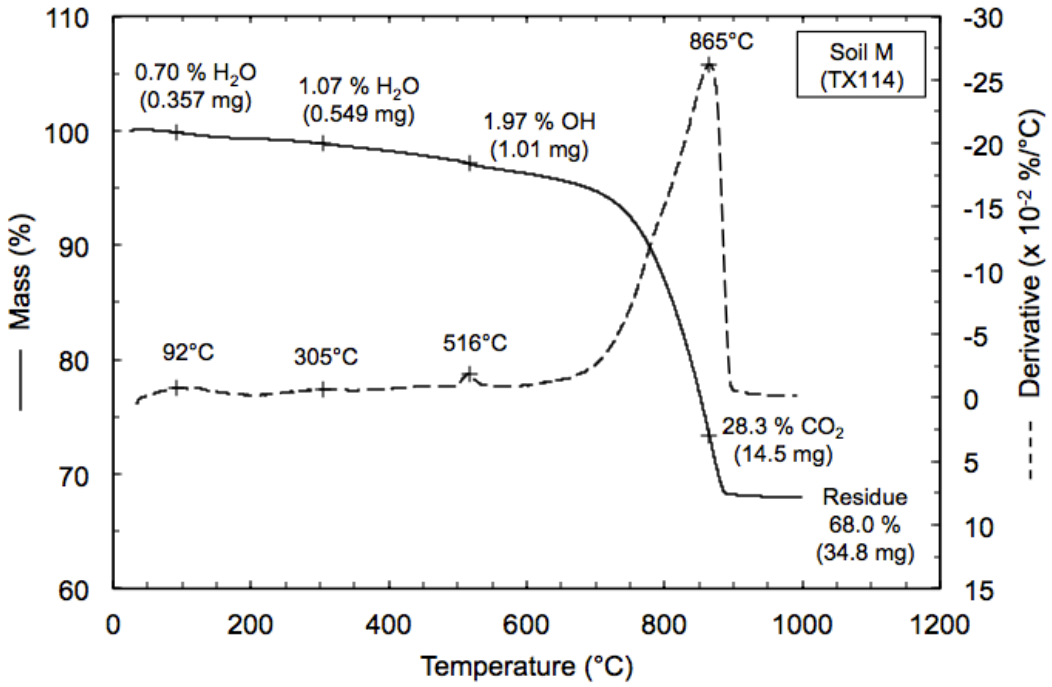

Figure C-17: Thermogravimetric analysis curve of soil M (51.2 mg sample, 20°C/min heating rate, 20 mL/min N_2 purge)

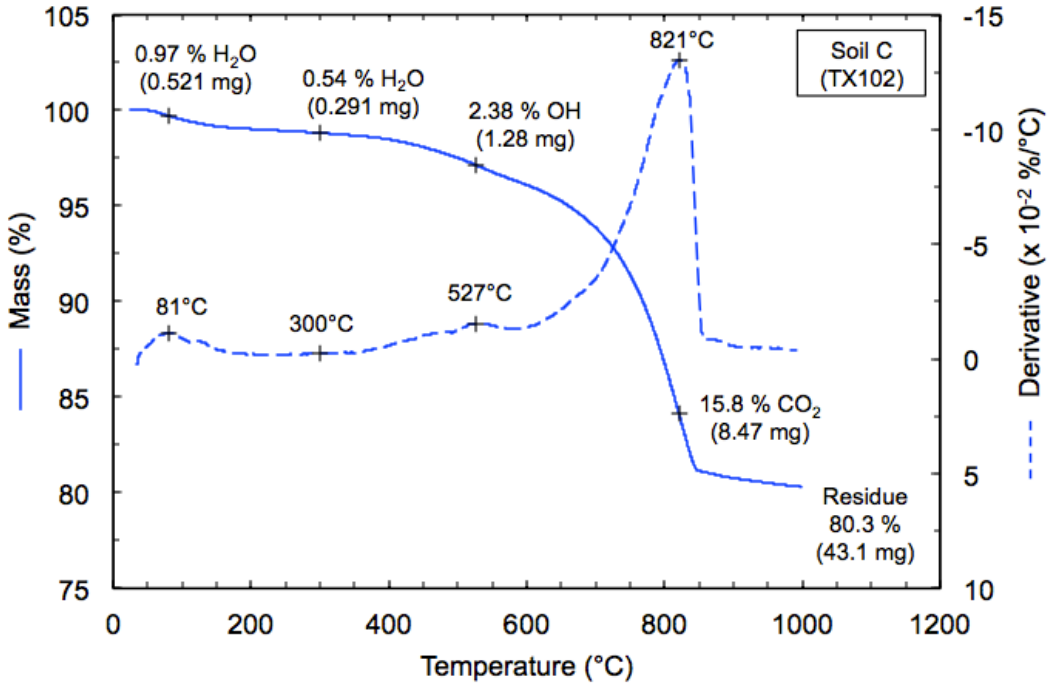

Figure C-18: Thermogravimetric analysis curve of soil C (53.6 mg sample, 20°C/min heating rate, 20 mL/min N_2 purge)

Table C-7: Mass loss during thermogravimetric analysis of soil M and soil C

Sample	Percentage mass loss at				
	25-200°C	200-300°C	400-600°C	>600°C	Total
Soil M	0.70	1.07	1.97	28.3	32.0
Soil C	0.97	0.54	2.38	15.8	19.7

C.4.2.1 Effect of carbonates on TGA curves:

As an attempt to identify the different amounts of carbonate minerals present in marl (calcite, dolomite, aragonite for soil M; calcite, dolomite for soil C), the shell aragonite as well as the three different pure minerals (calcite, dolomite, and quartz) described in Section C.4.1 were analyzed using TGA. The normalized results are summarized in Figure C-19. As expected, the TGA curve for quartz does not show any mass loss since quartz mineral is known to be an inert material and very stable even when heated to moderately high temperatures (Drees et al., 1989). All three carbonates (calcite, dolomite, and shell aragonite)

decompose around the same temperature range (700 - 900°C), which makes the distinction between them using TGA curves almost impossible. However, a comparison between the relative abundance of calcite and dolomite in soil M and soil C can be still made. Figure C-19 shows that shell aragonite and dolomite decarbonate at almost the same temperature, whereas calcite decarbonates at slightly higher temperature. Similar observation was reported by Doner and Lynn (1989) and Bish and Duffy (1990) but at different reaction temperatures, which is mainly caused by the differences in the testing conditions. Great care must be taken in comparing data obtained in different laboratories on different samples due to the number of instrument- and sample-related factors that can affect TGA results. This is illustrated in Figure C-20, which presents normalized thermogravimetric analysis curves of natural calcite heated at different testing conditions. The figure shows that generally, the reaction temperatures shift to higher values with (i) larger sample mass (curve 3 to 4); (ii) higher heating rate (curve 2 to 3); and (iii) lower N_2 purge rate (curve 1 to 2). TGA curve 1 was obtained using the same sample mass, heating rate, and N_2 purge employed by Bish and Duffy (1990), which led to similar decarbonation temperature.

Since the decarbonation temperature of calcite is higher than that of dolomite (as reported above), it would be expected that the decarbonation temperature shifts to a higher value with an increase in calcite content. As shown in Figure C-17 and Figure C-18, the carbonate breakdown for soil M occurs at relatively higher temperatures compared with soil C (soil M: DTG_{max} ~ 865°C; soil C: DTG_{max} ~ 821°C). In addition, the mass loss plateau for soil M is reached at higher temperature (~880°C) compared to soil C (~840°C). These observations lead to the conclusion that soil M contains relatively more calcite than soil C, whereas the latter is richer in dolomite. This is in agreement with the XRD results.

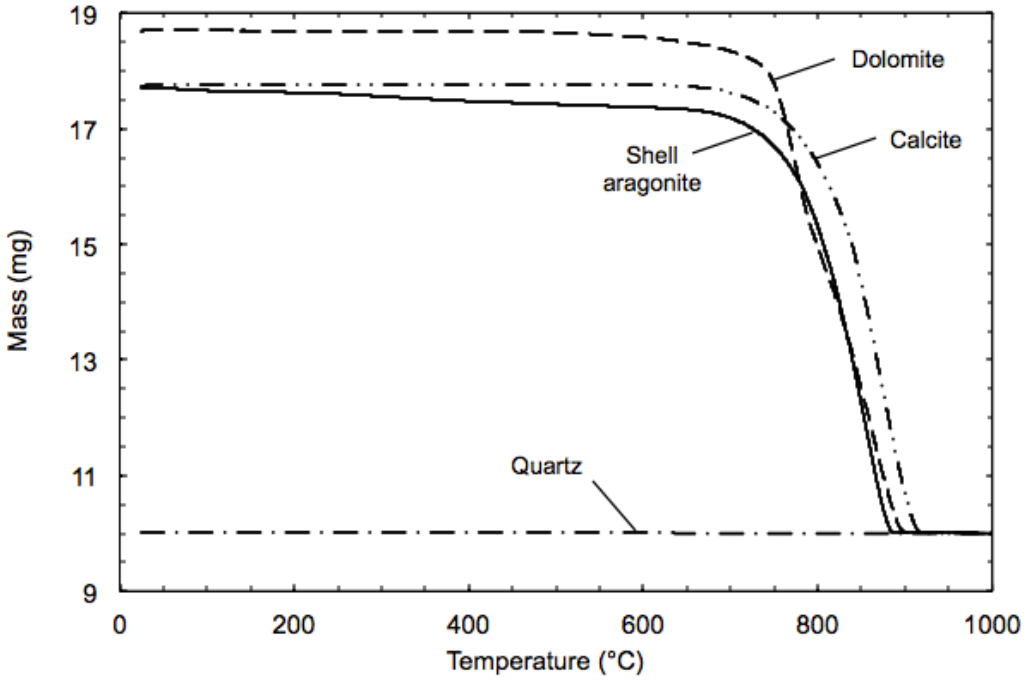

Figure C-19: Normalized thermogravimetric analysis curves of shell aragonite, natural calcite, natural dolomite, and natural quartz (~50 mg samples, 20°C/min heating rate, 20 mL/min N_2 purge)

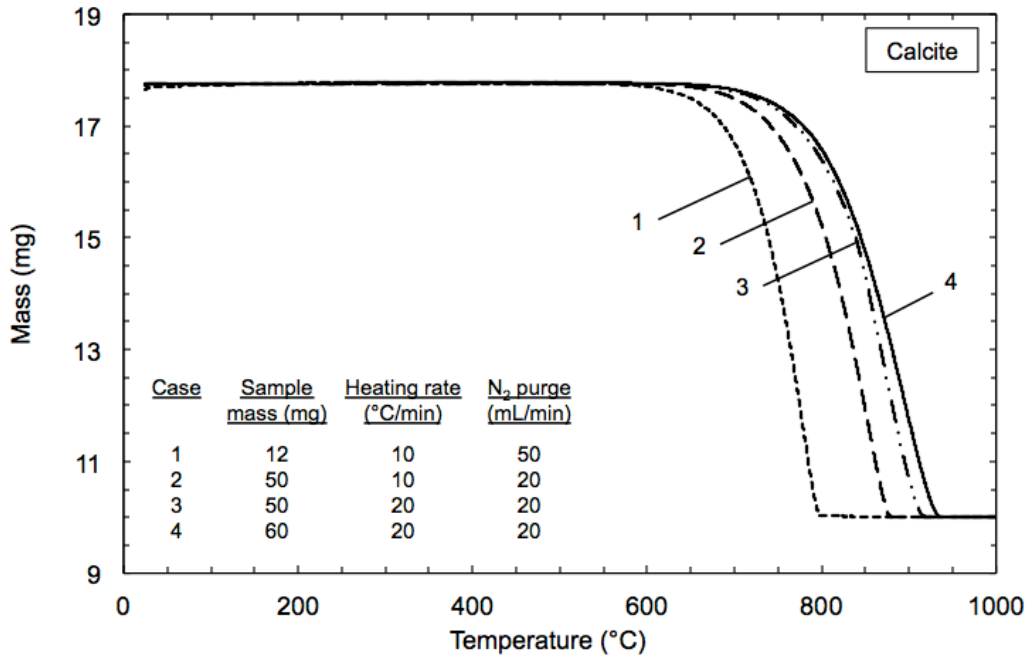

Figure C-20: Normalized thermogravimetric analysis curves of natural calcite showing the effect of sample mass, heating rate, and N_2 purge on decarbonation temperature

In order to study the effect of shells on the TGA curves, soil M was subjected to different pre-treatment procedures and the following samples were examined using TGA:

a. soil M in its natural state;
b. soil M without shells; this was achieved carefully wet sieving the soil on the #200 (75 μm) sieve to remove the shells;
c. soil M without all carbonates; this was achieved removing the shells through wet sieving and treating the soil passing the #200 (75 μm) sieve with sodium acetate-acetic acid solution. The premise of testing this sample is to assess the effectiveness of sodium acetate-acetic acid solution treatment in removing carbonates.

Figure C-21 shows the TGA curves of the three samples described above. TGA curves for soil C (natural state) and shell aragonite are included for comparison. This investigation leads to the following conclusions:

1. Shell aragonite contributes to a small portion of the carbonates present in soil M; the carbonates minerals present in this soil are mostly calcite and dolomite.
2. Even after removing the shells from soil M, the TGA curve (“Soil M – no shells”) still shows a mass loss event that is about twice that of soil C. this indicates that the presence of shells is not the only difference between soil M and soil C but there is also a difference between the soil matrix; the total calcite/dolomite content in soil M is larger than the one in soil C.
3. The complete disappearance of the mass loss event corresponding to the carbonates breakdown (700 - 900°C) indicates that the sodium acetate-acetic acid solution treatment was effective in removing the carbonates present in the soil.

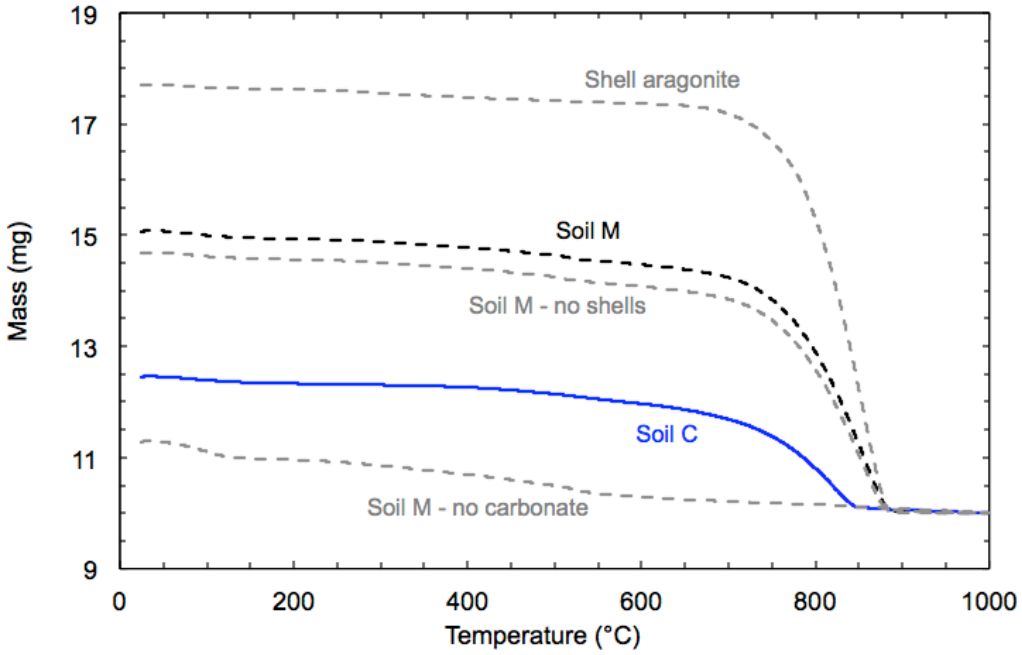

Figure C-21: Normalized thermogravimetric analysis curves of soil M subjected to different pre-treatment procedures, soil C, and shell aragonite (~50 mg samples, 20°C/min heating rate, 20 mL/min N_2 purge)

C.4.2.2 Semi-quantitative analysis using TGA:

Additional analyses were conducted on samples prepared with the clay fraction (<2 μm) of soil M and soil C treated with pH 5, 1 M sodium acetate-acetic acid solution (described in Section C.4.1.1) to remove carbonates. The TGA and DTG curves for soil M and soil C are shown in Figure C-22 and Figure C-23, respectively. The premise of testing treated samples of marl using TGA is to identify the mass losses that correspond to the clay portion. This is expected to complement the XRD results presented in Section C.4.1 and aid in understanding the fundamental differences between soil M and soil C that might be influencing their engineering behavior. Earnest (1980) reported that quantitative analysis using TGA ideally requires that the components of a mixture do not have overlapping mass losses. This is not the case for marl, since it is composed of kaolinite and illite that dehydroxylize at the same temperature range (450 – 600°C) as well as chlorite and smectite (>600°C). However the clay mineral composition obtained in the semi-quantitative analysis using XRD

(Section C.4.1.4) can be used to estimate the expected mass loss in each temperature range.

From the semi-quantitative analysis using XRD data (Section C.4.1.4), the clay fraction (<2 μm) of soil M contains about 50% smectite, 27% illite, 12% chlorite, and 11% kaolinite; whereas that of soil C contains about 5% smectite, 62% illite, 30% chlorite, and 3% kaolinite. These numbers can be used to estimate the percentage mass losses for the 450 – 600°C range (dehydroxylation of kaolinite and illite) and >600°C (dehydroxylation of chlorite and smectite). Table C-8 summarizes the ideal hydroxyl (OH) water loss (wt.%) due to the dehydroxylation of each mineral as well as the expected mass loss (wt. %) calculated based on each mineral fraction estimated using XRD. The total expected mass loss (at temperature > 450°C) is 6.1% for soil M and 6.7% for soil C. These numbers are generally in good agreement with the observed mass losses recorded using TGA: 7.3% for soil M (temperature > 450°C in Figure C-22) and 5.7% for soil C (temperature > 450°C in Figure C-23).

Table C-8: Semi-quantification of clay minerals present in soil M and soil C using TGA

Sample	Mineral	Ideal OH loss (%)	Dehydroxylation temp. (°C)	References*	Mineral fraction from XRD (%)	Expected mass loss** (%)
Soil M	Kaolinite	14	450 - 550 °C	[1], [2]	11	1.5
	Illite	5	500 - 600 °C	[3], [2]	27	1.4
	Chlorite	10	> 600°C	[4], [2]	12	1.2
	Smectite	4	> 600°C	[4], [2]	50	2.0
Soil C	Kaolinite	14	450 - 550 °C	[1], [2]	3	0.4
	Illite	5	500 - 600 °C	[3], [2]	62	3.1
	Chlorite	10	> 600°C	[4], [2]	30	3.0
	Smectite	4	> 600°C	[4], [2]	5	0.2

* [1] Brindley & Lemaitre (1987); [2] Velde (1992); [3] Fanning et al. (1989); [4] Bish & Duffy (1990)
** Expected mass loss = (mineral fraction from XRD) x (ideal OH loss) / 100

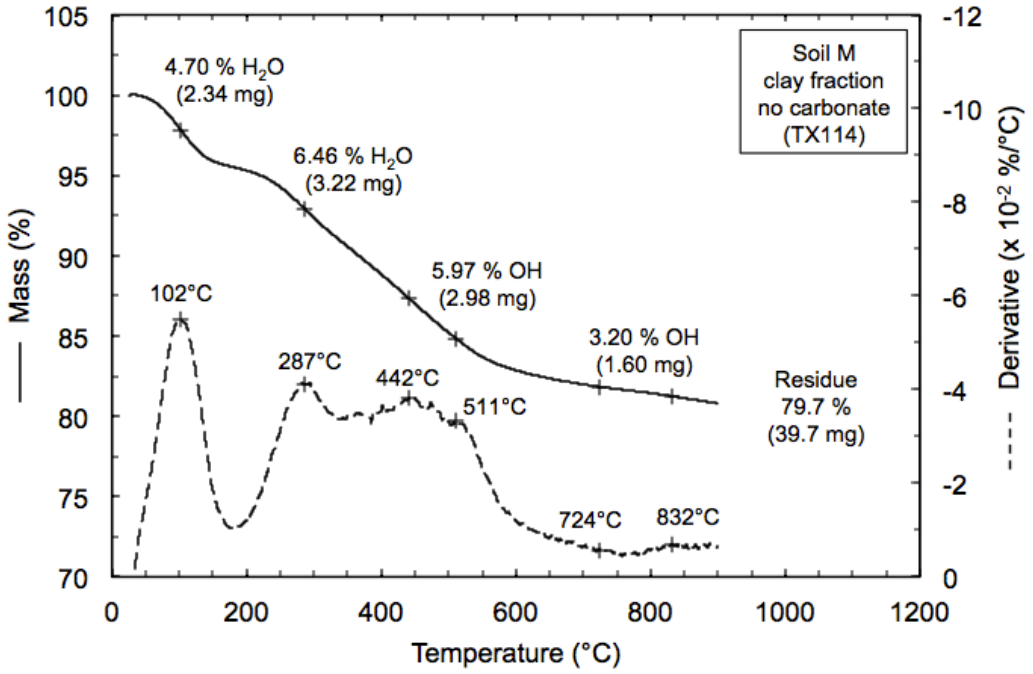

Figure C-22: Thermogravimetric analysis curve of the clay fraction (<2 µm) of soil M treated with sodium acetate-acetic acid solution (49.9 mg sample, 20°C/min heating rate, 20 mL/min N_2 purge)

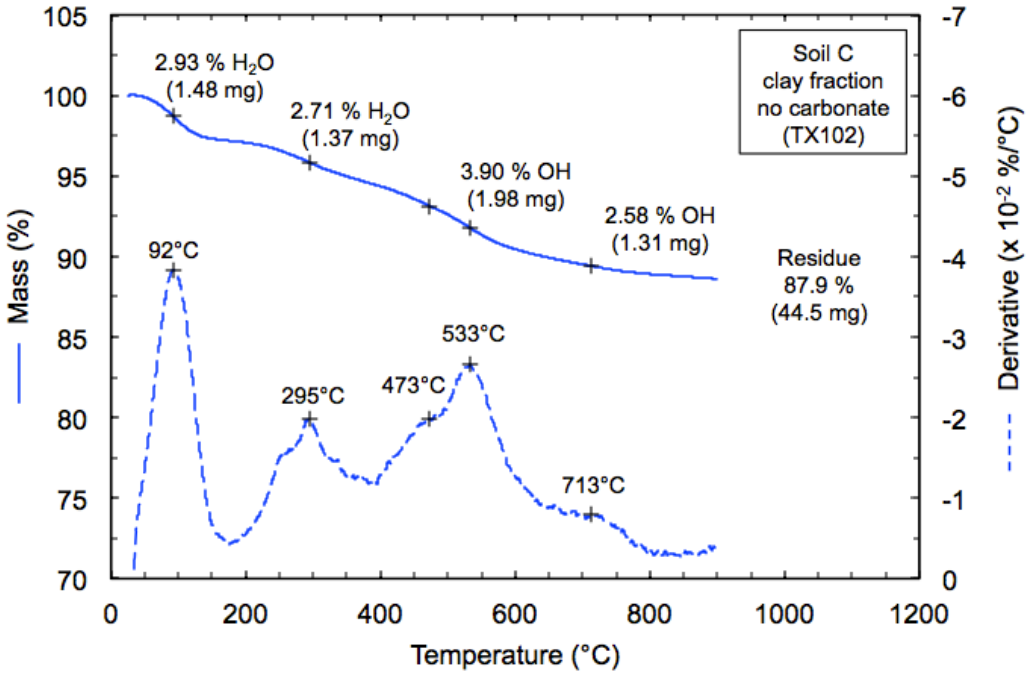

Figure C-23: Thermogravimetric analysis curve of the clay fraction (<2 µm) of soil C treated with sodium acetate-acetic acid solution (50.7 mg sample, 20°C/min heating rate, 20 mL/min N_2 purge)

C.4.3 Scanning Electron Microscopy (SEM)

Scanning electron microscopy was employed to gain insight into the microstructure of the two types of marl. Each sample was allowed to dry at room temperature for ~1 week and then broken to create a free fractured face that was mounted on a sampler holder using graphite paste (Figure C-24). All samples were imaged without coating. Images were obtained at the Purdue University's Life Science Microscopy facility with the FEI Quanta 3D FEG SEM using the low vacuum LVSED detector as well as the backscattered BSE detector (with 20kV, Spot 6.0, and 10mm WD). Magnifications ranged between 250x and 4000x. X-ray analysis (EDX) was done with an Oxford INCA Xstream-2 with Xmax80 detector (Oxford Instruments, Peabody, MA) using 20kV, 6.5 spot, 10mm WD, 50µm objective aperture, and P4. EDX was used to analyze the chemical composition of the objects of interest in the SEM.

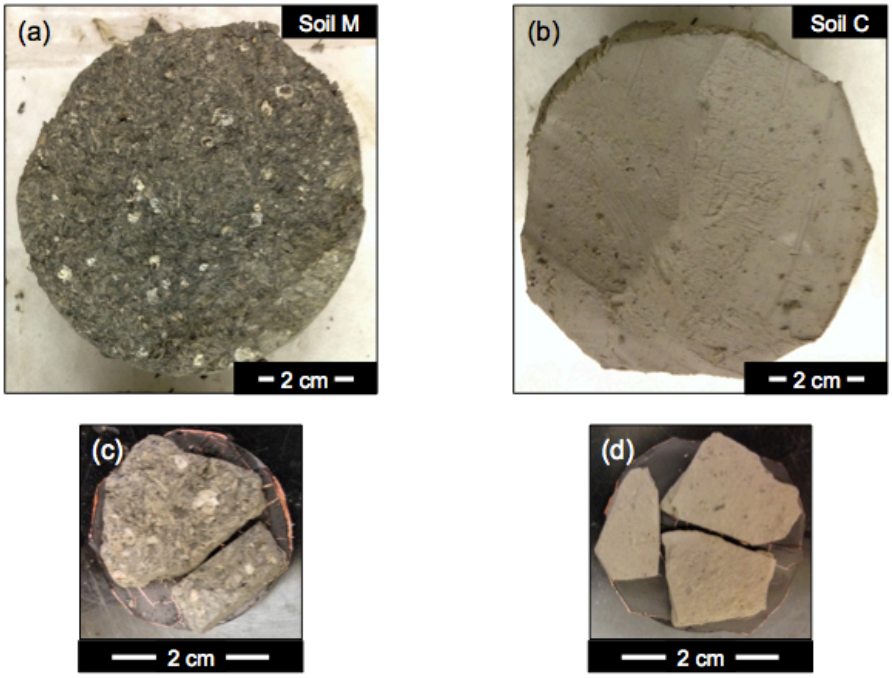

Figure C-24: (a)-(b) Samples immediately after removal from Shelby tubes, and (c)-(d) after mounting on holders for SEM analyses

Figure C-25 shows the scanning electron micrographs for soil M. The length in micrometers (μm) of each scale bar is given below the micrographs. The figures illustrate different types of microfossils and shells of snails (Figure C-25(a)) and bivalves (Figure C-25(b)) that are integrated into the soil matrix. Figure C-25(c) shows the presence of calcite crystals as part of the soil matrix resulting in a higher calcite content in soil M as reported in the XRD results. The micrographs also show the presence of 5 – 30 microns framboidal pyrite (iron sulfide), consisting of crystallites ranging from 0.5 – 3 microns (Figure C-25(d-f)). These different features were identified chemically using EDX.

Figure C-26 shows the scanning electron micrographs of soil C. the SEM observations confirm that there are no shells; however, iron sulfide was detected, although not in the framboidal form observed in soil M. This might be an indication of the different environmental conditions (e.g. presence of water, temperature) in which the soil was deposited. In general, soil M shows a more open microstructure compared with soil C, which is consistent with the higher void ratio reported in Section C.3.3 (soil M: e ~ 1.7; soil C: e ~ 1.2).

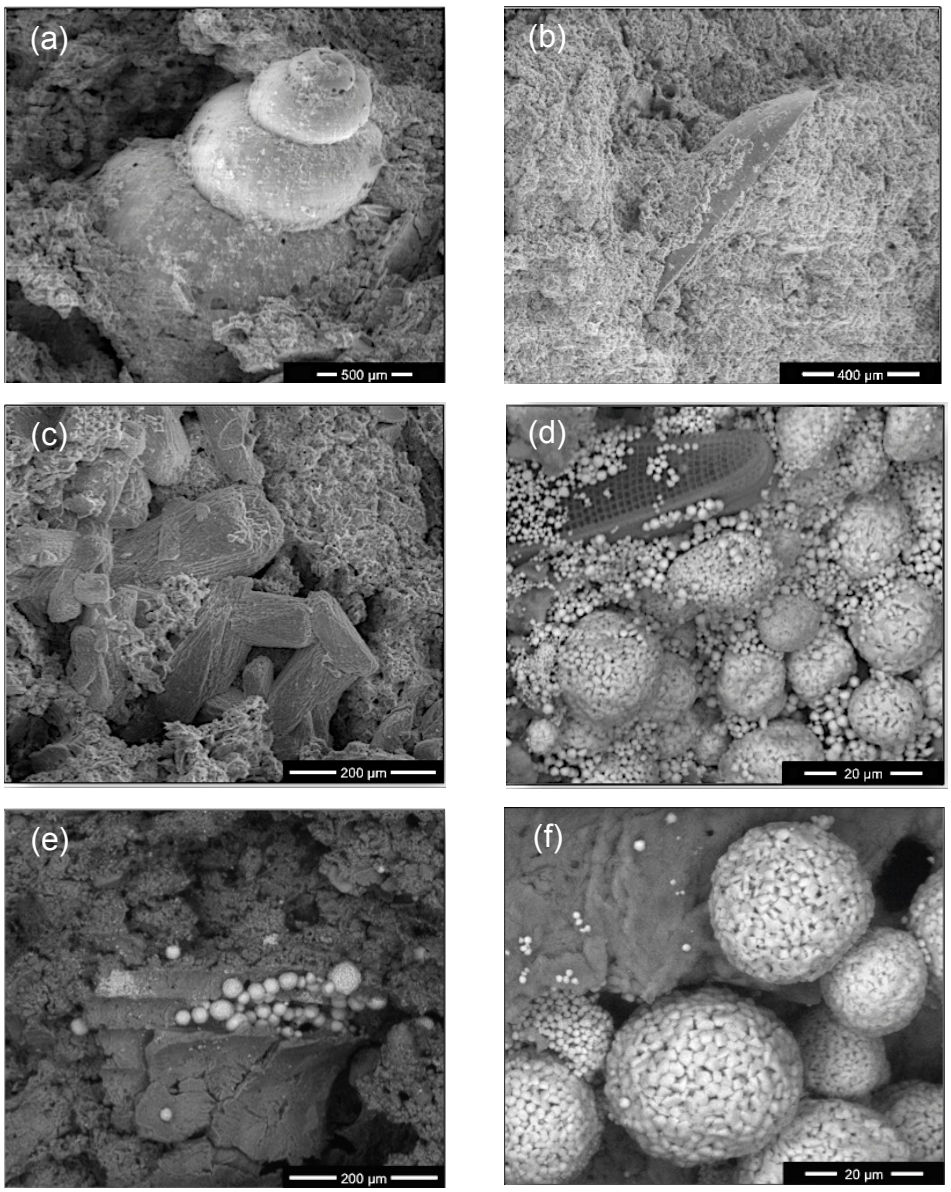

Figure C-25: Scanning electron micrographs for soil M showing different types of microfossils and framboidal pyrite that are integrated into the soil matrix

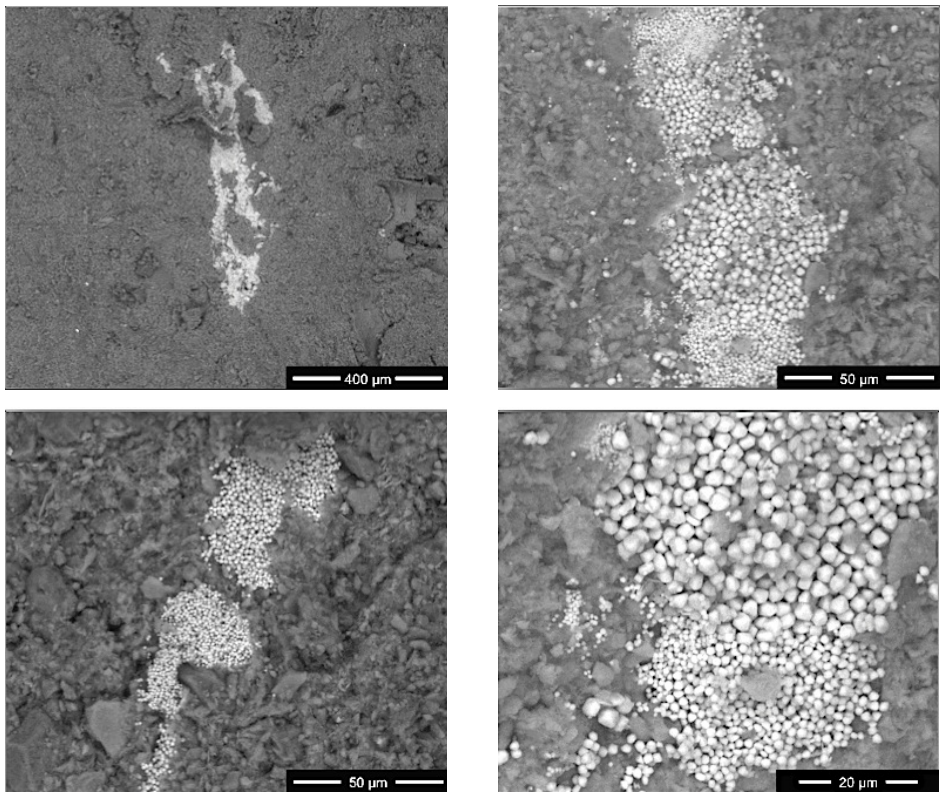

Figure C-26: Scanning electron micrographs for soil C

EDX was applied to map the distribution of chemical elements in the samples. This is a powerful tool that can aid in identifying the objects of interest in the SEM and detecting any trace minerals or metals that are present in the soil. For example, Figure C-27 shows how EDX was used to map the chemical elements in soil C. It can be seen that iron (Fe) and sulfur (S) are detected where the SEM analysis showed the existence of iron sulfide; whereas the soil matrix in the background has silicon (Si), oxygen (O), aluminum (Al) and calcium (Ca).

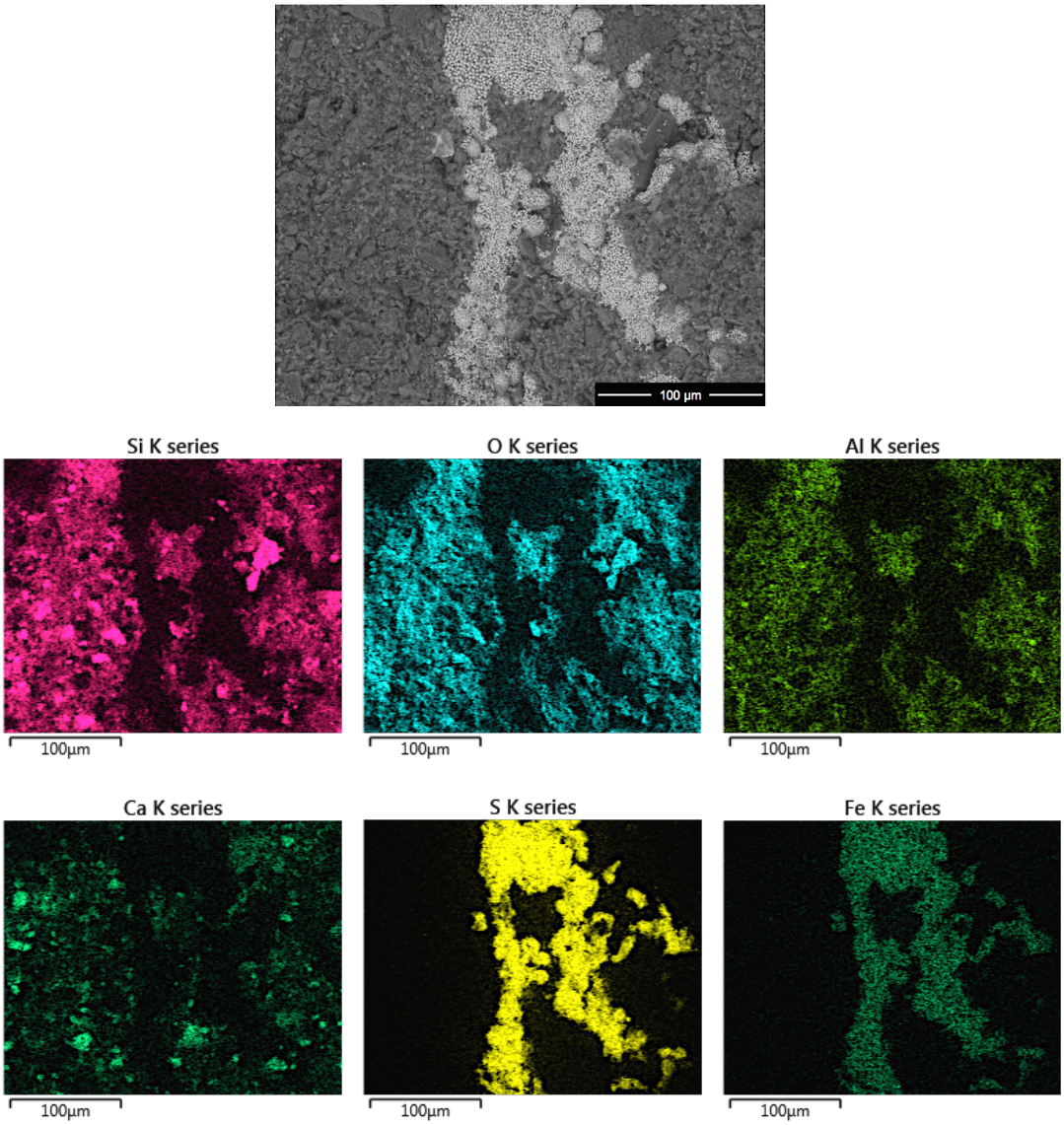

Figure C-27: EDX analysis for soil C identifying the different chemical elements

Appendix D. Engineering Properties

D.1 Introduction

This appendix provides a detailed evaluation of results from consolidation tests and triaxial tests, conducted on undisturbed samples of marl. The consolidation tests, performed using constant rate of strain (CRS) and incremental loading (IL), were used to derive the stress history, consolidation and creep properties, whereas the shear strength tests were used to derive the undrained shear strength profiles and the soil's SHANSEP parameters. Section D.2 summarizes the sample preparation and testing procedures used during consolidation and shear tests. The stress history and consolidation properties are summarized in Section D.3, while the undrained shear behavior is presented in Section D.4.

In this study, a total of seven CRS consolidation, four IL consolidation, and eleven triaxial tests were performed on marl samples obtained from different boreholes at various depths (a summary log is provided in APPENDIX I). Table D-1 and Table D-2 present a summary of the tests location, and index properties of soil M and soil C specimens, respectively. The index properties include: the carbonate content ($CaCO_3$), the natural water content (w_n), the plastic limit (PL), the liquid limit (LL), the clay content, the specific gravity (G_s), the in situ void ratio (e_0), the in situ degree of saturation (S_i), the total unit weight (γ_t), the salt concentration, and the pH.

Table D-1: Summary of tests location and index properties of soil M specimens

Test # Depth (m)	Boring Sample	$CaCO_3$ (%)	w_n (%)	PL (%)	LL (%)	Clay (%)	G_s	e_0	S_i (%)	γ_t (kN/m^3)	Salt conc (g/l)	pH
CRS103 6.83	MR#2 ST4	45.5	64.4	----	----	----	2.686	1.74	99	15.77	----	----
CRS105 9.27	MR#1 ST7	35.9	53.7	29.0	67.1	----	2.675	1.44	100	16.49	----	----
CRS106 8.10	MR#3 ST6	60.9	60.2	32.6	66.0	18	2.705	1.67	97	15.89	----	----
CRS108 8.67	MR#2 ST7	55.4	60.5	29.4	62.0	----	2.732	1.72	96	15.80	----	----
CRS110 7.59	MR#1 ST4	50.2	50.5	----	----	----	2.705	1.43	95	16.39	----	----
CRS112 7.02	MR#4 ST4	55.0	65.2	----	----	----	----	1.81	97	15.60	----	----
IL101 6.95	MR#2 ST4	48.8	66.6	----	----	----	2.686	1.82	98	15.56	2.14	7.66
IL103 9.11	MR#3 ST7	46.9	52.7	----	----	----	2.798	1.49	99	16.81	----	----
TX107 8.48	MR#3 ST6	59.6	58.4	34.7	61.7	16	2.713	1.63	98	16.05	3.33	7.82
TX108 7.01	MR#2 ST4	48.5	65.7	40.6	66.4	23	2.699	1.80	99	15.67	2.68	7.53
TX109 7.11	MR#2 ST4	54.6	65.9	33.8	65.7	22	2.706	1.81	99	15.68	3.15	7.91
TX111 7.06	MR#3 ST5	61.8	68.5	33.1	74.2	19	2.705	1.89	98	15.50	2.74	7.85
TX112 7.16	MR#3 ST5	60.6	68.5	37.9	66.4	18	2.701	1.86	99	15.59	3.15	7.71
TX114 7.44	MR#4 ST5	63	62.2	33.4	73.7	15	2.707	1.74	97	15.72	3.19	7.77

Table D-2: Summary of tests location and index properties of soil C specimens

Test # Depth (m)	Boring Sample	$CaCO_3$ (%)	w_n (%)	PL (%)	LL (%)	Clay (%)	G_s	e_0	S_i (%)	γ_t (kN/m^3)	Salt conc (g/l)	pH
CRS109 7.54	MR#1 ST4	33.9	42.1	----	----	----	2.789	1.20	98	17.66	----	----
IL104 7.87	MR#1 ST4	48.8	49.6	----	----	----	2.759	1.40	98	16.87	----	7.94
IL105 8.29	MR#1 ST4	39.5	48.7	----	----	----	----	1.36	99	17.15	----	----
TX102 8.31	MR#3 ST6	36.7	36.6	19.9	40.1	36	2.805	1.11	93	17.86	5.07	7.72
TX103 7.47	MR#1 ST4	34.7	39.7	21.3	46.7	45	2.789	1.14	98	17.90	4.51	7.80
TX105 7.67	MR#1 ST4	37.4	52.2	25.5	52.4	33	2.758	1.46	99	16.77	2.73	7.88
TX115 7.58	MR#4 ST5	33.7	47.0	20.0	47.7	45	2.771	1.32	99	17.20	----	----
TX116 7.66	MR#4 ST5	38.4	37.3	18.8	44.7	36	2.819	1.08	98	18.28	4.44	7.57

D.2 Specimen Preparation and Testing Procedures

D.2.1 Specimen Preparation

Specimens were prepared for all the engineering tests using the following procedure. The Shelby tube was cut above and below the selected specimens using a horizontal band saw with lengths appropriate for each consolidation or shear test to reduce disturbance due to extrusion. The remaining segments of the tube were resealed with wax and plastic caps and stored in the humid room for later use. The specimen was extruded following the method described by Ladd and DeGroot (2003). In summary, a piano wire was penetrated through the soil along the inside of the tube with the help of a thin hypodermic tube. The wire was used to debond the soil by rotating the tube 3-4 times. The specimen was then gently pushed by hand out of the tube. The resulting specimen, ~7.4 cm (~2.9 in) diameter, was trimmed in different manners and dimensions depending on the specific type of test (see Section D.2.2).

D.2.2 Testing Procedures

The general procedures of consolidation and triaxial tests include specimen setting up, saturation, consolidation, and undrained shearing (for triaxial test only). Since most of these steps are controlled by a computer and the techniques are well published (e.g. Shehan & Germaine, 1992; Hwang, 2006; and Germaine & Germaine, 2009), only a brief summary is provided.

CRS and IL consolidation tests were performed using computer controlled CRS apparatuses available at Purdue University's Bechtel geotechnical laboratory, which are based on the original apparatus developed by Wissa et al. (1971). All tests were conducted under single drainage conditions with measurements of the excess pore-water pressure at the base of the specimens. The extruded specimen described in Section D.2.1 was trimmed into a stainless steel confining ring (6.35 cm (2.5 in) diameter and 2.54 cm (1 in) height). Trimming was conducted by advancing the ring in small increments while trimming the soil ahead of the ring using a thin spatula to reduce disturbance caused by the ring advancement. The top and bottom ends of the specimen were cut with a wire saw and flattened with a razor-sharp stainless steel straight edge. Porous stones and filter papers were used at each end of the specimens. The specimen was backpressure saturated at constant volume to 200 kPa (29 psi) for a period of 24 hours. The saturation pressure and time were chosen based on the work reported by Black and Lee (1973), and they were also confirmed by satisfactory Skempton's pore-pressure parameters ($B = \Delta u/\Delta\sigma_{cell}$) measured in the triaxial tests. For CRS tests, consolidation was performed by imposing a constant rate of displacement equivalent to a strain rate varying between 1%/hr and 3%/hr. For IL tests, the consolidation was performed by doubling the applied load, i.e. load increment ratio (LIR) equals to one, and each load increment was maintained for 24 hours. An IL consolidation test can take several weeks to complete compared with the CRS consolidation test, which can be completed in much shorter period

of time and results in a continuous compression curve. However, IL consolidation tests were still needed in order to derive the creep properties of marl.

Triaxial tests were K_0 consolidated tests sheared under undrained conditions in compression loading ($CK_0UTC(L)$). The tests were performed using computer controlled triaxial apparatuses available at Purdue University's Bechtel geotechnical laboratory. The triaxial cell features an internal load cell to measure the axial load, eliminating the need to correct for the piston friction and uplift force caused by the cell pressure. Soil specimens were all trimmed using a wire saw into a cylindrical shape (3.8 cm (1.5 in) diameter and 7.6 cm (3 in) height). The top and bottom of the specimen were trimmed using a razor-sharp stainless steel straight edge. Porous stones and filter papers were used at each end of the specimens. Vertical filter drains (eight 6-mm wide filter strips) were used to provide lateral drainage and two thin membranes (i.e., non-lubricated prophylactics) were used to enclose the specimen and isolate it from the cell fluid. Silicon oil was used for the cell fluid for two main reasons: (i) prevent membrane leakage, and (ii) provide a non-conductive medium for the submerged load cell and its connections. Data were corrected for the change in the specimen area during deformation, membranes resistance, and filter drains resistance (Germaine & Ladd 1988). The specimens were all backpressure saturated to 200 kPa for 24 hours before consolidation, which resulted in an average B value of 0.99 ± 0.01SD for 11 triaxial tests. For all the triaxial tests, SHANSEP procedures were followed. After backpressure, the specimens were K_0 consolidated to stresses higher than $2\sigma'_p$, at a strain rate varying between 0.5%/hr and 2%/hr. The specimens were allowed to creep for a period of 24 hours to dissipate the excess pore pressure. They were either sheared normally consolidated (OCR = 1) or swelled to the desired OCR, where they were sheared following a second creep stage. All undrained shear stages were conducted using a strain rate of 0.5%/hr.

D.3 Stress History and Consolidation Properties

D.3.1 Introduction

This section provides a detailed evaluation of results from consolidation tests conducted on undisturbed samples of marl (soil M and soil C). The evaluation includes development of the stress history profile; determination of the compressibility properties, coefficient of consolidation, and permeability; estimation of the lateral stress ratio (K_0); and determination of the creep properties.

The consolidation data for marl were obtained from the CRS consolidation tests, the IL consolidation tests, and the consolidation phase of SHANSEP triaxial tests. The stress history profile and the compressibility properties were determined based on the compression curves from all tests. In addition, the lateral stress ratio was estimated from the K_0 consolidated triaxial tests. The CRS and IL consolidation tests provided information about the coefficient of consolidation and the permeability of the marl deposit. The IL consolidation tests were used to determine the creep properties.

The consolidation data for the CRS consolidation, IL consolidation, and SHANSEP $CK_0UTC(L)$ tests for soil M and soil C are summarized in Table D-3 and Table D-4, respectively. The tables give the tests location, the in situ phase data (w_n, e_0, and S_i), the overburden stress (σ'_{v0}), the preconsolidation stress (σ'_p), the overconsolidation ratio (OCR), the maximum virgin compression ratio (CR_{max}), the normally consolidated lateral stress ratio (K_{0NC}), and the consolidation strain rate (%/hr).

Table D-5 presents a summary of all consolidation properties for soil M and soil C. The following subsections will discuss the results of the various consolidation properties in greater detail.

Table D-3: Summary of consolidation data for the CRS consolidation, IL consolidation, and SHANSEP $CK_0UTC(L)$ tests for soil M

Test #	Boring	In situ			Stress history (kPa)			CR_{max}	Strain rate (%/hr)
Depth (m)	Sample	w_n (%)	e_0	S_i (%)	σ'_{v0}	σ'_p	OCR	K_{0NC}	
CRS103 6.83	MR#2 ST4	64.4	1.74	99	73.1	136	1.86	0.28 ----	1.0
CRS105 9.27	MR#1 ST7	53.7	1.44	100	89.4	193	2.16	0.23 ----	1.0
CRS106 8.10	MR#3 ST6	60.2	1.67	97	81.6	166	2.03	0.25 ----	1.0
CRS108 8.67	MR#2 ST7	60.5	1.72	96	85.4	175	2.05	0.26 ----	1.0
CRS110 7.59	MR#1 ST4	50.5	1.43	95	78.2	130	1.66	0.24 ----	2.0
CRS112 7.02	MR#4 ST4	65.2	1.81	97	74.4	161	2.17	0.28 ----	3.0
IL101 6.95	MR#2 ST4	66.6	1.82	98	73.8	153	2.07	0.29 ----	----
IL103 9.11	MR#3 ST7	52.7	1.49	99	88.3	151	1.71	0.24 ----	----
TX107 8.48	MR#3 ST6	58.4	1.63	98	84.1	154	1.83	0.28 0.495	2.0
TX108 7.01	MR#2 ST4	65.7	1.80	99	74.3	129	1.74	0.27 0.477	2.0
TX109 7.11	MR#2 ST4	65.9	1.81	99	75.0	129	1.72	0.27 0.483	2.0
TX111 7.06	MR#3 ST5	68.5	1.89	98	74.6	120	1.61	0.27 0.469	0.5
TX112 7.16	MR#3 ST5	68.5	1.86	99	75.3	133	1.77	0.28 0.492	0.5
TX114 7.44	MR#4 ST5	62.2	1.74	97	77.2	158	2.05	0.26 0.488	0.5

Table D-4: Summary of consolidation data for the CRS consolidation, IL consolidation, and SHANSEP $CK_0UTC(L)$ tests for soil C

Test # Depth (m)	Boring Sample	In situ			Stress history (kPa)			CR_{max} K_{0NC}	Strain rate (%/hr)
		w_n (%)	e_0	S_i (%)	σ'_{v0}	σ'_p	OCR		
CRS109 7.54	MR#1 ST4	42.1	1.20	98	77.8	118	1.52	0.24 ----	2.0
IL104 7.87	MR#1 ST4	49.6	1.40	98	80.0	111	1.39	0.19 ----	----
IL105 8.29	MR#1 ST4	48.7	1.36	99	82.9	116	1.40	0.24 ----	----
TX102 8.31	MR#3 ST6	36.6	1.11	93	82.9	91	1.10	0.16 0.559	1.0
TX103 7.47	MR#1 ST4	39.7	1.14	98	77.3	100	1.29	0.20 0.554	2.0
TX105 7.67	MR#1 ST4	52.2	1.46	99	78.7	118	1.50	0.28 0.569	2.0
TX115 7.58	MR#4 ST5	47.0	1.32	99	78.1	102	1.31	0.28 0.559	0.5
TX116 7.66	MR#4 ST5	37.3	1.08	98	78.6	94	1.20	0.24 0.532	0.5

Table D-5: Summary of consolidation properties

	Soil M		Soil C	
	Range	Mean ± SD	Range	Mean ± SD
Overburden stress, σ'_{v0} (kPa)	73.1 – 89.4	78.9 ± 5.7	77.3 – 82.9	79.5 ± 2.2
Preconsolidation stress, σ'_p (kPa)	120 – 193	149 ± 20.8	91.0 – 118	106 ± 10.9
Overconsolidation ratio, OCR	1.6 – 2.2	1.9 ± 0.2	1.1 – 1.5	1.3 ± 0.1
Virgin compression index, C_c	0.56 – 0.81	0.72 ± 0.08	0.34 – 0.67	0.52 ± 0.11
Maximum virgin compression ratio, CR_{max}	0.23 – 0.29	0.26 ± 0.02	0.16 – 0.28	0.23 ± 0.04
Permeability change index, C_k	0.648 – 0.709	0.671 ± 0.029	0.529	0.529
Normally consolidated lateral stress ratio, K_{0NC}	0.469 – 0.495	0.484 ± 0.010	0.532 – 0.569	0.555 ± 0.014
$K_0 = K_{0NC}(OCR)^n$	K_{0NC} = 0.48; n = 0.40		K_{0NC} = 0.55; n = 0.37	
$C_{\alpha e}/C_c$	0.041		0.036	
$\Delta e/e_0$	0.016 – 0.049	0.033 ± 0.009	0.027 – 0.055	0.041 ± 0.009

D.3.2 Compression Curves

A total of 22 one-dimensional compression curves obtained from IL consolidation tests, CRS consolidation tests, and the K_0-consolidation stage of triaxial tests performed on undisturbed samples of marl are presented in Figure D-1, where the dashed black lines represent soil M and the continuous blue lines represent soil C. In general, both types of marl show similar compressibility properties that fall in the range of soft clays. Figure D-1(a-b) show the compression curves in the void ratio- effective stress space, whereas Figure D-1(c-d) show the compression curves in the strain- effective stress space. All results show a consistent behavior, i.e., the compression curves are characterized by a clear break in correspondence to the preconsolidation stress σ'_p, and have an S-shape, which is evidence of the soil's high sensitivity. This S-shape is more pronounced for soil C and the compression curves are characterized by a larger decrease in the virgin compression ratio (CR) along the virgin compression line (VCL) compared with soil M.

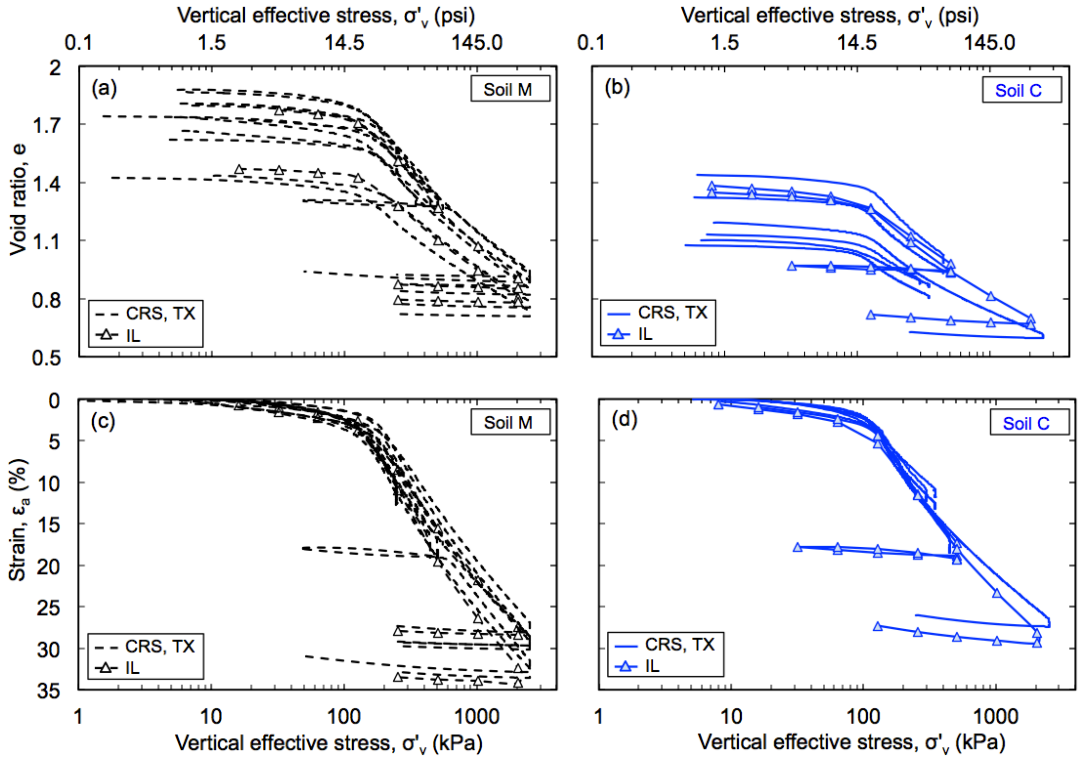

Figure D-1: e- compression curves for (a) soil M and (b) soil C and ε- compression curves for (c) soil M and (d) soil C from CRS, IL consolidation and SHANSEP $CK_0UTC(L)$ tests

D.3.3 Stress History Profile

When building on soft soils, it is essential to develop a reliable stress history profile, which is most useful for: (i) estimation of long term consolidation settlements that are highly affected by the amount of precompression ($\sigma'_p - \sigma'_{v0}$); and (ii) estimation of the undrained shear strength of marl, which is directly related to the vertical effective stress and OCR via the SHANSEP equation (see Section D.4).

Figure D-2 presents the stress history for the marl deposit. Overburden stress (σ'_{v0}), preconsolidation stress (σ'_p), and OCR are tabulated for all tests in Table D-3 and Table D-4. The overburden (effective) stress (σ'_{v0}) profile was calculated by subtracting the pore water pressure (u_0) from the total overburden stress (σ_{v0}). The total overburden stresses were calculated based on the soil profiles and estimated unit weights shown in Figure B-2. The pore water pressure profile was calculated based on hydrostatic water pressures with water table located at 1.9 m (6.25 ft) below the ground surface, as reported in Section B.2. The preconsolidation stress was estimated using the strain energy technique proposed by Becker et al. (1987), which is based on the work per unit volume. This method is less subjective and less empirical compared with other methods proposed in the literature (e.g., Casagrande, 1936 and Schmertmann, 1955) and can be easily computerized.

Figure D-2(a) and Figure D-2(b) show the variation with depth of preconsolidation stress and overconsolidation ratio, respectively. Different symbol shapes are used to indicate different types of tests (square, triangle and circle for CRS consolidation, IL consolidation, and TX tests, respectively), while different colors are used to indicate the different types of marl (hollow black symbols correspond to soil M and solid blue circles correspond to soil C). In general, there is no clear difference between the results obtained from the different types of tests (CRS, IL, and TX). However, a clear difference can be observed between soil M and soil C.

The preconsolidation stress for soil M shows an increasing trend with depth ranging between 120 and 193 kPa (mean σ'_p = 149 kPa ± 20.8SD). This trend was not observed for soil C due to the limited number of data points and the significant scatter; however, its average preconsolidation stress (mean σ'_p = 106 kPa ± 10.9SD) is lower than that of soil M. These stresses correspond to OCR ($=\sigma'_p/\sigma'_{v0}$) values around 1.9 ± 0.2SD for soil M and around 1.3 ± 0.1SD for soil C (see Figure D-2(b)). The higher values of OCR for soil M might be attributed to the natural cementation caused by the higher carbonate content present in soil M, as illustrated by the mineralogical analysis (Section C.4.1.3).

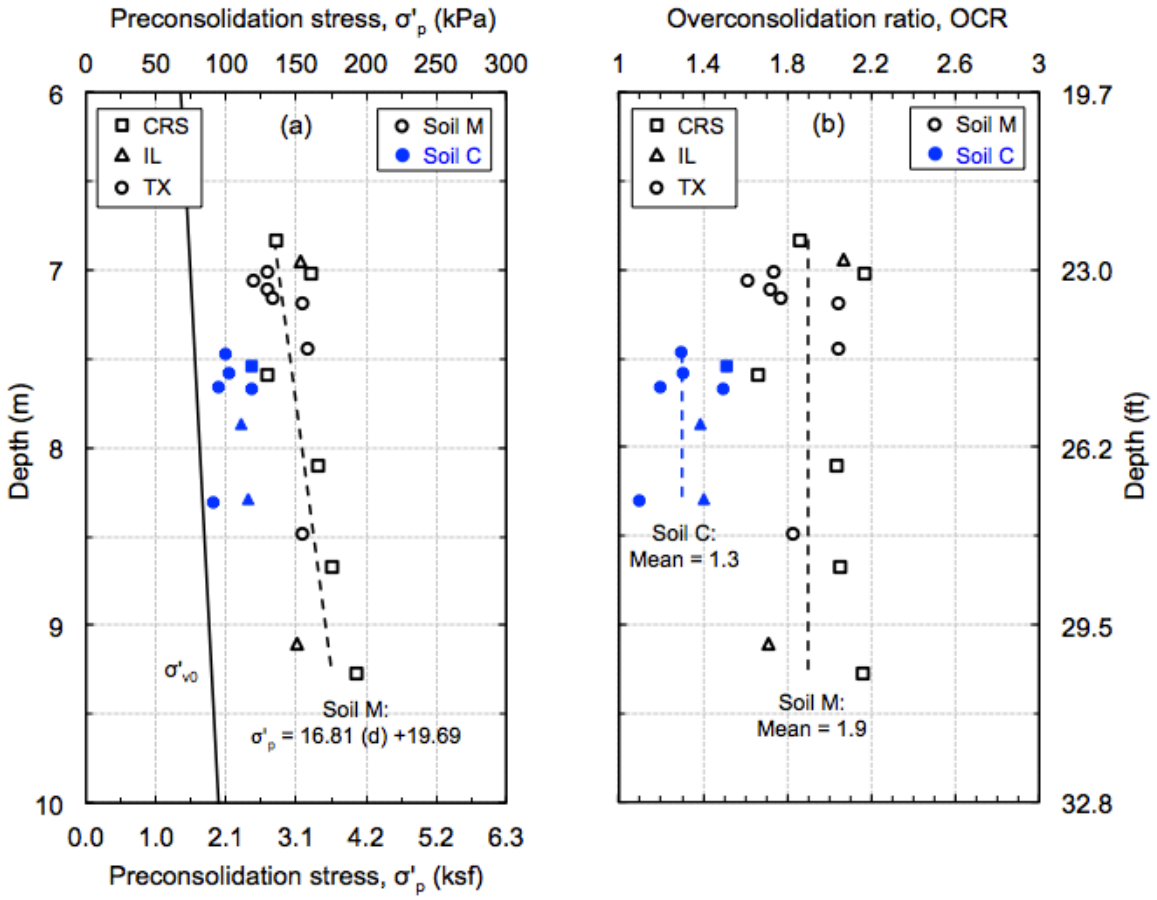

Figure D-2: Stress history profile: (a) preconsolidation stress and overburden stress; and (b) OCR with depth

D.3.4 Compressibility

The virgin compression index (C_c) and compression ratio ($CR=C_c/(1+e_0)$) were obtained for each CRS consolidation, IL consolidation, and triaxial test. In order to the obtain comparable results that are not influenced by the S-shape observed in the compression curves (see Section D.3.2), the maximum values of C_c and CR were derived from the consolidation curves between 2 σ'_p and 3 σ'_p, and their variation with depth is presented in Figure D-3. The maximum compression ratio for all tests is reported in Table D-3 and Table D-4.

In general, there is no clear difference between the results obtained from the different types of tests (CRS, IL, and TX). However, a clear difference can be observed between soil M and soil C. As shown in Figure D-3(a), the compression index for soil M shows a decreasing trend with depth ranging between 0.56 and 0.81 (mean C_c = 0.72 ± 0.08SD), which is expected since the initial void ratio (e_0) also decreases with depth (Section C.3.3). This is consistent with the trends reported in the literature relating C_c and e_0 (see discussion below). This trend was not observed for soil C due to the limited number of data points and the significant scatter; however, its average compression index (mean C_c = 0.52 ± 0.11SD) is lower than that of soil M. Given the values of C_c as high as 0.8, marl can be classified as highly compressible. As a reference, typical values of the compression index for other soils obtained from the literature are presented in Table D-6.

Figure D-3(b) plots the variation of compression ratio with depth. Since the values of CR are obtained by normalizing with the initial void ratio, it can be seen that the results are more uniform, with a collective average value of CR equals to 0.25 ± 0.03SD.

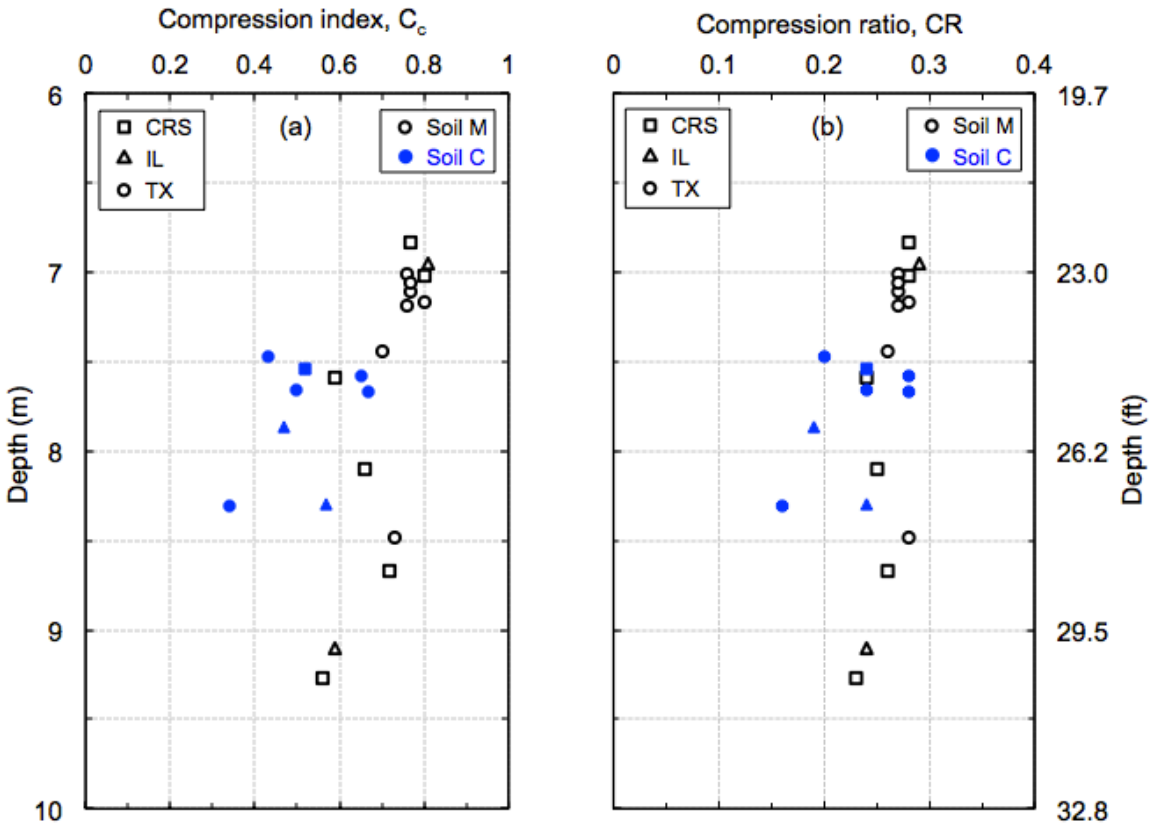

Figure D-3: Values of (a) compression index, and (b) compression ratio with depth

Table D-6: Typical values of the compression index C_c (modified after Holtz & Kovacs, 1981)

Soil	C_c
San Francisco Bay Mud (CL)	0.4 to 1.2
San Francisco Old Bay clays (CH)	0.7 to 0.9
Vicksburg buckshot clay (CH)	0.5 to 0.6
Bangkok clay (CH)	0.4
Boston blue clay (CL)	0.3 to 0.5
Chicago silty clay (CL)	0.15 to 0.3

The virgin compression index (C_c) and compression ratio (CR) are necessary for settlement calculation. These parameters are found from consolidation tests conducted on undisturbed soil samples. Because of the time and expense involved in consolidation testing, several researchers (e.g. Nishida, 1956; and Terzaghi & Peck, 1967) have investigated alternative ways to obtain the values

of compressibility of clayey soils. The compression index can be related to the physical properties of soils such as: initial void ratio, natural water content, and liquid limit. Table D-7 summarizes some of the relationships reported in the literature.

Table D-7: Summary of consolidation data for the CRS consolidation, IL

Equations	Applicability	References
$C_c = 0.54\ (e_0 - 0.35)$ $C_c = 0.01404\ (w_n - 13.46)$	Natural soils ($S_t < 1.5$)	Nishida (1956)
$C_c = 0.4\ (e_0 - 0.25)$ $C_c = 0.01\ (w_n - 5)$	All natural soils	Azzouz et al. (1976)
$C_c = 0.75\ (e_0 - 0.50)$	Soils with low plasticity (moderately sensitive, $S_t < 5$)	Bowles (1979)
$C_c = 0.01\ w_n$	Chicago & Alberta clays ($S_t < 1.5$)	Koppula (1981)
$C_c = 0.009\ (LL - 10)$	Natural clays (moderately sensitive, $S_t < 5$)	Terzaghi & Peck (1967)

Note: S_t = Sensitivity of the soil

As expected, these proposed relationships differ from each other since they are based on different types of soils. As an attempt to obtain correlations that are more applicable for the marl deposit, the compression index was plotted against the initial void ratio, natural water content, and liquid limit in Figure D-4, Figure D-5, and Figure D-6, respectively. Using linear regression analysis, the following equations for marl are proposed:

$$C_c = 0.451\ (e_0 - 0.104) \qquad (r^2 = 0.861) \qquad \text{(Eq. D-1)}$$

$$C_c = 0.012\ (w_n + 1) \qquad (r^2 = 0.873) \qquad \text{(Eq. D-2)}$$

$$C_c = 0.010\ (LL + 6.8) \qquad (r^2 = 0.602) \qquad \text{(Eq. D-3)}$$

In general, the first two equations yield C_c values that are close to the ones proposed by Nishida (1956) (Table D-7). However, when soil M and soil C are considered separately, the regression analysis for soil C yields a correlation ($C_c = 0.746\ (e_0 - 0.52)$) that is very close to the one proposed by Bowles (1979) for

moderately sensitive soils with low plasticity; while the one for soil M (C_c = 0.51 (e_0 – 0.304)) is very close to the one proposed by Nishida (1956) for natural soils. This is in good agreement with the fact that soil C has relatively lower plasticity (CL) and higher sensitivity (depicted by the strong S-shape compression curves) compared with soil M.

Note that the coefficient of determination for the third equation (C_c vs LL) is relatively low (r^2 = 0.602), which might be partially caused by the fundamental differences between the mineralogy of soil M and soil C, as illustrated by the mineralogical analysis (Section C.4.1.3).

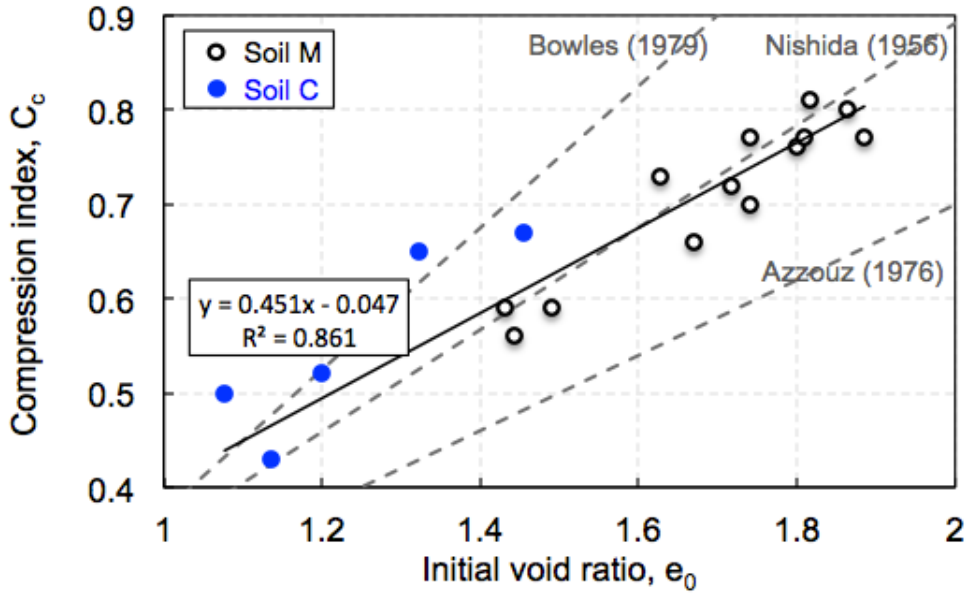

Figure D-4: Compression index versus initial void ratio

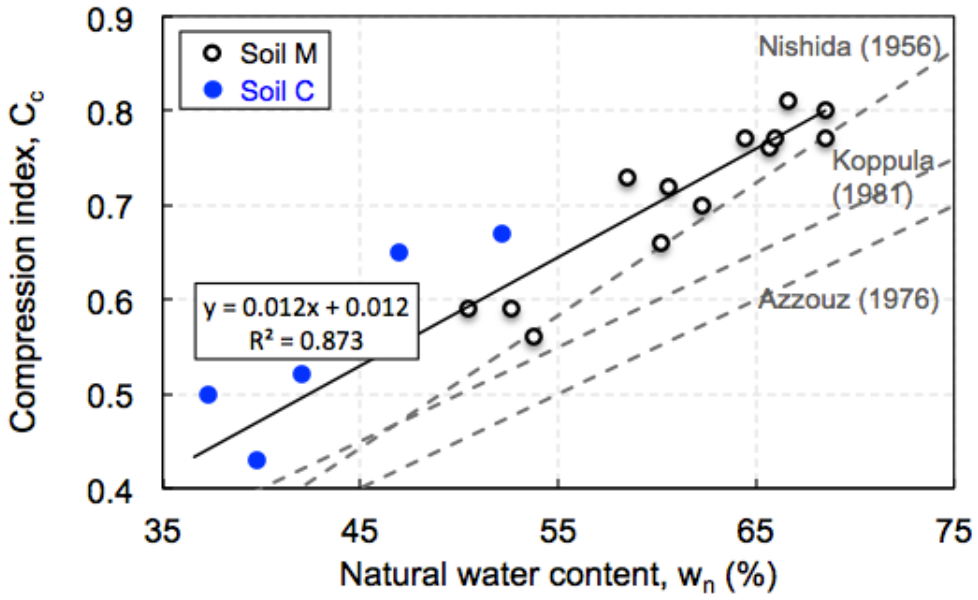

Figure D-5: Compression index versus natural water content

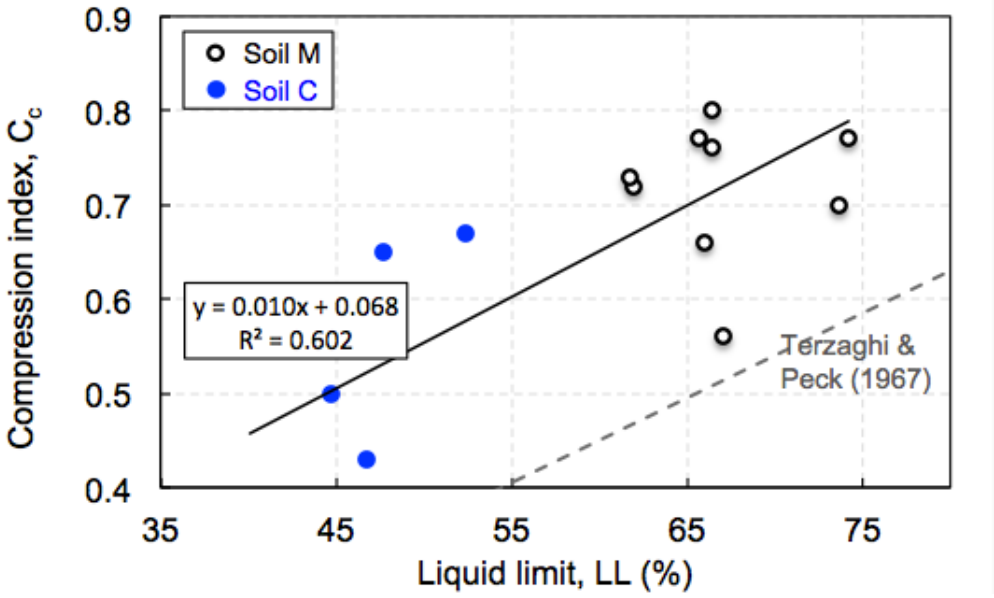

Figure D-6: Compression index versus liquid limit

D.3.5 Coefficient of Consolidation and Permeability

This section presents a summary of the coefficients of consolidation (C_v) and the permeability (k) of marl. The results presented are based on six CRS consolidation tests and four IL consolidation tests.

For the CRS consolidation tests, the values of k and C_v are calculated based on the CRS consolidation theory developed by Wissa et al. (1971). The permeability is first calculated from the excess pore pressure (u_e) recorded at the base of the specimen due to loading, and then C_v is calculated from the permeability and compressibility using the following equation:

$$C_v = k / (m_v \cdot \gamma_w) \qquad \text{(Eq. D-4)}$$

where k is the permeability, mv ($=\Delta\varepsilon/\Delta\sigma'_v$) is the coefficient of volume change, and γ_w is the unit weight of water.

For the IL consolidation tests, the values of C_v represent the average of the logarithm of time (Casagrande, 1936) and the square root of time (Taylor, 1948) curve fitting methods. The logarithm of time method is based on similarity between theoretical and experimental curves when plotted versus log of time; it uses the time corresponding to 50% consolidation (t_{50}) to calculate C_v. For the square root of time, however, curves are plotted versus the square root of time and t_{90} corresponding to 90% consolidation is used for C_v calculation. The values of k are then calculated from C_v and m_v using the above equation.

Figure D-7 shows the coefficient of consolidation versus the vertical effective stress for the loading and unloading range obtained from CRS (denoted by lines) and IL (denoted by triangles) consolidation tests. The results show a decrease in C_v during loading followed by a slight increase in the normally consolidated region. For all tests, the results are characterized by an increasing value of C_{vNC}, similar trends were reported by Berman (1993) and Abdulhadi (2009). As a

reference, typical values of the coefficient of consolidation for other soils obtained from the literature are presented in Table D-8.

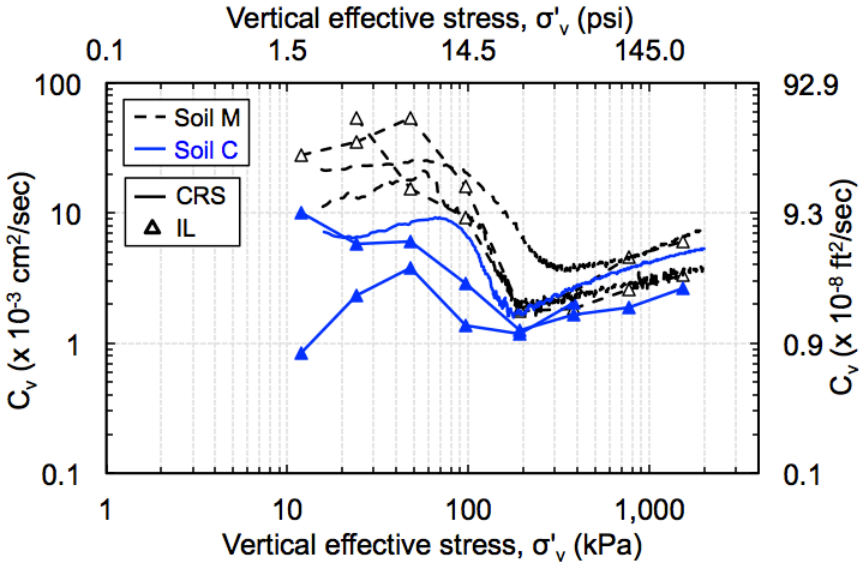

Figure D-7: Coefficient of consolidation versus vertical effective stress from CRS and IL consolidation tests

Table D-8: Typical values of the coefficient of consolidation C_v (modified after Holtz & Kovacs, 1981)

Soil	C_v (x 10^{-4} cm^2/s)
Boston blue clay (CL)	40 ± 20
Chicago silty clay (CL)	8.5
San Francisco Bay Mud (CL)	2 to 4
Glacial lake clays (CL)	6.5 to 8.7
Mexico City clay (MH)	0.9 to 1.5

The void ratio (e) versus the log of the permeability during loading is shown in Figure D-8. The decrease in permeability with compression is due to the reduction in the size of the macropores. As can be seen, there is an approximate linear relationship between the void ratio and log-k. The slope of the e-log k line is referred to as the permeability change index and denoted by C_k. In general,

soil M has a C_k value higher than soil C. The average value of C_k is 0.671 ± 0.029SD for soil M and 0.573 ± 0.062SD for soil C.

Tavenas et al. (1983) examined the permeability of different natural soils and suggested that for clay and silt deposits C_k/e_0 = 0.5. Figure D-9 shows that the empirical correlation for marl deposits is C_k/e_0 = 0.42. This value is similar to the one reported by Berman (1993) for Boston blue clay.

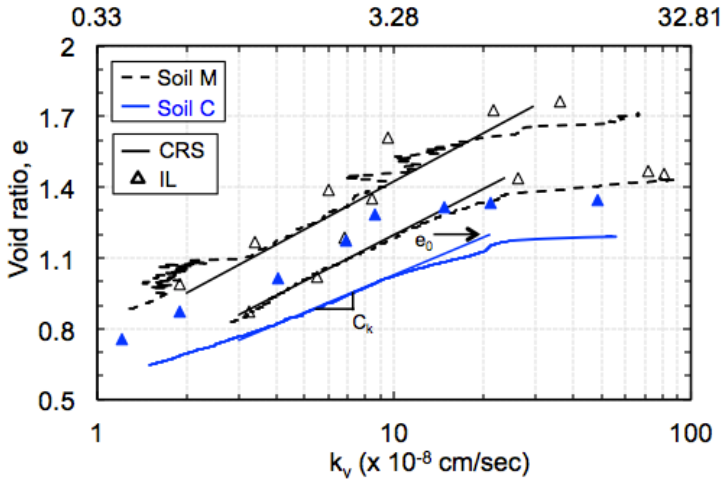

Figure D-8: Void ratio versus permeability from CRS consolidation tests

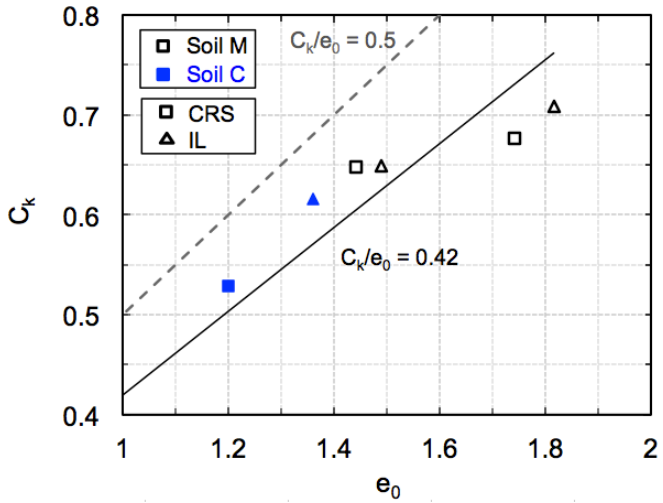

Figure D-9: C_k versus initial void ratio from CRS consolidation tests

D.3.6 Lateral Stress Ratio K_0

The lateral stress ratio (or coefficient of earth pressure) at rest, K_0 ($=\sigma'_h/\sigma'_v$) is an important soil parameter used in many geotechnical applications. For instance, it is necessary for the estimation of the in situ horizontal stresses (σ'_h). Values of K_0 were derived from the K_0-consolidation stage of the triaxial tests.

Figure D-10 presents the variation of K_0 with vertical effective stress for each of the tests performed. The figure shows that K_0 decreases as the specimen is loaded, reaches a minimum and then increases again reaching a constant value in the normally consolidated region, which is referred to as the normally consolidated value of K_0 (K_{0NC}). This behavior is typical of structured soils. The average value of K_{0NC} for soil C (0.555) exceeds that of soil M (0.484). This is consistent with the friction angle values measured on these two soils (see Section D.4). Upon unloading K_0 increases once again.

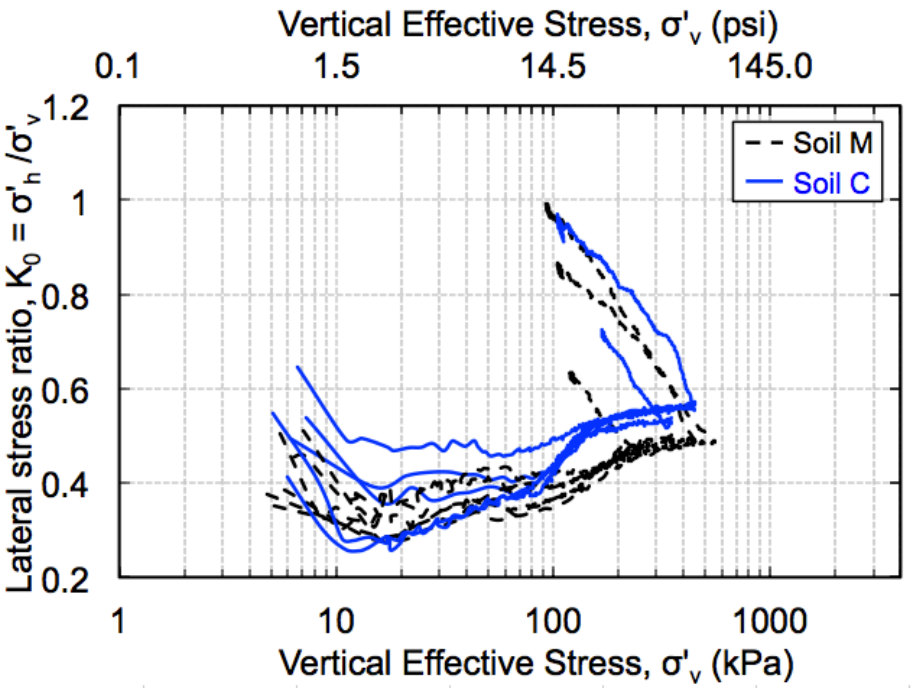

Figure D-10: Lateral stress ratio versus vertical effective stress from consolidation phase of SHANSEP $CK_0UTC(L)$ tests

Schmidt (1966) and Alpan (1967) developed an empirical equation that links OCR to K_0 as shown below:

$$K_0 = K_{0NC} (OCR)^n \qquad \text{(Eq. D-5)}$$

where K_0 is the lateral stress ratio, K_{0NC} is the normally consolidated value of K_0, OCR is the overconsolidation ratio, and n is a constant. This equation was used to estimate K_0 as a function of OCR for the marl deposit. To do so, five of the eleven triaxial tests were swelled to different OCR values (OCR=2.0, 4.1, and 5.8) following K_0 conditions, i.e. the volumetric strain (ε_v) is always equal to the axial strain (ε_a), hence maintaining a constant cross-sectional area at all time, and the overconsolidated lateral stress ratio was calculated (K_{0OC}). Figure D-11 plots the lateral stress ratio (overconsolidated and normally consolidated) versus OCR on a log-log plot. The data lie on two straight lines that can be represented by K_{0NC} = 0.48, n = 0.40, and r^2 = 1.00 for soil M; and K_{0NC} = 0.55; n = 0.37; and r^2 = 0.99 for soil C.

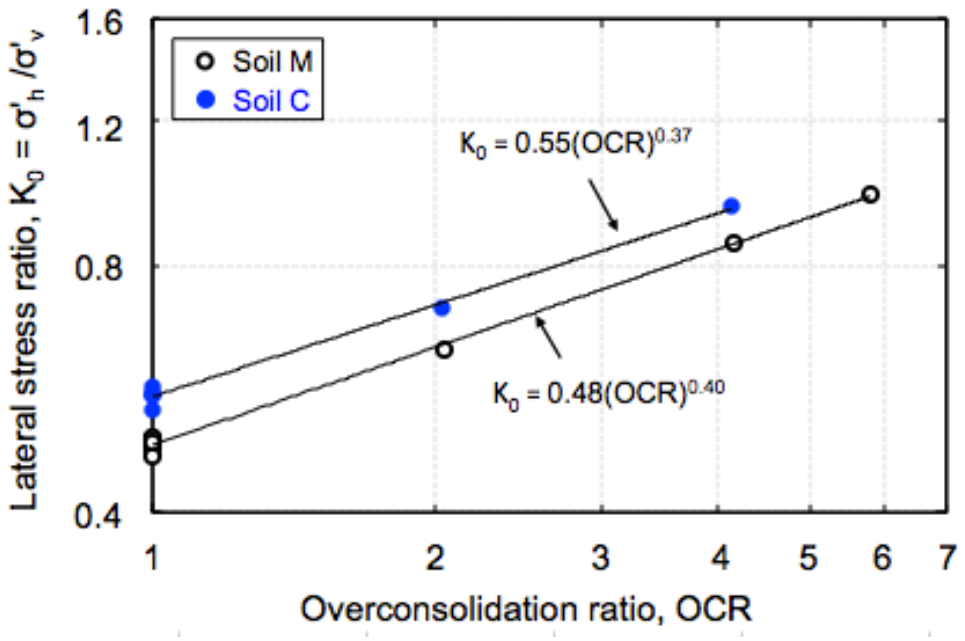

Figure D-11: Lateral stress ratio versus oversonsolidation ratio from consolidation phase of SHANSEP $CK_0UTC(L)$ tests

D.3.7 Creep Properties

Mesri and Godlewski (1977) developed the C_α/C_c concept of compressibility for the analysis of secondary settlement. The authors studied the compressibility of wide variety of natural soils and showed that for any one soil there is a unique relationship between the secondary compression index $C_{\alpha e} = \Delta e/\Delta \log t$ and the compression index $C_c = \Delta e/\Delta \log \sigma'_v$. This relationship holds true at all combinations of time, effective stress, and void ratio. For most soils, $C_{\alpha e}/C_c$ varies between 0.02 to 0.08, with an average value of about 0.05. Typical values of $C_{\alpha e}/C_c$ for natural soils are summarized in Table D-9.

Table D-9: Values of $C_{\alpha e}/C_c$ for natural soils (modified after Mesri & Godlewski, 1977)

Soil	$C_{\alpha e}/C_c$
Peat	0.075 to 0.085
San Francisco Bay Mud	0.04 to 0.06
Calcareous organic silts	0.035 to 0.06
Leda clay (Canada)	0.03 to 0.06
Mexico City clay	0.03 to 0.035
Soft blue clay (Victoria, B.C.)	0.026

According to the concept of compressibility, the secondary compression behavior of any one soil can be defined from the value of $C_{\alpha e}/C_c$ and the end-of-primary (EOP) e-log σ'_v compression curve. This concept was adopted in this research and the ratio $C_{\alpha e}/C_c$ was calculated for marl using four IL consolidation tests. Figure D-12 plots the secondary compression index $C_{\alpha e}$ versus the compression index C_c. These values were determined graphically from all increments (both in the overconsolidated and normally consolidated range) according to the method proposed by Mesri and Castro (1987). The authors reported that near the preconsolidation stress σ'_p, the slope e versus log σ'_v, i.e., C_c, significantly increases with the increase in σ'_v. Therefore, care must be exercised in choosing the corresponding values of $C_{\alpha e}$ and C_c. The value of C_c is not simply the slope of

the e-log σ'_v curve at the EOP consolidation, but it is the slope at the same void ratio at which $C_{\alpha e}$ was selected.

As shown in Figure D-12, the results lie on straight line with a slope ($C_{\alpha e}/C_c$) equals to 0.041 for soil M (r^2 = 0.99) and 0.036 for soil C (r^2 = 0.97). This value falls in the range of soils with relatively high creep rate (Mesri & Godlewski, 1977).

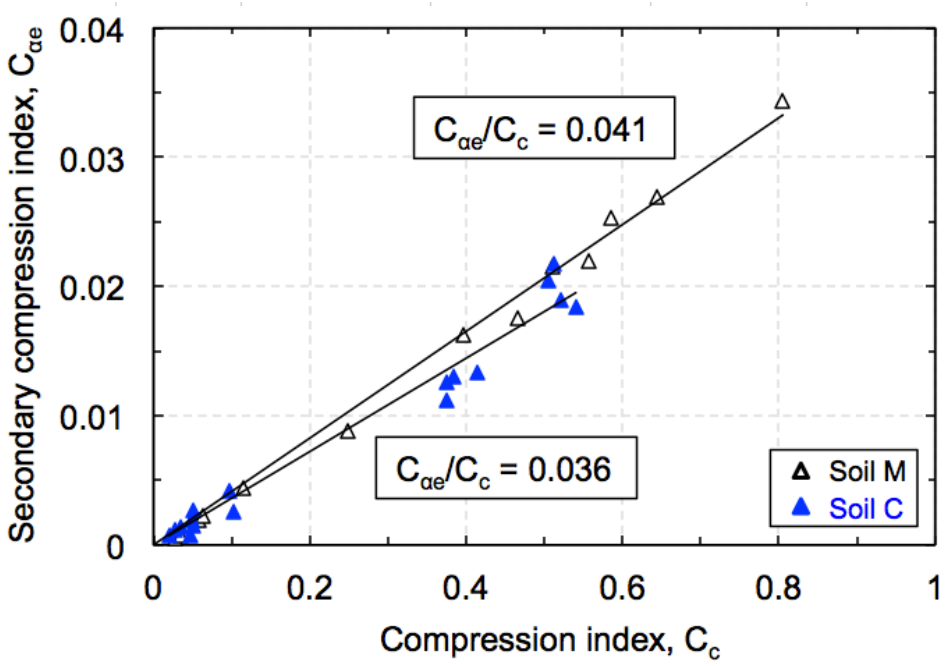

Figure D-12: Relationship between secondary compression index and compression index for marl.

D.3.8 Assessment of sample quality

Sample disturbance is the most significant issue affecting the quality and reliability of laboratory test data for soft soils. Santagata et al. (2006) defined sampling disturbance as the alteration of the true in situ soil properties due to sampling operation. The authors stated that disturbance might result from drilling, sampler penetration, sample retrieval, transportation, storage, extrusion, and preparation for laboratory testing. There has been a large effort on quantifying this disturbance. Table D-10 summarizes the two common methods used for quantitative evaluation of sample quality: the Sample Quality Designation (SQD) method (Terzaghi et al., 1996) and the Norwegian Geotechnical Institute (NGI) method (Lunne et al., 1997). The SQD method quantifies the sampling

disturbance based on the reconsolidation volumetric strain (ε_v), i.e. the volumetric strain required to reconsolidate the soil specimen to the in situ stresses. Specimens are ranked from A to E; where very good quality specimens that experienced little strains during reconsolidation are classified as A and the poorest quality specimens that experienced large strains are classified as E. The NGI method, on the other hand, proposes that the normalized change in void ratio ($\Delta e/e_0$) may be a good parameter for evaluating sample quality, where Δe is the change of the void ratio associated with reconsolidation of the soil to the in situ stresses and e_0 is the initial void ratio. This method is more robust because it is also dependent on OCR. According to the criterion proposed by Lunne et al. (1997) for evaluating sample disturbance, for OCR values between 1 and 2, the quality of soil specimen is considered to be "very good to excellent" if $\Delta e/e_0$ is less than 0.04; "good to fair" if $\Delta e/e_0$ is between 0.04 and 0.07; "poor" if $\Delta e/e_0$ is between 0.07 and 0.14; and "very poor" if $\Delta e/e_0$ is greater than 0.14.

Table D-10: Quantification of sampling disturbance based on specimen volume change during laboratory reconsolidation to σ_{v0}' (adapted from DeGroot, 2003)

Specimen Quality Designation (SQD) (Terzaghi et al. 1996)		$\Delta e/e_0$ (Lunne et al. 1997)		
Volumetric Strain (%)	SQD	OCR = 1-2	OCR = 2-4	Rating
		$\Delta e/e_0$	$\Delta e/e_0$	
< 1	A	< 0.04	< 0.03	Very good to excellent
1 – 2	B	0.04 – 0.07	0.03 – 0.05	Good to fair
2 – 4	C	0.07 – 0.14	0.05 – 0.10	Poor
4 – 8	D	> 0.14	> 0.10	Very poor
> 8	E			

Both evaluation methods were employed to assess the quality of the specimens tested in this study. Variations in $\Delta e/e_0$ obtained from the consolidation (CRS and IL) tests, and the K_0 consolidation phase of triaxial tests are shown in (a). All the data fall below 0.055, indicating that the samples can be designated as "excellent" to "good" based on the NGI method suggested by Lunne et al. (1997). This

highlights the effectiveness of the techniques used in this study (i.e., drilling using mud rotary, sampling using fixed piston sampler, extrusion using a piano wire to debond the soil along the inside of the tube, trimming using wire saw) to obtain high quality and reliable laboratory test data for soft soils.

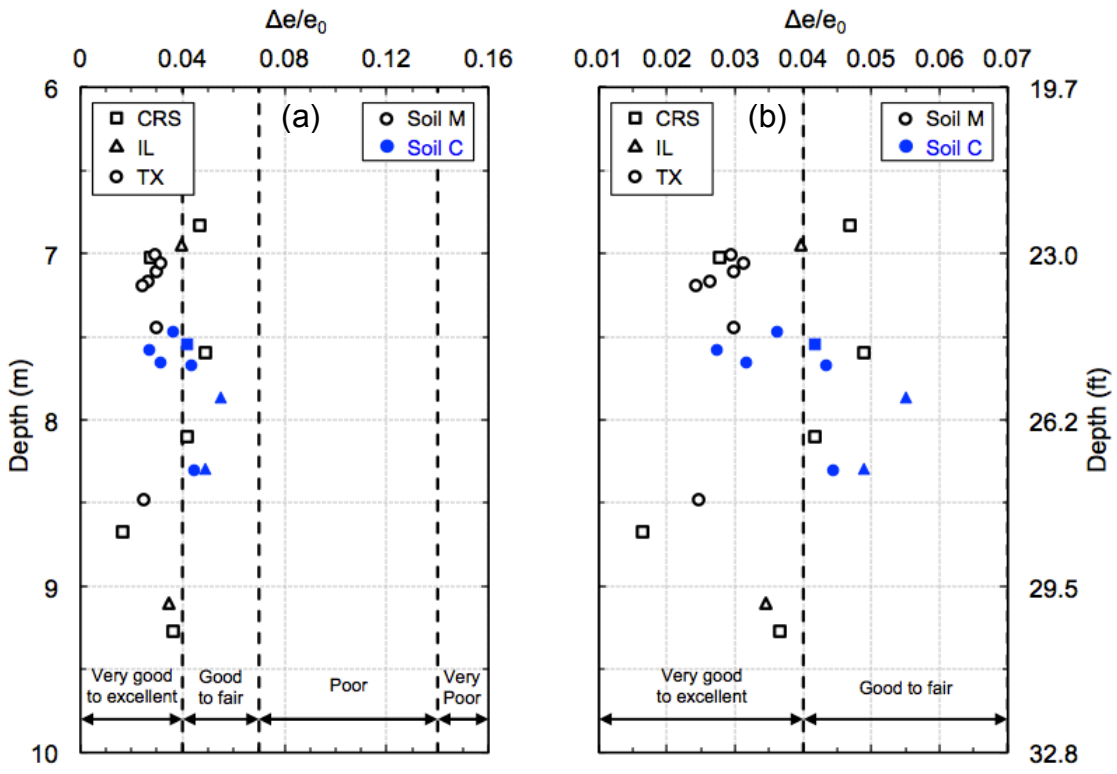

Figure D-13: Evaluation of sample quality for marl specimens according to the NGI method (Lunne et al., 1997)

A close up view for the $\Delta e/e_0$ values is presented in Figure D-13(b). In general, despite some limited scatter, values of $\Delta e/e_0$ obtained from tests on soil M specimens (average $\Delta e/e_0$ = 0.033 ± 0.009SD) are smaller than those obtained from tests performed on soil C (average $\Delta e/e_0$ = 0.041 ± 0.009SD). This is in agreement with the fact that soil C is more sensitive (depicted by the strong S-shape compression curves), which makes it more susceptible to disturbance.

A distinction is also made between values of $\Delta e/e_0$ obtained from the K_0 consolidation phase of triaxial tests and those derived from IL and CRS consolidation tests. As shown in the figure, for the same type of soil, the values

of the $\Delta e/e_0$ obtained from the K_0 consolidation phase of triaxial tests are generally smaller than those obtained from the consolidation tests. This might be attributed to (i) the additional disturbance imposed on the CRS/IL specimens while inserting the consolidation ring; and (ii) the difference in diameter for these two types of specimens (6.35 cm (2.5 in) and 3.8 cm (1.5 in) for CRS/IL and triaxial specimens). Due to the fact that the soil in proximity to the wall of the Shelby tube is subjected to higher degree of disturbance (Santagata et al., 2006), smaller diameter specimens (i.e. triaxial specimens) are expected to be less disturbed, resulting in lower values of $\Delta e/e_0$.

Figure D-14 shows the variation of the reconsolidation volumetric strain (ε_v). In general all the data fall below 3.5%, indicating that the samples can be designated as “A” to “C” based on the SQD method suggested by Terzaghi et al. (1996).

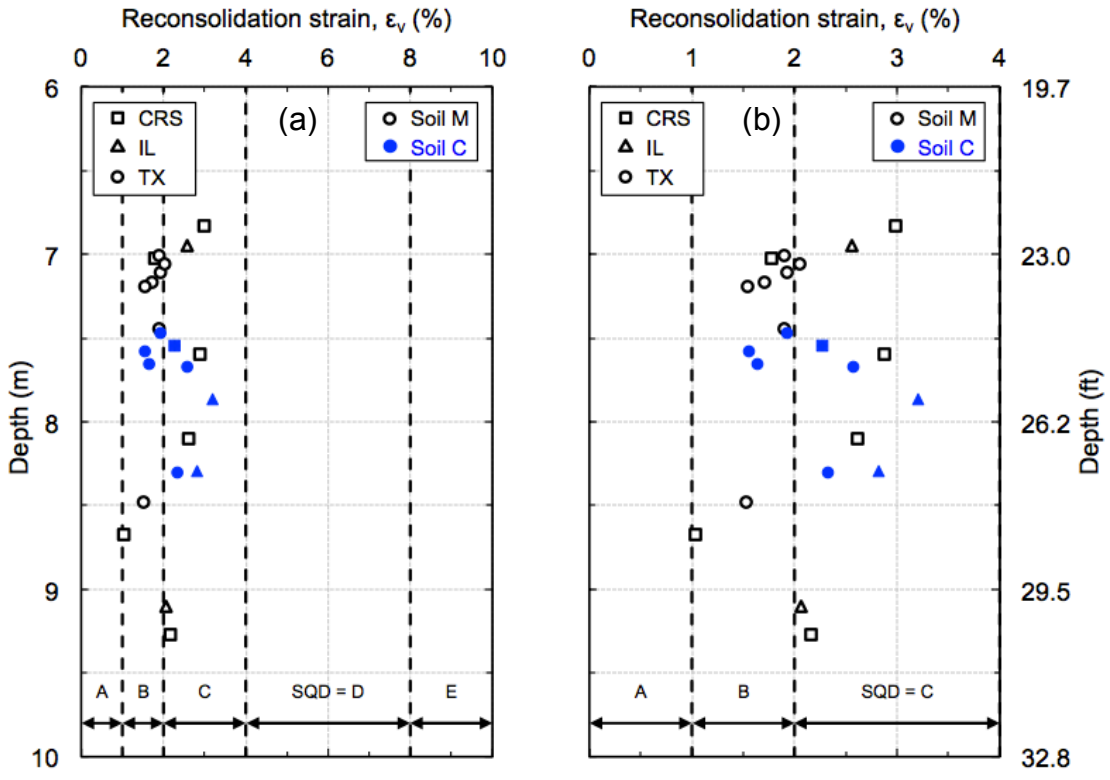

Figure D-14: Evaluation of sample quality for marl specimens according to the SQD method (Terzaghi et al. 1996)

D.4 Undrained Shear Behavior

D.4.1 Introduction

This section provides a detailed evaluation of results from SHANSEP triaxial tests conducted on undisturbed samples of marl (soil M and soil C). The evaluation includes derivation of the undrained shear strength profiles and the soil's SHANSEP parameters for the marl deposit. One-dimensional compression data from the consolidation phase of SHANSEP triaxial tests were also used to determine the stress history profile, the compressibility properties, and the in situ lateral stress ratio (K_0) for the marl deposit as discussed in Section D.3. This section is organized in three major sub-sections: the general undrained shear behavior is summarized first, followed by a discussion of the undrained strength ratio and the effective stress failure envelope.

A total of eleven K_0-consolidated SHANSEP triaxial compression tests ($CK_0UTC(L)$) were performed on marl samples obtained from different boreholes at various depths. Six of these tests were sheared at OCR of 1, and five were sheared at OCR values varying between approximately 2 and 6. The data from these tests are summarized in Table D-11 and Table D-12 for soil M and soil C, respectively. The tables present a summary of the tests location; the in situ phase data (w_n, e_0, S_i, and σ'_{v0}); the pre-shear conditions; the shear parameters at peak and at maximum obliquity; as well as the normalized undrained modulus at 0.1% axial strain ε_a ($E_{0.1}/\sigma'_{vc}$) and at peak ($E_{u,\,max}/\sigma'_{vc}$).

Table D-13 presents a summary of all shear properties for soil M and soil C. The following subsections will discuss the results of the various shear properties in greater detail.

Table D-11: Summary of shear data from SHANSEP $CK_0UTC(L)$ tests for soil M

Test #	In situ		Pre shear			At peak			At maximum obliquity		$E_{0.1}/\sigma'_{vc}$
Depth	w_n e_0	S_i σ'_{v0}	K_c e_c	σ'_{vm} σ'_{vc}	OCR ε_v	q/σ'_{vc} p'/σ'_{vc}	ε_{af} ϕ'	A_f	q/σ'_{vc} p'/σ'_{vc}	ε_a ϕ'	$E_{u,max}/\sigma'_{vc}$
TX107 8.48	58.4 1.63	98 84.1	0.495 1.277	345.8 345.8	1.00 13.10	0.325 0.711	0.305 27.2	0.590	0.243 0.395	10.53 37.9	133.0 52.8
TX108 7.01	65.7 1.80	99 74.3	0.477 1.447	247.0 247.0	1.00 12.47	0.345 0.660	0.736 31.5	0.801	0.275 0.419	10.65 41.0	130.1 25.9
TX109 7.11	65.9 1.81	99 75.0	0.483 1.277	443.7 443.7	1.00 18.91	0.333 0.678	0.543 29.4	0.772	0.263 0.420	10.07 38.7	123.0 30.0
TX111 7.06	68.5 1.89	98 74.6	0.630 1.556	248.1 121.3	2.04 11.23	0.646 1.109	1.298 35.6	0.173	0.520 0.798	10.26 40.6	425.3 76.2
TX112 7.16	68.5 1.86	99 75.3	0.852 1.382	445.3 107.1	4.16 16.84	1.127 1.805	2.460 38.6	0.084	1.052 1.658	7.17 39.4	479.4 89.3
TX114 7.44	62.2 1.74	97 77.2	0.979 1.275	552.5 94.9	5.82 16.84	1.489 2.401	2.092 38.3	0.027	1.281 1.978	1.11 40.4	531.3 143.8

(Note: depth in m; stresses in kPa; w_n, S_i, and ε in %; ϕ' in °)

Table D-12: Summary of shear data from SHANSEP $CK_0UTC(L)$ tests for soil C

Test #	In situ		Pre shear			At peak			At maximum obliquity		$E_{0.1}/\sigma'_{vc}$
Depth	w_n e_0	S_i σ'_{v0}	K_c e_c	σ'_{vm} σ'_{vc}	OCR ε_v	q/σ'_{vc} p'/σ'_{vc}	ε_{af} ϕ'	A_f	q/σ'_{vc} p'/σ'_{vc}	ε_a ϕ'	$E_{u,max}/\sigma'_{vc}$
TX102 8.31	36.6 1.11	93 82.9	0.559 0.866	347.8 347.8	1.00 11.28	0.278 0.729	0.332 22.4	0.786	0.197 0.392	11.19 30.2	111.2 39.7
TX103 7.47	39.7 1.14	98 77.3	0.554 0.883	296.6 296.6	1.00 11.56	0.273 0.740	0.339 21.6	0.683	0.202 0.416	12.11 29.1	100.1 35.0
TX105 7.67	52.2 1.46	99 78.7	0.569 0.983	447.6 447.6	1.00 18.62	0.279 0.718	0.512 22.9	0.824	0.211 0.413	11.83 30.7	108.7 27.0
TX115 7.58	47.0 1.32	99 78.1	0.943 0.956	444.6 107.8	4.12 15.75	0.749 1.580	4.217 28.3	0.091	0.730 1.531	6.45 28.5	431.5 36.3
TX116 7.66	37.3 1.08	98 78.6	0.712 0.813	346.7 170.4	2.03 12.56	0.509 1.098	1.005 27.6	0.179	0.395 0.777	8.81 30.5	411.4 78.2

(Note: depth in m; stresses in kPa; w_n, S_i, and ε in %; ϕ' in °)

Table D-13: Summary of shear properties

		Soil M				Soil C		
OCR		1.0*	2.0	4.1	5.8	1.0*	2.0	4.1
At peak	q/σ'_{vc}	0.334	0.646	1.127	1.489	0.277	0.509	0.749
	p'/σ'_{vc}	0.683	1.109	1.805	2.401	0.729	1.098	1.580
	ε_{af}	0.528	1.298	2.460	2.092	0.394	1.005	4.217
	ϕ'	29.4	35.6	38.6	38.3	22.3	27.6	28.3
	A_f	0.721	0.173	0.084	0.027	0.764	0.179	0.091
At maximum obliquity	q/σ'_{vc}	0.260	0.520	1.052	1.281	0.203	0.395	0.730
	p'/σ'_{vc}	0.411	0.798	1.658	1.978	0.407	0.777	1.531
	ε_a	10.42	10.26	7.17	1.11	11.71	8.81	6.45
	ϕ'	39.2	40.6	39.4	40.4	30.0	30.5	28.5
$E_{0.1}/\sigma'_{vc}$		128.7	425.3	479.4	531.3	106.7	411.4	431.5
$E_{u,\,max}/\sigma'_{vc}$		36.2	76.2	89.3	143.8	33.9	78.2	36.3
$S_u/\sigma'_{v0} = S\,(OCR)^m$		S = 0.34; m = 0.85				S = 0.28; m = 0.72		
ϕ'_{mo}		39°				30°		

* The data corresponds to the average of three NC tests.

D.4.2 General Undrained Shear Behavior

Figure D-15 and Figure D-16 show the results of the SHANSEP triaxial compression tests carried out on marl at OCRs of approximately 1.0, 2.0, 4.1, and 5.8. The dashed black lines represent soil M and the continuous blue lines represent soil C. Figure D-15(a-c) show the normalized shear stress (q/σ'_{vc}), the normalized excess pore pressure ($u_e/\sigma'_{vc} = [\Delta u - \Delta\sigma_h] / \sigma'_{vc}$), and the obliquity ($R = \sigma'_v/\sigma'_h$) versus axial strain ($\varepsilon_a$). The same results are presented in Figure D-16(a-b) for smaller axial strain values (up to strain at failure, ε_{af}), this is important to evaluate the soil response prior to failure, especially the complex behavior observed at low strains for the pore pressure response. The following general observations were made from these curves:

1) For both soil M and soil C, increasing OCR results in:
   i. transition from a ductile behavior to a strain-softening behavior;
   ii. an increase in the peak value of the normalized shear stress (q_f/σ'_{vc});
   iii. an increase in the axial strain at failure (ε_{af}). This is also illustrated in Figure D-17, which shows that ε_{af} increases linearly with increasing OCR on a log-log plot from about 0.5% for OCR of 1 to about 3.7% for OCR equal to 6 (r^2 = 0.84 on collective data). No clear difference was identified between soil M and soil C.
2) For the same value of OCR, the marl with higher $CaCO_3$ content (soil M) has higher normalized undrained shear strength than the marl with lower $CaCO_3$ content (e.g. for OCR=1, q_f/σ'_{vc} ~ 0.33 vs. 0.28). This might be attributed to the shear reinforcement provided by the shells as well as the cementation caused by the higher carbonate content present in soil M (Section C.4).
3) In all normally consolidated tests, the normalized excess pore pressure (u_e/σ'_{vc}) increases with increasing axial strain. However, in overconsolidated tests, the u_e/σ'_{vc} initially increases then gradually decreases when q_f is approached, but directly after peak large positive excess pore pressures start to develop. This behavior was also observed for Boston blue clay BBC (Berman, 1993), resedimented Boston blue clay RBBC (Santagata, 1998), and Avezzano (AZ) silt in the Fucino basin (Burghignoli et al., 2010). In general, at small strains (ε_a <0.5%), u_e/σ'_{vc} increases with increasing OCR, but at large strains, u_e/σ'_{vc} decreases with increasing OCR. For NC marl, no clear difference was observed between soil M and soil C. However, for OC marl, Soil M has slightly higher u_e/σ'_{vc} than soil C.

The pore pressure parameter ($A = [\Delta u - \Delta\sigma_h] / [\Delta\sigma_v - \Delta\sigma_h]$) is plotted in Figure D-16(c). It can be observed that for OCR=1, A-parameter increases with increasing

axial strain until reaching failure. For OCR >1, however A-parameter decreases with axial strain, this is typical for a wide range of clay reported in the literature (e.g. BBC, Sheahan 1991; Taipei clay, Chin et al. 2007). The figure also shows that the pore pressure parameter at failure (A_f) decreases with OCR. This is also illustrated in Figure D-18, which shows that A_f decreases linearly with increasing OCR on a log-log plot from about 0.72 for OCR of 1 to about 0.03 for OCR equal to 6 (r^2 = 0.97 on collective data). No clear difference was identified between soil M and soil C.

Figure D-15(c) plots the obliquity ($R = \sigma'_v/\sigma'_h$) versus axial strain (ε_a). Despite the initial heterogeneity (e.g. void ratio, water content, plasticity index) of the different specimens, the obliquity R (Figure D-15(c)) at large strain appears to converge to a certain value (with minor scattering), which may be identified as the critical state condition. Soil M has an average value equal to 3.86, corresponding to a friction angle of 36 degrees. This value is lower for soil C (2.71), corresponding to a friction angle of 27 degrees.

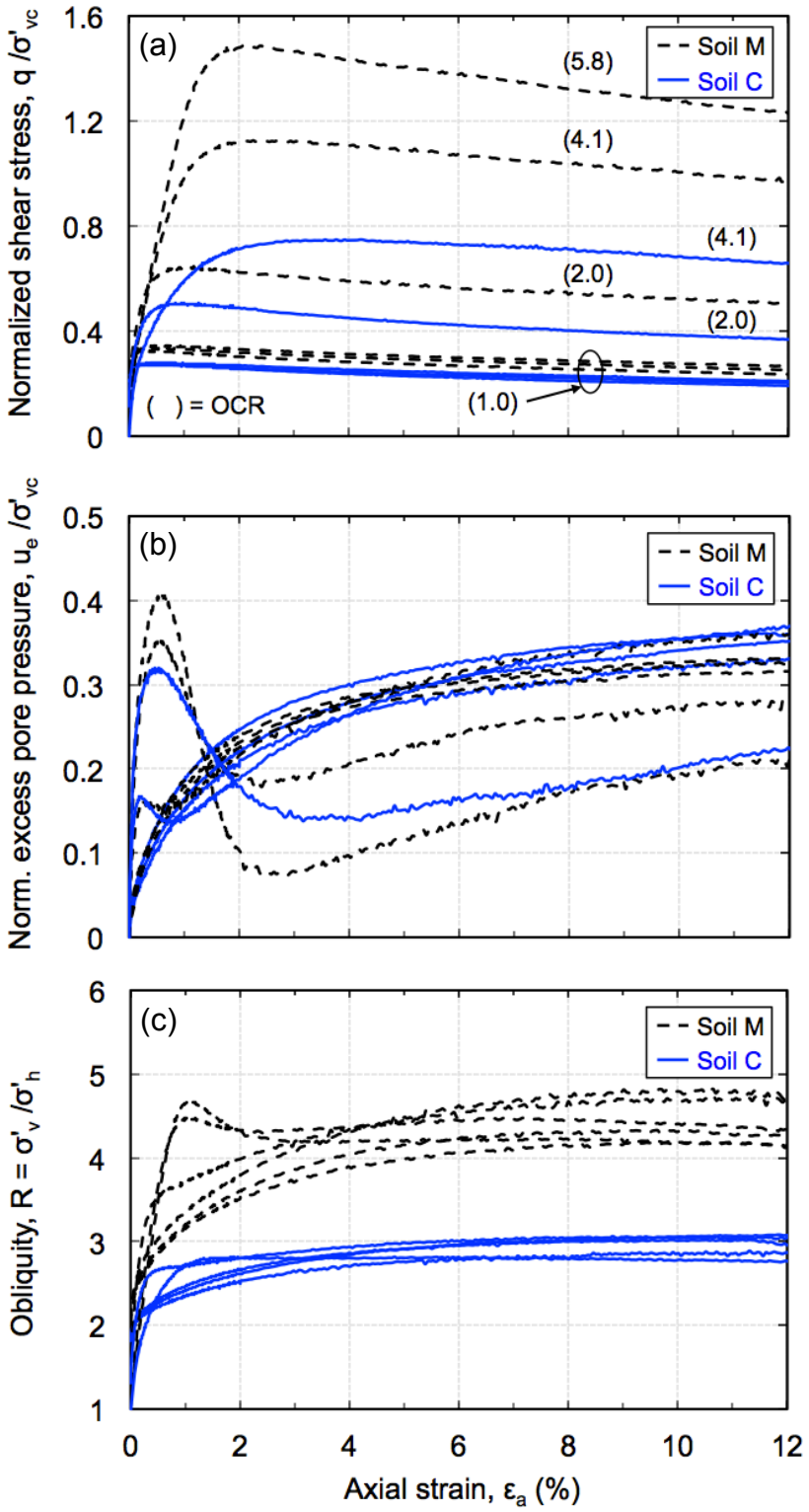

Figure D-15: Results for SHANSEP $CK_0UTC(L)$ tests of marl: (a) normalized shear stress, (b) norm. excess pore pressure, and (c) obliquity vs. axial strain

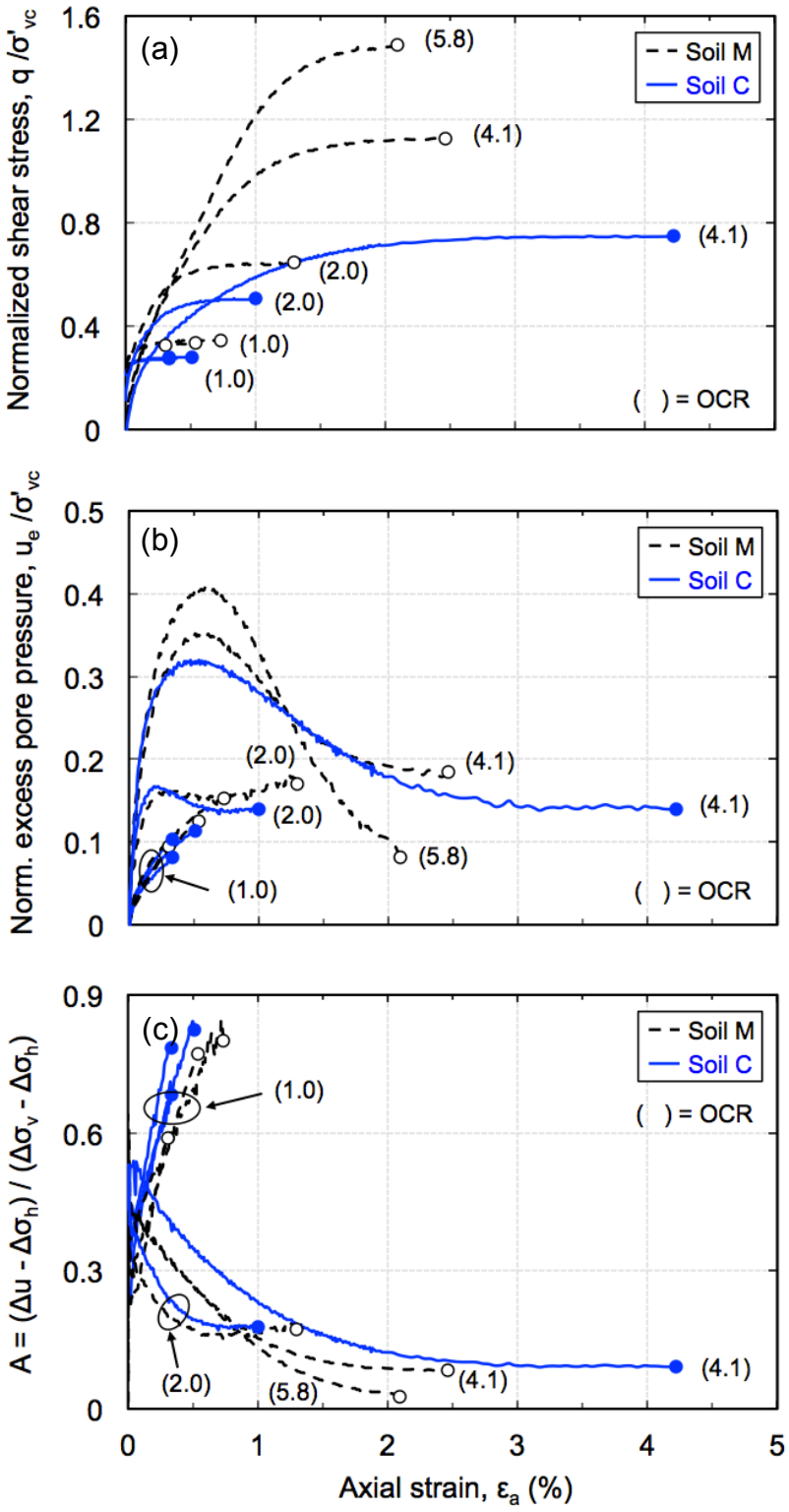

Figure D-16: Results for SHANSEP $CK_0UTC(L)$ tests of marl: (a) normalized shear stress, (b) norm. excess pore pressure, and (c) A-parameter vs axial strain

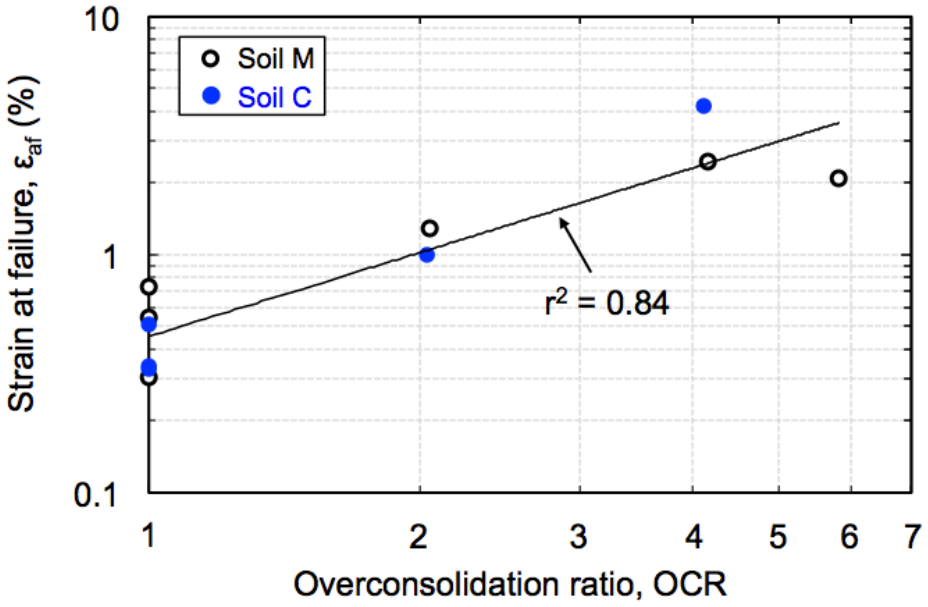

Figure D-17: Strain at failure versus OCR for marl

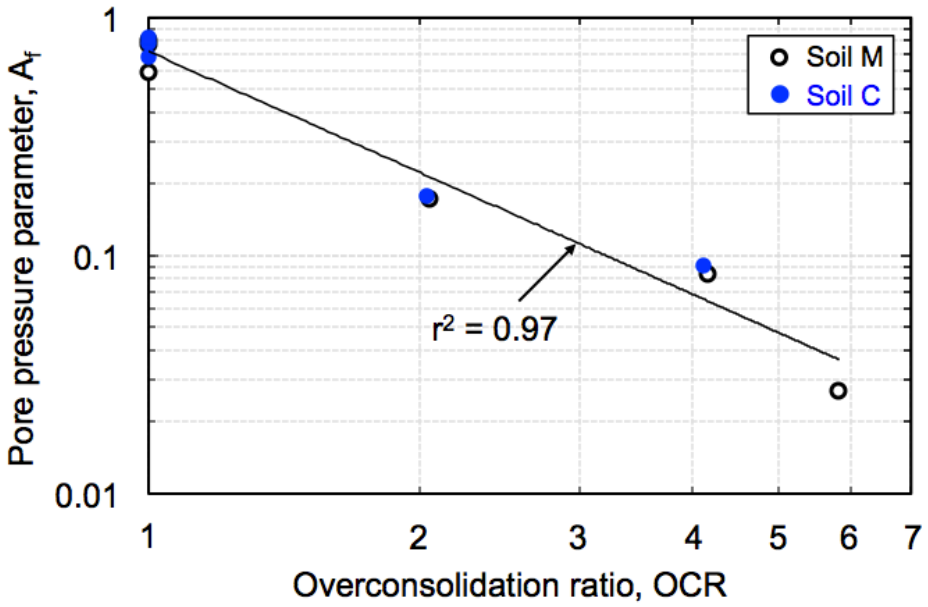

Figure D-18: Pore pressure parameter at failure versus OCR for marl

D.4.3 Young's Modulus

The normalized undrained secant Young's modulus (E_u/σ'_{vc}) are plotted versus the axial strain in Figure D-19. The degradation of modulus with increasing axial strain is apparent. In general, soil M has slightly higher values of E_u/σ'_{vc}

compared with soil C. The figure also shows that the values of E_u/σ'_{vc} increases with OCR at the same level of ε_a.The E_u/σ'_{vc} for NC soil is consistently smaller than the OC soil at all strain levels.

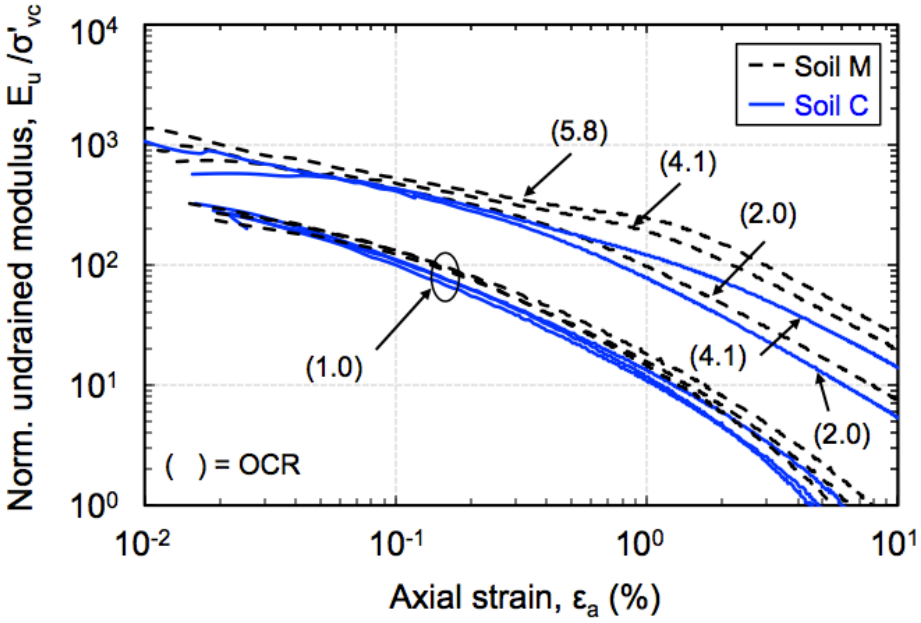

Figure D-19: Normalized undrained modulus degradation for SHANSEP

D.4.4 Undrained Strength Ratio

Ladd and Foott (1974) suggested that for a large range of natural clays the undrained shear strength (S_u) of soil at any depth can be directly related to its in situ vertical effective stress (σ'_{v0}) and OCR via the SHANSEP (Stress History and Normalized Soil Engineering Properties) equation:

$$S_u/\sigma'_{v0} = S\,(OCR)^m \qquad \text{(Eq. D-6)}$$

where S (= the normally consolidated value of S_u/σ'_{v0}) and m (= the strength increase exponent) are the two SHANSEP parameters. This concept has significant practical value as it provides a useful framework for comparing and relating the behavioral characteristics of different cohesive soils and allows estimation of the undrained shear strength profile as the vertical effective stress

and stress history profiles of the site change. Thus, the SHANSEP design method is ideally suited for the design of staged construction/preloading procedures (Ladd, 1991), which are commonly employed in marl deposits.

The SHANSEP testing program carried out in this study shows that marl exhibits normalized behavior and can be described by the SHANSEP equation. Figure D-20 presents the undrained shear strength ratio versus OCR on a log-log plot for six NC tests and five OC tests. Overall, the data lie on two straight lines that can be represented by S = 0.34; m = 0.85; r^2 = 1.00 for soil M; and S = 0.28; m = 0.72; and r^2 = 0.99 for soil C. Although these values fall in the range of soft soils previously documented in the literature (e.g. BBC: S = 0.28 and m = 0.70, Sheahan 1991; Taipei clay: S = 0.32 and m = 0.82, Chin et al. 2007), it is important to note the significant difference between soils M and C.

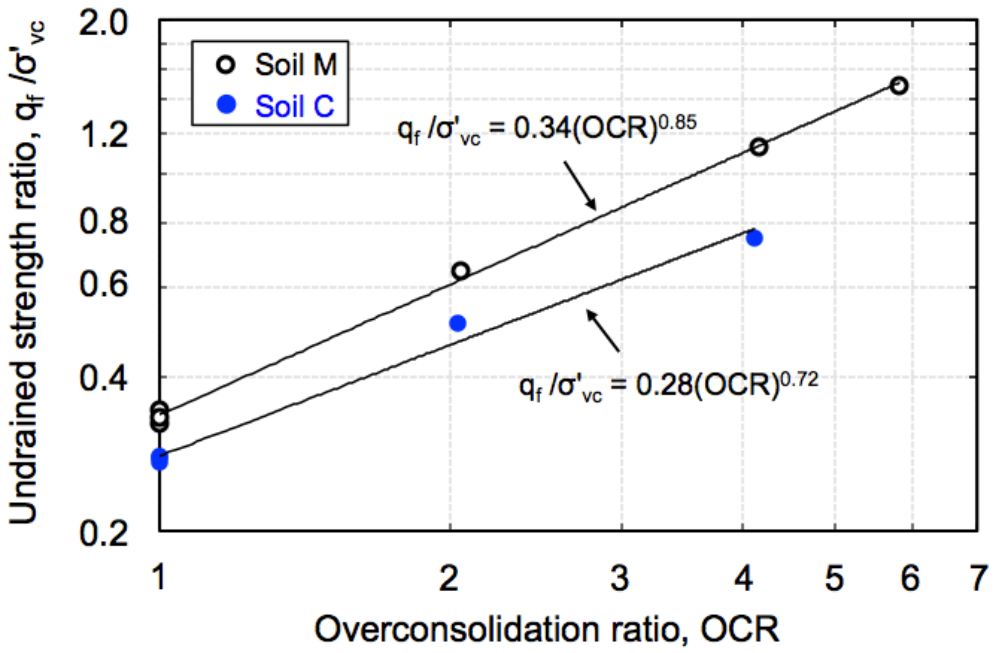

Figure D-20: Undrained strength ratio vs. OCR for SHANSEP $CK_0UTC(L)$ tests of marl

D.4.5 Effective Stress Failure Envelope

Figure D-21 and Figure D-22 present the effective stress paths and the effective stress paths normalized to the maximum vertical consolidation stress (σ'_{vm}),

respectively for SHANSEP $CK_0UTC(L)$ tests conducted on NC and OC marl. The MIT stress path convention was used where the shear stress is calculated as $q = (\sigma'_v - \sigma'_h) / 2$ and the average effective stress is calculated as $p' = (\sigma'_v + \sigma'_h) / 2$. The results show that the effective stress paths approach a common failure envelope at large strains. The p'-q effective stress failure envelope (ESFE) is defined by a linear regression through the shear stress and average effective stress at maximum obliquity represented with hollow black diamonds for soil M and solid blue diamonds for soil C. The linear regression on the data yields a friction angle at maximum obliquity (ϕ'_{mo}) of 39° for soil M and 30° for soil C and a negligible cohesion intercept ($c' \sim 0$) for both soils. As mentioned earlier, the higher friction angle measured on soil M might be attributed to the shear reinforcement provided by the shells as well as the cementation caused by the higher carbonate content present in soil M.

Note that the higher the OCR, the lower the strain at which the maximum obliquity failure envelope is mobilized (ε_a>10% for NC marl) and that only for OCR equal 6 does the soil reach the maximum obliquity envelope before reaching the peak undrained strength (see Figure D-15(c)).

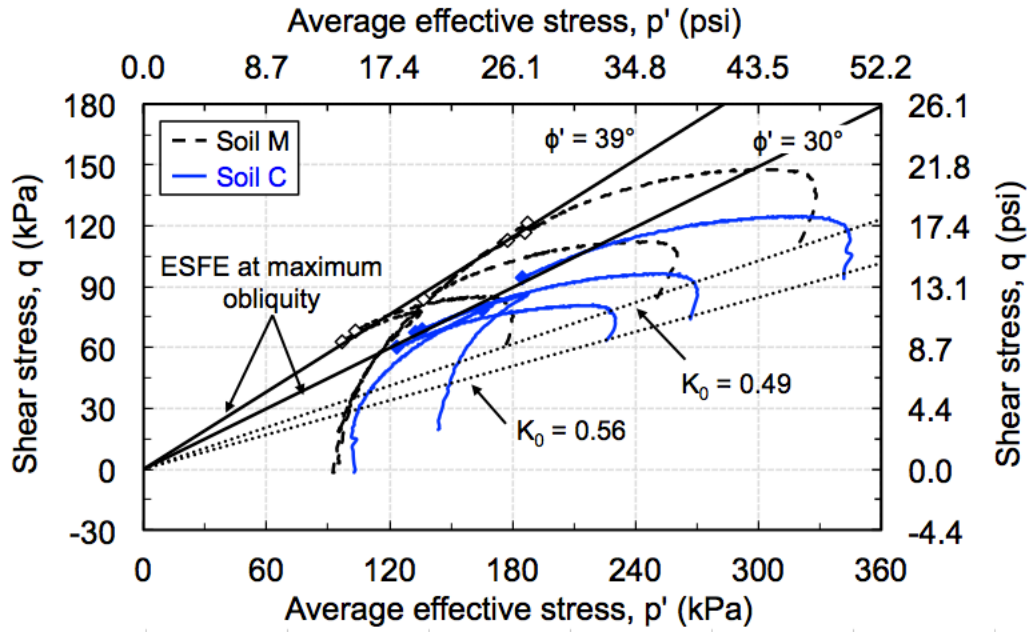

Figure D-21: Effective stress paths for SHANSEP $CK_0UTC(L)$ tests of marl

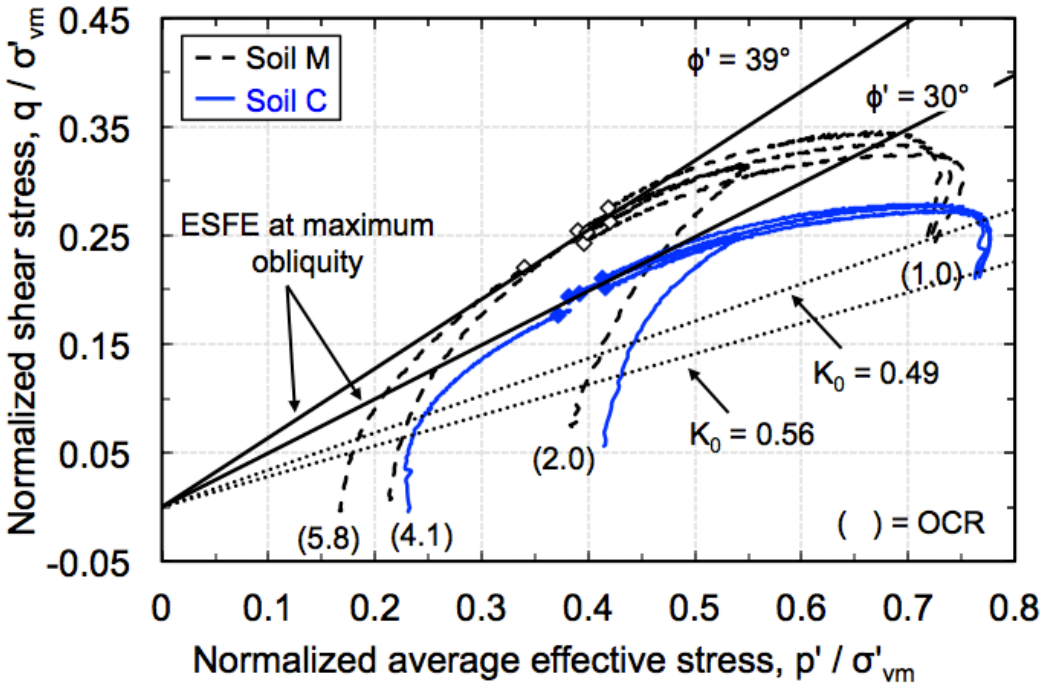

Figure D-22: Normalized effective stress paths for SHANSEP $CK_0UTC(L)$ tests of marl

Appendix E. Integration of Laboratory and Field Data

E.1 Introduction

This appendix presents a detailed evaluation of the results from the field tests described in Section B.6. The evaluation includes further analysis of the basic results summarized in Section B.7 as well as integration of laboratory and field data. The appendix is organized in two sections: (i) field vane tests and (ii) piezocone tests. Section E.2 discusses the field vane tests results and provides a comparison between the corrected field vane undrained shear strength and the reference strength obtained from laboratory SHANSEP $CK_0UTC(L)$ tests. Section E.3 analyzes the piezocone tests results and provides marl specific correlations to estimate shear wave velocity, stress history, and undrained strength from the Piezocone penetration measurements.

Figure E-1 shows the soil profile and index properties at the site. The figures include the results of index tests conducted on undisturbed samples of marl (described earlier in Section C.3) as well as additional tests performed on undisturbed samples collected from the split spoons retrieved from the soil above and below the marl layer. The data presented in Figure E-1 show the elevated natural water content, Atterberg limits and $CaCO_3$ content in the marl layer compared with the soil above and below.

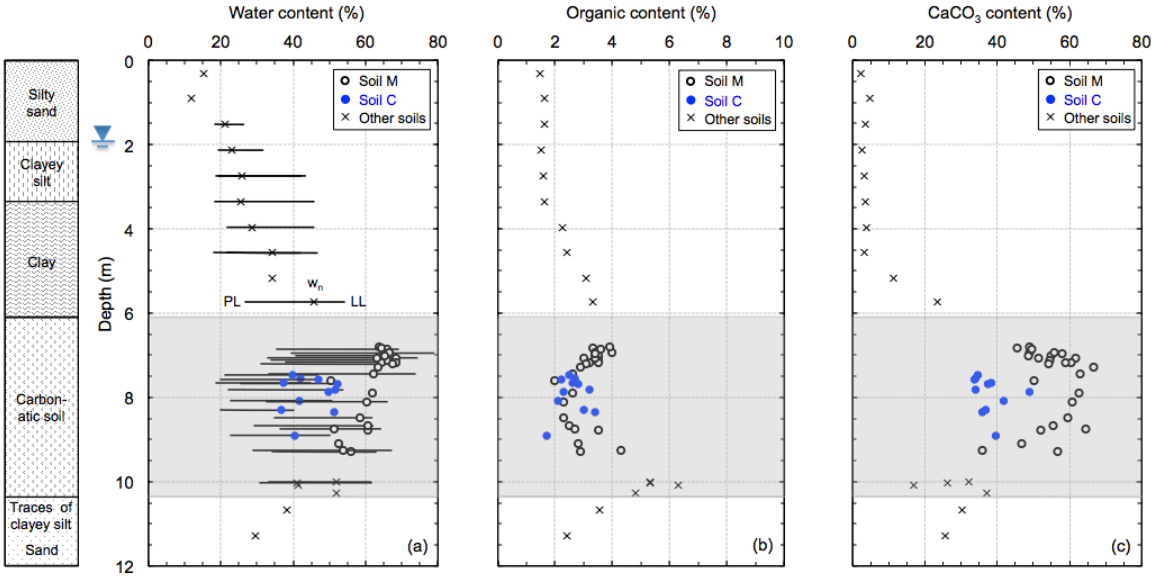

Figure E-1: Index properties: (a) water content, (b) organic content, and (c) $CaCO_3$ content versus depth

E.2 Field Vane (FV) Test

Field vane tests were performed in this study in order to obtain the in-situ undrained shear strength profile for marl and compare it to the one measured in the laboratory using SHANSEP triaxial program. The equipment and testing procedures are summarized in Section B.6.3 and the measured peak and remolded strengths are presented in Section B.7.3. It is well established that the measured field vane strengths should be corrected for use in undrained stability analyses due to installation disturbances, mode of failure, strain rate, and anisotropy effects. Bjerrum (1972) studied a number of excavation and embankment failures for which field vane data were available and derived an empirical correction factor (μ) versus plasticity index (PI); this correlation as well as more recent case histories are shown in Figure E-2. For a plasticity index of 20%, the Bjerrum's factor μ equals to 1.0.

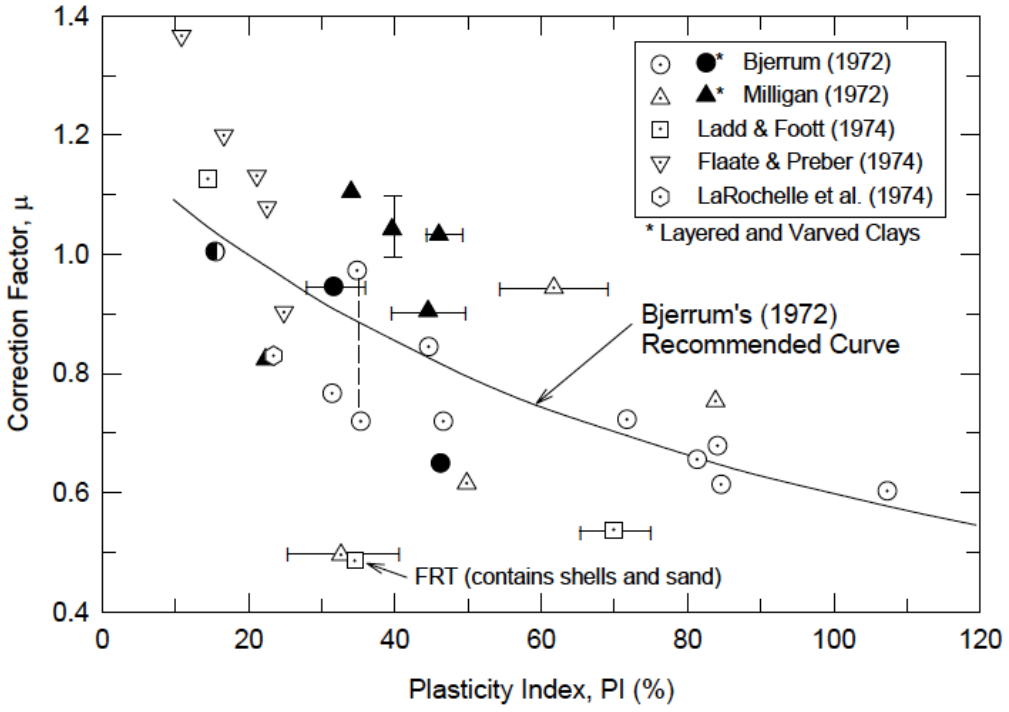

Figure E-2: Field vane correction factor versus plasticity index derived from embankment failures (Ladd et al. 1977)

The plasticity index of marl is higher than 20%, but is not uniform across the deposit. As reported earlier, the marl layer is not homogenous and is composed of two types of soils, i.e. soil M and soil C, that are repeated in horizontal thin layers. These layers are shown in the soil profile column on the left side of Figure E-3, where soil M is represented in gray and soil C is represented in blue. It can be seen that soil M is prominent.

The total vane height including the taper ends is about 0.3 m (1 ft); hence it can be assumed that the soil sheared by the vane is about 0.3 m (1 ft). The Bjerrum's factor for each FV test was determined based on a weighted average PI, with PI equals to 33.1 and 25.9 for soil M and soil C respectively. Figure E-3(a) shows the measured peak and remolded FV strengths, as well as the undrained strength corrected using Bjerrum's factor μ. As can be seen, there is no appreciable difference between the corrected and uncorrected peak FV strength for this deposit ($\mu > 0.9$). For reference, the undrained shear strength profiles obtained from the SHANSEP $CK_0UTC(L)$ tests for both soil M and soil C are also plotted in Figure E-3(a). The SHANSEP equations presented in Section D.4.4 were used with OCR equals to 1.9 and 1.3 for soil M and soil C, respectively. On Figure E-3(b), the comparison is made in terms of profiles of normalized shear strength.

The different types of soils (M and C) were carefully examined in the laboratory, and special effort has been made to conduct tests on specimens with only one type of soil. However, this is not the case for the field vane test where $S_u(FV)$ represents the shear behavior of about 0.3 m (1 ft) of soil and the result is influenced by the relative abundance of each type of soil. This can be seen by examining the two FV tests FV4 and FV5. The $S_u(FV)$ obtained from test FV4 conducted at depth ~7.2 m (23.5 ft) is close to the $S_u(TX)$ for soil M, which is consistent with the fact that only soil M is found at that depth (see the soil profile column in Figure E-3). On the other hand, relatively high concentration of soil C

is found at a depth of ~7.8 m (25.5 ft), where test FV5 is conducted resulting in much lower S_u(FV) ~ 18 kPa, which is close to the S_u(TX) for soil C. The higher sensitivity (~10) observed at this depth (see Figure B-29) is in good agreement with the fact that soil C has higher sensitivity (depicted by the strong S-shape compression curves) compared with soil M (see Figure D-1).

Despite this difference between soil M and soil C, S_u(FV) is generally lower than the weighted average peak strength in triaxial compression S_u(TX) of soil M and soil C, which is also reported by Lefebvre et al. (1988). The authors reported that the measured S_u(FV) is close to the undrained shear strength determined in direct simple shear (DSS) tests, which is intermediate between the peak triaxial compression (TC) and triaxial extension (TE) strengths.

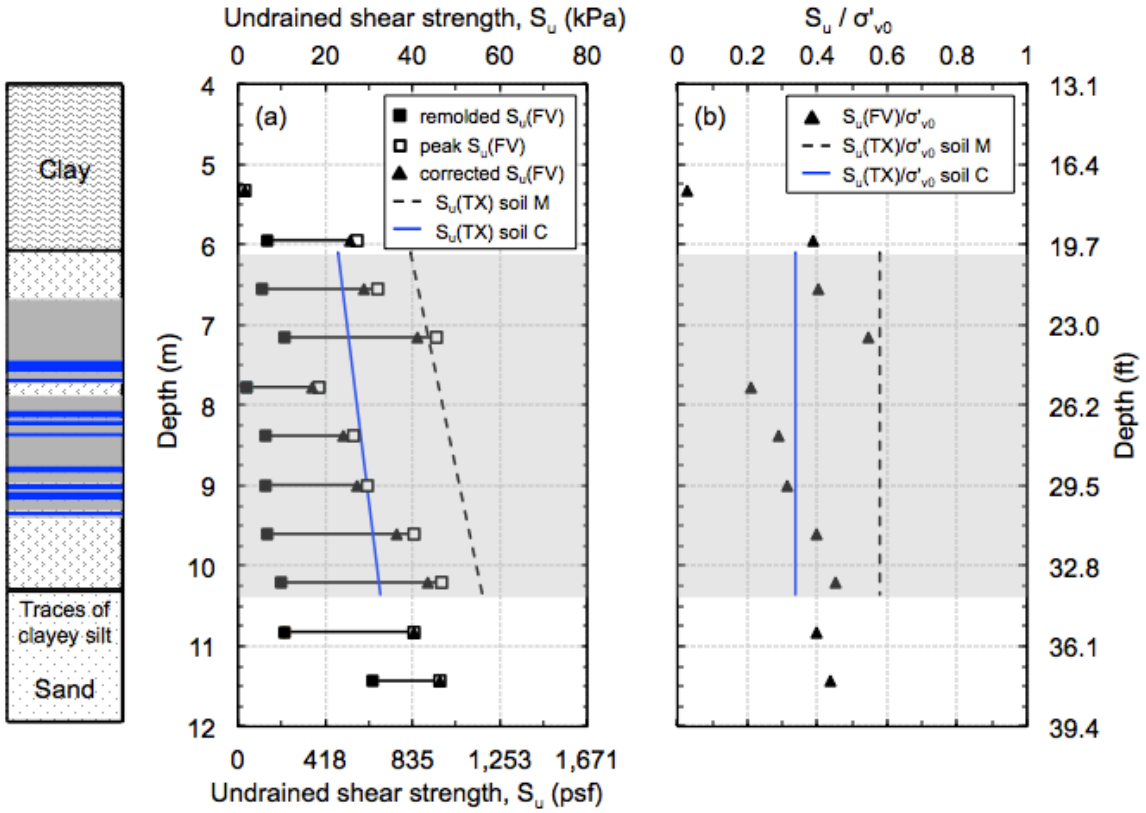

Figure E-3: (a) Undrained shear strength and (b) normalized undrained shear strength as obtained from field vane and laboratory SHANSEP $CK_0UTC(L)$ tests.

E.3 Piezocone Test (CPTu)

Due to its numerous advantages over other in-situ tests, the CPT has been increasingly used for conducting site investigations for exploring soft soils. Extensive work has been conducted to correlate soil parameters from CPT results. The main objective of the piezocone testing program in this research was to investigate the current correlations reported in the literature and provide site-specific correlations for marls to be used for preliminary design.

Seven different CPTs were performed in the field, as shown in Figure B-23. At all seven locations records of tip resistance, excess pore pressure, and sleeve friction as a function of depth were obtained. Additionally, CPT#4 and CPT#5 were used to obtain profiles of the shear wave velocity with depth, whereas measurements of the excess pore pressure dissipation were conducted at CPT#3A and CPT#6. The CPT field data were examined to derive correlations for three major soil properties: shear wave velocity (V_s), preconsolidation stress (σ'_p), and undrained shear strength (S_u).

E.3.1 Shear Wave Velocity

Various researchers have studied relationships between CPT data and V_s. The studies explored correlation relationships between V_s and different parameters such as: q_t, f_s, soil behavior type index (I_c), σ'_v, and depth (D). Correlation equations that were reviewed for this study are summarized in Table E-1. The equations are grouped in three different categories depending on the soils types (i.e., all soils, sand, and clay). The correlation equations presented in Table E-1 were analyzed for the seven CPTs and the derived V_s values were compared with the field seismic measurements of V_s at CPT#4 and CPT#5 presented in Figure B-26. This investigation shows that the V_s of the soil above and below the marl layer can be best estimated using the correlation provided by Mayne (2006) for “all soils” type, whereas for the marl layer, the correlation developed by Andrus et al. (2007) for all soils with a Pleistocene geologic age should be used.

Table E-1: CPT-V_s correlation equations

Soil Type	V_s (m/s)	Geologic Age	Reference
All soils	$(10.1 \log(q_t)-11.4)^{1.67} (100\ f_s/q_t)^{0.3}$	Quaternary	Hegazy & Mayne (1995)
	$32.3\ q_t^{0.089}\ f_s^{0.121}\ D^{0.215}$	Holocene	Piratheepan (2002)
	$118.8 \log(f_s)+18.5$	Quaternary	Mayne (2006)
	$2.62\ q_t^{0.395}\ I_c^{0.912}\ D^{0.124}\ SF^a$	Holocene & Pleistocene	Andrus et al. (2007)
	$[(10^{(0.55Ic+1.68)}) (q_t- \sigma_v) / p_a]^{0.5}$	Quaternary	Robertson (2009)
Sand	$134.1 + 0.0052\ q_t$	----	Sykora & Stokoe (1983)
	$17.48\ q_t^{0.13}\ \sigma'^{0.27}_v$	Holocene	Baldi et al. (1989)
	$13.18\ q_t^{0.192}\ \sigma'^{0.179}_v$	Quaternary	Hegazy & Mayne (1995)
	$12.02\ q_t^{0.319}\ f_s^{-0.0466}$	Quaternary	Hegazy & Mayne (1995)
	$25.3\ q_t^{0.163}\ f_s^{0.029}\ D^{0.155}$	Holocene	Piratheepan (2002)
Clay	$3.18\ q_t^{0.549}\ f_s^{0.025}$	Quaternary	Hegazy & Mayne (1995)
	$1.75\ q_t^{0.627}$	Quaternary	Mayne & Rix (1995)
	$11.9\ q_t^{0.269}\ f_s^{0.108}\ D^{0.127}$	Holocene	Piratheepan (2002)

Units: q_t, f_s, σ_v, and σ'_v are in kPa, depth (D) in meters, p_a = 100 kPa.
[a]SF = 0.92 for Holocene and 1.12 for Pleistocene.

Figure E-4(a) compares the field seismic measurements of V_s with the values correlated from the seven CPTs. The values derived using Mayne (2006) are represented by dashed lines, while the ones derived using Andrus et al. (2007) are represented by continuous lines. Hollow squares and solid black triangles are used to represent the field measurements of V_s obtained from the seismic measurements conducted at both CPT#4 and CPT#5, respectively.

Figure E-4(b) shows the same measurements of V_s (square and triangle symbols) along with the estimates of V_s obtained applying the above-cited correlations to the data obtained from CPT#4 and CPT#5 only. The following conclusions can be drawn from Figure E-4:

1. the estimates of V_s from the CPT data form a band that reflects the variability in tip resistance and sleeve friction measured in the field;

2. the values of V_s obtained from the seismic measurements at CPT#4 and CPT#5 are generally consistent with each other over the entire deposit;
3. in general, the estimates of V_s obtained from the correlations with the CPT data are in a good agreement with the values of V_s derived from the seismic measurements over the entire deposit;
4. the correlation by Andrus et al. (2007) is effective in predicting the V_s of marl deposits;
5. the correlation by Mayne (2006) is effective in predicting the V_s of soil above and below the marl layer, but is not applicable for marl.

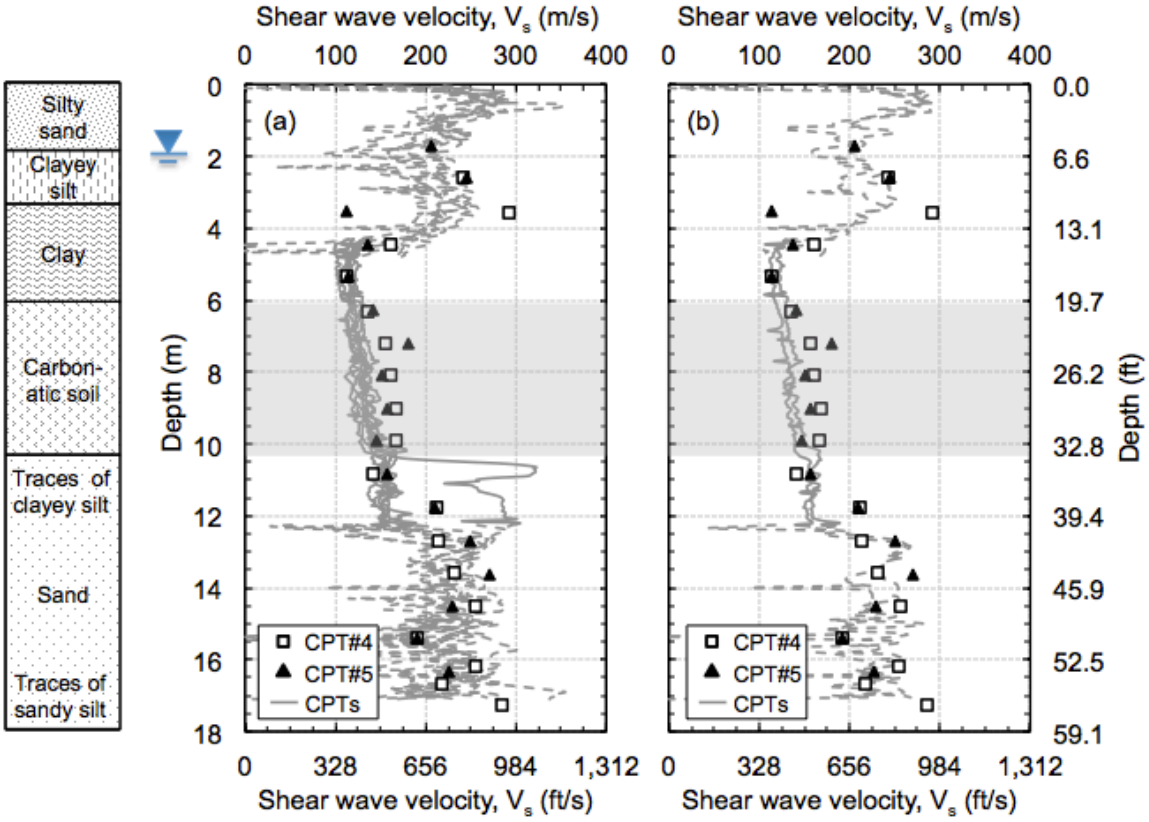

Figure E-4: Shear wave velocity as obtained from CPT correlations and seismic measurements from (a) all CPTs and (b) from CPT#4 and CPT#5.

E.3.2 Preconsolidation Stress

The preconsolidation stress can be estimated from: (i) the net tip resistance, $q_t - \sigma_{v0}$, using the equation proposed by Mayne (1995) ($\sigma'_p = 0.33\ [q_t - \sigma_{v0}]$); (ii) the

effective tip resistance, $q_t - u_2$, using the equation proposed by Mayne (2005) ($\sigma'_p = 0.60\ [q_t - u_2]$); and the excess pore pressure, $u_2 - u_0$, using the equation proposed by Chen and Mayne (1996) ($\sigma'_p = 0.53\ [u_2 - u_0]$).

These three relations were used to examine the ability to predict the preconsolidation stress of the marl deposit investigated in this research from the CPT results by comparing the derived σ'_p values with the laboratory measurements of σ'_p presented in Figure D-2. This investigation shows that the σ'_p of marl can be best estimated using the correlation provided by Mayne (1995). The values of σ'_p obtained applying this correlation to the traces of each of the seven CPTs performed are shown in Figure E-5(a). The curve highlighted in black corresponds to CPT#1, the sounding closest to the locations of the borings (MR#1, #2, #3 and #4) from which the soil used for the laboratory consolidation tests was obtained (see Figure B-9). The symbols shown in Figure E-5(a) pertain to the laboratory values for soil M (white symbols) and soil C (blue symbols). Figure E-5(b) shows the corresponding values of the overconsolidation ratio (OCR). It is found that the correlation by Mayne (1995) is effective in capturing the values of the preconsolidation stress for soil M, while slightly overestimating σ'_p for soil C. This might be due to the fact that soil M is more prominent, and thus controls the measured tip resistance.

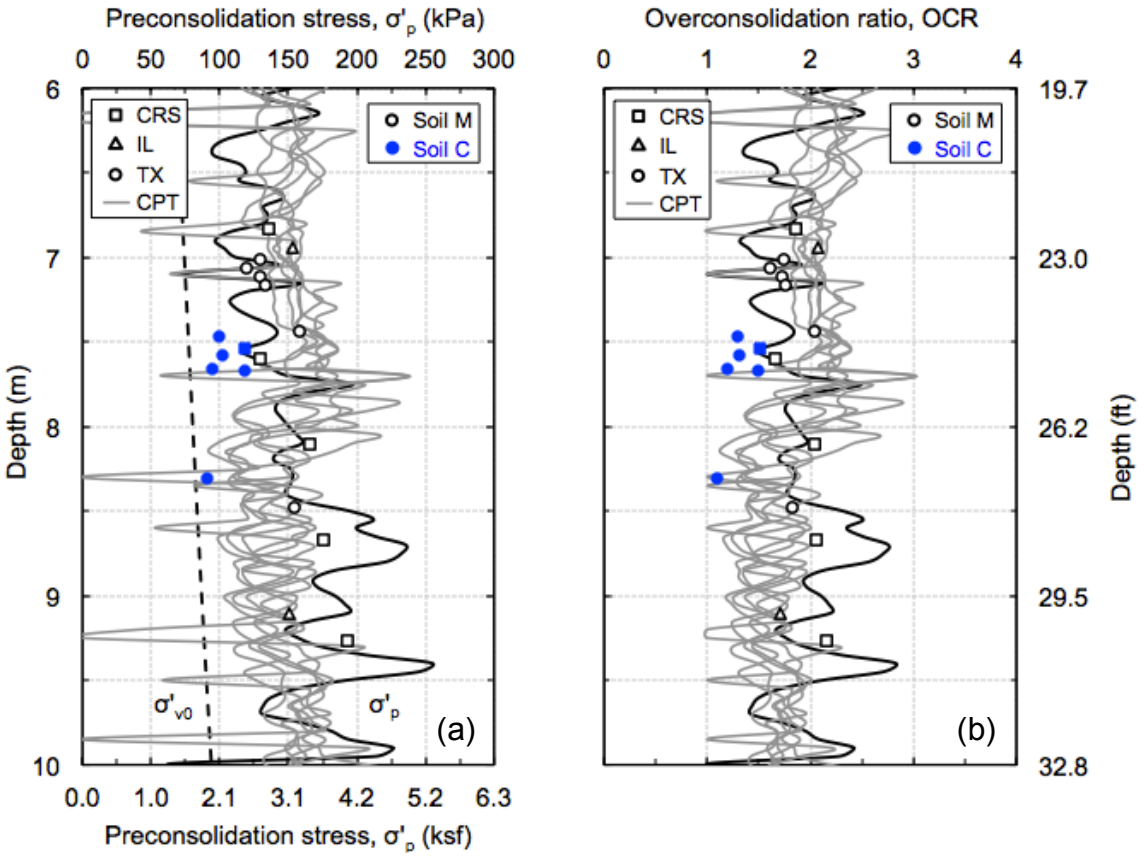

Figure E-5: (a) Preconsolidation stress and (b) overconsolidation ratio as obtained from CPT correlations and laboratory tests.

E.3.3 Undrained Shear Strength

The undrained shear strength, S_u, can be estimated from the net tip resistance, $q_t - \sigma_{v0}$, by substituting the cone tip resistance, q_t, the total overburden stress, σ_{v0}, and the empirical cone factor, N_{kt}, at given depths into the following equation:

$$S_u = (q_t - \sigma_{v0}) / N_{kt} \qquad \text{(Eq. E-1)}$$

The value of N_{kt} was backcalculated using the cone resistance measurements obtained at all seven CPTs, and the $CK_0UTC(L)$ SHANSEP profile as the reference undrained shear strength. Figure E-6(a) and Figure E-6(b) present the N_{kt} profiles calculated from all seven CPTs for soil M and soil C respectively, using the two SHANSEP equations resulting from the $CK_0UTC(L)$ testing program (Soil M: $S_u = \sigma'_{v0} \times 0.34\ (1.9)^{0.85}$; and soil C: $S_u = \sigma'_{v0} \times 0.28\ (1.3)^{0.72}$) to calculate the reference strength. The curves highlighted in black and dark blue

correspond to CPT#1, the sounding closest to the locations of the borings (MR#1, #2, #3 and #4) from which the soil used for the laboratory consolidation tests was obtained (see Figure B-9). As shown in both figures, no clear variation in N_{kt} was observed with depth. The mean values of N_{kt} derived from all CPTs for soil M and soil C are 10 and 17, respectively. Similar mean values were obtained when considering CPT#1 only.

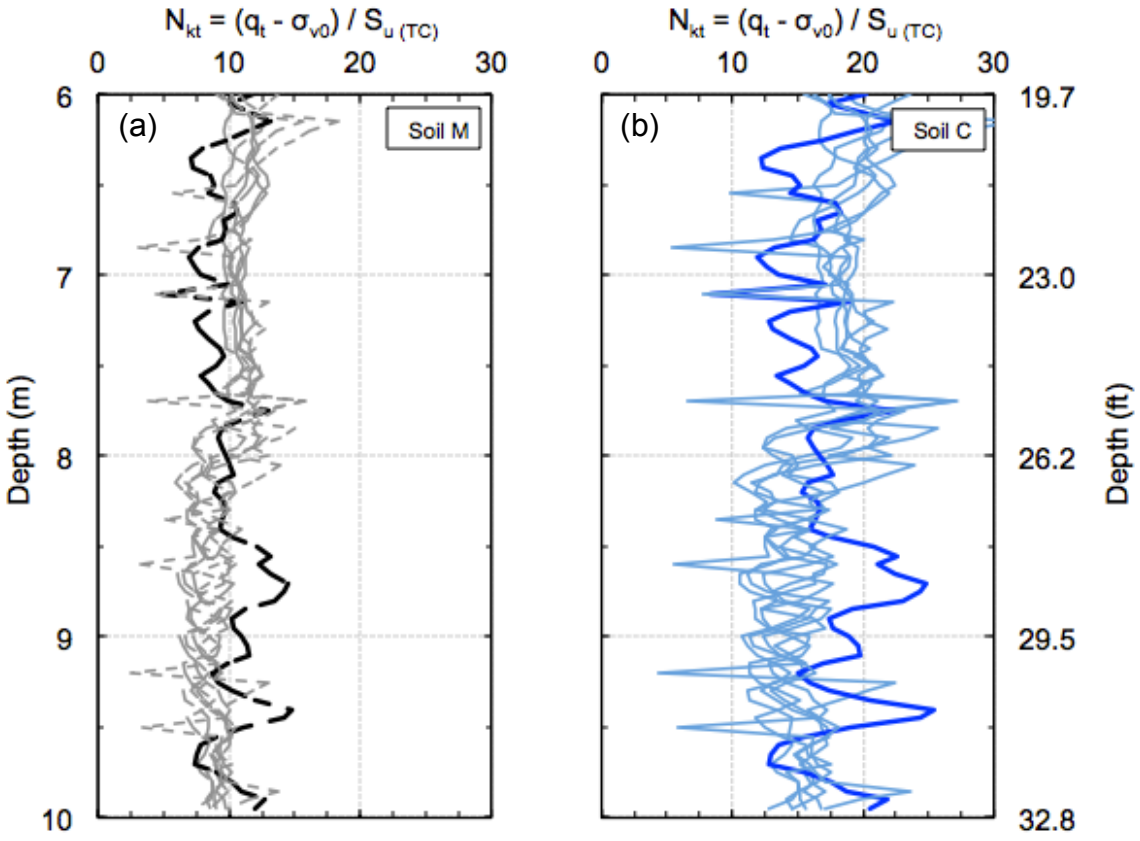

Figure E-6: Empirical cone factor $N_{kt(TC)}$ derived from all CPTs for (a) soil M and (b) soil C

The TC undrained strength profiles at the locations of boreholes CPT#1 to CPT#7 were calculated using N_{kt} = 10 assuming the deposit is composed of soil M only, and N_{kt} = 17 assuming the deposit is composed of soil C only. Note that when building on marl deposits, the value of N_{kt} selected for deriving the TC undrained strength profile should consider the presence of both types of soils (M

and C) and a representative value should selected depending on the prevalence of each.

The undrained shear strength profiles and the normalized undrained shear strength profiles as obtained from CPT (using N_{kt} = 10) and laboratory SHANSEP $CK_0UTC(L)$ tests for soil M are shown in Figure E-7(a) and Figure E-7(b), respectively. Figure E-8 shows the profiles as obtained from CPT (using N_{kt} = 17) and laboratory SHANSEP $CK_0UTC(L)$ tests for soil C.

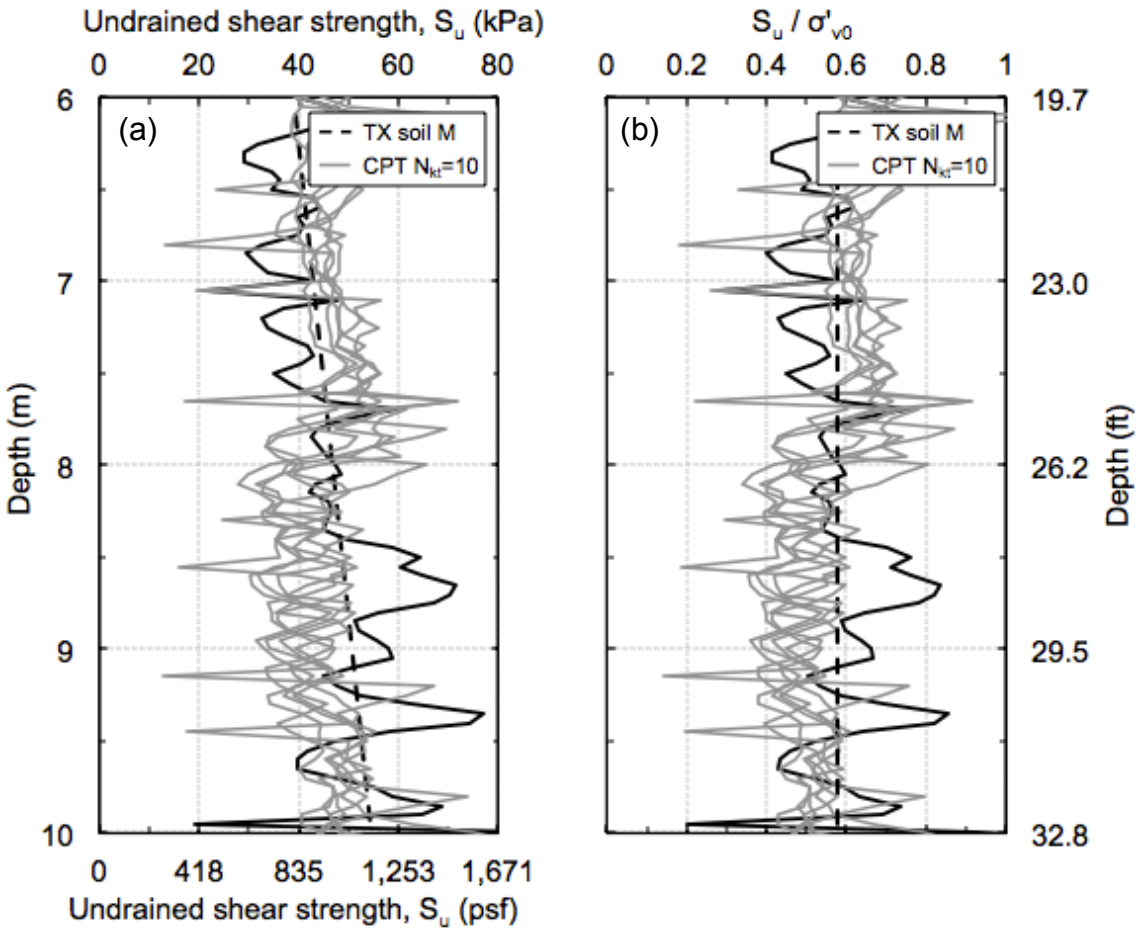

Figure E-7: (a) Undrained shear strength and (b) normalized undrained shear strength as obtained from CPT (using N_{kt} = 10) and laboratory SHANSEP $CK_0UTC(L)$ tests for soil M

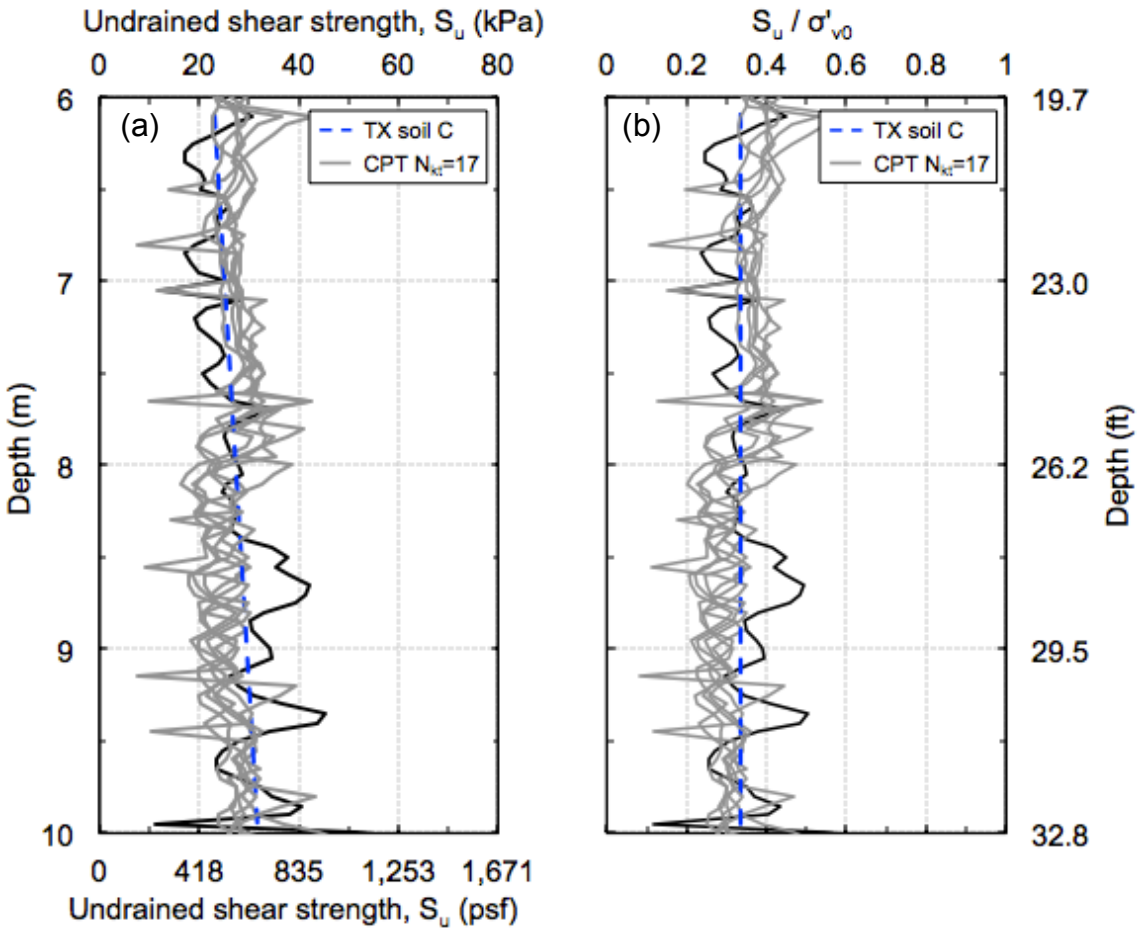

Figure E-8: (a) Undrained shear strength and (b) normalized undrained shear strength as obtained from CPT (using N_{kt} = 17) and laboratory SHANSEP $CK_0UTC(L)$ tests for soil C

It is important to note the significant difference between soils M and C, which is mainly caused by the large difference in $S_{u(TC)}$ derived from the SHANSEP program. This large variation indicates that there is no unique N_{kt} value that can be applied for all marl deposits and that site-specific calibration should be conducted for CPT data to account for the presence/absence of both types of soils (M and C) and representative values should be selected depending on the prevalence of each. In addition, the reported N_{kt} values are used to derive the S_u in triaxial compression mode, which is not necessarily the only mode of failure experienced by the soil. For instance, when building an embankment, Ladd (1991) shows that the soil under the embankment experiences three different modes of failures: extension, direct simple shear and compression. Hence,

higher values of N_{kt} should be used to derive the S_u in triaxial extension mode or direct simple shear mode.

Below is a summary of the three correlations that are found to better match the results for the marl deposit investigated:

Shear Wave Velocity:

$$V_s = 2.93\ q_t^{0.395}\ I_c^{0.912}\ D^{0.124} \qquad \text{(Eq. E-2)}$$

Where V_s = shear wave velocity (in m/s)

q_t = tip resistance (in kPa)

I_c = soil behavior type index = $[(3.47 - \log Q)^2+(1.22+\log F)^2]^{0.5}$

Q = normalized tip resistance = $(q_t - \sigma_{v0})/ \sigma'_{v0}$

F = normalized friction = $f_s / (q_t - \sigma_{v0}) * 100$

D = depth (in meters)

Preconsolidation Stress:

$$\sigma'_p = 0.33\ (q_t - \sigma_{v0}) \qquad \text{(Eq. E-3)}$$

where σ'_p = preconsolidation stress

q_t = tip resistance

σ_{v0} = total overburden stress

Undrained Shear Strength (Triaxial Compression):

$$S_{u(TC)} = (q_t - \sigma_{v0}) / N_{kt} \qquad \text{(Eq. E-4)}$$

where S_u = undrained shear strength

q_t = tip resistance

σ_{v0} = total overburden stress

N_{kt} = empirical cone factor = 10 for soil M and 17 for soil C

(Note that N_{kt} should be selected with caution as discussed above)

Appendix F. Summary of Boring Logs

This appendix summarizes the boring logs for the six boreholes (MR#1, MR#2, MR#3, MR#4, HAS#1, and FV#1) that were drilled as part of the field program.

SCHOOL OF CIVIL ENGINEERING
PURDUE UNIVERSITY

LOG OF TEST BORING

Boring No. : *MR#1*
Location: *Madison, Daviess, IN*
Date: *Monday 10/31/2011*

Latitude: *38.898745*
Longitude: *-86.990570*
Elevation: *150.84m (494.88ft)*
Sheet *1* of *3*

SAMPLE						DESCRIPTION/CLASSIFICATION	SOIL PROPERTIES		
No.	Rec. (in)	Rec. (%)	SPT	Depth (m)	Depth (ft)		Pen.	HCl reaction	Observations
SS1	13	54	2-4-6-7	0	0				
SS2	8	33	5-4-3-5	0.6	2	***Silty Sand**, yellow, moist, loose*			
SS3	12	50	2-1-3-2	1.2	4				
						1.7m (5.5ft)			
				1.8	6				
									Could not retrieve because the centerbid was not used
SS4	18	75	2-3-4-5	2.4	8	***Clayey Silt**, brown, moist, medium stiff*	1.5		
SS5	24	100	2-2-2-3	3	10		0.5 2		
						3.5m (11.5ft)			
SS6	16	67	1-2-2-2	3.7	12		1.5		
SS7	23	96	WOH-WOH-1-1	4.3	14	***Clay**, blue, moist, very soft*	0.25		
						4.9m (16ft)			
ST1				4.9	16	*Shelby tubes with fixed piston (drilling using mud rotary ϕ = 82.55mm = 3.25in)*	0.5	None	
ST2				5.5	18			Medium	
				6.1	20	*Blue, soft*			

GENERAL OBSERVATIONS:

SS = split spoon
ST = shelby tube
WOH = weight of hammer

SCHOOL OF CIVIL ENGINEERING
PURDUE UNIVERSITY

LOG OF TEST BORING

Boring No. : *MR#1*
Location: *Madison, Daviess, IN*
Date: *Tuesday 11/01/2011*

Latitude: *38.898745*
Longitude: *-86.990570*
Elevation: *150.84m (494.88ft)*
Sheet *2* of *3*

SAMPLE						DESCRIPTION/CLASSIFICATION	SOIL PROPERTIES		
No.	Rec. (in)	Rec. (%)	SPT	Depth (m)	Depth (ft)		Pen.	HCl reaction	Observations
ST3				6.1	20			Low	Lost 4 in from bottom
				6.7	22		Drilling to deeper depth by mistake		
ST4				7.3	24		0.75	Medium	
ST5				7.9	26		1	Medium	
ST6				8.5	28		0.25	Medium	
ST7				9.1	30		1	Low	
ST8				9.8	32		1.25	Low	Stiff soil
SS8				10.4	34		0.75 0.25	Split spoons (top, middle, bottom in ziplock). Driller thinks it's hard to push ST	
ST9				11.0	36		0.75		
SS9	24	100	2-9-13-15	11.6 12.2	38 40	11.7m (38.5ft) **Sand**, brown, loose	0.75		

GENERAL OBSERVATIONS: SS = split spoon
ST = shelby tube

SCHOOL OF CIVIL ENGINEERING
PURDUE UNIVERSITY

LOG OF TEST BORING

Boring No. : *MR#1*
Location: *Madison, Daviess, IN*
Date: *Tuesday 11/01/2011*

Latitude: *38.898745*
Longitude: *-86.990570*
Elevation: *150.84m (494.88ft)*
Sheet *3* of *3*

SAMPLE						DESCRIPTION/CLASSIFICATION	SOIL PROPERTIES		
No.	Rec. (in)	Rec. (%)	SPT	Depth (m)	Depth (ft)		Pen.	HCl reaction	Observations
SS10	20	83	3-9-9-8	12.2	40		1		
SS11	19	79	3-4-4-5	12.8	42		0.25		
SS12	22	92	1-2-2-1	13.4	44	***Sand**, brown, loose*	0		*Note that penecrometer is not applicable for sand (it was found for illustration purpose only)*
SS13	15	63	2-6-7-9	14.0	46		0		
SS14	14	58	3-2-2-2	14.6	48		0.75	V. Low	
						14.9m (49ft) ***Silty sand***			
				15.2	50				

GENERAL OBSERVATIONS:
SS = split spoon
ST = shelby tube

SCHOOL OF CIVIL ENGINEERING
PURDUE UNIVERSITY

LOG OF TEST BORING

Boring No. : *MR#2*
Location: *Madison, Daviess, IN*
Date: *Tuesday 11/01/2011*

Latitude: *38.898745*
Longitude: *-86.990615*
Elevation: *150.84m (494.88ft)*
Sheet *1* of *3*

SAMPLE						DESCRIPTION/CLASSIFICATION	SOIL PROPERTIES		
No.	Rec. (in)	Rec. (%)	SPT	Depth (m)	Depth (ft)		Pen.	HCl reaction	Observations
SS1	9	38	2-6-7-8	0	0	***Silty Sand**, yellow, moist, loose*	1.5		
SS2	8	33	2-6-7-8	0.6	2		0.75		
SS3	22	92	2-2-2-3	1.2	4	*1.2m (4ft)*	0.75		
SS4	22	92	1-1-3-3	1.8	6	***Clayey Silt**, brown, moist, medium stiff to stiff*	0.75 1.25		*Some gravel*
SS5	20	83	1-3-3-4	2.4	8		1.5 2		*Very hard to cut*
SS6	18	75	1-2-2-4	3	10		1 1.5		
SS7	16	67	1-2-2-3	3.7	12	*3.5m (11.5ft)* ***Clay**, blue, moist, very soft*	1.5 0.75		
SS8	22	92	WOH-WOH-WOH-WOH	4.3	14		0.25		
ST1				4.9	16	*4.9m (16ft)* *Shelby tubes with fixed piston (drilling using mud rotary ϕ = 82.55mm = 3.25in)*			*Not good! almost empty! only 4in recovered*
ST2				5.5	18		0.5	Low	
				6.1	20				

GENERAL OBSERVATIONS:

SS = split spoon
ST = shelby tube
WOH = weight of hammer

SCHOOL OF CIVIL ENGINEERING
PURDUE UNIVERSITY

LOG OF TEST BORING

Boring No. : *MR#2*
Location: *Madison, Daviess, IN*
Date: *Wednesday 11/02/2011*

Latitude: *38.898745*
Longitude: *-86.990615*
Elevation: *150.84m (494.88ft)*
Sheet *2* of *3*

SAMPLE						DESCRIPTION/CLASSIFICATION	SOIL PROPERTIES		
No.	Rec. (in)	Rec. (%)	SPT	Depth (m)	Depth (ft)		Pen.	HCl reaction	Observations
ST3				6.1	20		0.25	Medium	
ST4				6.7	22		0.75	Medium	
ST5				7.3	24		0.25	Medium	Lost 4 in from bottom
ST6				7.9	26		0.75	Strong	Lost 4 in from bottom
ST7				8.5	28		0.5	Medium	
ST8				9.1	30		0.5	Medium	
ST9				9.8	32		0.5	Medium	Stiff soil
ST10				10.4	34		0.5	Medium	Stiff soil
X				11.0	36		Forgot the piston below the tube edge		
ST11				11.6	38	11.9m (39ft)	0		
				12.2	40	***Sand***, *brown, loose*			

GENERAL OBSERVATIONS: ST = shelby tube

SCHOOL OF CIVIL ENGINEERING
PURDUE UNIVERSITY

LOG OF TEST BORING

Boring No. : *MR#2*
Location: *Madison, Daviess, IN*
Date: *Wednesday 11/02/2011*

Latitude: *38.898745*
Longitude: *-86.990615*
Elevation: *150.84m (494.88ft)*
Sheet *3* of *3*

SAMPLE						DESCRIPTION/CLASSIFICATION	SOIL PROPERTIES		
No.	Rec. (in)	Rec. (%)	SPT	Depth (m)	Depth (ft)		Pen.	HCl reaction	Observations
SS9	14	58	2-2-2-3	12.2	40		0		
SS10	21	88	4-3-2-2	12.8	42		0		Note that penecrometer is not applicable for sand (it was found for illustration purpose only)
SS11	15	63	2-3-2-3	13.4	44	***Sand***, *brown, loose*	0		
SS12	18	75	2-6-12-16	14.0	46		0.25		Some gravel
SS13	15	63	5-5-3-2	14.6	48		0		Some gravel
						15.1m (49.5ft)	0.25		
				15.2	50	***Silty sand***			

GENERAL OBSERVATIONS:

SS = split spoon
ST = shelby tube

SCHOOL OF CIVIL ENGINEERING
PURDUE UNIVERSITY

LOG OF TEST BORING

Boring No. : *FV#1 (+piezometer)*
Location: *Madison, Daviess, IN*
Date: *Wednesday 11/02/2011*

Latitude: *38.898770*
Longitude: *-86.990570*
Elevation: *150.84m (494.88ft)*
Sheet *1* of *2*

SAMPLE						DESCRIPTION/CLASSIFICATION	SOIL PROPERTIES		
No.	Rec. (in)	Rec. (%)	SPT	Depth (m)	Depth (ft)		Pen.	HCl reaction	Observations
SS1	18	75	2-2-5-5	0	0		2.75		
				0.6	2	***Silty Sand**, yellow, moist, loose*			
SS2	13	54	3-5-6-7				2.5		
				1.2	4				
SS3	18	75	1-3-3-3			*1.5m (5ft)*	1.5		
							0.75		
				1.8	6				
SS4	23	96	WOH-2-4-4			***Clayey Silt**, brown & yellow, moist, medium stiff to stiff*	0.25		
				2.4	8				
SS5			1-2-3-4				1.25		
						3m (10ft)	1.5		
				3	10				
SS6			1-2-2-2			***Clay**, blue & yellow, moist, very soft*	1		
				3.7	12				
SS7	20	83	1-1-2-2				1.25		
				4.3	14	*4.3m (14ft)*			
FV0						*Vane shear test (drilling using hollow stem auger ϕ = 107.95mm = 4.25in)*			
				4.9	16				
FV1						*→ undisturbed test*			*Very soft*
						→ remolded test			
				5.5	18	*→ collection of disturbed soil using SS*			
FV2						*→ installed piezometer when done*			
				6.1	20				

GENERAL OBSERVATIONS:

SS = split spoon
FV = field vane shear test
WOH = weight of hammer

SCHOOL OF CIVIL ENGINEERING
PURDUE UNIVERSITY

LOG OF TEST BORING

Boring No. : *FV#1 (+piezometer)*
Location: *Madison, Daviess, IN*
Date: *Friday 11/04/2011*

Latitude: *38.898770*
Longitude: *-86.990570*
Elevation: *150.84m (494.88ft)*
Sheet *2* of *2*

SAMPLE No.	Rec. (in)	Rec. (%)	SPT	Depth (m)	Depth (ft)	DESCRIPTION/CLASSIFICATION
FV3				6.1	20	
FV4				6.7	22	
FV5	*V. low remolded strength (~1 div) High sensitivity*			7.3	24	
FV6				7.9	26	
FV7				8.5	28	
FV8				9.1	30	
FV9	*Disturbed but good! Tested only top 6in. then push 1.5ft & test*			9.8	32	
FV10				10.4	34	
FV11				11.0	36	
				11.6	38	
				12.2	40	

8.2m (27ft)
8.8m (29ft)
9.1m (30ft)
10.7m (35ft)
11.6m (38ft)

OPEN PIPE PIEZOMETER

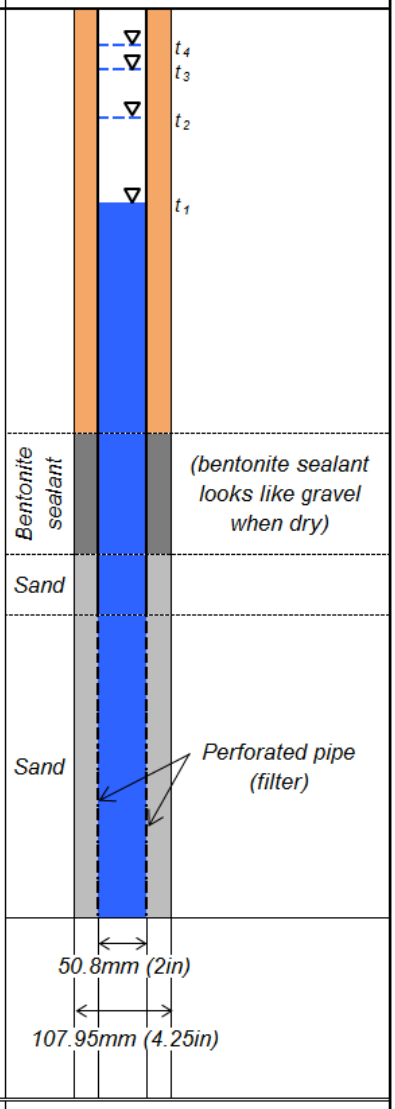

Piezometer was installed on Monday 11/07/2011

GENERAL OBSERVATIONS: FV = field vane shear test

SCHOOL OF CIVIL ENGINEERING
PURDUE UNIVERSITY

LOG OF TEST BORING

Boring No. : *HSA#1*
Location: *Madison, Daviess, IN*
Date: *Monday 11/07/2011*

Latitude: *38.898795*
Longitude: *-86.990570*
Elevation: *150.84m (494.88ft)*
Sheet *1* of *2*

SAMPLE						DESCRIPTION/CLASSIFICATION	SOIL PROPERTIES		
No.	Rec. (in)	Rec. (%)	SPT	Depth (m)	Depth (ft)		Pen.	HCl reaction	Observations
SS1	12	50	2-4-4-5	0	0		2.5		
SS2	10	42	4-3-3-3	0.6	2	***Silty Sand***, *yellow, moist, loose*	2.5		*bottom 6in: more silt compared with previous borings*
SS3	18	75	2-3-3-4	1.2	4		2.5 1.5		*more silt compared with previous borings*
						1.7m (5.5ft)			
SS4	19	79	2-3-3-5	1.8	6		2 1.75		
SS5	20	83	2-2-3-3	2.4	8	***Clayey Silt***, *brown to blue, moist, medium stiff to stiff*	1		*some roots*
SS6	24	100	2-3-4-4	3	10		1.75		*some roots very hard to cut*
						3.7m (12ft)			
SS7	18	75	1-1-2-2	3.7	12		1		
SS8	24	100	WOH-WOH-WOH-WOH	4.3	14	***Clay***, *blue, moist, very soft*	0.25	None	
						4.9m (16ft)			
ST1				4.9	16	*Shelby tubes with fixed piston (drilling using hollow stem auger ϕ = 82.55mm = 3.25in)*	0.25	None	*Missing 3in from top*
ST2				5.5	18		0.5	Medium	*Good*
				6.1	20				

GENERAL OBSERVATIONS:

SS = split spoon
ST = shelby tube
WOH = weight of hammer

SCHOOL OF CIVIL ENGINEERING
PURDUE UNIVERSITY

LOG OF TEST BORING

Boring No. : *HSA#1*
Location: *Madison, Daviess, IN*
Date: *Tuesday 11/08/2011*

Latitude: *38.898795*
Longitude: *-86.990570*
Elevation: *150.84m (494.88ft)*
Sheet *2* of *2*

SAMPLE						DESCRIPTION/CLASSIFICATION	SOIL PROPERTIES		
No.	Rec. (in)	Rec. (%)	SPT	Depth (m)	Depth (ft)		Pen.	HCl reaction	Observations
ST3				6.1	20		0.5	Strong	Not good! Lost 6in top coz piston stuck (using wrong spring)
ST4				6.7	22		0.5	Strong	Good
ST5				7.3	24		0.5	Strong	Missing 2in from bottom
X				7.9	26		Fixed piston stucked because he used the wrong spring fot the piston		
ST6				8.5	28		0.5	Medium	Good
ST7				9.1	30		0.5	Medium	Good
ST8				9.8	32		0.75	Medium	Good
ST9				10.4	34		0.75	Low	Good
ST10				11.0	36		0.5	Low	Missing 2in from top (no vacuum)
				11.6	38	11.6m (38ft)			
				12.2	40				

GENERAL OBSERVATIONS: ST = shelby tube

SCHOOL OF CIVIL ENGINEERING
PURDUE UNIVERSITY

LOG OF TEST BORING

Boring No. : *MR#3*
Location: *Madison, Daviess, IN*
Date: *Thursday 11/10/2011*

Latitude: *38.898770*
Longitude: *-86.990610*
Elevation: *150.84m (494.88ft)*
Sheet *1* of *2*

SAMPLE				Depth		DESCRIPTION/CLASSIFICATION	SOIL PROPERTIES		
No.	Rec. (in)	Rec. (%)	SPT	(m)	(ft)		Pen.	HCl reaction	Observations
				0	0				
				0.6	2				
				1.2	4				
				1.8	6				
				2.4	8				
				3	10				
				3.7	12				
				4.3	14	*4.3m (14ft)*			
ST1	*Not machined*			4.9	16	*Shelby tubes with fixed piston (drilling using mud rotary ϕ = 82.55mm = 3.25in)*	*0.5*	*Low*	*Not good! half empty!*
ST2	*Very soft*			5.5	18		*0*	*None*	*Not good! almost empty! only 4in recovered*
ST3				6.1	20		*0.5*	*Medium*	*Not good! Missing 9in top & 4in bottom*

GENERAL OBSERVATIONS: ST = shelby tube

Machined ST (ICR = 0)

Not machined ST (ICR > 0)

SCHOOL OF CIVIL ENGINEERING
PURDUE UNIVERSITY

LOG OF TEST BORING

Boring No. : *MR#3*
Location: *Madison, Daviess, IN*
Date: *Thursday 11/10/2011*

Latitude: *38.898770*
Longitude: *-86.990610*
Elevation: *150.84m (494.88ft)*
Sheet *2* of *2*

SAMPLE						DESCRIPTION/CLASSIFICATION	SOIL PROPERTIES		
No.	Rec. (in)	Rec. (%)	SPT	Depth (m)	Depth (ft)		Pen.	HCl reaction	Observations
ST4				6.1	20		0.25	Medium	Good
ST5				6.7	22		0.25	Strong	Good
X				7.3	24		Drilling to deeper depth by mistake		
ST6				7.9	26		0.75	Strong	Good
ST7				8.5	28		0.25	Medium	Good
ST8				9.1	30		0.25	Medium	Good
ST9				9.8	32		0.5	Medium	Missing 2in from top
ST10				10.4	34		0.25	Medium	missing 4in from top
ST11				11.0	36		0.5	None	Good
				11.6	38	***Sand*** *at bottom of ST 11.6m (38ft)*			
				12.2	40				

GENERAL OBSERVATIONS: ST = shelby tube

SCHOOL OF CIVIL ENGINEERING
PURDUE UNIVERSITY

LOG OF TEST BORING

Boring No. : *MR#4*
Location: *Madison, Daviess, IN*
Date: *Thursday 11/10/2011*

Latitude: *38.898785*
Longitude: *-86.990600*
Elevation: *150.84m (494.88ft)*
Sheet *1* of *3*

SAMPLE				Depth		DESCRIPTION/CLASSIFICATION	SOIL PROPERTIES		
No.	Rec. (in)	Rec. (%)	SPT	(m)	(ft)		Pen.	HCl reaction	Observations
				0	0				
				0.6	2				
				1.2	4				
				1.8	6				
				2.4	8				
				3	10				
				3.7	12				
				4.3	14				
				4.9	16	*4.9m (16ft)*			
ST1	Very soft					*Shelby tubes with fixed piston (drilling using mud rotary ϕ = 82.55mm = 3.25in)*	0	None	*Not good! Empty ST (with vacuum & waited 15 min)*
				5.5	18				
ST2				6.1	20		0.25		*missing 1in from top & 1in from bottom (with vacuum)*

GENERAL OBSERVATIONS: ST = shelby tube

SCHOOL OF CIVIL ENGINEERING
PURDUE UNIVERSITY

LOG OF TEST BORING

Boring No. : *MR#4*
Location: *Madison, Daviess, IN*
Date: *Friday 11/11/2011*

Latitude: *38.898785*
Longitude: *-86.990600*
Elevation: *150.84m (494.88ft)*
Sheet 2 of 3

SAMPLE						DESCRIPTION/CLASSIFICATION	SOIL PROPERTIES		
No.	Rec. (in)	Rec. (%)	SPT	Depth (m)	Depth (ft)		Pen.	HCl reaction	Observations
ST3				6.1	20		0.25	Medium	Good
ST4				6.7	22		0.5	Medium	Good
ST5				7.3	24		0.75	Strong	Good (not too much vacuum)
ST6				7.9	26		0.75	Medium	missing 2.5in bottom (no vacuum)
ST7	Fixed piston was not used			8.5	28	Nothing was recovered. Use not machined ST with fixed piston again to recover the disturbed soil	Highly disturbed! Do not use for eng. Properties. Only for classification (missing 4in top & 4 in bottom)		
ST8	Not machined			9.1	30			Strong	
ST9				9.8	32		0.75	Medium	Good
ST10				10.4	34		0.5	Low	missing 3in top
ST11				11.0	36			None (bottom of ST)	Good
				11.6	38	11.6m (38ft)	1		
ST12				12.2	40	***Sand*** *at top & bottom of ST*	0.5	None	

GENERAL OBSERVATIONS: ST = shelby tube
ICR = inside clearance ratio

Machined ST (ICR = 0)

Not machined ST (ICR > 0)

SCHOOL OF CIVIL ENGINEERING
PURDUE UNIVERSITY

LOG OF TEST BORING

Boring No. : *MR#4*
Location: *Madison, Daviess, IN*
Date: *Friday 11/11/2011*

Latitude: *38.898785*
Longitude: *-86.990600*
Elevation: *150.84m (494.88ft)*
Sheet *3* of *3*

SAMPLE						DESCRIPTION/CLASSIFICATION	SOIL PROPERTIES		
No.	Rec. (in)	Rec. (%)	SPT	Depth (m)	Depth (ft)		Pen.	HCl reaction	Observations
SS1	17	71	1-1-2-2	12.2	40				
SS2	17	71	4-5-3-2	12.8	42				
SS3	20	83	2-3-4-5	13.4	44	***Sand***, *brown, wet, loose*			
SS4	16	67	8-11-14-16	14.0	46				
SS5	16	67	5-9-3-7	14.6	48				
				15.2	50	*15.1m (49.5ft)* ***Silty sand***		*None*	*Some gravel*

GENERAL OBSERVATIONS:
SS = split spoon
ST = shelby tube

Appendix G. Piezocone Penetration Profiles

This appendix summarizes the Piezocone penetration profiles for the seven Piezocone penetration tests (CPT#1, CPT#2, CPT#3A, CPT#4, CPT#5, CPT#6, and CPT#7) that were conducted as part of the field program.

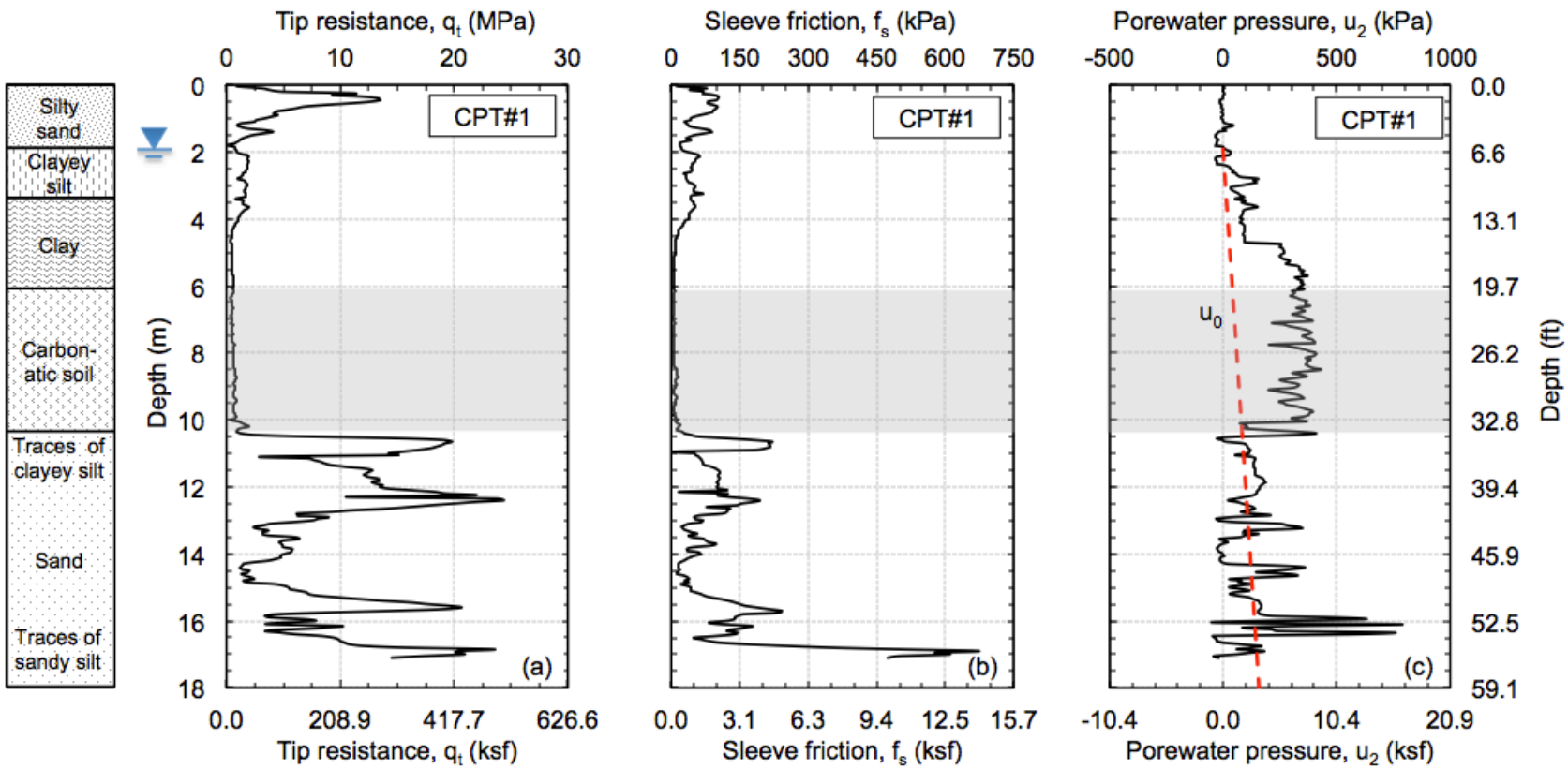

Figure G-1: CPT#1 results: (a) tip resistance, (b) skin friction, and (c) porewater pressure versus depth

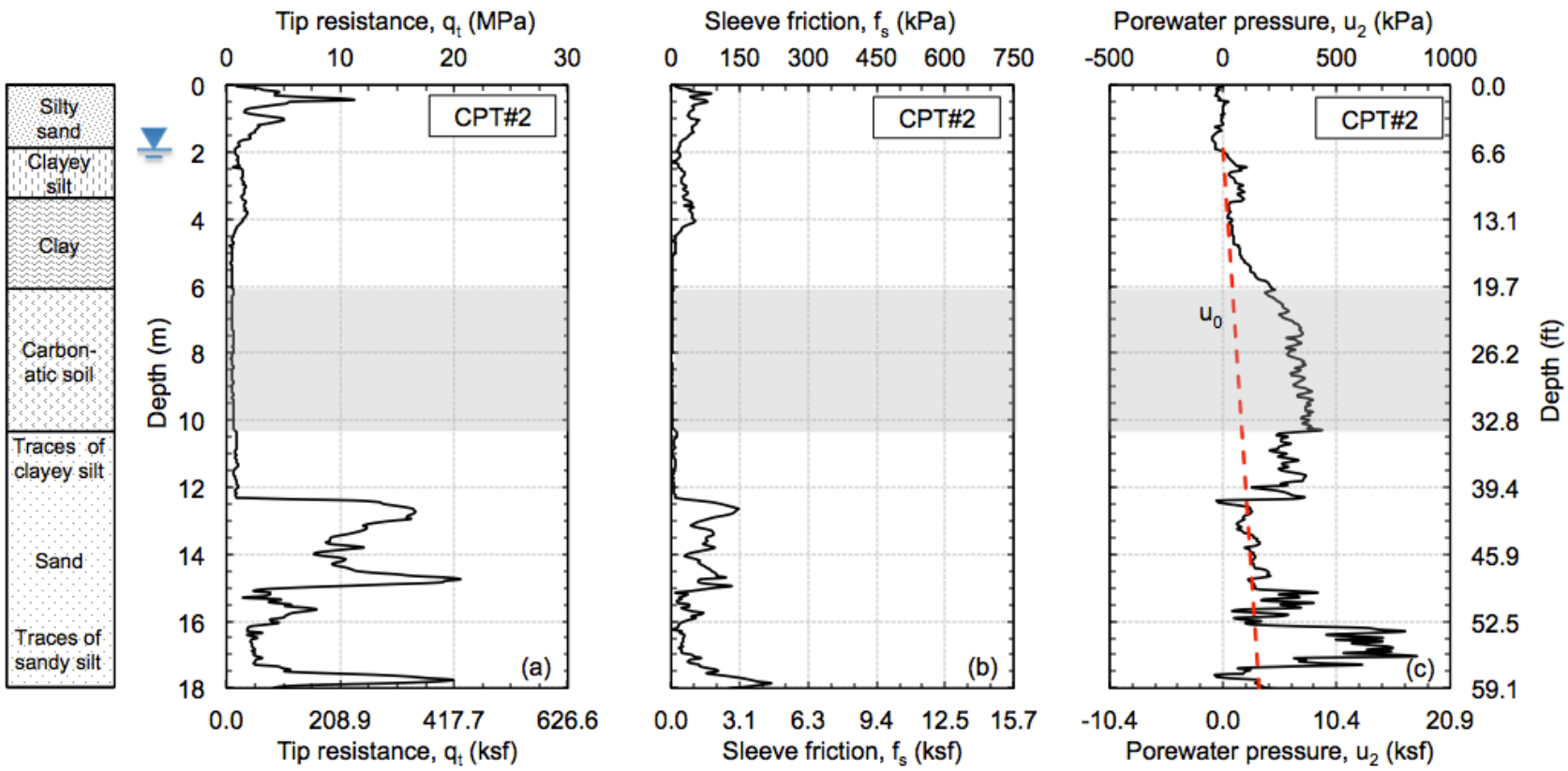

Figure G-2: CPT#2 results: (a) tip resistance, (b) skin friction, and (c) porewater pressure versus depth

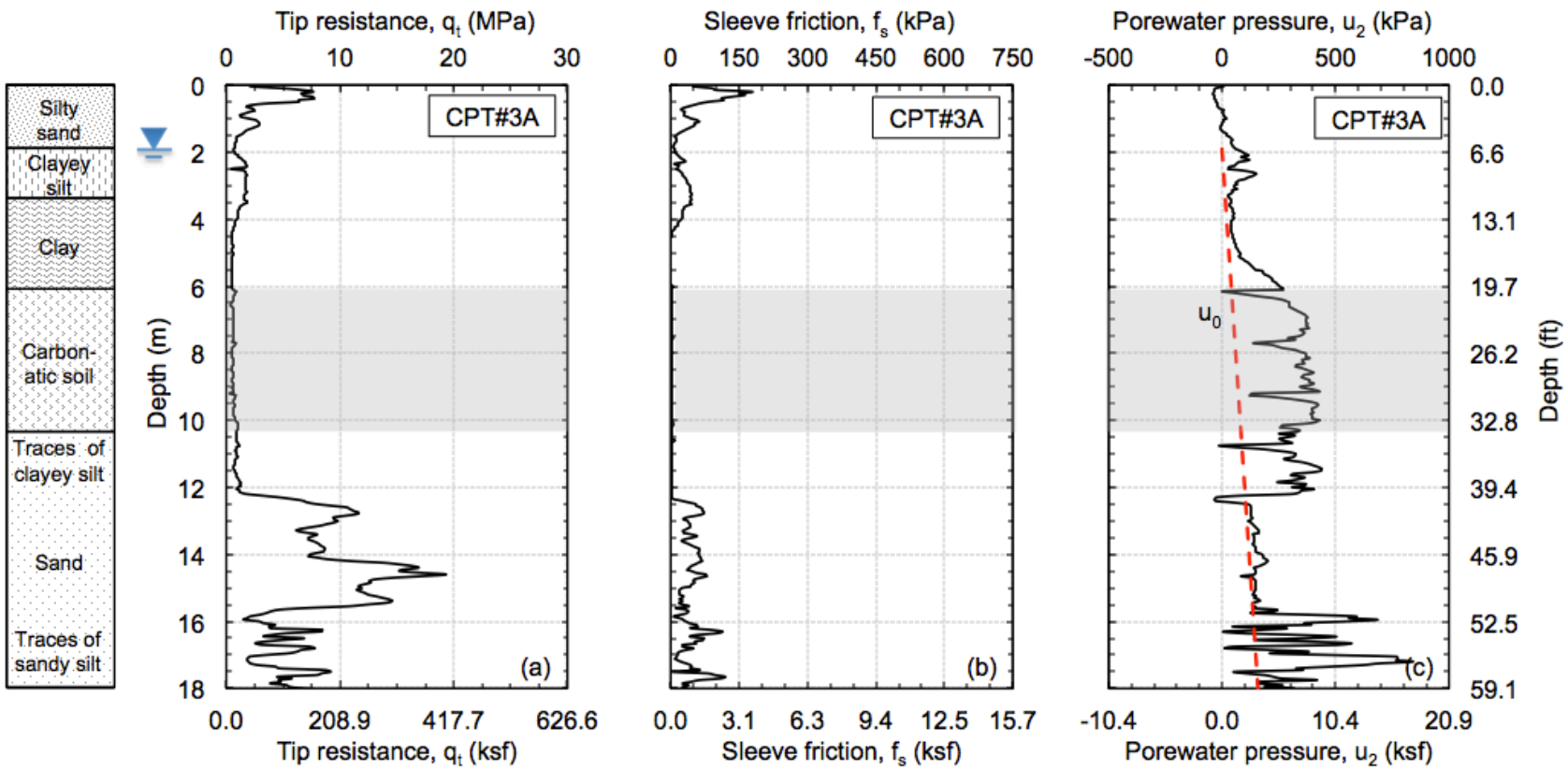

Figure G-3: CPT#3A results: (a) tip resistance, (b) skin friction, and (c) porewater pressure versus depth

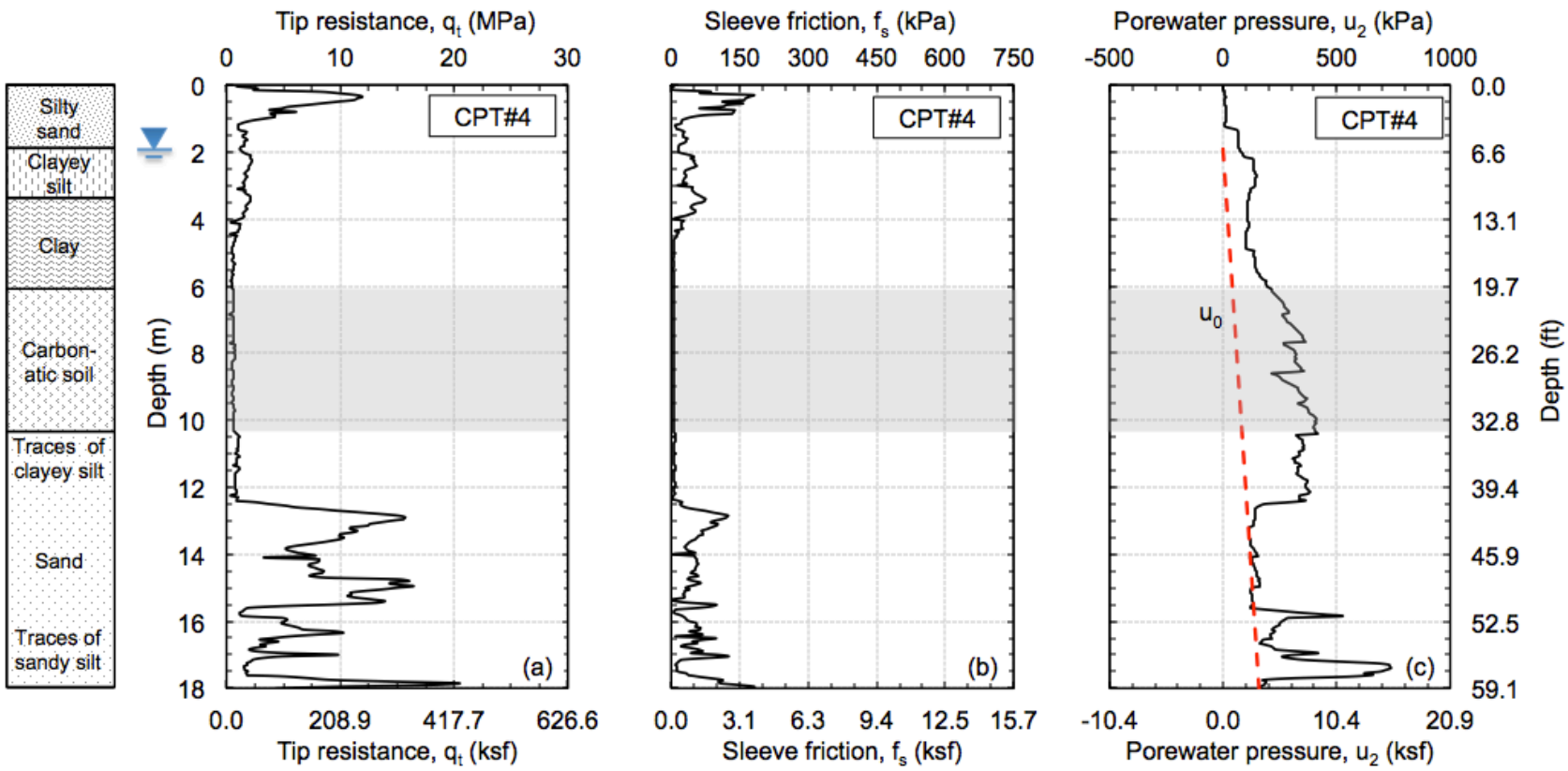

Figure G-4: CPT#4 results: (a) tip resistance, (b) skin friction, and (c) porewater pressure versus depth

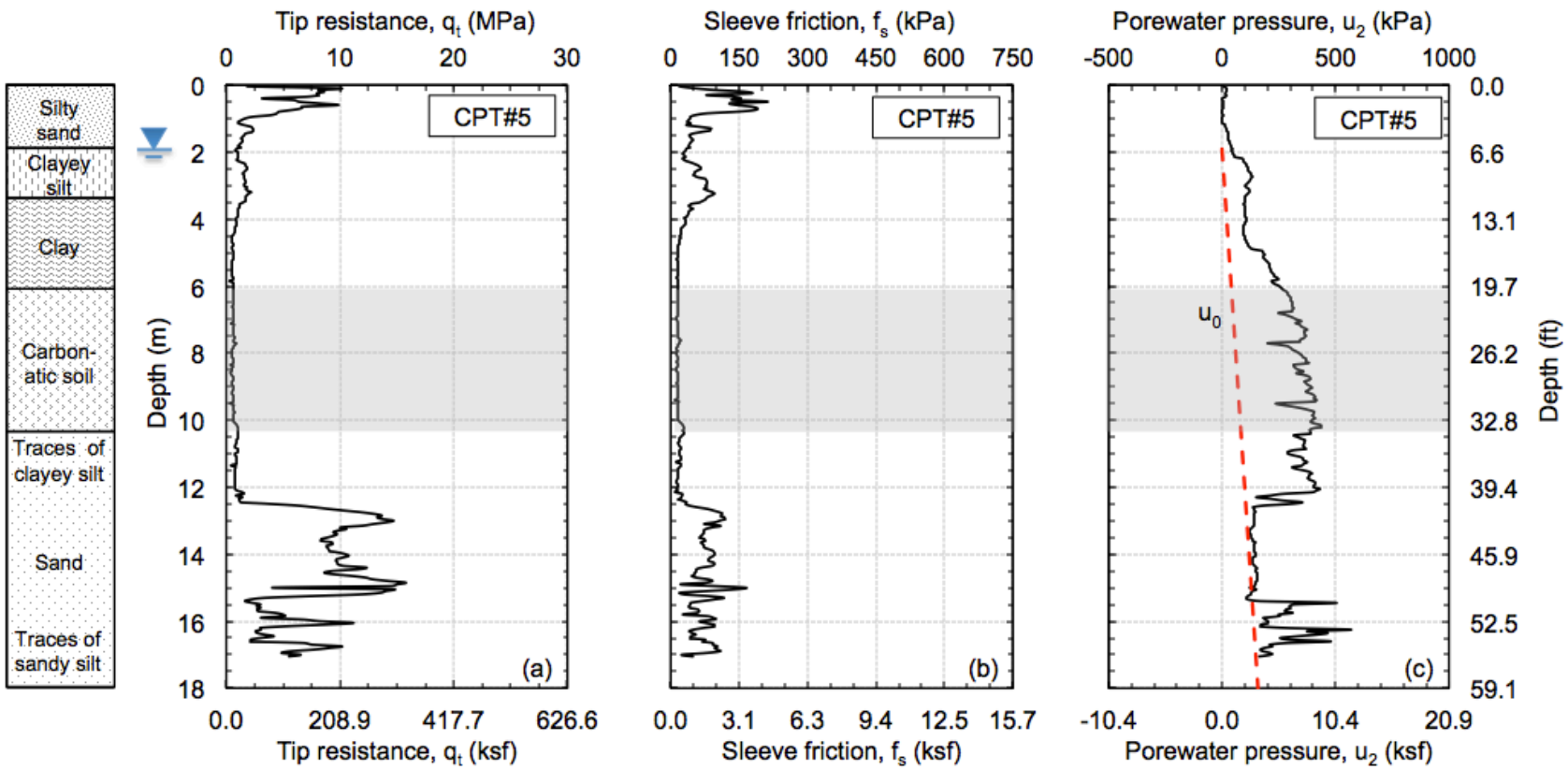

Figure G-5: CPT#5 results: (a) tip resistance, (b) skin friction, and (c) porewater pressure versus depth

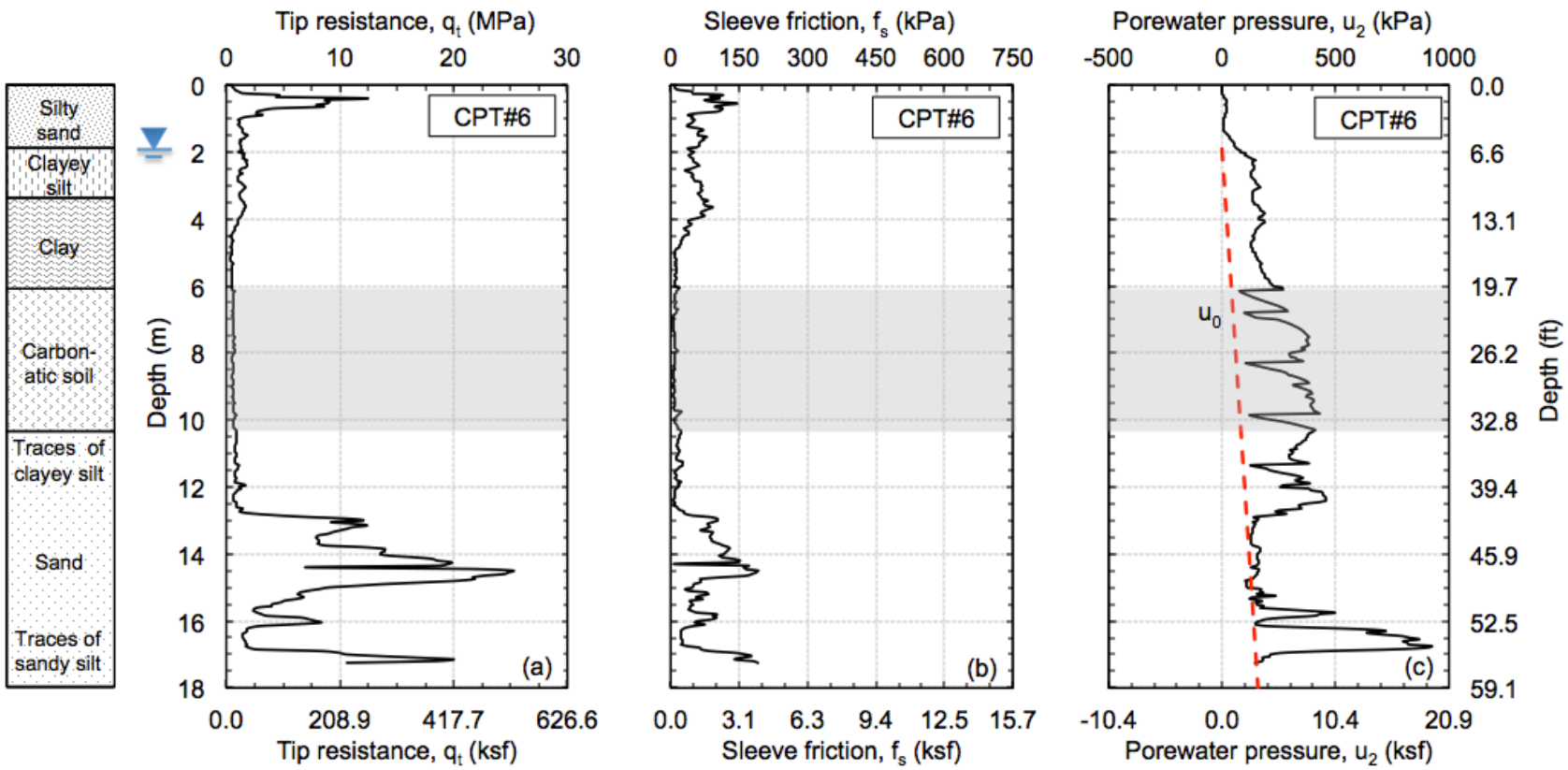

Figure G-6: CPT#6 results: (a) tip resistance, (b) skin friction, and (c) porewater pressure versus depth

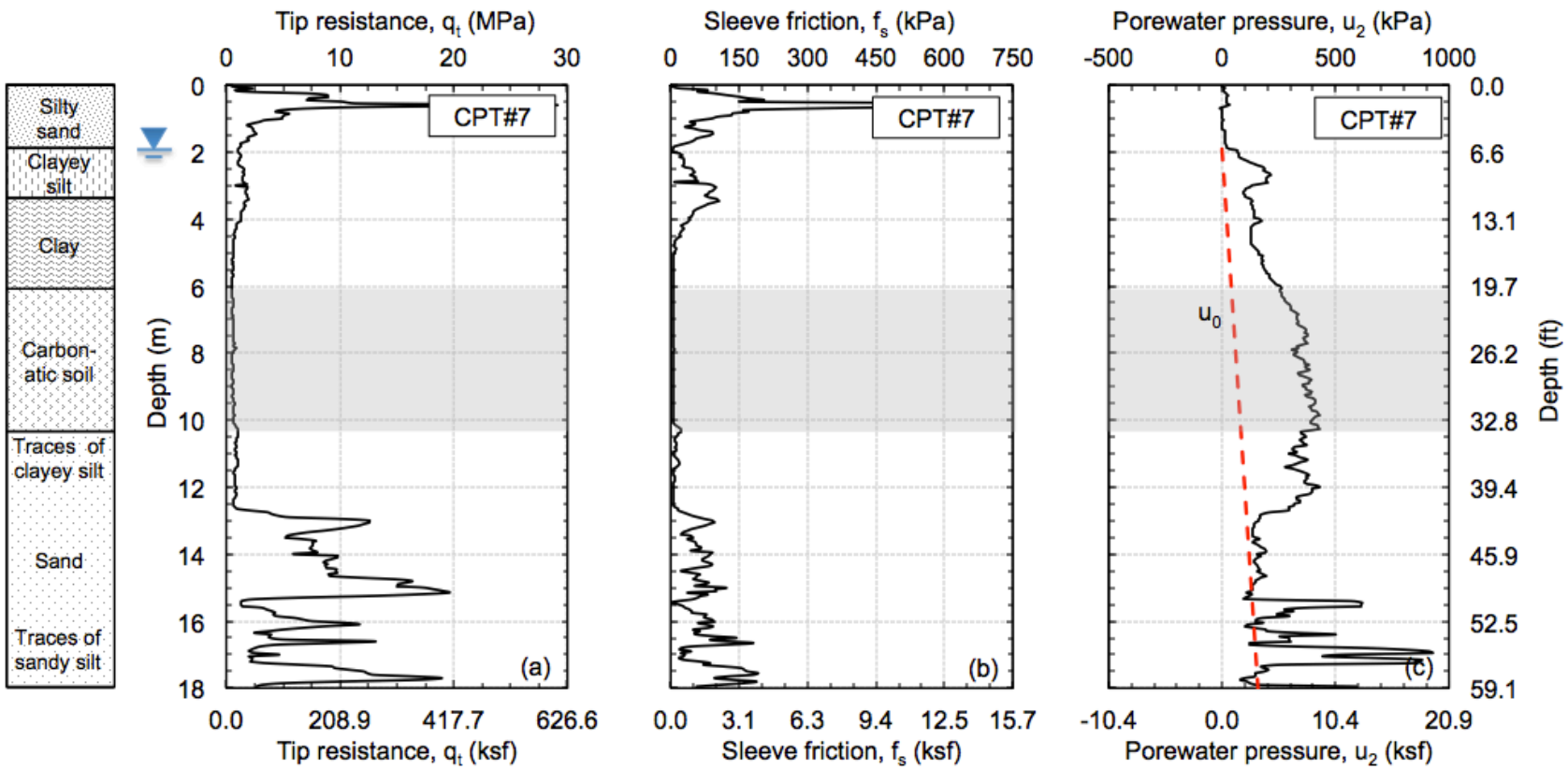

Figure G-7: CPT#7 results: (a) tip resistance, (b) skin friction, and (c) porewater pressure versus depth

Appendix H. Field Vane Shear Tests

This appendix summarizes the results of the eleven field vane shear tests conducted at various depths as part of the field program.

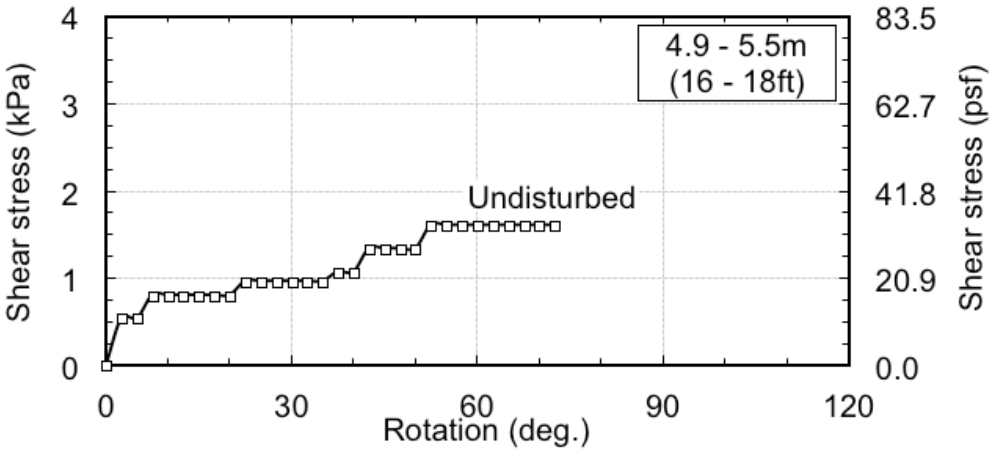

Figure H-1: Results of field vane shear test (FV1) conducted at ~5.3 m (17.5 ft)

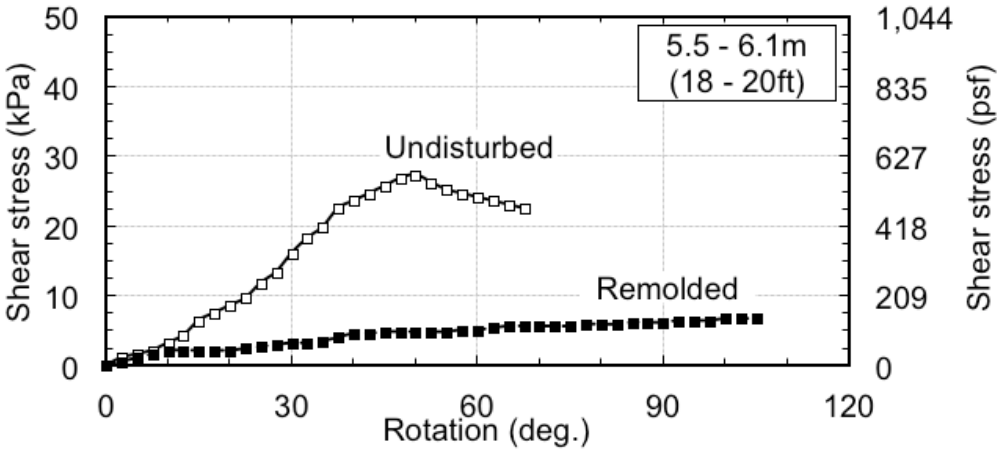

Figure H-2: Results of field vane shear test (FV2) conducted at ~5.9 m (19.5 ft)

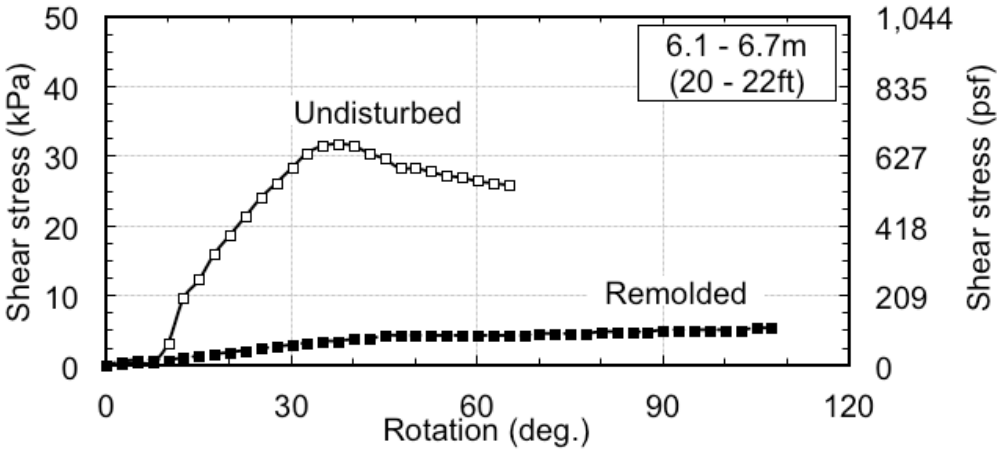

Figure H-3: Results of field vane shear test (FV3) conducted at ~6.6 m (21.5 ft)

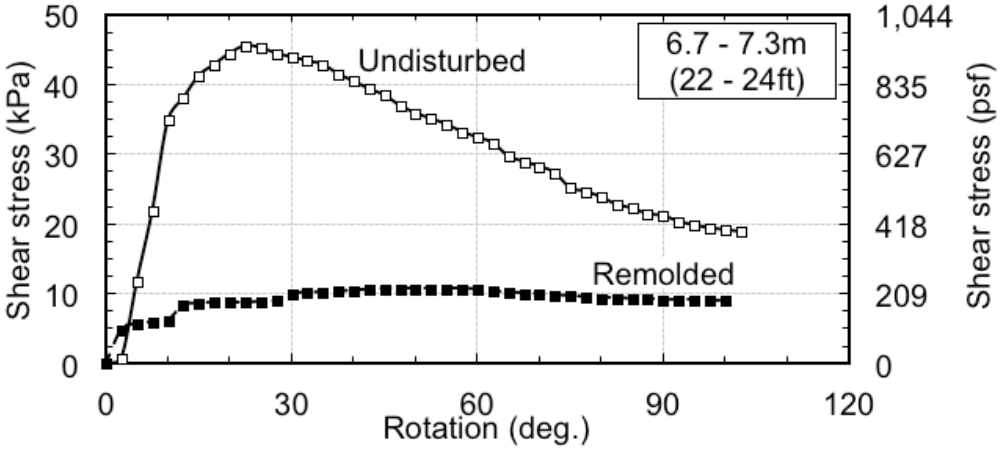

Figure H-4: Results of field vane shear test (FV4) conducted at ~7.2 m (23.5 ft)

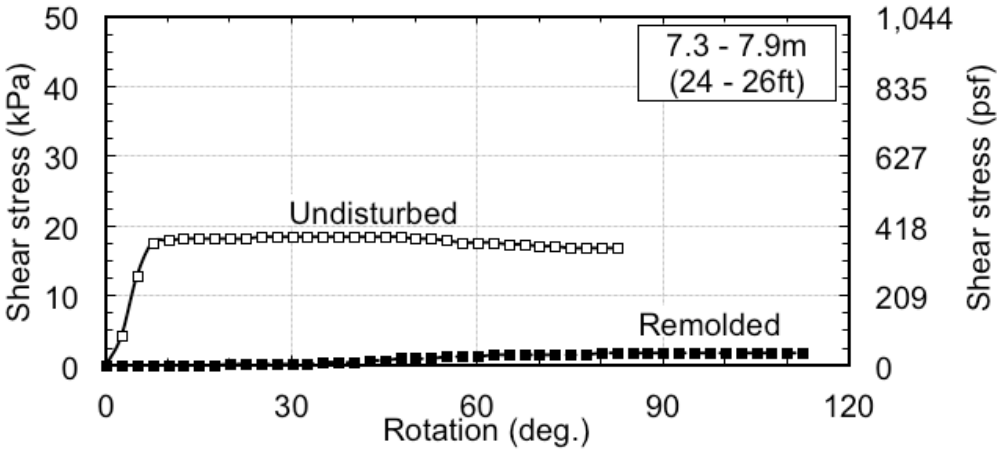

Figure H-5: Results of field vane shear test (FV5) conducted at ~7.8 m (25.5 ft)

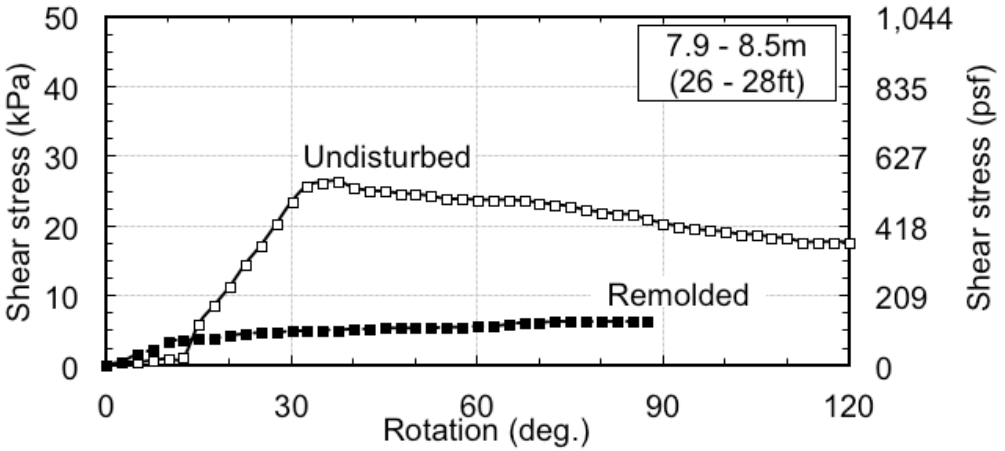

Figure H-6: Results of field vane shear test (FV6) conducted at ~8.4 m (27.5 ft)

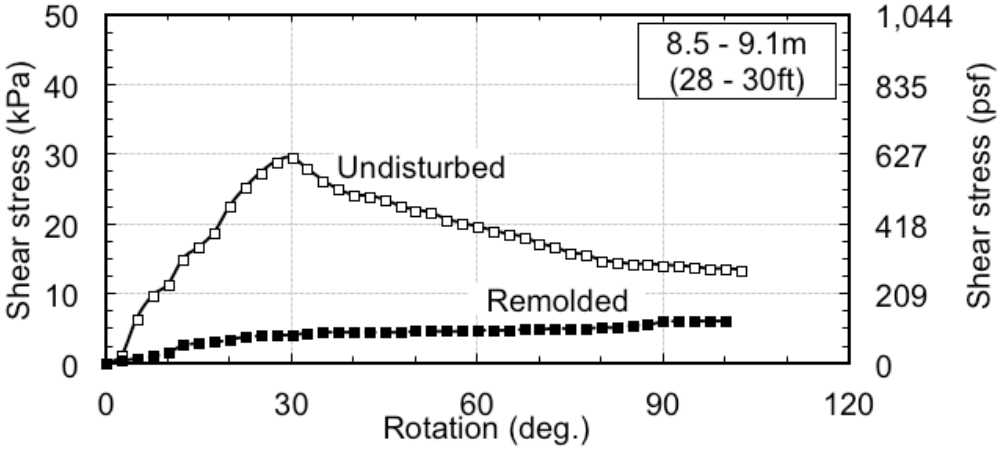

Figure H-7: Results of field vane shear test (FV7) conducted at ~9.0 m (29.5 ft)

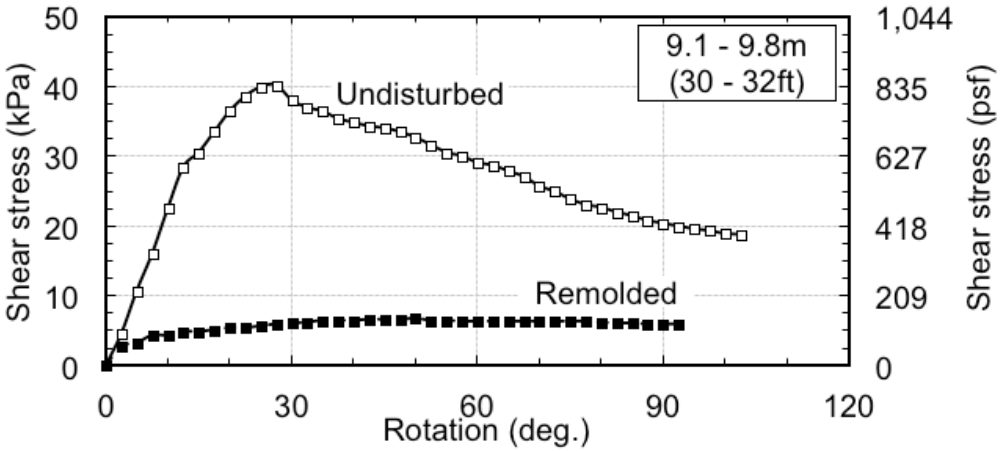

Figure H-8: Results of field vane shear test (FV8) conducted at ~9.6 m (31.5 ft)

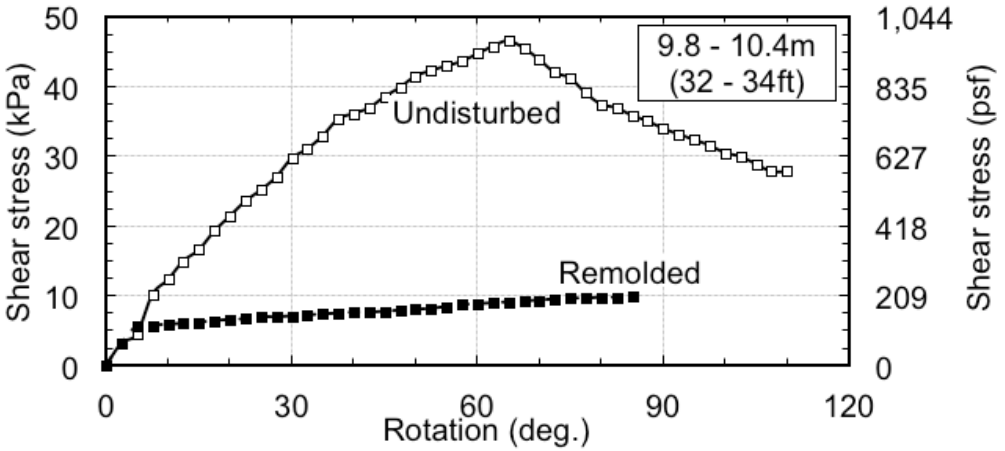

Figure H-9: Results of field vane shear test (FV9) conducted at ~10.2 m (33.5 ft)

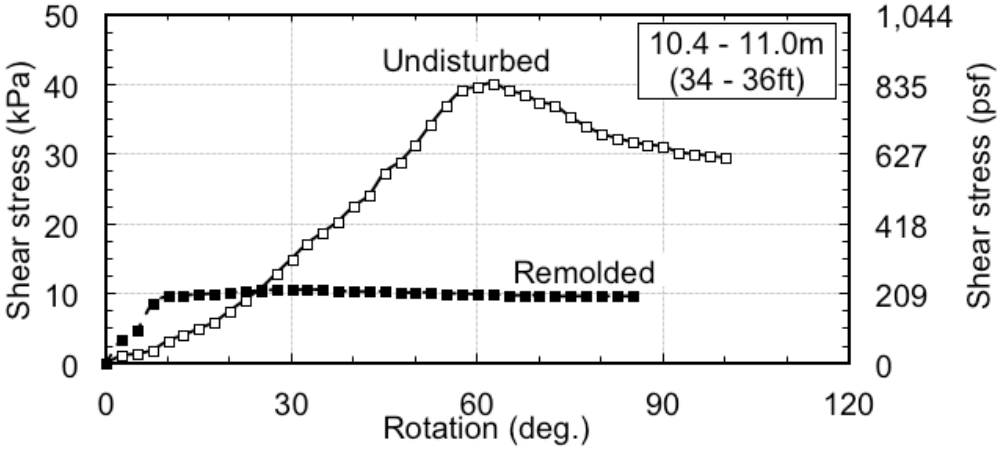

Figure H-10: Results of field vane shear test (FV10) conducted at 10.8 m (35.5 ft)

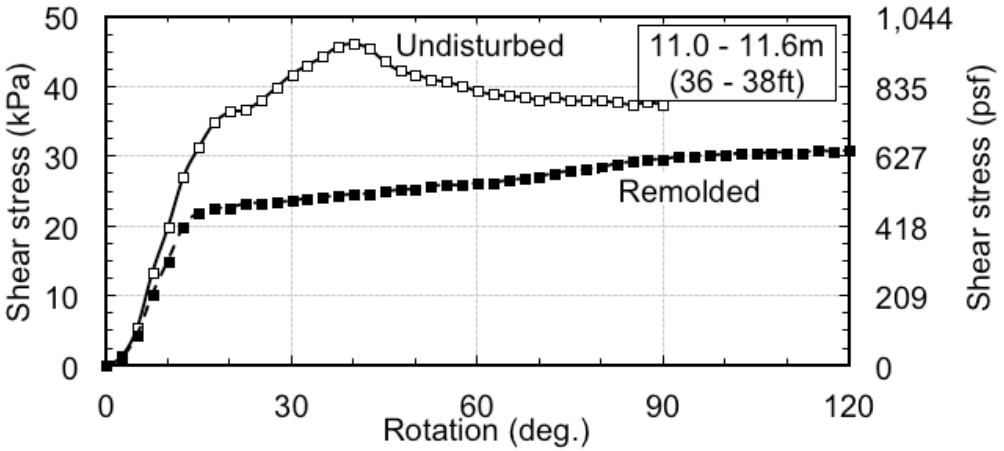

Figure H-11: Results of field vane shear test (FV11) conducted at 11.4 m (37.5 ft)

Appendix I. Location of Engineering Tests

This appendix summarizes the location of all the engineering tests (CRS, IL, and TX) performed on samples obtained from the boreholes MR#1, MR#2, MR#3, and MR#4.

SCHOOL OF CIVIL ENGINEERING
PURDUE UNIVERSITY

LOG OF ENGINEERING TESTS

Sheet 1 of 3

Depth (m)	Depth (ft)	MR#1	MR#2	MR#3	MR#4
6.71	22.0				
			CRS103 (M)		TX123 (M)
6.86	22.5				
			IL101 (M)		
7.01	23.0		TX108 (M)		CRS112 (M)
				TX111 (M)	
			TX109 (M)		
7.16	23.5			TX112 (M)	TX119 (M)
7.32	24.0				
					TX114 (M)
7.47	24.5	TX103 (C)			
		CRS109 (C)			
		CRS110 (M)			TX115 (C)
7.62	25.0	TX105 (C)			TX116 (C)
7.77	25.5				
		IL104 (C)			
7.92	26.0				

MR = mud rotary drilling technique
( ) = soil type: M for soil M and C for soil C

IL = incremental loading consolidation test
CRS = constant rate of strain consolidation test
TX = triaxial shear test

SCHOOL OF CIVIL ENGINEERING
PURDUE UNIVERSITY

LOG OF ENGINEERING TESTS

Sheet 2 of 3

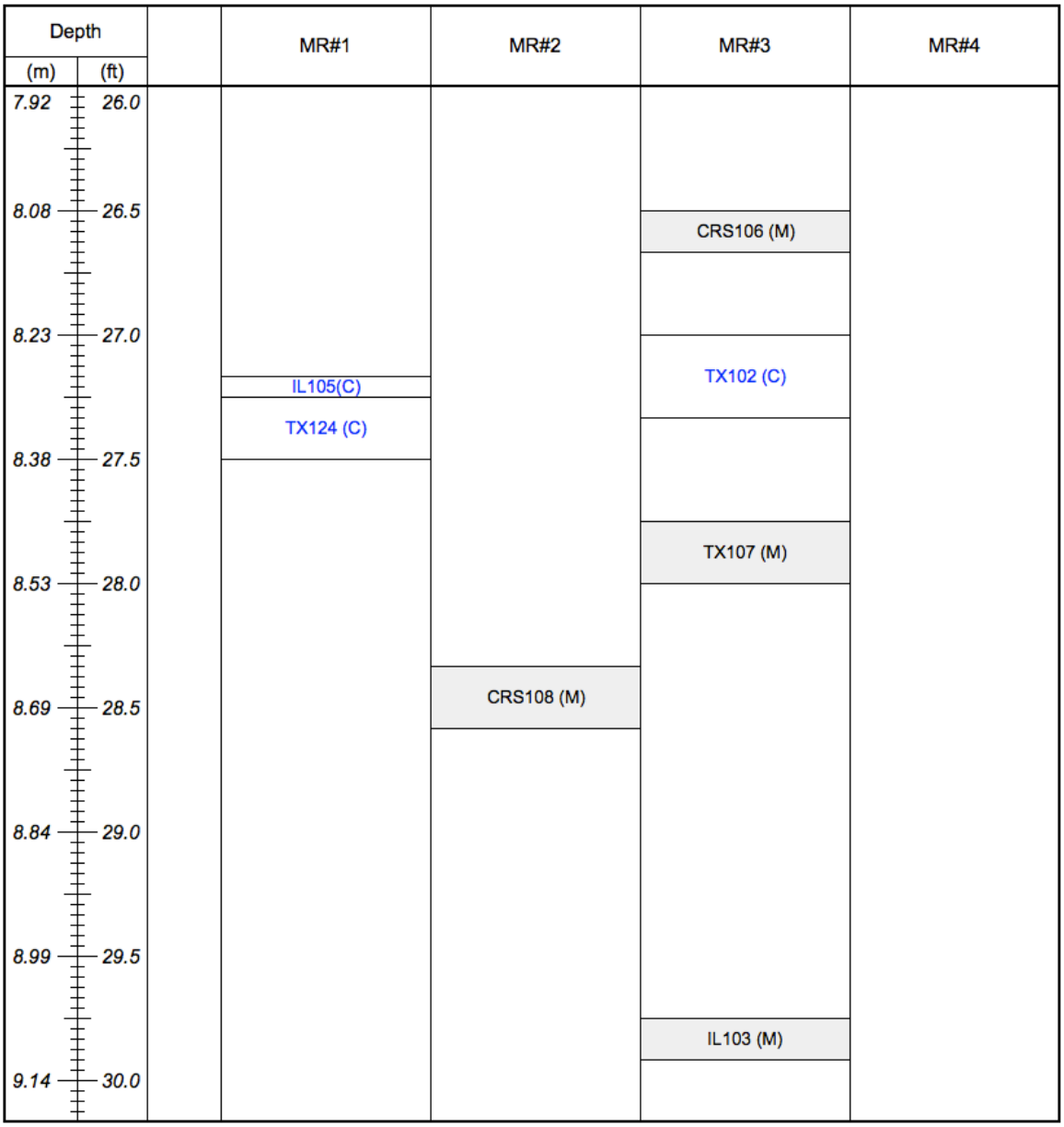

MR = mud rotary drilling technique
( ) = soil type: M for soil M and C for soil C

IL = incremental loading consolidation test
CRS = constant rate of strain consolidation test
TX = triaxial shear test

SCHOOL OF CIVIL ENGINEERING
PURDUE UNIVERSITY

LOG OF ENGINEERING TESTS

Sheet 3 of 3

Depth (m)	Depth (ft)		MR#1	MR#2	MR#3	MR#4
9.14	30.0					
			CRS105 (M)			
9.30	30.5					
9.45	31.0					
9.60	31.5					
9.75	32.0					
9.91	32.5					
10.1	33.0					
10.2	33.5					
10.4	34.0					

MR = mud rotary drilling technique
( ) = soil type: M for soil M and C for soil C

IL = incremental loading consolidation test
CRS = constant rate of strain consolidation test
TX = triaxial shear test

Appendix J. Carbon Dating Calibration Curves

This appendix presents the calibration curves for the nine samples tested for carbon dating. These curves, obtained using CALIB v. 7.1, IntCal13 database, convert the radiocarbon ages obtained from the AMS measurements into “real” calendar years ‘before present’ (BP), which refers to 1950.

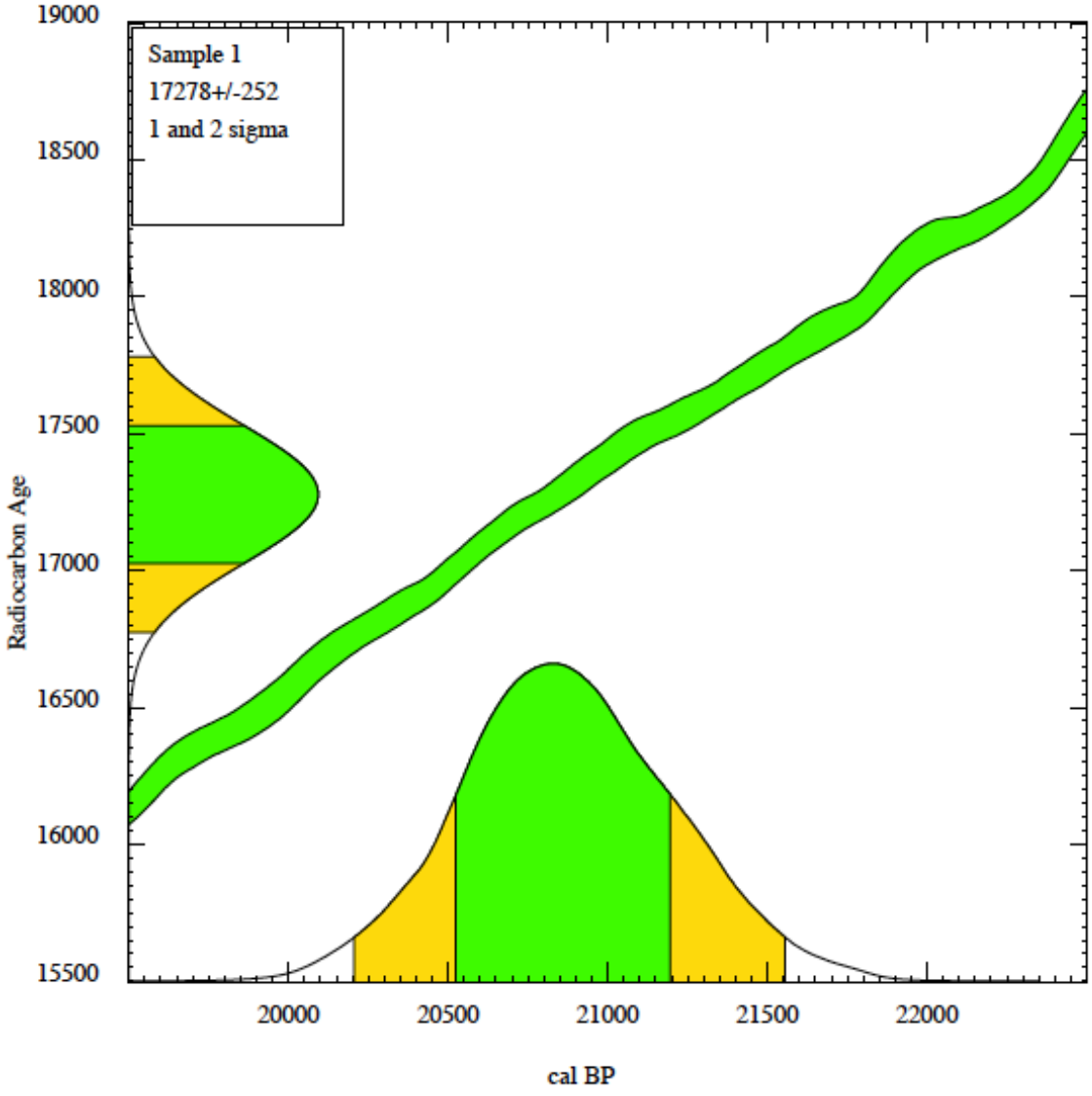
Sample 1
17278+/-252
1 and 2 sigma
Radiocarbon Age
19000
18500
18000
17500
17000
16500
16000
15500
20000
20500
21000
21500
22000
cal BP

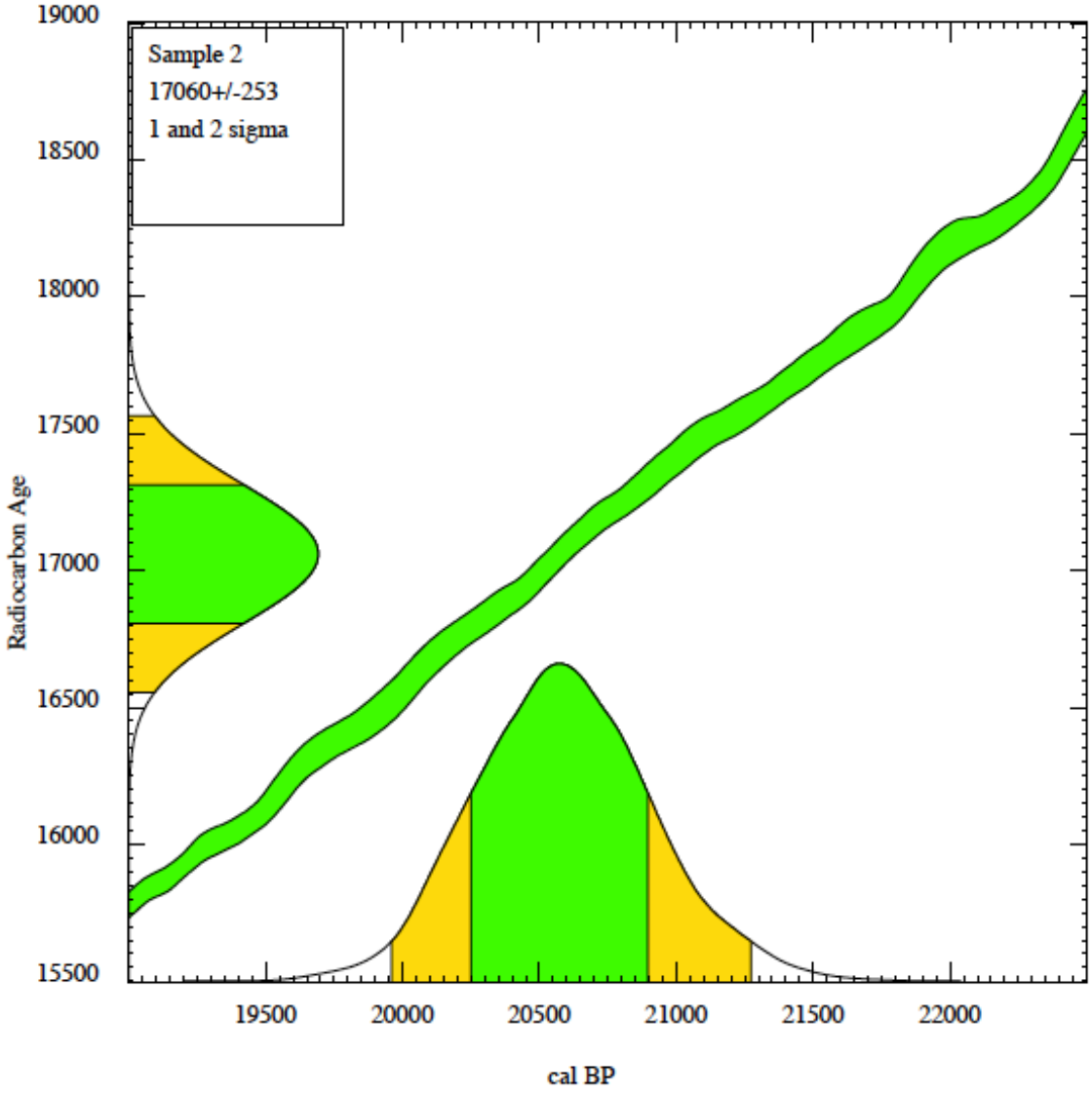
Sample 2
17060+/-253
1 and 2 sigma
Radiocarbon Age
19000
18500
18000
17500
17000
16500
16000
15500
19500
20000
20500
21000
21500
22000
cal BP

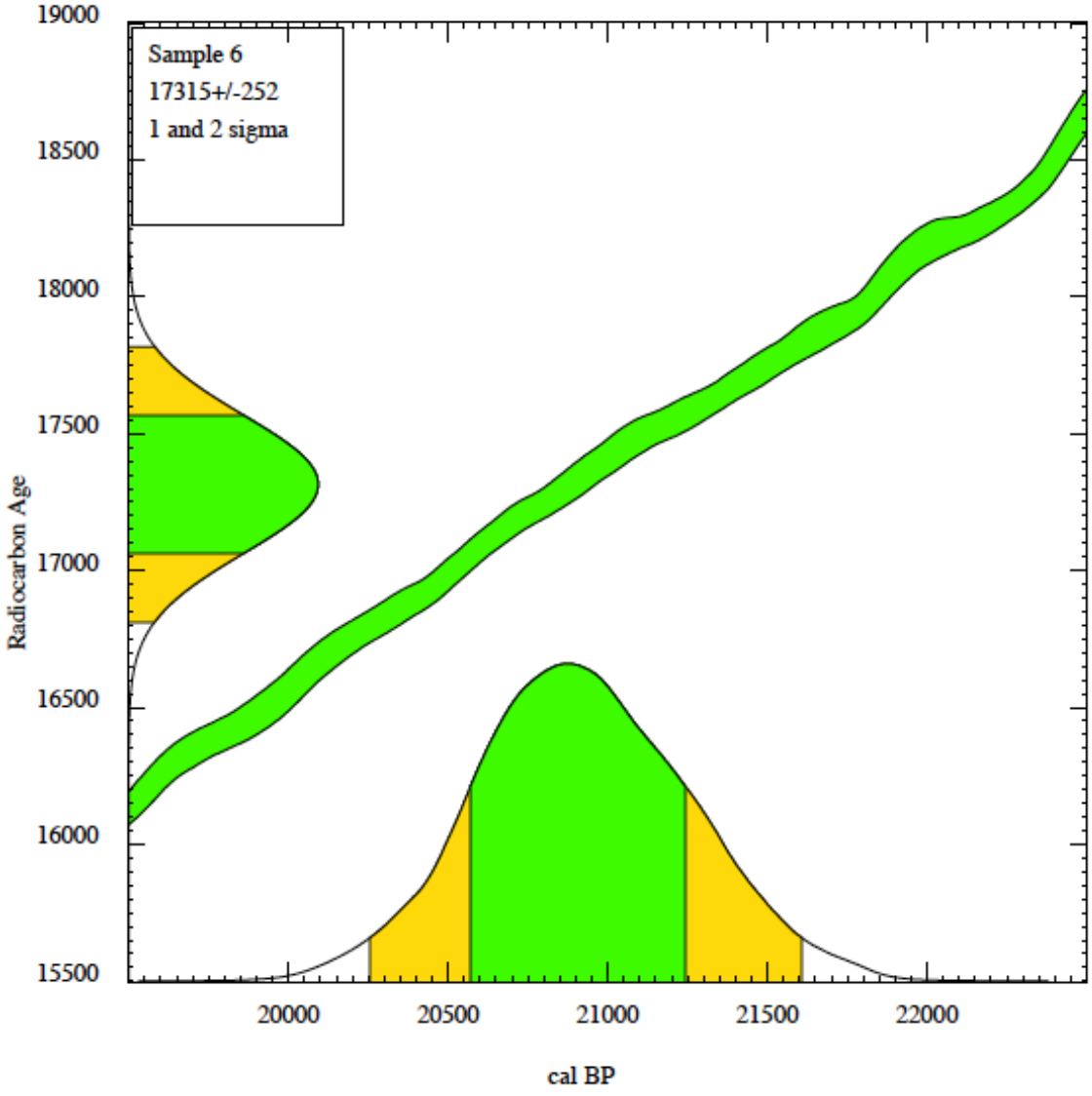
Sample 6
17315+/-252
1 and 2 sigma
19000
18500
18000
17500
17000
16500
16000
15500
Radiocarbon Age
20000
20500
21000
21500
22000
cal BP

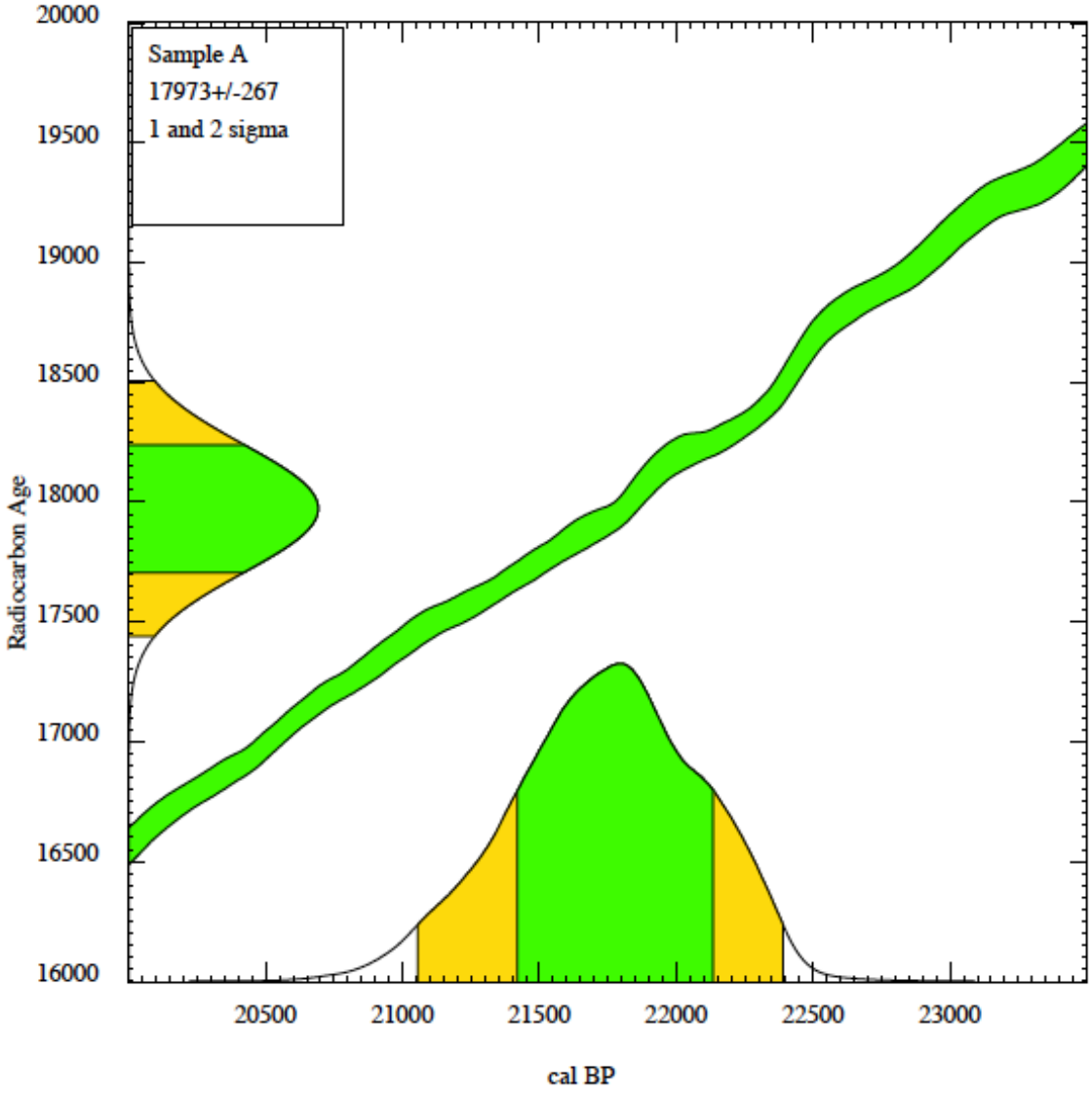
Sample A
17973+/-267
1 and 2 sigma
Radiocarbon Age
20000
19500
19000
18500
18000
17500
17000
16500
16000
20500
21000
21500
22000
22500
23000
cal BP

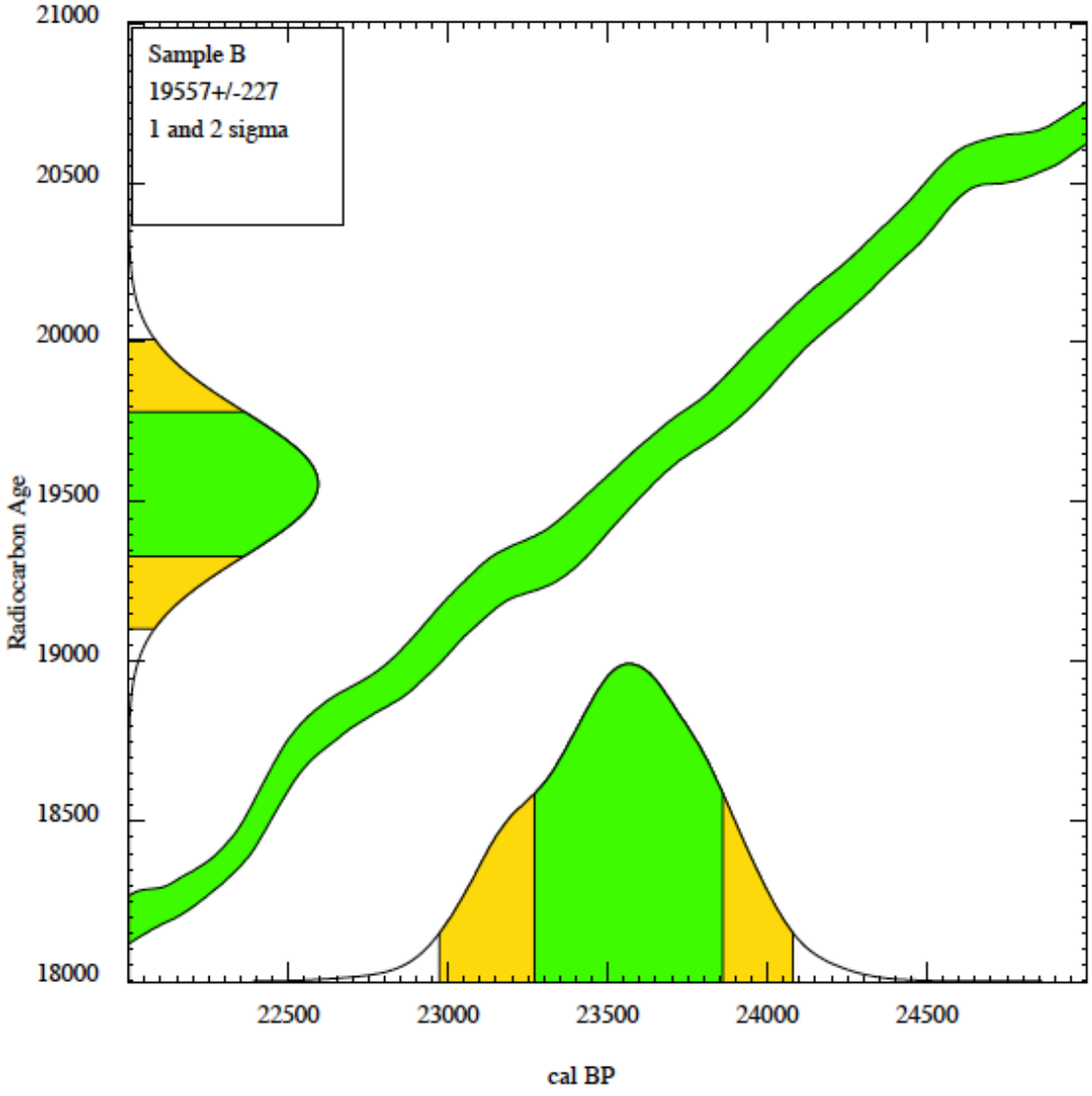
Sample B
19557+/-227
1 and 2 sigma
Radiocarbon Age
21000
20500
20000
19500
19000
18500
18000
22500
23000
23500
24000
24500
cal BP

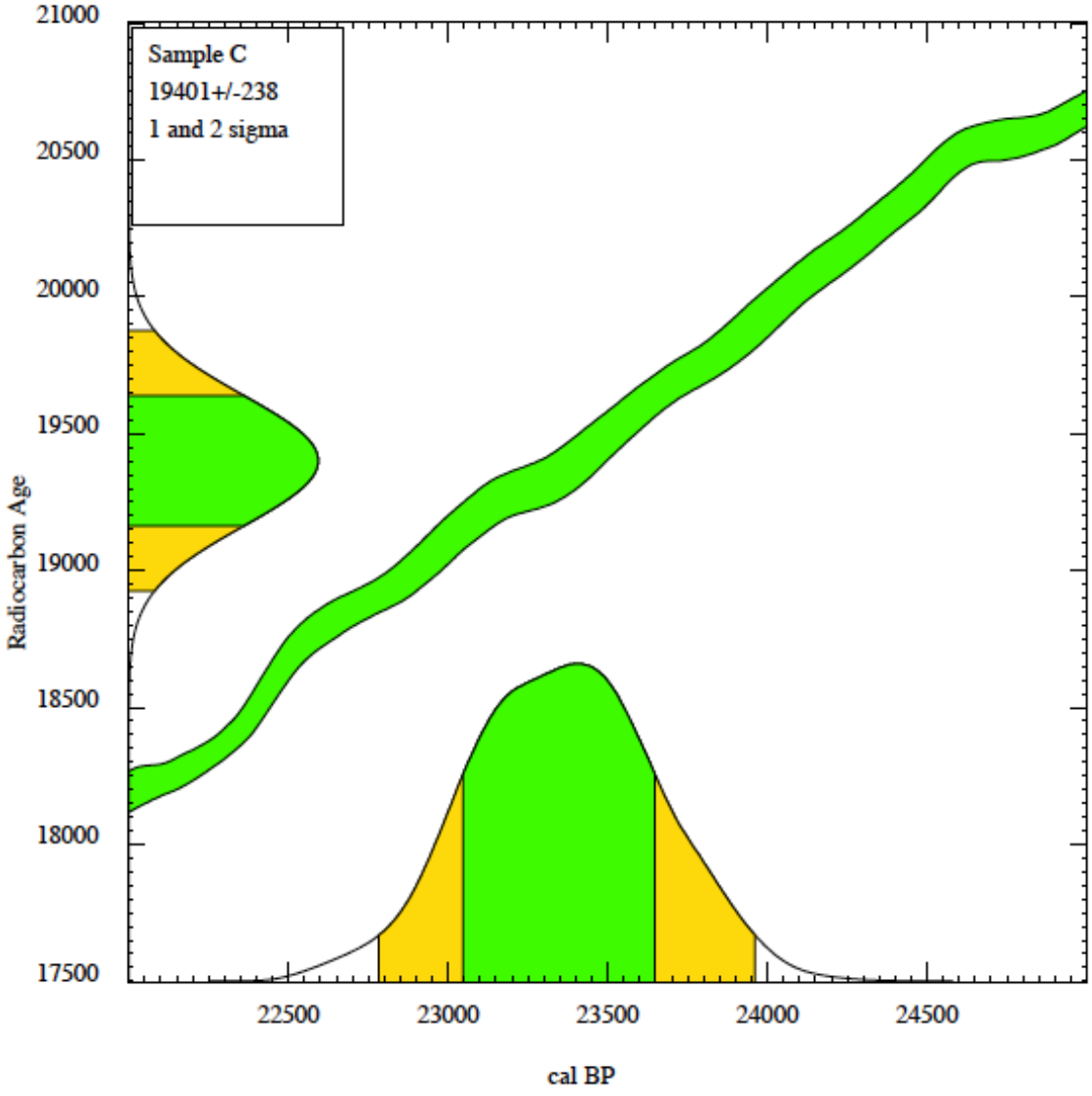
Sample C
19401+/-238
1 and 2 sigma
Radiocarbon Age
21000
20500
20000
19500
19000
18500
18000
17500
22500
23000
23500
24000
24500
cal BP

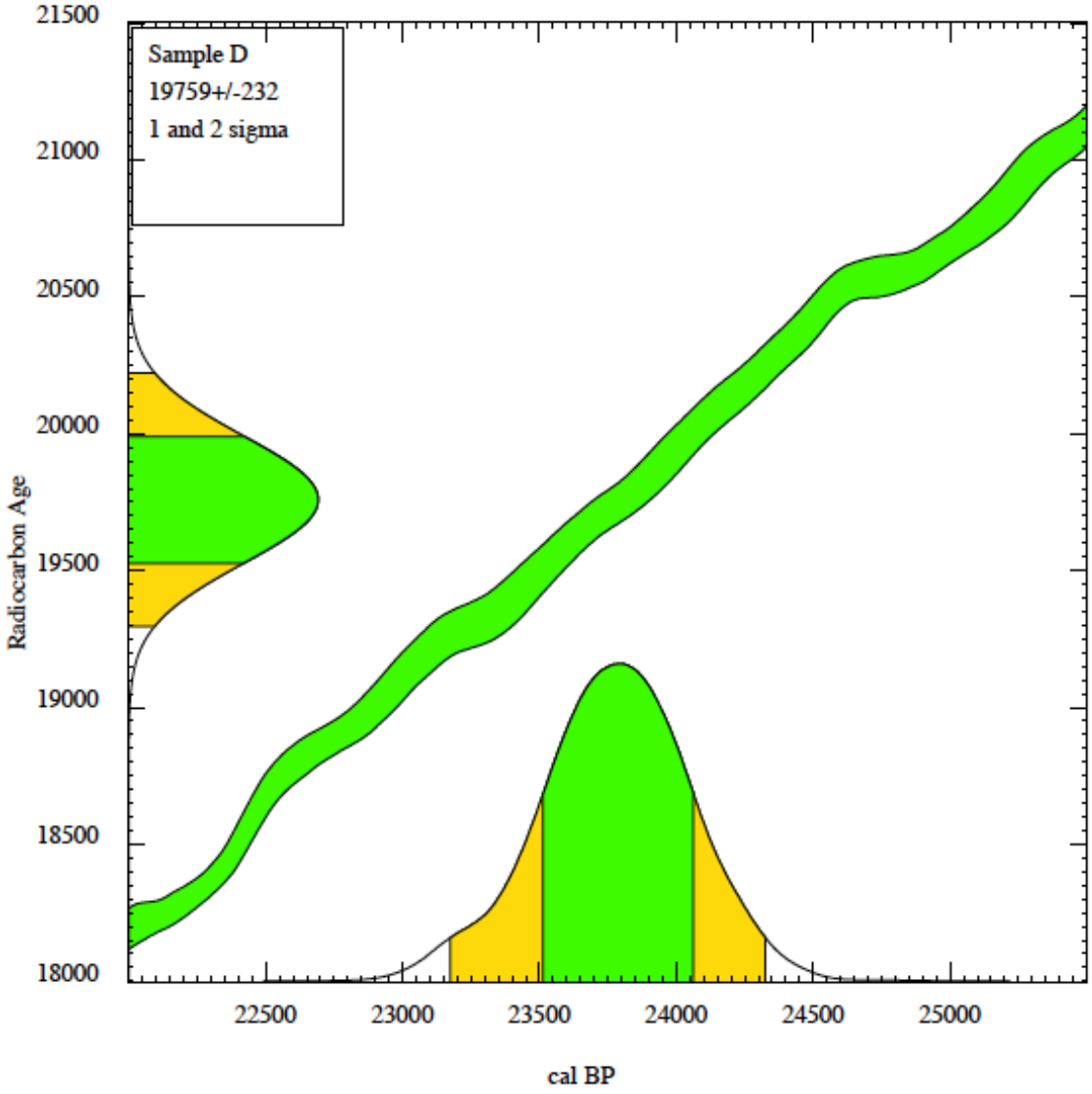
Sample D
19759+/-232
1 and 2 sigma
Radiocarbon Age
21500
21000
20500
20000
19500
19000
18500
18000
22500
23000
23500
24000
24500
25000
cal BP

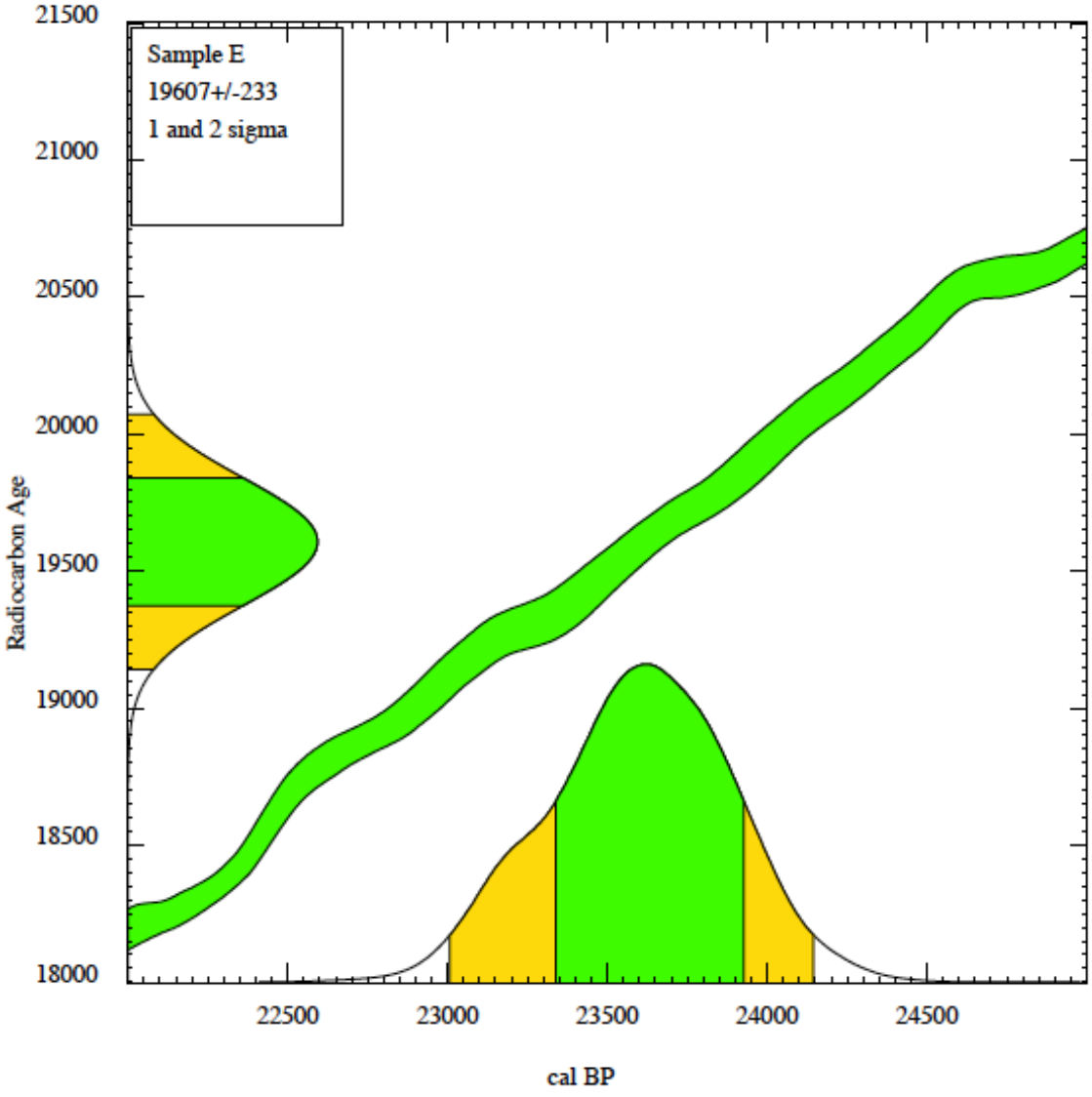
Sample E
19607+/-233
1 and 2 sigma
21500
21000
20500
20000
19500
19000
18500
18000
Radiocarbon Age
22500
23000
23500
24000
24500
cal BP

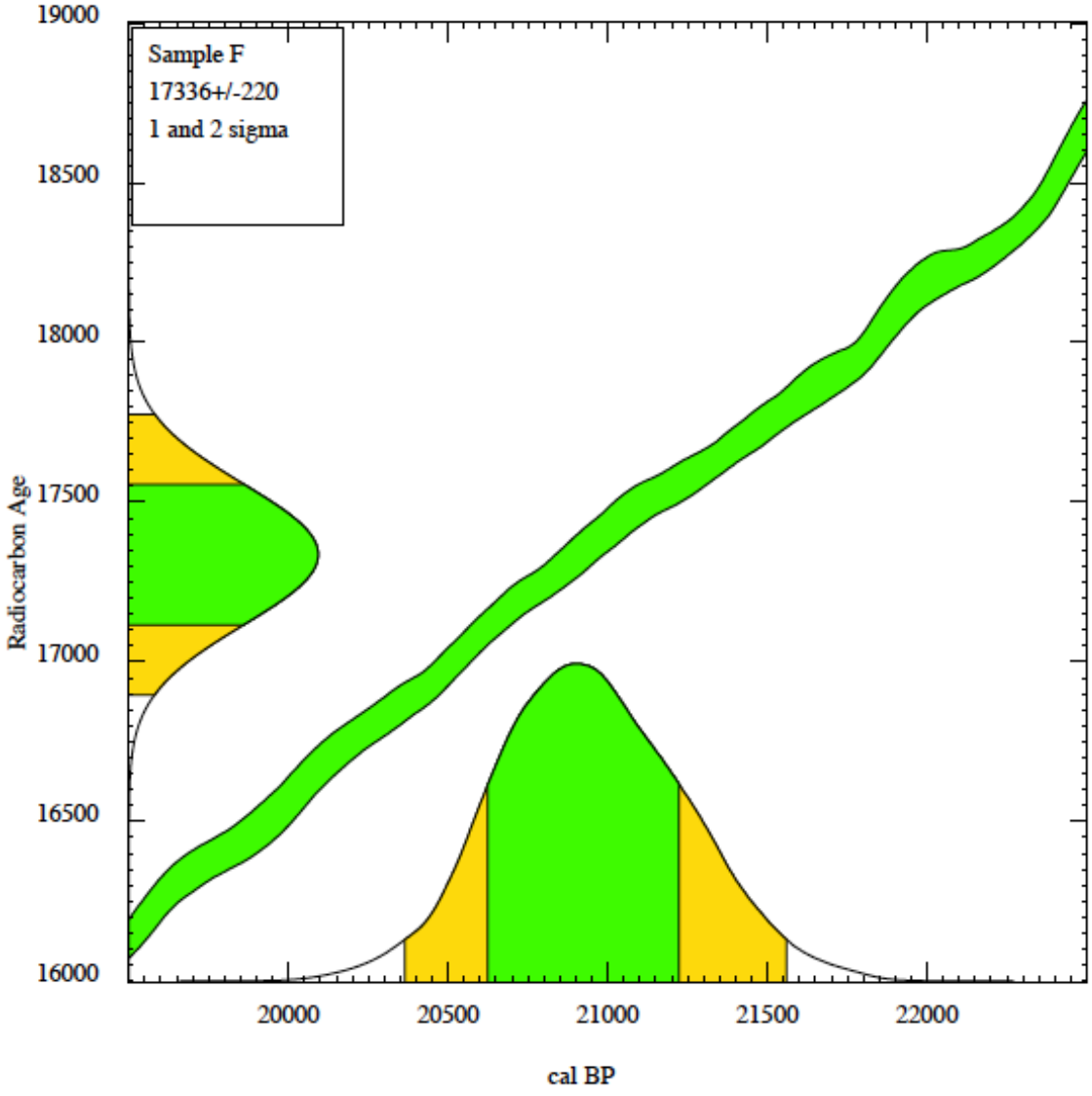
Sample F
17336+/-220
1 and 2 sigma
Radiocarbon Age
19000
18500
18000
17500
17000
16500
16000
20000
20500
21000
21500
22000
cal BP

Appendix K. Properties of an Artificially Cemented Clay

To further understand the formation mechanism of carbonate cementation in natural fine-grained soil deposits, clay samples cemented in the laboratory were produced and tested using SEM. The cementing agent was $CaCO_3$.

Several techniques have been reported in the literature for the preparation of artificially cemented soils using $CaCO_3$. For example, Fischer et al. (1978) produced artificially cemented clay using diffusion. Calcium chloride ($CaCl_2$) and sodium carbonate (Na_2CO_3) were flushed at the bottom and top of an undisturbed oedometer size Drammen Clay causing precipitation of $CaCO_3$ throughout the soil sample. Jiang et al. (2012) produced artificially structured loess by mixing the soil with calcium oxide (CaO), also known as lime, then submerging the mixture into water to produce calcium hydroxide and finally driving CO_2 into the cell, which caused the precipitation of $CaCO_3$ that induced interparticle bonding. A similar method was used by Haeri et al. (2009) to produce cemented gravely sand. Ismail et al. (2000) and Sharma & Fahey (2003) proposed the calcite in-situ precipitation system (CIPS) that consists of flushing a mixture of chemical solutions (mainly composed of urea [$(NH_2)_2CO$], $CaCl_2$, and enzyme urease that acts as catalyst) through a porous medium, leading to precipitation of calcite at the particles contacts due to the reaction of the solution ingredients. More recent work (e.g. Ozdogan, 2010; Minder & Puzrin, 2013) has focused on introducing microbes into the soil to induce calcite precipitation. This method is commonly known as biogrout or microbial induced calcite precipitation (MICP). The bacteria injected into the soil matrix consume the CO_2 leading to calcite precipitation. This technique is more applicable to granular soils since bacteria cannot survive in very small pores such as in clays.

Some of the techniques summarized above either require lengthy time (e.g. diffusion process, bacteria growth) or have other chemicals (e.g. urea $(NH_2)_2CO$

for the CIPS technique) that might interact with the clay particles. This study proposes a novel laboratory technique to produce artificially cemented clays that resembles better the natural formation process in lacustrine deposits. The method relies on mixing clay particles into a supersaturated calcium bicarbonate solution, then modifying the solution conditions (i.e., temperature, amount of CO_2, pH) to induce calcite precipitation. Since calcite particles are generally positively charged they preferably precipitate on the negatively charged clay minerals surfaces, which act as attractive nucleation sites for calcite crystals growth (Fischer et al., 1978; Palomino et al., 2008). The hypothesis is that calcite precipitated on various clay mineral particles will eventually coalesce, forming bridges between particles.

Precipitated calcium carbonate (PCC) was selected for the experiments. It was obtained from Imerys, Pigments and Additives Group and is a high-purity commercial product called 'OPTI-CAL® CP'. It is manufactured under carefully controlled environment as a rhombohedral form of calcite crystal precipitated through the reaction of calcium oxide, water and CO_2 (Imerys, 2003). The PCC product is a dry white powder characterized by a specific gravity of 2.71 (Imerys, 2003), specific area of 10 m^2/g (Palomino et al., 2008), 50% of the particles have a diameter (d_{50}) finer than 1.2 μm (obtained using hydrometer analysis), and a pH in deionized water of 8.82.

The clay used in this study is a dry beige kaolinite in powder form characterized by a specific gravity of 2.6 (Palomino et al., 2008), d_{50} equals to 1.7 μm (obtained using hydrometer analysis), and a pH in deionized water of 5.5. It was selected due to its high purity, which provides less complex system compared to natural soil; and relatively large particle size, which yields into more clear SEM analysis. The purity of the kaolinite used in this study was tested by performing XRD analysis on a randomly-oriented powder sample. The results are shown in Figure K-1. The XRD pattern shows that only kaolinite minerals are found in the soil.

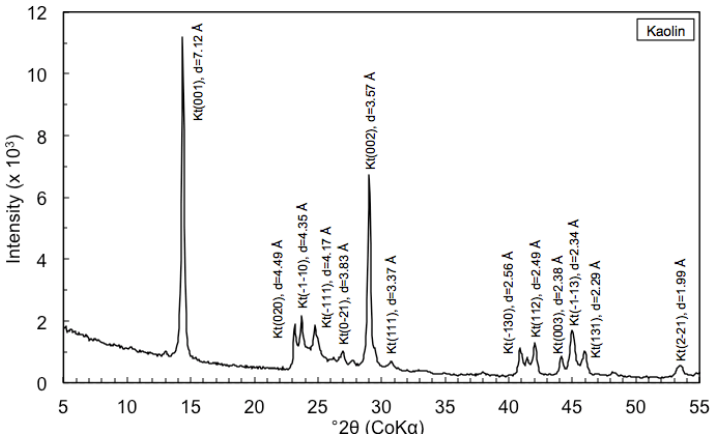

Figure K-1: XRD patterns (randomly-oriented powder) of kaolinite used in this study. Mineral code: Kt = kaolinite

Several researchers (e.g. Donahue 1965; Bathurst, 1971; Reddy et al. 1981) have prepared supersaturated calcium bicarbonate solutions by dissolving finely powdered calcium carbonate in water under carefully controlled conditions. Based on their work as well as the fact that calcite solubility increases with decreasing temperature, increasing amount of CO_2 in water, and decreasing pH (as described in section A.3), supersaturated calcium bicarbonate solutions were prepared by adding 1 g of PCC to 1 L of deionized water and mixing using a magnetic stirrer at 4 °C (submerged in a controlled temperature water bath) with 100% CO_2 bubbled for a period of 24 hours (see Figure K-2(a)). The pH was continuously monitored using a high precision (resolution ±0.01 pH) pH meter. PCC dissolution was considered to have reached a steady state if, after 24 hours, no change of pH was detected over a period of 2 hours. With the addition of CO_2 and reduction of temperature, the pH of the calcite/water mixture reduced from 8.82 (atmospheric condition; CO_2 partial pressure [P_{CO2} = 3.5 x 10^{-4} atm] at 22.6 °C) to 5.75 (100% CO_2 bubbled [P_{CO2} = 1 atm] at 4.4 °C).

The maximum amount of $CaCO_3$ that can be dissolved in distilled water was determined based on the solubility equation of calcite combined with the equilibrium equations of CO_2 and water, as well as the effect of temperature

(detailed calculations are included in APPENDIX L). Calcite is poorly soluble in pure water at ambient conditions (47 mg/L at atmospheric CO_2 partial pressure and at 25 °C), however this value may be increased to 1 g/L by increasing the CO_2 partial pressure to 1 atm and reducing the temperature to 4°C. This was also confirmed experimentally by monitoring the pH as well as observing the change in color from white to fully transparent (indicating the full dissolution of $CaCO_3$).

Three different samples were prepared to investigate the effect of $CaCO_3$ cementation in clays: (1) kaolinite with PCC mixture; (2) kaolinite with calcite precipitated from a supersaturated solution; and (3) kaolinite with calcite precipitated from chemical reaction between calcium chloride ($CaCl_2$) and sodium carbonate (Na_2CO_3). They are denoted as S1, S2, and S3. S1 consists of a mixture of kaolinite and PCC powder, hence no cementation is expected. However, cementation could be expected to occur in S2 as the calcite crystals are precipitated from solution and may grow at the clay surface. S3 was prepared based on the work proposed by Fischer et al. (1978) and aims at analyzing the different calcite crystal shapes and sizes that form with various precipitation techniques. Note that for lacustrine carbonatic deposits, the formation process is best simulated by S2 (see section A.3).

S1 was prepared by adding 1 g of PCC to 1 L of deionized water and mixing using a magnetic stirrer at room temperature (22.6 °C), without the addition of CO_2, for a period of 24 hours. Then 4 g of kaolinite was added and the solution was mixed for another 24 hours. S2 was prepared by adding 4 g of kaolinite to 1 L of supersaturated calcium bicarbonate solution prepared based on the procedure described earlier in this section. The solution was then mixed using a heating magnetic stirrer while slowly raising the temperature from 4 °C to 60 °C (~10 °C/hr) and then maintained constant for a period of 8 days. Heating facilitates the precipitation of calcite by releasing the CO_2 dissolved in the solution. The pH was continuously monitored and calcite precipitation was

considered to have reached a steady state after 8 days since no change of pH was detected. S3 was prepared by first dissolving 1.11 g of $CaCl_2$ in 960 mL of deionized water, to which 4 g of kaolinite was added and mixed using a magnetic stirrer at room temperature (23.0 °C) for a period of 24 hours, Then 1.06 g of Na_2CO_3 dissolved in 40 mL of deionized water was added to the solution and mixed for another 3 days.

The basic reaction for the formation of calcium carbonate precipitate from $CaCl_2$ and Na_2CO_3 is given in the following equation:

$$CaCl_{2\,(aq)} + Na_2CO_{3\,(aq)} \rightarrow CaCO_{3\,(s)} + 2\,NaCl_{(aq)} \qquad \text{(Eq. K-1)}$$

111 g/mol 106 g/mol 100 g/mol 58.4 g/mol

Knowing the molecular weights, the masses used were chosen to produce a total of 1 g $CaCO_3$. However, the disadvantage of this technique is that it produces a total of 1.17 g sodium chloride (NaCl) which increases the ionic strength of the solution and alters the clay double layer thickness.

The remaining of the preparation procedure is the same for all three samples: the solution was transferred into a 1 L hydrometer cylinder at the bottom of which a trap was installed to collect the settled sample (see Figure K-2(b)). The soil was allowed to settle for a period of 4 days and then gently removed from the hydrometer cylinder. The sample, which was few millimeters thick, was allowed to dry slowly (2-3 days) at room temperature before SEM analysis. Note that all images were obtained by analyzing the bottom side of the samples, since the top was covered with very small clay particles that prevented clear imaging.

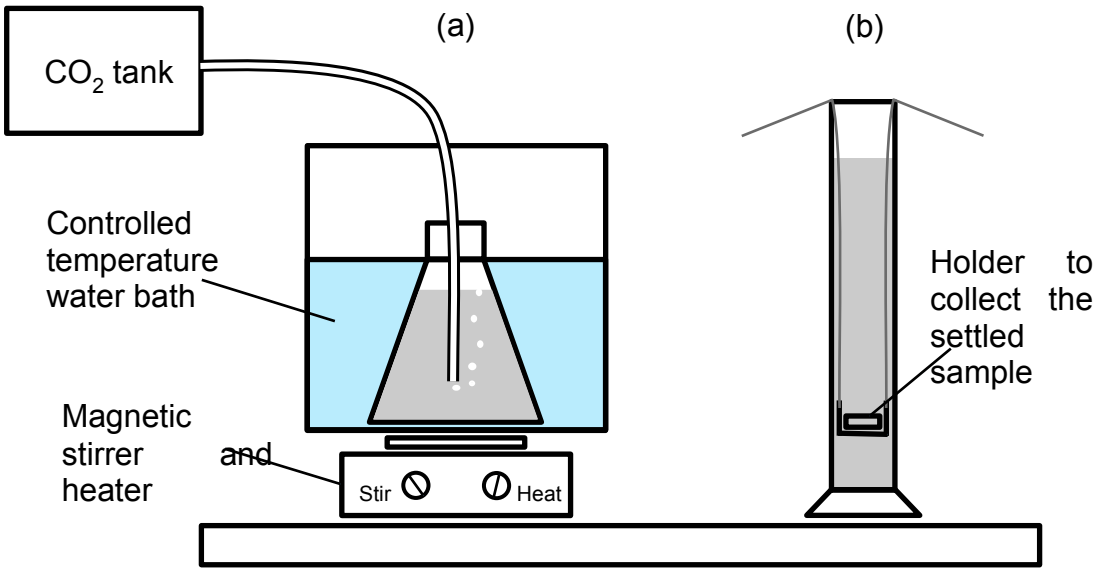

Figure K-2: Experimental setup used to produce artificially cemented clays: (a) preparation of kaolinite-calcite mixture, and (b) sedimentation setup

Scanning electron micrographs for S1, S2, and S3 are shown in Figure K-3(a-b), Figure K-3(c-d) and Figure K-3(e-f), respectively. Figure K-3(a) shows the morphology of S1, which is composed of kaolinite platelets and PCC particles that are present as individual particles with no cementation. This may be explained by the fact that PCC is introduced into the sample as well-formed particles, hence no chemical interaction between kaolinite and PCC is observed. A higher magnification is shown in Figure K-3(b), in which kaolinite platelets and PCC can be clearly distinguished.

The morphology of S2 is shown in Figure K-3(c) and Figure K-3(d) at two different magnifications. The micrographs reveal that S2 is formed of large calcite crystals coating kaolinite particles and bridging. Unlike the micrographs for S1, it is difficult to distinguish kaolinite and calcite since they are chemically bonded.

Figure K-3(e) shows the morphology of S3, which is again composed of distinct kaolinite platelets and calcite chemically precipitated with no cementation. A higher magnification is shown in Figure K-3(f), in which calcite crystals can be clearly observed.

The SEM analysis reveals three different forms of calcite that are characterized by distinct shapes and sizes. The calcite crystals observed in S1 are the original PCC particles obtained from Imerys. The particles are small acicular crystals (~1-2 μm), with an approximate length to diameter ratio of 3:1 (Figure K-3(b)). On the other hand, the calcite crystals precipitated from the supersaturated solution in S2 are much larger in size (~30-40 μm) and are interconnected forming a large continuous network. The third form of calcite can be observed in S3, in which individual crystals are precipitated from chemical reaction between $CaCl_2$ and Na_2CO_3. The calcite particles formed in S3 are relatively large crystals (~5-15 μm) with cubic shape (Figure K-3(f)). The identification of the different calcite crystals was confirmed using EDX analysis.

Although all three samples are composed of both kaolinite platelets and calcite (as shown in Figure K-3), the interaction between kaolinite and calcite is not the same. The morphology of S1 and S3 appears to be formed of evenly distributed well-defined calcite particles that are not bonded with the kaolinite platelets. However, S2 clearly shows cementation where the precipitated calcite grows on the clay surfaces, which act as attractive nucleation sites for calcite crystals growth that eventually coalesce forming bridges between particles creating a large network.

Maps of EDX analyses conducted on S1 and S2 were generated and the distribution of different chemical elements were analyzed. Figure K-4 shows typical results of EDX analyses performed at 3,000x magnification. Similar to the analysis conducted on the natural soil (see CHAPTER 3), the distribution of Ca, represented in cyan color, can be interpreted as a rough carbonate distribution map, while Si represented in red color can be indicative of the distribution of kaolinite particles. Note that Mg was not included since the carbonates used in the laboratory (S1, S2, and S3) are pure calcite. The calcite crystals observed in S1 and S2 can be easily identified by EDX analysis (cyan color in Figure K-4(c)).

Moreover, the map of EDX analysis performed on S2 reveals that the large calcite crystals are composed of both Ca and Si (Figure K-4(d)), which indicates that the calcite is not only bridging between kaolinite platelets but also growing on the clay surface. Note that the texture of the calcite crystals is not the same as the one observed in the natural samples (soils M and C) which can be explained by the fact that the natural soil was formed in a lacustrine environment for thousands of years, a much slower precipitation rate than that accomplished in the laboratory over a period of just eight days.

Based on this investigation, different preparation methods used in the laboratory result in completely different structure, i.e., both calcite crystal shape and size, and the way they interact with the clay particles (presence or absence of cementation). The preparation method used to produce S2 (precipitation of calcite from supersaturated bicarbonate solution) better resembles the natural formation process in lacustrine deposits since it results in cemented soils composed of clay platelets that are coated with calcite film and interconnected by large calcite crystals. Additional work is needed to examine the effect of time and temperature in the laboratory.

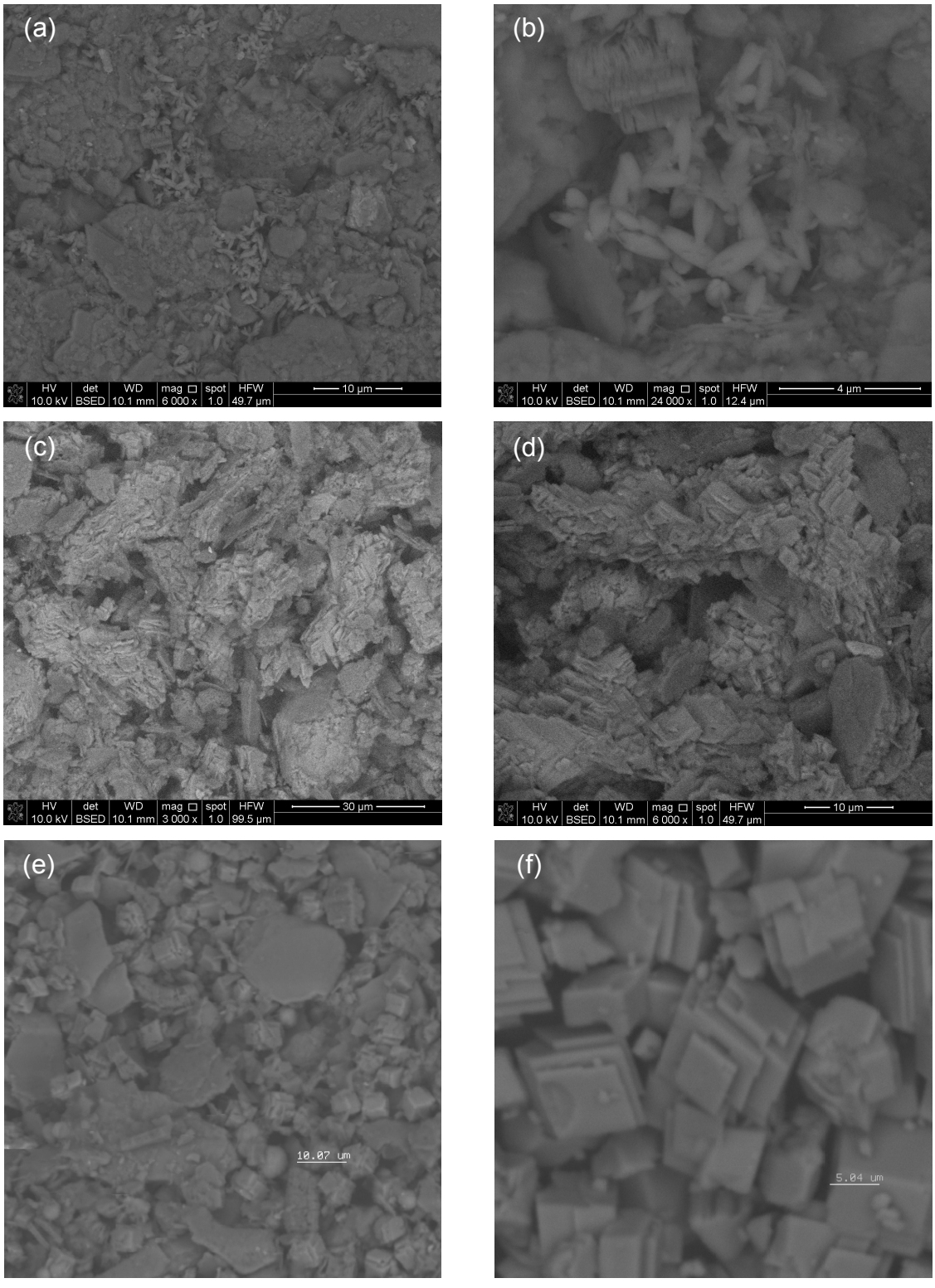

Figure K-3: SEM micrographs showing (a,b) S1: kaolinite platelets and PCC (no cementation), (c, d) S2: large calcite crystals coating kaolinite particles and bridging, and (e, f) S3: kaolinite platelets and calcite chemically precipitated (no cementation)

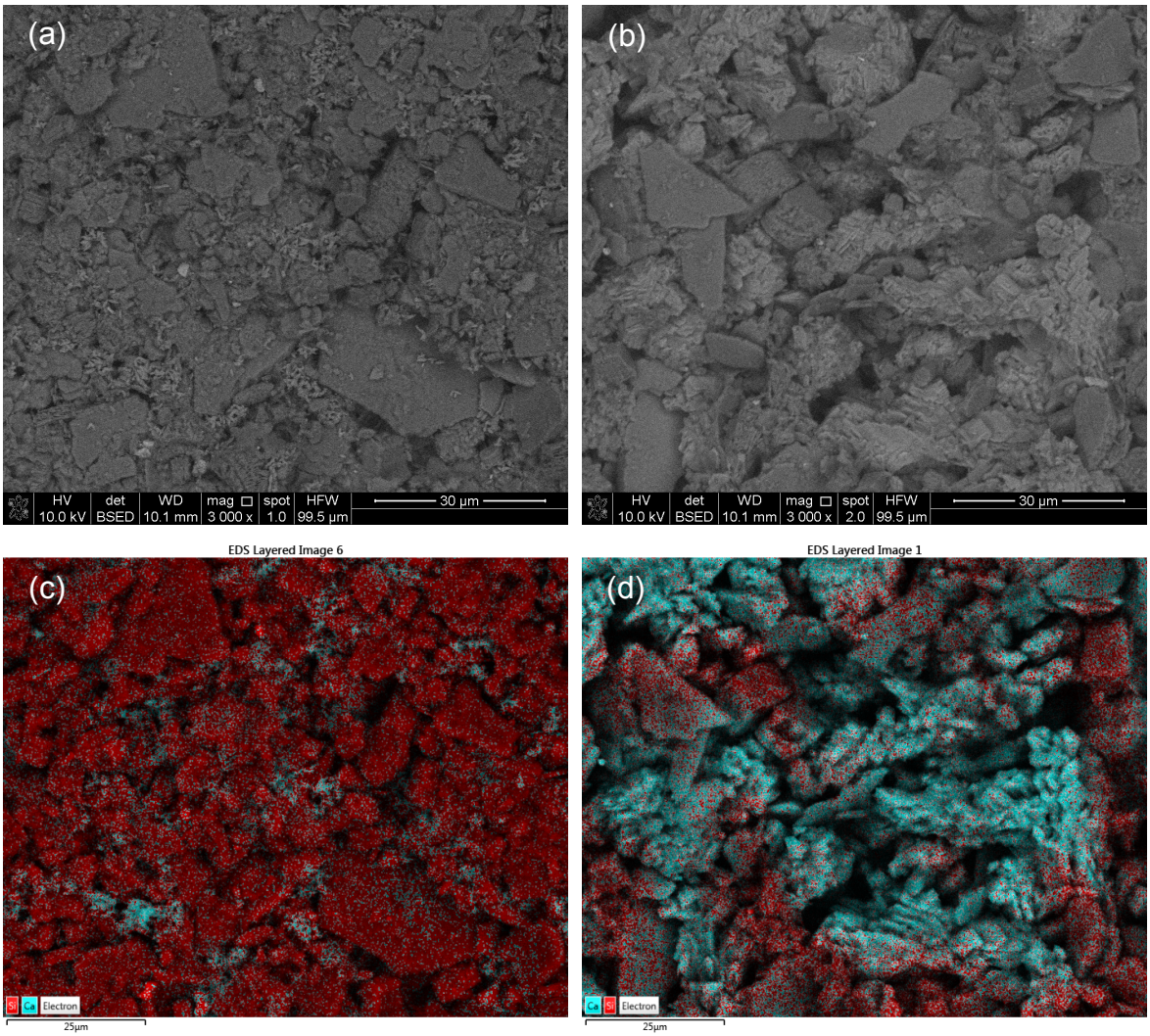

Figure K-4: SEM micrographs for samples: (a) S1 and (b) S2. Maps of EDX analyses performed on: (c) S1 showing the distribution of Ca and Si; (d) S2 showing the distribution of Ca and Si

Appendix L. Calcite Solubility as a Function of CO_2 Partial Pressure

The appendix presents the calculations made to derive calcite solubility as a function of CO_2 partial pressure (P_{CO_2}) in water at 25 °C. This is determined based on the solubility equation of calcite combined with the equilibrium equations of CO_2 and water. The chemical equations and their corresponding equilibrium constants were obtained from Doner & Lynn (1989), Doner & Grossl (2002) and Lide (2005)

$CaCO_3 = Ca^{2+} + CO_3^{2-}$	$K_{sp} = 4.47\times10^{-9}$	at 25 °C
$HCO_3^- = H^+ + CO_3^{2-}$	$K_{a_2} = 5.61\times10^{-11}$	at 25 °C
$H_2CO_3 = H^+ + HCO_3^-$	$K_{a_1} = 2.50\times10^{-4}$	at 25 °C
$CO_{2_{(aq)}} + H_2O = H_2CO_3$	$K_h = 1.70\times10^{-3}$	at 25 °C
$H_2O = H^+ + OH^-$	$K = 1.00\times10^{-14}$	at 25 °C

Dissolved CO_2 is in equilibrium with atmospheric CO_2 according to:

$$P_{CO_2} = k_H \cdot [CO_2] \qquad k_H = 29.76\ \text{atm}/(\text{mol/L})$$

At equilibrium, the solution must be electrically neutral:

$$2\,[Ca^{2+}] + 2\,[H^+] = [HCO_3^-] + 2\,[CO_3^{2-}] + [OH^-]$$

From the above chemical equations and their corresponding equilibrium constants, the following seven equations can be written:

$$K_{sp} = [Ca^{2+}] \cdot [CO_3^{2-}] = 4.47\times10^{-9} \qquad \text{(Eq. L-1)}$$

$$K_{a_2} = \frac{[H^+] \cdot [CO_3^{2-}]}{[HCO_3^-]} = 5.61\times10^{-11} \qquad \text{(Eq. L-2)}$$

$$K_{a_1} = \frac{[H^+] \cdot [HCO_3^-]}{[H_2CO_3]} = 2.50\times10^{-4} \qquad \text{(Eq. L-3)}$$

$$K_h = \frac{[H_2CO_3]}{[CO_2]} = 1.70\times10^{-3} \quad \text{(Eq. L-4)}$$

$$K = [H^+]\cdot[OH^-] = 1.00\times10^{-14} \quad \text{(Eq. L-5)}$$

$$P_{CO_2} = k_H \cdot [CO_2] \quad \text{(Eq. L-6)}$$

$$2\,[Ca^{2+}] + 2\,[H^+] = [HCO_3^-] + 2\,[CO_3^{2-}] + [OH^-] \quad \text{(Eq. L-7)}$$

This results into a system of 7 equations and 8 unknowns, which has as solution a forth order equation relating $[H^+]$ and P_{CO_2}:

$$A\cdot[H^+]^4 + B\cdot[H^+]^3 + C\cdot[H^+] + D = 0 \quad \text{(Eq. L-8)}$$

$$A = \frac{2}{P_{CO_2}}\cdot\frac{[k_H\cdot K_{sp}]}{[K_{a_2}\cdot K_{a_1}\cdot K_h]}$$

$$B = 2$$

$$C = -\left[K + P_{CO_2}\cdot\frac{K_h\cdot K_{a_1}}{k_H}\right]$$

$$D = -2\,P_{CO_2}\cdot\frac{[K_{a_2}\cdot K_{a_1}\cdot K_h]}{k_H}$$

Table L-1 and Figure L-1 summarize the variation of $CaCO_3$ solubility and pH as a function of P_{CO_2}. As expected, increasing P_{CO_2} results in increasing calcite solubility and decreasing pH. This is caused by the dissolution of CO_2 in water, forming carbonic acid (H_2CO_3) and hydrated CO_2. The data summarized in Table L-1 shows that the solubility of calcite at 25°C increases from 47 mg/L to 658 mg/L and the pH decreases from 8.27 to 5.96 when changing the solution condition from atmospheric (P_{CO_2} = 3.5 x 10^{-4} atm) to pure CO_2 (P_{CO_2} = 1 atm).

Table L-1: Calcite solubility and pH as a function of CO_2 partial pressure at 25°C

P_{CO_2}* (atm)	pH	[$CaCO_3$] (mmol/L)**	Solubility of $CaCO_3$ (mg/L)	Comments
10^{-6}	9.83	0.120	12	Deaired water
10^{-4}	8.62	0.316	31.6	-
3.5×10^{-4}	8.27	0.470	47	Atmosphere
10^{-3}	7.96	0.662	66.2	-
3.5×10^{-3}	7.60	1.00	100	Soil air
10^{-2}	7.30	1.42	142	-
10^{-1}	6.63	3.05	305	-
1	5.96	6.58	658	Pure CO_2
10	5.30	14.2	1420	-

* P_{CO_2} is the partial pressure of CO_2
** at 25 °C ($K_{sp} = 4.47 \times 10^{-9}$)

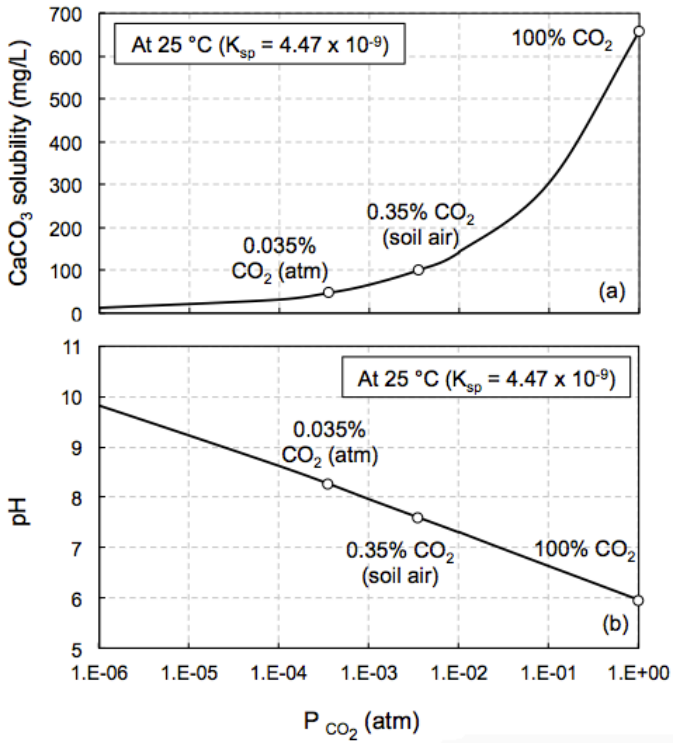

Figure L-1: (a) calcite solubility and (b) pH as a function of P_{CO_2} at 25°C

LIST OF REFERENCES

LIST OF REFERENCES

AASHTO T267-86 (2008). Standard method of test for determination of organic content in soils by loss on ignition. American Association of State Highway and Transportation Officials, Washington, D.C.

Abdulhadi, N.O. (2009). An experimental investigation into the stress-dependent mechanical behavior of cohesive soil with application to Wellbore instability. PhD Thesis, Department of Civil and Environmental Engineering, Massachusetts Institute of Technology, Cambridge, MA.

Allman, M.A. & Poulos, H.G. (1988). Stress-strain behaviour of an artificially cemented calcareous soil. Proceedings of International Conference on Calcareous Soil (Perth), Balkema, 1, pp. 51-60.

Alonso, E.E. & Gens, A. (1994). On the mechanical behaviour of arid soils. Keynote lecture. Int. Symp. on the Engineering Characteristics of Arid Soils, Fookes & Parry (Eds.), Balkema, pp. 173-205.

Alpan, I. (1967). The empirical evaluation of the coefficient K0 and K0R. Soils and Foundations, 7 (1), pp. 31-40.

Alt & Witzig (2010). Geotechnical Engineering Report, I-69 Extension, Section 3 – US 50 to US 231, Segment 12 – I-69 Mainline Roadway, CR 1400N to CR 700E, Daviess County. Prepared for Indiana Department of Transportation.

Andrus, R.D., Mohanan, N.P., Piratheepan, P., Ellis, B.S., & Holzer, T.L. (2007). Predicting shear-wave velocity from cone penetration resistance, Proc., 4th Inter. Conf. on Earthq. Geotech. Eng., Thessaloniki, Greece.

ASTM D1586-11 (2011). Standard Test Method for Standard Penetration Test (SPT) and Split-Barrel Sampling of Soils. Annual Book of ASTM Standards, ASTM International, West Conshohocken, PA.

ASTM D2573-08 (2008). Standard Test Method for Field Vane Shear Test in Cohesive Soil. Annual Book of ASTM Standards, ASTM International, West Conshohocken, PA.

ASTM D422-63 (2007). Standard test method for particle-size analysis of soils. Annual Book of ASTM Standards, ASTM International, West Conshohocken, PA.

ASTM D4318-10 (2010). Standard test methods for liquid limit, plastic limit, and plasticity index of soils. Annual Book of ASTM Standards, ASTM International, West Conshohocken, PA.

ASTM D4972-13 (2013). Standard test method for pH of soils. Annual Book of ASTM Standards, ASTM International, West Conshohocken, PA.

ASTM D6519-08 (2008). Standard practice for sampling of soil using the hydraulically operated stationary piston sampler. Annual Book of ASTM Standards, ASTM International, West Conshohocken, PA.

ASTM D7400-14 (2014). Standard Test Methods for Downhole Seismic Testing. Annual Book of ASTM Standards, ASTM International, West Conshohocken, PA.

ASTM D854-14 (2014). Standard test methods for specific gravity of soil solids by water pycnometer. Annual Book of ASTM Standards, ASTM International, West Conshohocken, PA.

ASTM E1131-08 (2014). Standard test method for compositional analysis by thermogravimetry. Annual Book of ASTM Standards, ASTM International, West Conshohocken, PA.

Azzouz, A.S., Krizek, R.J., & Corotis, R.B. (1976). Regression analysis of soil compressibility. Soils and Foundations, 16 (2), pp. 19-29.

Baldi, G., Bellotti, R., Ghionna, V.N., Jamiolkowski, M., & LoPresti, D.C.F. (1989). Modulus of sands from CPTs and DMTs. Proc., 12th Inter. Conf. Soil Mech. and Foundation Eng., Rio de Janeiro, 1, pp. 165-170.

Baligh, M.M., Azzouz, A., & Chin, C.T. (1987). Disturbances due to "ideal" tube sampling. Journal of Geotechnical Engineering, ASCE, 113(7), pp. 739-757.

Barnhisel, R.I., & Bertsch, P.M. (1989). Chlorites and hydroxy-interlayered vermiculite and smectite. In J.B. Dixon & S.B. Weed (Eds.), Minerals in Soil Environments (pp. 729-788). Soil Science Society of America, Madison, Wisconsin.

Bathurst, R.G.C. (1971). Carbonate sediments and their diagenesis. Developments in sedimentology. Vol.12, Elsevier, Amsterdam: The Netherlands.

Becker, D. E., Crooks, J. H. A., Been, K., & Jefferies, M.G. (1987). Work as a criterion for determining in situ and yield stresses in clays. Canadian Geotechnical Journal, 24(4), pp. 549-564.

Berman, D.R. (1993). Characterization of the engineering properties of Boston blue clay. MS Thesis, School of Civil Engineering, MIT, Cambridge, MA.

Beta Analytic Inc. (2016). Radiocarbon dating shell, coral, and CaCO3: Reservoir effect on shells. Retrieved February 17, 2016 from http://www.radiocarbon.com/carbon-dating-shells.htm

Bish, D.L., & Duffy, C.J. (1990). Thermogravimetric Analysis of Minerals. In J. W. Stucki, D. L. Bish & F. A. Mumpton (Eds.), Thermal analysis in clay science (pp. 96-157). Clay Minerals Society Workshop Lectures, Boulder, Colorado.

Bjerrum, L. (1954). Geotechnical properties of Norwegian marine clays. Geotechnique, 4(2), 49-69.

Bjerrum, L. (1972). Embankments on soft ground. Proceedings of the ASCE Conference on Performance of Earth-Supported Structures, Purdue University, 2, pp. 1-54.

Bjerrum, L. & Wu, T.H. (1960). Fundamental shear strength properties of the Lilla Edet clay. Geotechnique, 10, pp. 101-109.

Black, D.K., & Lee, K.L. (1973). Saturating laboratory samples by back pressure. Journal of the Soil Mechanics and Foundations Division, ASCE 1, pp. 75-93.

Boone, S.J. & Lutenegger, A.J. (1997). Carbonates and cementation of glacially derived cohesive soils in New York State and southern Ontario. Canadian Geotechnical Journal, 34, pp. 534-550.

Bowles, J.W. (1979). Physical and geotechnical properties of soils. New York: McGraw Hill.

Bozzano, F., Marcoccia, S., & Barbieri, M. (1999). The role of calcium carbonate in the compressibility of Pliocene lacustrine deposits. Quarterly Journal of Engineering Geology, 32, pp. 271-289.

Brindley, G.W., & Brown, G. (1980). Crystal structures of clay minerals and their x-ray identification. Mineralogical Society, London.

Brindley, G.W., & Lemaitre, J. (1987). Thermal, oxidation and reduction reactions of clay minerals. In: A. C. D. Newman (ed.), Chemistry of Clays and Clay Minerals (pp. 319-370). Mineralogical Society Monograph No.6, Mineralogical Society, London.

Burch, J.B., & Tottenham, J.L. (1980). North American freshwater snails: Species list, ranges and illustrations. Walkerana 3.

Burghignoli, A., Cavalera, L., Chieppa, V., Jamiolkowski, M., Mancuso, C., Marchetti, S., Pane, V., Paoliani, P., Silvestri, F., Vinale, F., & Vittori, E. (1991). Geotechnical characterization of Fucino clay. 10th European Conference on Soil Mechanics and Foundation Engineering (Florence), 1, pp. 27-40.

Burghignoli, A., Miliziano, S., & Soccodato, F.M. (2010). Cementation effects in two lacustrine clayey soils. Geotech Geol Eng 28, pp. 815-833.

Burland, J.B. (1990). On the compressibility and shear strength of natural clays. Geotechnique, 40, pp. 329-378.

Burland, J.B., Rampello, S., Georgiannou, V.N., & Calabresi, G. (1996). A laboratory study of the strength of four stiff clays. Geotechnique, 46(3), pp. 491-514.

Casagrande, A. (1936). The determination of the pre-consolidation load and its practical significance. Proceedings of the 1st International Conference on Soil Mechanics and Foundation Engineering. Cambridge, MA 3, pp. 60-64.

Chandler, R.J. (2000). Clay sediments in depositional basins: the geotechnical cycle. Q. J. Engng Geol. Hydrogeol., 33(1), pp. 7-39.

Chandler, R.J., de Freitas, M.H., & Marinos, P. (2004). Geotechnical characterisation of soils and rocks: A geological perspective, In: R.J. Jardine, D.M. Potts, & K.G. Higgins (Eds.), Advances in Geotechnical Engineering, The Skempton Conference, Thomas Telford, London, 1, pp. 67-102.

Chen, B.S.-Y., & Mayne, P.W. (1996). Statistical Relationships Between Piezocone Measurements and Stress History of Clays. Canadian Geotechnical Journal, 33 (3), pp. 488-498.

Chin, C.-T., Chen, J.-R., Hu, I.-C., Yao, D.T.C., & Chao, H.-C. (2007). Engineering characteristics of Taipei clay. In Proceedings International Workshop on Characterization and Engineering Properties of Natural Soils ("Natural Soils 2006"). NUS Singapore, December. Tan, T. S. et al. (eds.) 3, pp. 1755-1804. London: Taylor & Francis.

Clayton, C.R.I., Siddique, A., & Hopper, R.J. (1998). Effects of sampler design on tube sampling disturbance – numerical and analytical investigations. Geotechnique, 48(6), pp. 847-867.

Conlon, R.J. (1966). Landslide on the Toulnustouc River, Quebec. Canadian Geotechnical Journal, 3, pp. 113-144.

Cotecchia, F. & Chandler, R.J. (1997). The influence of structure on the pre-failure behaviour of a natural clay. Geotechnique, 47(3), pp. 523–544.

De Kimpe, C.R., Laverdiere, M.R., & Martel, Y.A. (1979). Surface area and exchange capacity of clay in relation to the mineralogical composition of gleysolic soils. Canadian Journal of Soil Science, 59 (4), pp. 341-347.

DeGroot, D.J. (2003). Laboratory measurement and interpretation of soft clay mechanical behavior in soil behavior and soft ground construction, ASCE GSP 119, pp. 167-200.

Demars, K.R. & Chaney, R.C. (Eds). (1982). Geotechnical properties, behavior, and performance of calcareous soils. American Society for Testing and Materials, Special Technical Publication STP 777. ASTM Philadelphia.

Donahue, J. (1965). Laboratory growth of pisolite grains. J. Sediment Petrol., 35, pp. 251-256.

Doner, H.E. & Lynn, W.C. (1989). Carbonate, halide, sulfate, and sulfide minerals. In J.B. Dixon & S.B. Weed (Eds.), Minerals in Soil Environments (pp. 279-330). Soil Science Society of America, Madison, Wisconsin.

Doner, H.E., & Grossl, P.R. (2002). Carbonates and evaporites. In J.B. Dixon & D.G. Schulze (Eds.), Soil mineralogy with environmental applications (pp. 199-228). Soil Science Society of America, Madison, Wisconsin.

Drees, L.R., Wilding, L.P., Smeck, N.E., & Senkayi, A.L. (1989). Silica in soils: Quartz and disordered silica polymorphs. In J.B. Dixon & S.B. Weed (Eds.), Minerals in Soil Environments (pp. 913-974). Soil Science Society of America, Madison, Wisconsin.

Earnest, C.M. (1980). The application of differential thermal analysis and thermogravimetry to the study of kaolinite clay minerals. Perkin-Elmer Thermal Analysis Application Study, 30 (11).

Earth Exploration (2010). Geotechnical Engineering Report, I-69 Extension, Section 3 – US 50 to US 231, Segment 13 - I-69 Mainline Roadway & Access Roads CR 700E to US 231, Daviess and Greene Counties. Prepared for Indiana Department of Transportation.

Egashira, K., Miyazaki, M., Yamada, S., Yamashita, D., Isoda, M., Abe, T., & Inabe, V. (1999). Clay mineralogical composition of the Quaternary sediments collected in the North Coast of Ariake Bay, and the relation to depositional environment and weathering in the terrestrial condition. Nendo Kagaku 39 (2), pp. 65-75.

Eriksson L.G. (1989). Temperature effects on conso-lidation properties of sulphide clays. Proc. 12th ICSMFE, Rio de Janeiro, 3, pp. 2087-2090.

Fanning, D.S., Keramidas, V.Z., & El-Desoky, M.A. (1989). Micas. In J.B. Dixon & S.B. Weed (Eds.), Minerals in Soil Environments (pp. 551-634). Soil Science Society of America, Madison, Wisconsin.

Fearon, R.E. & Coop, M.R. (2000). Reconstitution: what makes an appropriate reference material? Geotechnique, 50(4), pp. 471-477.

Fearon, R.E. & Coop, M.R. (2002). The influence of landsliding on the behaviour of a structurally complex clay. Q. J. Engng Geol. Hydrogeol., 35(1), pp. 25-32.

Fidlar, M.M. (1948). Physiography of the lower Wabash Valley. Indiana Dept. Cons., Div. Geol. Bull. 2, 112 p.

Fischer, K.P., Andersen, K.H., & Moum, J. (1978). Properties of an artificially cemented clay. Canadian Geotechnical Journal, 15, pp. 322-331.

Gens, A. & Alonso, E.E. (1992). A framework for the behavior of unsaturated expansive clays. Can. Geotech. J., 29, pp. 1013-1032.

Germaine, J.T. & Germaine, A.V. (2009). Geotechnical laboratory measurements for engineers. Hoboken, NJ: John Wiley and Sons, Inc.

Germaine, J.T., & Ladd, C.C. (1988). Triaxial testing of saturated cohesive soils. Advanced Triaxial Testing of Soil and Rock, ASTM STP 977. In R.T. Donaghe, R.C. Chaney, & M.L. Silver (Eds.), ASTM (pp.421-459). Philadelphia.

Gibbard, P. & Van Kolfschoten, T. (2004). The Pleistocene and Holocene Epochs. In Gradstein et al. (eds.) A Geologic Time Scale 2004. pp. 441-452. Cambridge University Press: Cambridge.

Haeri, S.M., Shahcheraghi, S.A., Shakeri, R., & Seiphoori, A. (2009). Mechanical behavior of a cemented gravely sand under monotonic and cyclic loading-case study of Tehran alluvium. 8th International Congress on Civil Engineering. May 11-13, 2009, Shiraz University, Shiraz, Iran.

Hegazy, Y.A., & Mayne, P.W. (1995). Statistical correlations between Vs and cone penetration data for different soil types, Proc., Inter. Symp. on Cone Penetration Testing, CPT '95, Linkoping, Sweden, 2, pp. 173-178.

Holtz, R. & Kovacs, W. (1981). An introduction to geotechnical engineering. New Jersey: Prentice-Hall.

Horseman S.T., Winter M.G., & Entwistle D.C. (1987). Geotechnical characterisation of Boom Clay in relation to the disposal of radio-active waste. Luxembourg, Office of Official Publications of the European Communities.

Huang, P., Bobet, A., & Santagata, M. (2012). Identification of low-organic-content soils: an engineering approach. Geotechnical Testing Journal, 35(4), pp. 596-606.

Hwang, J. (2006). Effects of cement treatment on the 1-D consolidation behavior of a highly organic soil. PhD Thesis, School of Civil Engineering, Purdue University, West Lafayette, IN.

IMERYS (2016). OPTI-CAL® CP - Technical data sheet. Retrieved July 9, 2015, from www.imerys-carbonates.com.

Integrating Spatial Educational Experiences Isee (2016). Retrieved February 17, 2016 from http://isee.purdue.edu/

Islam, A.K.M.E. & Lotse, G. (1986). Quantitative mineralogical analysis of some Bangladesh soils with X-ray, ion exchange and selective dissolution techniques. Clay Minerals, 21, pp. 31-42.

Ismail, M.A., Joer, H.A., & Randolph, M.F. (2000). Sample preparation technique for artificially cemented soils. Geotech. Test. J., 23(2), pp. 171-177.

Jackson, M.L. (1973). Soil Chemical Analysis: Advanced course. Published by the author, Madison, Wisconsin.

Jamiolkowski, M., Ladd, C.C., Germaine, J.T., & Lancellotta, R. (1985). New developments in field and laboratory testing of soils. Proceedings of the 11th International Conference on Soil Mechanics and Foundation Engineering (San Francisco), 1, pp. 57-153.

Jiang M, Hu H, & Liu F. (2012). Summary of collapsible behaviour of artificially structured loess in oedometer and triaxial wetting tests. Canadian Geotechnical Journal, 49(10), pp. 1147-1157.

Jones, B.F. & Bowser, C.J. (1978). The mineralogy and related chemistry of lake sediments. In A. Lerman (Ed.), Lakes: Chemistry, Geology, Physics. Springer, New York, pp. 179-235.

Jung, C.M., Bobet, A., & Siddiki, N.Z. (2011). Simple method to identify marl soils. Transportation Research Record 2232, pp. 76-84.

Kavvadas M. & Anagnostopoulos A. (1998). A framework for the mechanical behaviour of structured soils. Proc. 2nd Int. Symp. on the Geotechnics of Hard Soils - Soft Rocks, Napoli, Oct. 1998, Balkema.

Kavvadas, M.J. (2000). General report: Modelling the soil behavior – selection of soil parameters. Proc 2nd Int. Conf. Geotech. Hard Soils-Soft Rocks, 2, pp. 1441-1481.

Kelts, K. & Hsu, K. (1978). Freshwater carbonate sedimentation. In A. Lerman (Ed.), Lakes: Chemistry, Geology, Physics. Springer, New York, pp. 295-323.

Kenney, T.C., Moum, J., & Berre, T. (1967). An experimental study of bonds in a natural clay. Proceedings of the Geotechnical Conference (Oslo), 1, pp. 65-69.

Koppula, S.D. (1981). Statistical estimation of compression index. Geotech. Test. J., 4 (2), pp. 68-73.

Ladd, C.C. (1991). Stability evaluation during staged construction: 22nd Terzaghi Lecture. Journal of Geotechnical Engineering, ASCE, 117(4), pp. 537-615.

Ladd, C.C. & DeGroot, D.J. (2003). Recommended practice for soft ground site characterization: Arthur Casagrande Lecture. Proc. 12th Panamerican Conf. on Soil Mechanics and Geotech. Eng. MIT, 1, pp. 3-57.

Ladd, C.C., & Foott, R. (1974). New design procedure for stability of soft clays. Journal of Geotechnical Engineering, ASCE, 100 (GT7), pp. 763-786.

Ladd, C.C., Foott, R., Ishihara, K., Schlosser, F., & Poulos, H.G. (1977). Stress-deformation and strength characterisitcs: SOA report. Proc., 9th Int. Conf. on Soil Mechanics and Foundation Eng., Tokyo, 2, pp. 421-494.

Lamas, F., Irigaray, C., & Chacon, J. (2002). Geotechnical characterization of carbonate marls for the construction of impermeable dam cores. Engineering Geology, Elsevier, 66, pp. 283-294.

Lambe, T.W. & Whitman, R.V. (1969). Soil mechanics. New York: Wiley.

Langmuir, D. (1997). Aqueous Environmental Geochemistry, Prentice-Hall, Inc., upper Sanddle River, NJ.

Lefebvre, G., Ladd, C.C., Paré, J.J. (1988). Comparison of field vane and laboratory undrained shear strength in soft sensitive clays. Vane shear strength testing in soils: field and laboratory studies. ASTM STP 1014, A.F. Richards (Ed.), ASTM, Philadelphia, pp. 233-246.

Leonards, G.A. & Ramiah, B.K. (1959). Time effects in the consolidation of clay. ASTM, Special Technical Publication No 254, pp. 116-130.

Leroueil, S. (1997). Critical state soil mechanics and the behaviour of real soils. Int Symp. On Recent Developments in Soil and Pavement Mechanics, Rio de Janeiro, pp. 41-80.

Leroueil, S. & Marques, M.E.S. (1996). Importance of strain rate and temperature effects in geotechnical engineering. State-of-the-art report, ASCE 1996 Annual Convention, Washington DC, November 1996.

Leroueil, S. & Vaughan, P.R. (1990). The general and congruent effects of structure in natural soils and weak rocks. Geotechnique, 40(3), pp. 467-488.

Leroueil, S., Kabbaj, M., Tavenas, F., & Bouchard, R. (1985). Stress-strain-strain rate relation for the compressibility of natural sensitive clays. Geotechnique, 35(2), pp. 159-180.

Lide, D.R. (Ed.) (2005). CRC Handbook of Chemistry and Physics (86th ed.). Boca Raton (FL): CRC Press.

Liu, M.D. & Carter, J.P. (1999). Virgin compression of structured soils. Geotechnique, 49(1), pp. 43-57.

Liu, M.D. & Carter, J.P. (2000). Modelling the destructuring of soils during virgin compression. Geotechnique, 50(4), pp. 479-483.

Locat, J. & Lefebvre, G. (1985). The compressibility and sensitivity of an artificially cemented clay soil: the Grande Baleine marine clay. Marine Geotechnology, Quebec, Canada, 6(1), pp. 1-27.

Loiselle, A., Massiera, M., & Sainani, U.R. (1971). A study of the cementation bonds of the sensitive clays of the Outardes River region. Canadian Geotechnical Journal, 8, pp. 479-498.

Long, M., & Lunne, T. (2003). Stiffness of Onsoy clay. In Deformation Characteristics of Geomaterials, Di Benedetto et al. (Eds.), Swete & Zeitlinger, Lisse, pp. 151-158.

Lunne, T., Berre, T., & Strandvik, S. (1997). Sample disturbance effect in soft low plasticity Norwegian clay. Proceedings of the Conference on Recent Developments in Soil Mechanics, Rio de Janeiro, pp. 81-102.

Malla, P.B. (2002). Vermiculites. In J.B. Dixon & D.G. Schulze (Eds.), Soil mineralogy with environmental applications (pp. 501-529). Soil Science Society of America, Madison, Wisconsin.

Marques, J.J., Teixeira, W.G., Schulze, D.G., & Curi, N. (2002). Mineralogy of soils with unusually high exchangeable Al from the western Amazon Region. Clay Minerals, 37, pp. 651-661.

Mayne, P.W. (1995). CPT determinations of overconsolidation ratio and lateral stresses in clean quartz sands, Proceedings, International Symposium on Cone Penetration Testing (CPT '95), Vol. 2, Swedish Geotechnical Society Report No.3:95, Linkoping, pp. 215-220.

Mayne, P.W. (2005). Integrated Ground Behavior: In-Situ and Lab Tests. Proc. Deformation Characteristics of Geomaterials, 2, Lyon, France. Taylor & Francis, London, United Kingdom, pp. 155-177.

Mayne, P.W. (2006). In situ test calibrations for evaluating soil parameters. Proc., Characterization and Engineering Properties of Natural Soils II, Singapore.

Mayne, P.W., & Rix, G. (1995). Correlations between shear wave velocity and cone tip resistance in natural clays. Soils and Foundations, 35 (2), pp. 107-110.

McGown, A.F. & Ladd, C.C. (1982). Effects of cementation on the compressibility of Pierre shale. In: K.R. Demars & R.C. Chaney (Eds.) Geotechnical properties, behaviour and performance of calcareous soils. ASTM Special Technical Publication, pp. 320-339.

Mesri, G., & Castro, A. (1987). The Ca/Cc concept and K0 during secondary compression. Journal of Geotechnical Engineering, ASCE, 113 (3), pp. 230-247.

Mesri, G., & Godlewski, P.M. (1977). Time- and stress-compressibility interrelationship. Journal of Geotechnical Engineering, ASCE, 103 (5), pp. 417-430.

Minder, P., & Puzrin, A.M. (2013). Combining biomineralization with chemically enhanced drainage in soils. In Manassero et al. (Eds.), Coupled phenomena in environmental geotechnics, Taylor & Francis Group: London.

Mitchell, J.K. (1993). Fundamentals of soil behavior. 2nd edition. John Wiley & Sons, Inc.: New York.

Muzikar, P., Elmore, D., and Granger, D.E. (2003). Accelerator mass spectrometry in geologic research. Geological Society of America Bulletin, v. 115, pp. 643-654.

Nishida, Y. (1956). A brief note on compression index of soils. Journal of Soil Mechanics and Foundations Division, ASCE, 82 (3), pp. 1027-1-1027-14.

Obura, P.A. (2008). Effect of soil properties on bioavailability of aluminum and phosphorus in selected Kenyan and Brazilian acid soils. PhD Thesis, Department of Agronomy, Purdue University, West Lafayette, IN.

Ohtsubo, M., Egashira, K., Tanaka, H., & Mishima, O. (2002). Clay minerals and Geotechnical index properties of marine clays in East Asia. Marine Georesources and Geotechnology, 20, pp. 223–235.

Ozdogan, A. (2010). A study on the triaxial shear behavior and microstructure of biologically treated sand specimens. PhD Thesis, University of Delaware.

Palomino, A.M., Burns, S.E., & Santamarina, J.C. (2008). Mixtures of fine-grained minerals—Kaolinite and carbonate grains. Clays Clay Miner., 56 (6), pp. 599-611.

Perret, D. (1995). Diagenese mecanique precoce des sediments fins du Fjord Saquenay. PhD Thesis, Universite Laval, Quebec, Canada.

Pigati, J.S., Rech, J.A., and Nekota, J.C. (2010). Radiocarbon dating of small terrestrial gastropod shells in North America, Quaternary Geochronology, 5, pp. 519-532.

Piratheepan, P. (2002). Estimating Shear-Wave Velocity from SPT and CPT Data. MS Thesis, Department of Civil Engineering, Clemson University, SC.

Reddy, M.M., Plummer, L.N., & Busenberg, E. (1981). Crystal growth of calcite from calcium bicarbonate solutions at constant PCO2 and 25 °C: a test of calcite dissolution model. Geochimica et Cosmochimica Acta, 45, pp. 1281-1289.

Reimer, P., Baillie, M., Bard, E., Bayliss, A., Beck, J., Blackwell, P., Ramsey, C.B., Buck, C., Burr, G., Edwards, R., Friedrich, M., Grootes, P., Guilderson, T., Hajdas, I., Heaton, T., Hogg, A., Hughen, K., Kaiser, K., Kromer, B., McCormac, F., Manning, S., Reimer, R., Richards, D., Southon, J., Talamo, S., Turney, C., van der Plicht, J., Weyhenmeyer, C., (2009). IntCal09 and Marine09 radiocarbon age calibration curves, 0–50,000 years cal B.P. Radiocarbon 51 (4), pp. 1111-1150.

Rich, C.I. & Barnhisel, R.I. (1977). Preparation of clay samples for X-ray diffraction analysis. In J.B. Dixon & S.B. Weed (Eds.), Minerals in soil environments (pp. 797-808). Soil Science Society of America, Madison, Wisconsin.

Robertson, P.K. (2009). Interpretation of cone penetration tests – a unified approach. Canadian Geotech. J., 46 (11), pp. 1337-1355.

Rosenqvist, I.T. (1975). Clay mineralogy applied to mechanics of landslides. Geologia Applicata e Idrogeologia, 10(2), pp. 21-31.

Sangrey, D.A. (1972). On the causes of natural cementation in sensitive soils. Canadian Geotechnical Journal, 9, pp. 117-119.

Santagata, M.C. (1998). Factors affecting the initial stiffness and stiffness degradation of cohesive soils. PhD Thesis, Department of Civil and Environmental Engineering, Massachusetts Institute of Technology, Cambridge, MA.

Santagata, M.C., Sinfield, J.V., & Germaine, J.T. (2006). Laboratory simulation of field sampling: comparison with ideal sampling and field data. Journal of Geotechnical and Geoenvironmental Engineering, 132 (3), pp. 351-362.

Schmertmann, J.H. (1955). The undisturbed consolidation of clay. Transactions, ASCE 120, pp. 1201-1233.

Schmidt, B. (1966). Earth pressures at rest related to stress history. Canadian Geotechnical Journal, 3 (4), pp. 239-242.

Schulze, D.G. (1984). The influence of aluminum on iron oxides. VIII. Unit-cell dimensions of Al-substituted goethites and estimation of Al from them. Clays and Clay Minerals, 32 (1), pp. 36-44.

Sharma S.S., & Fahey, M. (2003). Evaluation of cyclic shear strength of two cemented calcareous soils. J. Geot. Geoenviron. Eng., 129, pp. 608-618.

Sheahan, T.C. (1991). An experimental study of the time-dependent undrained shear behavior of resedimented Boston blue clay using automated stress path triaxial equipment. PhD Thesis, Department of Civil and Environmental Engineering, Massachusetts Institute of Technology, Cambridge, MA.

Sheahan, T.C., & Germaine, J.T. (1992). Computer automation of conventional triaxial equipment. Geotechnical Testing Journal, ASCE, 15 (4), pp. 311-322.

Shibuya, S., Hwang, S.C. & Mitachi, T. (1997). Elastic shear modulus of soft clays from shear wave velocity measurement. Geotechnique, 47 (3), pp. 593-601.

Skempton, A.W., & Northey, R.D. (1952). The sensitivity of clays. Geotechnique, 3 (1), pp. 30-53.

Sykora, D.E., & Stokoe, K.H. (1983). Correlations of in-situ measurements in sands of shear wave velocity. Soil Dyn. Earthq. Eng., 20, pp. 125-136.

Tavenas, F. & Leroueil, S. (1990). Laboratory and in-situ stress-strain-time behaviour of soft clays, state-of-the-art paper, Proc. Int. Symp. Geot. Engng Soft Soils, Mexico City, 2.

Tavenas, F.P., Leblond, P.J., & Leroueil, S. (1983). The permeability of natural soft clays, part II: Permeability characteristics. Canadian Geotechnical Journal, 20 (4), pp. 645-660.

Taylor, D.W. (1948). Fundamentals of soil mechanics. New York: John Wiley & Sons, Inc.

Terzaghi, K., & Peck, R.B. (1967). Soil mechanics in engineering practice. New York: John Wiley & Sons, Inc.

Terzaghi, K., Peck, R.B., & Mesri, G. (1996). Soil mechanics in engineering practice, 3rd Ed. New York: John Wiley & Sons, lnc.

Thornbury, W.D. (1937). Glacial geology of southern and south central Indiana. Indiana Dept. Cons., Div. Geol., 138 p.

Thornbury, W.D. (1940). Weathered zones and glacial chronology in southern Indiana. Jour. Geology 48 (5), pp. 449-475.

Thornbury, W.D. (1950). Glacial sluiceways and lacustrine plains of southern Indiana. Indiana Geological Survey Bulletin, 4, 21 p.

Thornbury, W.D., & Deane, H.L. (1955). The geology of Miami county, Indiana. Indiana Dept. Cons., Indiana Geol. Survey Bull. 8, 49 p.

Velde, B. (1992). Introduction to clay minerals: Chemistry, origins, uses and environmental significance. London: Chapman & Hill.

Wayne, W.J. (1965). The Crawfordsville and Knightstown moraines in Indiana. Indiana Dept. Cons., Indiana Geol. Survey Report of progress 28, 15 p.

Wayne, W.J. (1971). Marl resources of Indiana. Indiana Dept. of Natural Resources, Indiana Geol. Survey Bull. 42-G, 16 p.

Wayne, W.J., & Thornbury, W.D. (1951). Glacial geology of Wabash County, Indiana. Indiana Dept. Cons., Indiana Geol. Survey Bull. 5, 39 p.

Weiler, W.A.Jr. (1988). Small Strain Shear Modulus of Clay. Earthquake Engineering and Soil Dynamics II – Recent Advances in Ground-Motion Evaluation, ASCE Geotechnical Special Publication, No. 20, pp. 331-345.

Weir, A.H., Ormerod, E.C., & El Mansey, I.M.I. (1975). Clay mineralogy of sediments of the western Nile delta. Clay Miner., 10, pp. 369-386.

Wissa, A.E.Z., Christian, I.T., & Davis, E.H. (1971). Consolidation at constant rate of strain. Journal of Soil Mechanics and Foundation Division, 97 (10), pp. 1393–1413.

Zhu, L. (2009). An integrated study of steam-induced property changes of clay minerals. PhD Thesis, Department of Geological Sciences, Indiana University, IN.

VITA

VITA

Alain El Howayek completed his Bachelor of Engineering degree in Civil Engineering at the Lebanese American University in 2009. During his studies, he had a summer INTERN in Dubai with the Consolidated Contractors Company working in the Burj Dubai – The Dubai Mall Project. After graduation, he then moved to the United States and joined Purdue University, where he received his MS in Civil Engineering in 2011 and currently he is a PhD candidate of Civil Engineering.

Alain has served as the president and treasurer of the Geo-Institute Graduate Student Organization at Purdue and he is a student member of the Geo-Institute of the ASCE and the ASTM. He has received the 2016 outstanding graduate student award, the 2013 outstanding service scholarship, the first place in the GeoPoster competition at the 2012 Geo-Congress, and the Gerald and Beryl Leonards Fellowship in 2009.